DFT insight into the oxygen reduction reaction (ORR) on the $Pt_3Co(111)$ surface.

Thesis submitted for the degree of Master of Science in Engineering in Chemical Engineering at the University of Cape Town

by

Molefi Matsutsu

October 2012

Department of Chemical Engineering

Centre for Catalysis Research

Private Bag X3

Rondebosch 7701

South Africa

Synopsis

Proton exchange membrane fuel cells (PEMFC) are identified as future energy conversion devices, for application in portable and transportation devices. The preferred catalyst for the PEMFC is a Pt-catalyst. However, due to the slow oxygen reduction reaction (ORR) kinetics, high Pt loadings have to be used. The high Pt loadings lead to high costs of the PEMFC. Pt-Co alloys have been identified as catalysts having higher ORR activity higher than of a Pt-catalyst. Therefore, in the present study, the Density Functional Theory (DFT) technique is used to gain fundamental insight into the ORR on the $Pt_3Co(111)$ surface.

The calculations have been performed using the plane wave based code, the Vienna *ab-initio* Simulation Package (VASP). DFT spin-polarized calculations, utilizing the GGA-PW91 functional, have been used to study the adsorption of the ORR intermediates, viz. O_2, O, OOH, OH, H_2O and HOOH on the $Pt_3Co(111)$ surface. The results obtained on the $Pt_3Co(111)$ surface are compared to the results obtained on the Pt(111) surface. The adsorption strength of the ORR intermediates has been shown to be affected by the presence of Co to varying extents on the $Pt_3Co(111)$ surface relative to adsorption on the Pt(111) surface. The most strongly stabilised ORR intermediate on the $Pt_3Co(111)$ surface relative to adsorption on the Pt(111) surface is O: on the $Pt_3Co(111)$ surface O is 0.45 eV more strongly adsorbed than on the Pt(111) surface. The least affected ORR intermediate is H_2O: H_2O adsorption on the $Pt_3Co(111)$ surface is 0.20 eV more stable than on the Pt(111) surface. The energetically favorable, i.e. most strongly bound adsorption configurations for all the ORR intermediates involves a configuration in which the ORR intermediate is bonded to a surface Co atom. Therefore, the surface Co atom stabilizes the adsorption of the ORR intermediates, relative to adsorption on the Pt(111) surface.

Coadsorbed configurations have been used to study the formation and dissociation of the ORR intermediates. From the coadsorption studies, it is shown that there is an energy cost associated with moving the adsorbates from their lowest energy sites, while separately adsorbed, to the higher energy coadsorbed state, prior to reaction. Hence, adsorbate-adsorbate interactions are expected to destabilize the coadsorbed state at the coverages considered in the present study.

The Climbing Image Nudged Elastic Band (CI-NEB) method has been used to locate the transition states and to calculate the activation energies of the different elementary reaction steps. The calculated dissociation reaction activation energies for the $Pt_3Co(111)$ surface are found to be lower than the dissociation activation energies calculated on the Pt(111) surface. The most lowered dissociation activation energy is for the dissociation of O_2: on the $Pt_3Co(111)$ surface the activation energy is 0.08 eV, whilst on the Pt(111) surface the activation energy is 0.59 eV. For the hydrogenation reaction steps, only the hydrogenation of O to form OH occurs with a lower activation energy of 0.86 eV on the $Pt_3Co(111)$ surface, compared to 0.95 eV on the Pt(111) surface. For other hydrogenation reaction steps, the activation energies on the $Pt_3Co(111)$ surface are higher than those on the Pt(111) surface.

Based on the calculated activation energies of the elementary ORR reaction steps, the dissociative and the O-assisted H_2O dissociation mechanisms are identified as the mechanisms most likely to be dominant on the $Pt_3Co(111)$ surface, due to having lower activation energies relative to the associative mechanisms. For both mechanisms, the reaction step with the highest activation energy is the step involving O, i.e. O hydrogenation to form OH for the dissociative mechanism, and the $O^* + H_2O^* \rightarrow 2OH^*$ reaction for the O-assisted H_2O dissociation mechanism. Thus, the reaction step involving the reaction of the strongly adsorbed O species, is identified as the potential rate limiting step of the ORR. Both the dissociative and the O-assisted H_2O dissociation mechanisms are expected to be in competition on the $Pt_3Co(111)$ surface, since the potential rate limiting step for both mechanisms have similar activation energies. Hence, the preferred mechanism will depend on the relative abundances of the H species and H_2O on the $Pt_3Co(111)$ surface. A microkinetic analysis would be need needed to fully account for concentration and entropic contributions to the rate of reaction for the different ORR elementary reaction steps.

Acknowledgements

First and for most I would like to thank God the Almighty for giving me strength and guiding me through this journey from beginning to end. I thank you God.

I also would like to pass my sincere gratitude to my mother Mrs 'Mamatsutsu Emelina Matsutsu for always being there for me. Your constant checking up with me to find out how I am coping with my studies and encouraging me to work hard has kept me going. I also thank my brother, sister, nephew and niece for always showing me their love and support, "Ke ea leboha Basia ". Special mention also goes to my grandmother Mrs 'Mangoejane Molaoa, each time I depart home for school she always gives me the most potent weapon, which is to say a prayer. The words she always uses in her prayer, "the beginning of wisdom is to fear the Lord ", have always kept me going even during tough times.

My sincere gratitude also goes to my supervisors Professor Eric van Steen and Dr. Melissa Petersen. Thank you Prof. van Steen for introducing me to the exciting world of quantum chemistry and having allowed me to advance my knowledge in catalysis under your excellent supervision and expertise. To Dr. Petersen I would like to express my sincere appreciation for the amount of time, effort and technical expertise you invested in this project. Special thank you also for the effort you put in helping shape the write up of this thesis.

I thank my fellow molecular modelling colleagues at UCT, Thendo Madala, Junaid Cariem, Christian De Vries and Kyle Abrahams for their cooperation in sharing the computational resources we have. Thank you Thendo for the discussions and the assistance you offered with the calculations and also for having made your data available to me so that I could make comparisons to my results. Special thanks goes to Mr Graham Inggs (chimera system administrator) for the technical assistance with computer related issues.

I thank H*ySA* catalysis for their financial support for this study. The Centre for Catalysis Research at UCT is also acknowledged for affording me the opportunity to learn and broaden my knowledge.

The Centre for High Performance Computing of the CSIR is greatly appreciated for having allowed me access to use their supercomputes, without which the progress of this project would have been slowed.

I also thank my friends who have provided enjoyable company during the course of this study, Ts'epang Khonthu, Malibongwe Manono, Lusani Mulaudzi, Tshepo Ntsane, Gubevu Maduna, Conrad Ndimande, Ramonate Makha, Chakala Mphafi, Mopeli Khama,.... and many other friends, thank you very much gentlemen.

Plagiarism declaration

“I know the meaning of plagiarism and declare that all the work in the document, save for which is properly acknowledged is my own ”

Molefi Matsutsu 04/10/2012

Contents

List of Figures

List of Tables

Chapter 1

Introduction and Literature Review

1.1 Context and scope of project

1.1.1 Context

With volatile prices of crude oil, and the expected decline in crude oil reserves, a need has arisen for alternative energy sources. Such alternative energy sources include the fuel cell. The advantage of the fuel cell is that it produces water only as its by-product and is considered to be a clean technology and is environmentally friendly. A further merit of the fuel cell is that the maximum theoretically obtainable efficiency from it is higher than that obtainable from a Carnot cycle.

However promising as it appears, the implementation of fuel cell technology such that it can compete with current energy sources, must overcome several hurdles. These hurdles include the following: availability of H_2 as a fuel; catalyst stability under oxidizing conditions such as is found in proton exchange membrane fuel cells; high Pt catalyst loadings due to high overpotential losses; and the sluggish oxygen reduction reaction kinetics on the cathode.

Pt has been the catalyst of choice in fuel cells, owing to its high activity towards the oxygen reduction reaction (ORR) relative to other transition metals. However, there is a high overpotential associated with the ORR at the cathode when catalyzed by Pt. The high overpotential losses has led to increased loadings of Pt being required, but this has not led to improvements in activity of the ORR. Pt is a noble metal and as such it would be desirable to have a high utilization of it in a catalyst. In current Pt-based catalysts, the utilization of Pt is low because only a few atoms, those which are on the surface, are involved in catalytic reactions while the rest of the atoms sit inactive in the bulk of the catalyst.

Therefore, a better utilization of Pt with reduced Pt loadings is desired. Pt-based alloys are such catalysts with a reduced Pt content, since some of the Pt atoms are replaced with the alloying metal atoms. It is thus desirable that PtM alloys, where M is a less noble metal, e.g. a base metal, be used as a fuel cell catalyst. However, the PtM alloy must be such that the activity of the ORR is similar or even better than that of the pure Pt catalyst. Platinum-Cobalt alloys have been observed to be such alloys which have an activity of the ORR better than that of a pure Pt-based catalyst (Stamenković et al. 2002).

1.1.2 Scope

In this study, the focus will be on understanding how ORR activity-enhancement is attained on a $Pt_3Co(111)$ surface, by studying the adsorption of the intermediates on the surface and by determining the activation barriers for the different elementary steps for the ORR in proton exchange membrane fuel cells (PEMFC). The real fuel cell catalyst will not only expose the (111) facet, but will also expose other facets, although the percentage of other facets is expected to be

low relative to the (111) facets. The (111) facet is the lowest energy surface of Pt_3Co (Chiodo et al. 2009) and is most likely to be the dominantly exposed surface. Therefore, studying the ORR on the lowest energy surface, the (111) facet, which is most likely to be present in a real working fuel cell catalyst, is a necessary first step to gain insight into the ORR on the Pt_3Co alloy. The study is not concerned as to where the transition from ordered to disordered phase of the alloy occurs, but instead is focused on the ordered Pt_3Co phase, as this is the thermodynamically stable phase up to high temperatures including those under which low temperature fuel cells operate (50 - 100 ^oC) (Hansen and Anderko, 1958).

In the present study, only gas phase species interacting with the single crystal (111) surface plane will be investigated. Under fuel cell operating environments, the reactions on the surface occur in the presence of the liquid phase, but the effect of the liquid phase will not be investigated in this study. In the study by Sha et al.(2010) it was observed that the inclusion of solvent effects changes the adsorption energies of O_2, OOH, HOOH and OH are more stable in the presence of the solvent. The calculated activation barriers for the different elementary surface reaction steps were also affected by the presence of the solvent. Despite the difference between the calculated energies in the presence and absence of the solvent, the results followed the same qualitative trends as the calculations involving the solvent effect.

Other factors present in the fuel cell environment that will not be investigated in the current study are the the electric field effects, electric double layer effect, the electrode potential and the solvation (presence of water) effects, since their exclusion has been shown to result in qualitative reactivity trends similar to when they are included in the model. These factors are omitted since they have been studied on the Pt(111) surface (Sha et al. 2011; Karlberg et al. 2007; Hyman and Medlin, 2005), and their effect is known on the Pt(111) surface; hence it is approximately known a *priori* how much error is introduced by not explicitly including them. This assumption is assumed to hold for Pt_3Co as for Pt(111).

Karlberg et al. (2007) investigated the effect of including the local electric field on the ORR. The finding was that the local electric field only has a slight effect on the model predictions, hence the calculations performed without including the electric field effects are still valid. However, for accurate predictions at ORR potentials, inclusion of the field effects may be of importance. The change in $\triangle G_{ads}$ (free energy of adsorption) for the various ORR intermediates in the presence of the electric field was found to be modest, on the order of 0.10 eV. $\triangle G_{ads}$ is defined as $\triangle G_{ads} = \triangle G_0 + \triangle G_U + \triangle G_{pH} + \triangle G_{field}$, where $\triangle G_0$ is the difference in free energy of a gas phase species and a surface species, $\triangle G_U$ is the free energy change due to the electrode potential, $\triangle G_{pH}$ is the free energy change due to H^+ ions, and $\triangle G_{field}$ is the free energy change caused by the electric field, and is obtained by varying the external electric field in the density functional theory calculations.

The effect of applied electrode potential on the ORR has been incorporated by Nørskov et al. (2004) using density functional theory (DFT) techniques, by shifting the energy states involving proton and electron transfer by the quantity -**e**U, where U is the electrode potential and **e** is the electron charge.

1.2 Background to fuel cells

With the current energy requirements relying heavily on the dwindling natural reserves of oil, there is a need to seek alternative sources of energy. Added to this diminishing supply of crude oil is the CO_2, and other greenhouse gas emissions resulting from the combustion of oil and natural gas which is believed to lead to global warming. Thus, the sort of alternative energy conversion devices should be environmentally friendly and sustainable. A fuel cell is such an alternative energy conversion device. A fuel cell is a device that oxidises a fuel to produce energy and H_2O as the main by-product. The main fuel combusted in a fuel cell is hydrogen; other fuels include methanol, ethanol and formic acid, although the last two fuels are not easily oxidized by present-day catalysts (Gerwith and Thorum, 2010). The chemical energy released by the cell is directly converted to electrical energy, which is why the fuel cell is considered to be an efficient energy conversion device.

In Figure 1.1 a schematic of how a fuel cell operates is shown.

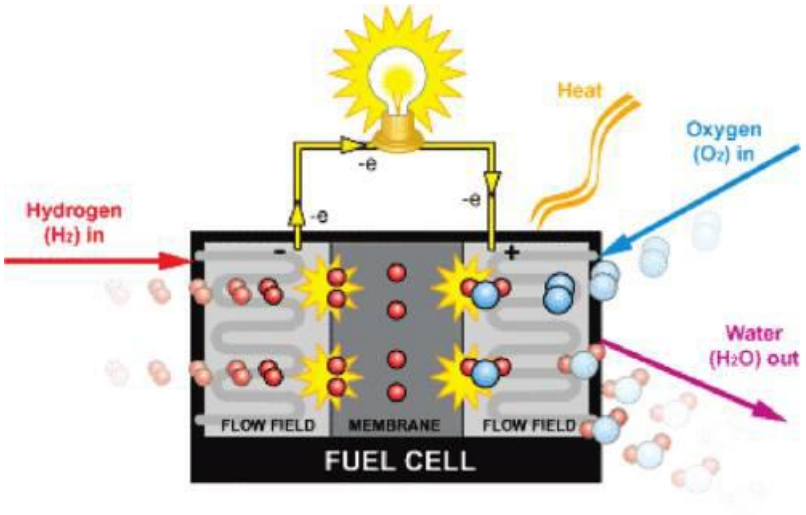

Figure 1.1: Schematic of a proton exchange membrane fuel cell operation (Gewirth and Thorum, 2010).

Regardless of the type of fuel cell, a fuel cell consists of two electrodes where the oxidation and reduction reactions occur. The electrode where the oxidation of the fuel occurs is termed the anode. Conversely, the electrode where the oxygen is reduced is known as the cathode. The anode is the negative terminal and the cathode is the positive terminal. The electrodes have a catalyst layer impregnated on them and the catalyst employed is normally Platinum supported on activated carbon. The two electrodes are separated by an electrolyte. The electrolyte allows ions to pass through it while it does not allow electrons through, if it did the electrons would be lost in it and would never reach the cathode (Larminie and Dicks, 2003). The electrons released at the anode travel to the cathode through the external circuit; in Figure 1.1 this is represented by the light bulb. The electrons participate in the reduction reaction to ensure the electroneutrality of the fuel cell. The mobile ions which pass through the electrolyte are either protons or hydroxyl ions depending on the type of fuel cell, i.e. acidic or basic cells.

1.3 Types of fuel cells

As already mentioned in the previous section, fuel cells can be categorized according to whether they are acidic or basic and further can be classified according to their operating temperature. Table 1.1 lists the classes of fuel cells together with their operating temperatures and the mobile ions in each class.

Table 1.1: Different classes of fuel cells, the mobile ions involved and the operating temperatures.

Class of fuel cell	**Mobile ions**	**Operating Temperature (°C)**
Alkaline Fuel Cells (AFC)	OH^-	50 - 200
Proton Exchange Membrane Fuel Cells (PEMFC)	H^+	50 - 100
Phosphoric Acid Fuel Cells (PAFC)	H^+	~ 220
Molten Carbonate Fuel Cells	CO_3^{2-}	~ 650
Solid Oxide Fuel Cells (SOFC)	O^{2-}	500 - 1000

In Table 1.2, a comparison is made between the advantages and disadvantages of the common low temperature fuel cell types, the AFC and the PEMFC (International energy agency, 2004)

Table 1.2: Comparison between the AFC and the PEMFC

Alkaline Fuel Cell (AFC)	**Proton Exchange Membrane Fuel Cell (PEMFC)**
1. Operating temperature (50 - 200 °C).	1. Operating temperature (50 - 100 °C).
2. Water formed at the anode.	2. Water formed at the cathode.
3. Mobile ions are OH^-. They move from	3. Mobile ions are H^+. They move from the anode
the cathode to the anode.	to the cathode.
4. Utilizes a liquid electrolyte (KOH).	4. Utilizes a solid membrane.
5. The ORR is more facile in alkaline media.	5. The ORR is slow in acid compared to alkaline
	medium.
6. Requires pure O_2 since the cell is	6. Does not require pure O_2 like the AFC and can
sensitive to CO_2 even to the trace amounts	take in air, this leads to less purification processes of
in air. The CO_2 forms carbonates which	the air which can be expensive.
precipitate into the electrolyte and thus leads	
to a reduction in cell efficiency and lifetime.	
7. Can utilize non-precious metals as catalysts	7. Utilizes the expensive precious noble metal Pt.
for both the anode and cathode, e.g. Ag, Ni	Cannot utilize the non-precious base metal catalysts.
and MnO_2.	
8. Improved material stability due to less	8. Poor material stability due to the strong oxidizing
oxidizing conditions than found in acid media.	conditions encountered in acid media.

1.4 Limitations of fuel cell operation

The fundamental technical problems associated with fuel cell operation are the slow reaction rates and the not so readily available hydrogen fuel (Larminie and Dick, 2003). One of the severe shortcomings to be overcome in order for the present-day fuel cell technology to be economically attractive is the low rate of the cathode reaction of oxygen reduction (Nørskov et al. 2004). The ORR is not facile even with a platinum catalyst, and this difficulty in oxygen reduction has been suggested to stem from the exceptionally strong oxygen double bond at 498 kJ/mol (Gewirth and Thorum, 2010). The activation of this bond is believed to be in general kinetically slow (Gewirth and Thorum, 2010). It is known that the ORR is the major barrier in the efficiency of the PEMFC (Pillay et al. 2010). The most important issue to solve for economic viability is to find more effective catalysts than Pt for the oxygen reduction reaction (Stamenković et al. 2006).

1.4.1 Hydrogen supply

Currently, hydrogen is not readily available as a fuel, it is manufactured through the following processes:

1. Natural gas reforming in the temperature range 700-1000 °C and the pressure range 3 -25 bar over a supported nickel or noble metal catalyst followed by the water gas shift reaction at lower temperatures to maximize hydrogen production. The low temperature water gas shift reaction occurs in the temperature range of 190- 210 °C over Cu supported on mixed zinc oxide and aluminium oxide catalyst and the high temperature water gas shift reaction occurs at 350 °C over Fe oxide promoted with chromium oxide catalyst. Supported noble metal catalyst are also tested for activity for the water gas shift reaction.
2. Coal gasification through reacting coal with oxygen and steam under high pressure conditions of c.a. 35 bar and high temperature of about 1200 °C to form synthesis gas. After removal of the impurities from the synthesis gas hydrogen production is maximised through the water gas shift reaction by reacting CO with steam.
3. Partial oxidation of natural gas by reacting methane and other hydrocarbons in natural gas with limited oxygen obtained from air in the temperature range 500-700 °C. Hydrogen production is maximised through the water gas shift reaction by reacting steam and the CO produced from the partial oxidation reaction.

The processes for H_2 production through natural gas reforming, coal gasification and partial oxidation of natural gas are multi-step processes and this leads to the high capital cost of the chemical plants leading to high costs of hydrogen. Furthermore these processes are accompanied by the production of CO and CO_2 as co-products, which are undesirable gases with CO being poisonous and CO_2 being a greenhouse gas believed to contribute to global warming. For a sustainable future, utilization of hydrogen generated through electrolysis of water using solar energy is desired (Gewirth and Thorum, 2010).

1.4.2 Slow oxygen reduction reaction (ORR) kinetics

Platinum is usually used as the ORR catalyst, but there is a considerable overpotential associated with this reaction on Pt (Nørskov et al. 2004). This cell overpotential directly affects the efficiency of the fuel cell, and consequently the slow ORR kinetics affects the thermodynamic efficiency of the cell (Gewirth and Thorum, 2010). One of the proposed causes of the slow ORR is a reduction or decrease in the number of active sites for O_2 adsorption caused by OH adsorption on Pt sites; the blocked sites are the sites which would have been available to adsorb and reduce O_2. Thus, OH adsorption on Pt has a poisoning effect (Nilekar and Mavrikakis, 2008; Stamenković et al. 2006).

The oxygen adsorption strength is thought to be key to the ORR, and the overpotential experienced in the cell has been linked to the oxygen adsorption strength (Stamenković et al. 2006; Wang et al. 2004). Nørskov et al. (2004) , Stamenković et al. (2006) and Markovic et al. (1996) argue that if atomic O is adsorbed weakly the ORR is limited by the dissociation of O_2 or charge transfer i.e. electrons and protons to the adsorbed molecular oxygen. Otherwise, for strongly adsorbed O the adsorption of O and OH on the surface is strong at the electrode potential where the cathode reaction is at equilibrium and thus the removal of these species on the surface limits the ORR.

Figure **1.2** is an illustration of the calculated cell voltage and the current obtained for fuel cell operation.

Nørskov et al. (2004) proposed from Figure 1.2 that substantial currents cannot be obtained for cells operating at cell voltages near the thermodynamic value of 1.23 V. At these very high potentials, Nørskov et al. (2004) argues that electron and proton transfer becomes impossible on the Pt(111) surface. In order to obtain appreciable currents, more driving force or overpotential is required, and this lowering in potential results in the transfer of protons and electrons

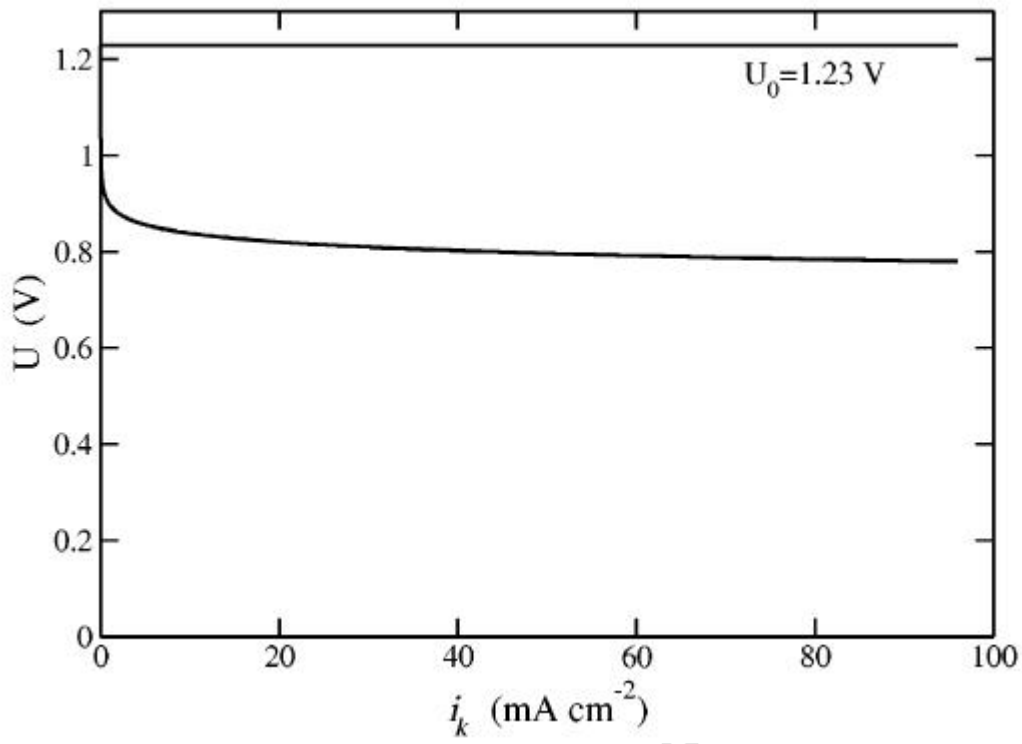

Figure 1.2: Graph of calculated cell voltage variation as a function of fuel cell current during operation (Nørskov et al. 2004)

on the Pt(111) surface. The reduction in potential leads to the transfer of protons and electrons occurring and thus the ORR reaction can proceed (Nørskov et al. 2004). Required currents are of the order of 1.5 A cm^{-2} of the membrane electrode assembly (MEA) area and in order to achieve these high currents only about 50% of the thermodynamic voltage is achieved in the cell due to the ORR overpotential losses and other losses such as mass transfer overpotentials and Ohmic loss overpotentials (Gewirth and Thorum, 2010).

At the electrode potential of about 0.80 V, water spontaneously dissociates and this is also the potential at which the proton and electron transfer to adsorbed O and OH becomes activated, the result of which is proposed to be the slowing down of the ORR process (Nørskov et al. 2004). The dissociation of water results in OH, which is argued to lead to OH blockage of the active sites for O_2 adsorption, further decreasing the rate of the ORR process (Fouda-Onana and Savagado, 2009).

The electrical efficiency ε of the fuel cell is related to the cell overpotential. The relationship is presented in the equation below:

$$\varepsilon = 1 - \frac{\eta_a + \eta_b}{\triangle E^{o}} \tag{1.1}$$

where η_a is the overpotential at the anode, η_b is the overpotential at the cathode and ΔE^o is the total cell potential. For current hydrogen oxygen fuel cells η_a is on the order of 50 mV and η_b is 500 - 600 mV for operation at 80 ^0C and 1.5 A cm^{-2} of the membrane electrode assembly area (Gewirth and Thorum, 2010). Current catalysts result in at best a low efficiency of 40 % relative to the maximum theoretical values (Gewirth and Thorum, 2010). A challenge remains to find a catalyst which leads to a higher efficiency for the fuel cell performance.

1.5 Reactions occurring during fuel cell operation

The fuel cell is divided into two terminals: the anode where oxidation of the fuel occurs, and the cathode where reduction of the oxidant occurs. The focus of the current study is on low temperature fuel cells, and thus only general cases of either acidic or alkaline fuel cells will be considered. The reactions occurring at the electrodes can be split into oxidation and reduction half reactions.

1.5.1 Anode reactions

The main reaction occurring at the anode for both acidic and alkaline fuel cells are presented below together with their electrode potentials relative to the standard hydrogen electrode (SHE).

Acidic fuel cell reactions

$2H_{2\,(g)} \rightarrow 4H^{+}_{(aq)} + 4e^{-}$ E^0= 0.000 V relative to SHE

Alkaline fuel cell reactions

$2H_{2\,(g)} + 4OH^{-}_{(aq)} \rightarrow 4H_2O_{(l)} + 4e^{-}$ E^0= 0.828 V relative to SHE

1.5.2 Cathode reactions

Acidic fuel cell reactions

$O_{2\,(g)} + 4e^{-} + 4H^{+}_{(aq)} \rightarrow 2H_2O_{(l)}$ E^0= 1.229 V relative to SHE

Alkaline fuel cell reactions

$O_{2\,(g)} + 4e^{-} + 2H_2O_{(l)} \rightarrow 4OH^{-}_{(aq)}$ E^0= 0.401 V relative to SHE

The two half reactions can be combined together to form an overall cell reaction. The overall cell reaction is identical for both the alkaline and the acid fuel cells.

1.5.3 Overall cell reaction for the acidic and alkaline fuel cell

$2H_{2\,(g)} + O_{2\,(g)} \rightarrow 2H_2O_{(l)}$

1.6 Oxygen reduction reaction mechanism

Despite the simplicity of the ORR reactants and products, the reaction mechanism is complex. Research is continuing on aspects such as the rate-limiting step and the nature of the surface intermediates (Nilekar and Mavrikakis, 2008).

The mechanism of the ORR is commonly classified into two broad categories which are thought to depend on the mode of O_2 adsorption on the surface, which subsequently dictates which path is followed. The categories for the ORR mechanisms are the following:

1. Dissociative mechanism
2. Associative mechanism

It has been proposed by Mustain and Prakash (2007) and Hagen, (2006) that on (111) facets of face centred cubic transition metal electrocatalysts, for adsorption of O_2 parallel to the catalyst surface the dissociative mechanism operates, resulting in adsorbed atomic oxygen that is then protonated and reduced to form water. For adsorption with the axis of the O_2 bond normal to the catalyst surface, the associative mechanism is thought to occur. In the associative mechanism

the O_2 is bonded to the surface with no bond cleavage. This mechanism proceeds via the formation of OOH which results from the partial reduction of O_2 . The OOH species is then proposed to be reduced to form water or protonated to form HOOH (Nørskov et al. 2004). Three different proposed adsorption modes of oxygen (Adzic and Wang, 1998) on metal surfaces are presented in Figure 1.3.

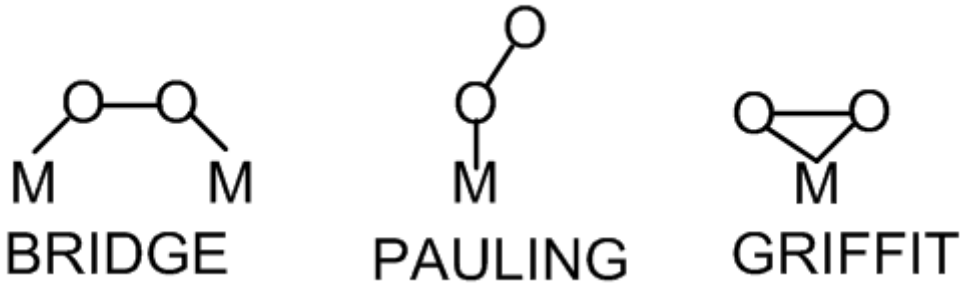

Figure 1.3: Different proposed adsorption modes of O_2 on the metal electrode surface (redrawn from Adzic and Wang, 1998)

The possible ORR mechanisms which may occur depending on the reaction conditions at the cathode proposed by Nørskov et al. (2004) are presented below:

(in the mechanisms * represents vacant sites on the catalyst and $(H^+ + e^-)$ represent the combined proton and electron transfer process)

The dissociative mechanism

$\frac{1}{2}O_2 + {}^* \longrightarrow O^*$

$O^* + (H^+ + e^-) \longrightarrow HO^*$

$HO^* + (H^+ + e^-) \longrightarrow H_2O + {}^*$

The associative mechanism

$O_2 + {}^* \longrightarrow O_2{}^*$

$O_2{}^* + (H^+ + e^-) \longrightarrow HO_2{}^*$

$OOH^* + (H^+ + e^-) \longrightarrow H_2O + O^*$ (a)

$O^* + (H^+ + e^-) \longrightarrow HO^*$

$HO^* + (H^+ + e^-) \longrightarrow H_2O + {}^*$

Instead of forming H_2O in step (a) the following reaction may occur to form hydrogen peroxide

$OOH^* + (H^+ + e^-) \longrightarrow H_2O_2 + {}^*$

The mechanism proposed by Nilekar and Mavrikakis (2008) and Shi et al. (2006) varies from the proposed associative mechanism by Nørskov et al. (2004), in that the associative mechanism is proposed to occur in two different mechanisms:

Associative mechanism 1

$O_2 + {}^* \longrightarrow O_2{}^*$

$O_2{}^* + (H^+ + e^-) \longrightarrow OOH^*$

$OOH^* + {}^* \longrightarrow O^* + OH^*$

$O^* + (H^+ + e^-) \longrightarrow OH^*$

$OH^* + (H^+ + e^-) \longrightarrow H_2O + ^*$

The difference between associative mechanism 1 and that proposed by Nørskov et al. (2004) is that the OOH^* dissociates to form $O^* + OH^*$, the dissociation occurs without any proton and electron transfer being involved, whereas the mechanism proposed by Nørskov et al. (2004) considers O-O bond scission in OOH^* coupled to proton addition and electron transfer to form H_2O and adsorbed O on the surface. Associative mechanism 1 does not include the possibility of forming HOOH.

Associative mechanism 2

$O_2 + ^* \longrightarrow O_2^*$

$O_2^* + (H^+ + e^-) \longrightarrow OOH^*$

$OOH^* + (H^+ + e^-) \longrightarrow HOOH^*$

$HOOH^* + ^* \longrightarrow 2OH^*$

$OH^* + (H^+ + e^-) \longrightarrow H_2O + ^*$

Associative mechanism 2 considers the formation of the species $HOOH^*$ which subsequently dissociates to form two adsorbed OH species on the surface. The dissociation occurs without any proton and electron transfer, and the adsorbed OH species can further be hydrogenated to form H_2O. In contrast the mechanism cited by Nørskov et al. (2004) considers only the formation of HOOH as the final product and no further reduction of HOOH to form H_2O.

Calculated activation energies of the order of 1.0 eV on Pt(111) for the hydrogenation of atomic oxygen have been reported (Michaelides and Hu, 2001) using DFT. The activation energy is considered high for the low temperature of operation of the PEMFC, rendering the direct hydrogenation of atomic oxygen not energetically favourable, leading to the postulate that a different elementary step for atomic oxygen removal during the ORR mechanism might be involved on Pt (Sha et al. 2011). The reaction of H_2O and O to form OH has been calculated to occur with much lower activation energies than the hydrogenation of atomic oxygen on Pt(111) (Michaelides and Hu, 2001). The lower activation energy for the reaction of H_2O and O, relative to the direct hydrogenation of O to form OH, has been interpreted to be an indication of a provision of viable routes for H_2O formation at low temperatures (Sha et al. 2011; Michaelides and Hu, 2001).

The proprosed new ORR mechanism termed the oxygen hydration mechanism (Sha et al. 2011) is as follows:

$O_2 + * \rightarrow O_2^*$

$O_2^* + (H^+ + e^-) \rightarrow OOH^*$

$OOH^* + * \rightarrow O^* + OH^*$

$H_2O^* + O^* \rightarrow 2OH^*$

$OH^* + (H^+ + e^-) \rightarrow H_2O^*$

Under ORR conditions, it is proposed that there is an abundant supply of water on the catalyst surface since humidified air is fed to the cathode as the membrane needs to be humidified in order to transport protons from the anode to the cathode, so that hydration of O becomes an essential step of the ORR (Sha et al. 2011).

The reaction of H_2O and O has been identified as an important step on which effort should be focused on identifying a catalyst for which the activation energy is lower than on the Pt(111) surface (Sha et al. 2011). Sha et al. (2011) proposed that by identifying a catalyst with a lower activation energy for the reaction step of H_2O and O to form OH, the efficiency of the PEMFC should be improved. The reaction step of H_2O and O to form OH has been studied through DFT on various transition metals and the lowest activation energies were reported for Ni (0.20 eV) and Co (0.04 eV) (Sha et al. 2011), the surfaces on which this reaction was studied on Ni and Co were not specified. Ni and Co have experimentally been observed to improve the efficiency of Pt cathode catalysts (Stamenković et al. 2002), therefore alloying Pt with Co or Ni is expected to improve Pt cathodes by lowering the activation energy of the potential rate-determining step which is postulated to be the disproportionation reaction step of H_2O and O to form OH (Sha et al. 2011).

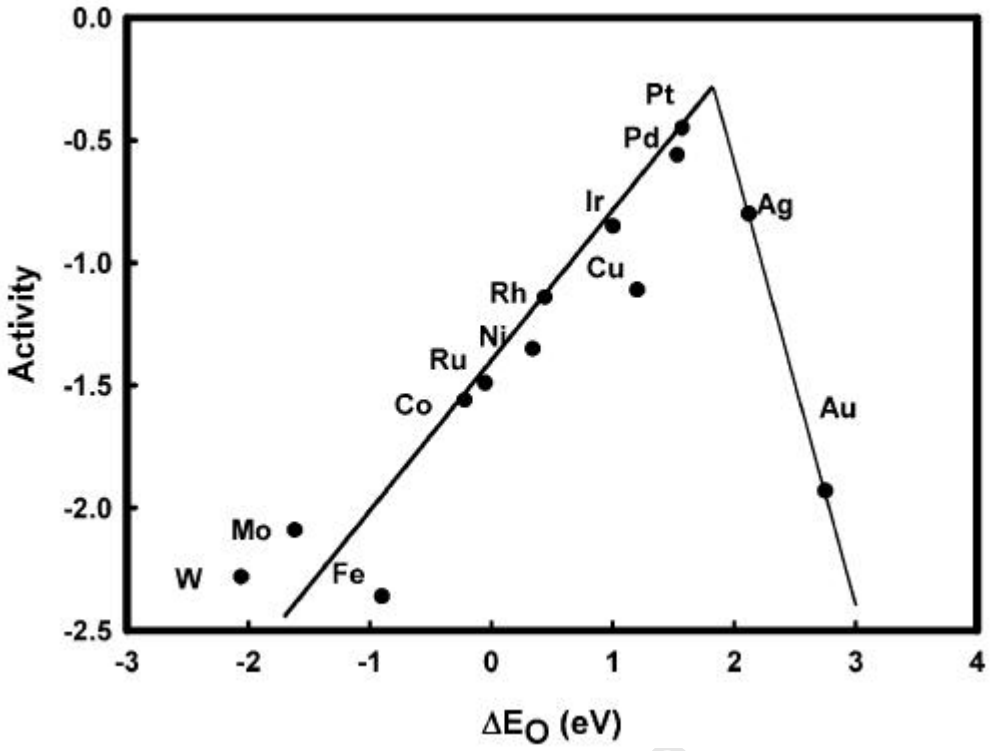

Figure 1.4: Trend in oxygen reduction activity as a function of atomic oxygen binding energy on different transition metals (Nørskov et al. 2004)

1.7 Platinum as the preferred electrocatalyst in fuel cells

Nørskov et al. (2004) have argued that a good electrocatalyst for the oxygen reduction reaction must be one in which the strength of the oxygen-metal bond is optimal, i.e neither too strong nor too weak. Based on a DFT study, Pt was demonstrated to satisfy these conditions (Zhang et al. 2005a) and as such was concluded the best mono-metallic catalyst for the ORR. The activity of the catalyst was calculated using the atomic oxygen binding energy as a descriptor of activity for a number of transition elements using DFT (Nørskov et al. 2004), as presented in Figure 1.4. The oxygen binding energy was used as a descriptor of surface reactivity, due to the fact that atomic oxygen probably interacts more strongly with the surface than any other proposed intermediate in the ORR mechanism (Zhang et al. 2005a). Therefore atomic oxygen adsorption was expected to be most sensitive to changes in surface properties, and hence was considered to be a good descriptor of activity.

From Figure 1.4 it is observed that a volcano plot was obtained for the activity as a function of atomic oxygen adsorption strength on the different transition metals (Nørskov et al. 2004). The volcano plot is in accordance with the Sabatier principle (Chorkendorff and Niemantsverdriet, 2007), where the best catalysts are those close to the top of the volcano. Platinum is close to the top and thus it was concluded to be the best catalyst for the ORR of the set of transition metals considered. From Figure 1.4 the metals which lie to the left of the top of the volcano plot such as Ru, Ni, Co etc were calculated to adsorb O so strongly that it is proposed that the surface of the metal fully oxidizes (Hyman and Meldin, 2007). Metals to the right of the maximum, such as Ag and Au, adsorb O_2 so weakly that it is proposed that molecular oxygen desorption is more favored over dissociation (Hyman and Medlin, 2007). Pt was calculated through DFT to adsorb oxygen strongly enough such that dissociation is favorable but not too strongly to oxidize the surface (Hyman and Medlin, 2007), and on this basis it was concluded that Pt qualifies as the best pure transition metal electrocatalyst for the ORR.

1.8 Ways of reducing Pt loadings in electrocatalysts

One of the main hindrances in commercializing fuel cells, e.g. PEMFC, is the expensive Pt catalyst which depends on scarce Pt reserves. Research has been undertaken to reduce Pt loadings while concurrently maintaining the cell potential. Simple reductions in the amount of Pt in the catalyst results in significant reductions in the cell voltage and power density (Gasteiger et al. 2005).

Currently-used electrocatalysts in PEMFCs are Pt-based catalysts supported on electrically-conductive porous carbon, denoted as Pt/C. To increase the relatively slow ORR kinetics and decrease the high overpotentials which may approach 0.3 V on Pt, high Pt loadings are used with values reported to be 40 wt % Pt/C corresponding to ca. 0.4 mg_{Pt}/cm^2 (Gasteiger et al. 2005). The Pt loading of 0.4 mg_{Pt}/cm^2 corresponds to mass activities of 0.16 A/mg_{Pt} at 0.9 V relative to the Reversible Hydrogen Electrode (RHE) potential (Gewirth and Thorum, 2010), the reversible hydrogen electrode is considered the reference potential which does not vary with changing pH.

For large-scale commercial PEMFC applications to be feasible, e.g. in motor vehicles, the target Pt loading is 0.10 mg/cm^2 of the MEA and the desired mass activity is 0.45 A/mg_{Pt} at 0.9 V relative to the RHE (Gasteiger et al. 2005).

To reduce Pt loadings in the catalyst, Pt nanoparticles of diameter ranges of ca. 3 - 4 nm and with active surface areas of ca. 90 $m^2{}_{Pt}/g$ have been synthesized (Gasteiger et al. 2005). These nanoparticles are supported on carbon. Reducing the Pt nanoparticle size to below 3 nm does not result in increased mass activity as compared to the state-of-the-art commercial catalyst of 40 wt % Pt/C, despite the nanoparticles having an increased active surface area (Gewirth and Thorum, 2010). The reason for the proposed size-dependence of the ORR is due to the particle-size-induced changes in the potential-dependent adsorption of oxygen-containing species such as OH_{ads}, which is thought to reduce ORR activity (Gasteiger et al. 2005).

Other techniques to reduce Pt loadings, while striving to achieve set targets of mass activities, include utilizing Pt nanoparticles with different morphologies. Pt nanoparticles with morphologies such as polyhedra, nanowires and branched structures have been synthesized (Chen et al. 2009). Despite some of these structures having higher specific activities than 40 wt % Pt/C, the improvements are more than compensated for by the reduced surface areas of the different morphologies (Gewirth and Thorum, 2010). Thus, there is no net gain in the mass activities of these particles compared to the 40 % Pt/C catalyst (Gewirth and Thorum, 2010).

It has been suggested by Gewirth and Thorum (2010) that the methods of reducing Pt loadings to achieve the desired targets (mass activities) for large-scale applications are highly unlikely to be achieved using a pure Pt catalyst.

1.9 Platinum alloys as electrocatalysts

Platinum loading in electrocatalysts can also be reduced by combining Pt with another metal in a bimetallic composition, the alloying element modifies the intrinsic catalytic activity of the Pt surface atoms (Gasteiger et al. 2005). The bimetallic alloys are in the form of Pt-M/C catalysts; examples of the alloying 3d transition element M are Fe, Ni, Co and Cu. The bimetallic alloys have been found to possess enhanced activity for the ORR over the state-of-the-art commercial Pt/C catalysts (Gasteiger et al. 2005). Various reasons for the activity-enhancement have been postulated, they include the following reasons:

1. Alloying Pt with a smaller base metal element results in the base metal entering the crystal structure, through substitution, and leads to lattice contraction (Jalan and Taylor, 1983). The increasing electrocatalytic activity of Pt alloys has been shown to correlate strongly with a decrease in interatomic or nearest-neighbor distance between Pt atoms (Mukerjee et al. 1995a; Mukerjee et al. 1995b; Toda et al. 1998; Balbuena et al. 2003). The resulting smaller Pt-Pt bond distance results in more favourable sites that enhance the dissociative adsorption of O_2 (Stamenković et al. 2002).

2. An increase in Pt 3d orbital vacancy. This is due to the formation of a thin Pt skin on the surface layer which has an increased d-electron vacancy (Toda et al. 1999; Mukerjee et al. 1995a; Mukerjee et al. 1995b; Stamenković et al. 2003; Stamenković et al. 2006)
3. Enhanced chemisorption of reaction intermediates. The other transition metal constituting the alloy results in an increase in the electron density at the catalytic sites (Seminario et al. 2005; Toda et al. 1999; Arenz et al. 2003).
4. Enhanced activity has been linked to a negative shift in the d-band center, which weakens the interaction of adsorbed intermediates with the surface, thereby leaving available active sites for O_2 adsorption (Toda et al. 1998; Toda et al. 1999; Mukerjee et al. 1995a; Mukerjee et al. 1995b; Lytle, 1976).
5. Surface roughening of Pt-alloys due to the leaching of the more oxidizable base metal in bulk alloys, this leads to higher activity due to surface area increase (Paffett et al. 1988).
6. Inhibition of the formation of the adsorbed hydroxyl species, Pt-OH, found on all the low index Platinum surfaces (Paulus 2002a; Paulus 2002b; Markovic and Ross, 1999; Stamenković et al. 2002).

Since the focus of the present study is on Pt-Co bimetallic alloys, the following section is devoted to the various methods of preparing binary Pt-Co alloys. The discussed techniques for the preparation of the Platinum bimetallic alloys will be based on the review article by Gewirth and Thorum, (2010). Under operating conditions the bimetallic alloys are argued to be in the form of Pt-skin structures, where the Pt segregates to the surface to form a monolayer of Pt underneath which is the alloy (Løvvik, 2005; Stamenković et al. 2003; Ruban et al. 1999). However, there is still debate as to whether the working catalyst is such that a complete monolayer of Pt, is formed. The following techniques have been outlined:

- Thermal annealing

Annealing is a heat treatment method used to change the micro-structure of a material, causing changes in properties such as strength, hardness and durability. The Pt-M alloys are annealed to form the Pt-skin structure.

- Electrochemical dealloying

This method is used to produce Pt-enriched surface alloy nanoparticles. In this technique, precursor particles containing Pt and the base metal on a carbon support are exposed to several hundred potential cycles. The potential cycles causes the base metal to leach out of the particles. After leaching out the base metal from the particles, a roughened Pt-enriched skin is left over the alloyed particle.

The Platinum-skin alloys prepared utilizing the methods above have higher surface areas and high specific activities, the high activities are attributed to electronic effects. The durability of the Pt-Co alloy has been found to be similar to that of carbon-supported Pt catalysts.

The noble metal loading in the ORR catalyst can also be lowered by using carbon-supported nanoparticles with non-noble metal cores and noble metal shells (Gewirth and Thorum, 2010). These type of structures are referred to as core-shell catalysts. An example of a core-shell electrocatalyst is a Pt monolayer on Carbon supported Co-Pd core-shell nanoparticles, with particle sizes of 3 - 4 nm in diameter.

In the present study the focus will be on studying the ORR on the $Pt_3Co(111)$ surface which together with the Pt-skin on $Pt_3Co(111)$ have experimentally been observed to exhibit a higher ORR activity than the Pt(111) surface by Stamenković et al. (2002). In this study the role of alloying Pt with Co and having Co present together with Pt on the surface layer will be explored in order to gain initial understanding of the effect of alloying Pt with Co on the ORR. The Pt-skin on $Pt_3Co(111)$ is not the focus of the present study since it is not known a *priori* how the surface enrichment in Pt will affect the composition of the layers near the surface. Therefore, it is prudent to focus on the bulk alloy of known composition of Pt_3Co for the surface layer and the subsurface layers, hence why the focus of the present study is on ordered Pt_3Co.

1.10 DFT and experimental studies to understand ORR enhancement on Platinum alloy surfaces

In this section, a review will be presented of experimental observations, DFT calculations performed to gain insight into the origin of the enhancement in ORR activity of Pt-based alloys. The DFT technique will be explained in detail in chapter 2. The review will focus on: *(i)*.ORR activity-enhancement on mixed-metal-monolayer PtM surfaces on Pd(111), where M is an alloying transition metal. *(ii)*.ORR activity of bulk ordered Pt_3M surfaces, and their corresponding Pt-skin structures on top of the bulk alloy, with M being a 3d transition metal element. *(iii)*.ORR activity-enhancement of Pt-monolayer supported on transition metal (111) facets. *(iv)*. ORR activity-enhancement on Pt alloys with modified electronic and geometric properties relative to Pt(111).

1.10.1 ORR activity-enhancement on mixed metal Pt-monolayer electrocatalysts

Zhang et al. (2005b) performed a combined experimental and DFT study of the oxygen reduction reaction on mixed-metal monolayer PtM surfaces on Pd(111). M was a late transition metal and the investigated metals were Ir, Ru, Rh, Pd, Au, Re and Os. The ratio between Pt and M was varied and the corresponding current densities measured for the different Pt:M ratios. The highest current density was obtained at a Pt:M ratio of 80:20. Experimentally $Pt_{(1-x)}Ir_x$/Pd/C was found to have a higher Pt mass-specific ORR activity than the pure Pt/Pd/C catalyst.

In line with the widely accepted view that OH on Pt inhibits the ORR, an enhanced ORR activity should correspond to a low OH coverage on Pt in $Pt_{(1-x)}Ir_x$/Pd/C (Zhang et al. 2005b). From in-situ X-ray absorption near edge structure spectroscopy (XANES) data on $Pt_{(1-x)}Ir_x$/Pd/C, it was suggested that Ir oxidation readily occurred on the mixed layer $Pt_{80}Ir_{20}$ monolayer catalysts, whilst Pt oxidation is suppressed on the same mixed layer monolayer catalysts, as it occurs only at higher potentials of 1.17 V (Zhang et al. 2005b).

DFT calculations were performed for the various metals M to gain insight into how the ORR enhancement occurs on such mixed-metal monolayer catalysts. For M which weakly adsorbs OH, e.g. Au, the result is a reduction in ORR kinetics relative to a pure Pt monolayer catalyst. For M which strongly adsorbs OH, e.g. Os and Ir, the result is enhancement of the ORR activity relative to a pure Pt monolayer catalyst. The enhanced activity of Os and Ir-based catalysts was linked to a strong adsorption of O and OH on these metals, the strongly adsorbed O and OH strongly repel OH on Pt sites. In the study it was observed that O adsorbed on M had a stronger repulsive force on OH on Pt than OH on M. The destabilization of OH on Pt by adsorbed O or OH on M was considered to be responsible for the enhanced ORR activity on the mixed-metal monolayer catalysts, due to a lower coverage of OH on Pt atoms.

1.10.2 ORR activity-enhancement on bulk-ordered $Pt_3M(111)$ and on Pt-skin on $Pt_3M(111)$ surfaces

Xu et al. (2004) performed DFT calculations where the adsorption energy of O_2 and O were used as descriptors for ORR activity on $Pt_3Co(111)$, $Pt_3Fe(111)$, a Pt-skin on $Pt_3Co(111)$, a Pt skin on $Pt_3Fe(111)$, Pt(111) and a 2 % compressed Pt(111) surface. The (111) surface was chosen since it is a thermodynamically stable surface and one of the most likely surfaces to be exposed (Xu et al. 2004). The study investigated gas phase species interacting with single crystal surfaces, and the authors acknowledged that under operating conditions of a fuel cell there are other parameters which may affect the results. These parameters include electric field effects, solvation effects and the role of exposed facets of the crystal other than the (111) facet (Xu et al. 2004). Xu et al. (2004) acknowledged, however, that important reactivity trends can be obtained in the absence of the solvent as was also concluded in a previous study by Christoffersen et al. (2001). The ordered Pt_3Co and Pt_3Fe alloys were studied because they are thermodynamically stable up to high temperatures (Hansen and Anderko, 1958).

Compressive strain was found to destabilize O_2 and O adsorption on the surface relative to adsorption on normal Pt(111). This appears to be in contrast to the postulate that ORR activity enhancement on Pt-alloys, can be attributed to a reduced Pt-Pt distance (Jalan and Taylor, 1983). However, in the Pt-alloys, the reduced Pt-Pt distance is coupled with modified electronic properties of Pt atoms, which is proposed to stabilize O_2 adsorption and enhance O_2 dissociation. On $Pt_3Co(111)$ and $Pt_3Fe(111)$ surfaces, O_2 and O adsorbed stronger than on Pt(111). From the calculated activation energies for O_2 dissociation, dissociation paths centred on Co had lower calculated activation energies than those centred on Pt on the $Pt_3Co(111)$ surface. On comparison, dissociation paths centred on Co had lower calculated O_2 dissociation activation energies than those calculated on Pt(111). Thus, it was concluded that the presence of Co allows O_2 to dissociate more easily on the alloy surface. A calculation of the d-band center of the surface atoms led to the proposition that surfaces with high-lying d-band centres adsorb O strongly, which enhances the kinetics of dissociation reactions producing the O adsorbate (Xu et al. 2004).

There is a strong view within the electrochemistry research community, that under fuel cell operating conditions the alloys do not adopt the bulk surface structures, but instead there is surface enrichment in Pt resulting in so-called Pt-skin structures (Løvvik, 2005; Stamenković et al. 2003; Xu et al. 2004; Ruban et al. 1993). To model the segregation phenomenon of Pt-enrichment, the Pt-skin structures were modelled with a monolayer of Pt epitaxially placed on top of the alloy surface.

On the Pt-skin structure of $Pt_3Co(111)$, O_2 and O adsorption was found to be destabilized relative to adsorption on Pt(111), resulting in high calculated activation energies for O_2 dissociation. Experimentally, the Pt-skin structures have been found to have higher mass-specific activity than Pt (Stamenković et al. 2002). Therefore, the O_2 and O adsorption strengths and the O_2 dissociation activation energy alone cannot explain the activity-enhancement on Pt-skin structures. In order to explain the experimentally-observed ORR enhancement on Pt-skin structures, Xu et al. (2004) proposed that for surfaces with low-lying d-band centres like the Pt-skin structure, O is adsorbed weaker on the Pt-skin structures than on Pt, and the weak adsorption of O facilitates the formation of bonds to the weakly adsorbed adsorbates such as O. The facilitation of bond formation was speculated to be responsible for enhanced ORR activity. The lesson learned from the study by Xu et al. (2004) is that focussing on one reaction step of a reaction mechanism and attempting to draw conclusions for the complete reaction mechanism is not sufficient. Therefore, there is a need to consider all elementary reaction steps comprising a reaction mechanism in order to draw meaningful conclusions.

1.10.3 ORR activity-enhancement on Pt monolayers supported on transition metal substrates

A combined DFT and experimental investigation was undertaken of ORR activity-enhancement on Pt monolayers supported on different transition metal substrates (Zhang et al. 2005a). The investigated transition metal substrates were: Ru(0001), Ir(111), Rh(111), Au(111) and Pd(111). The Pt(111) surface was used as a basis for comparison with the other Pt monolayer (Pt_{ML}) structures. From DFT calculations it was observed that a high-lying d-band center appeared to facilitate O-O bond breaking, whilst a low-lying d-band center facilitates bond formation, i.e. hydrogen addition (Zhang et al. 2005a). It was proposed by Zhang et al. (2005a) that the most active Pt_{ML} catalyst should have a d-band center with an intermediate value. The study revealed that on surfaces with compressive strain relative to Pt(111), i.e. Pt_{ML}on Ru(0001), Rh(111) and Ir(111), the d-band center is downshifted in energy relative to that of Pt(111), while for tensile strain the opposite effect is observed with an upward shift of the d-band center.

In the calculations, the adsorption strength of atomic oxygen (O) was used as a descriptor of ORR activity. The reason for using the O adsorption energy as a descriptor for activity is due to its sensitivity to changes in surface properties, and O's stronger interaction with the surface than any other ORR intermediate (Zhang et al. 2005a). The O-O bond breaking reaction in O_2 was considered to be representative of all O-O bond dissociation reactions, be it in O_2 , OOH

or HOOH. Similarly, the elementary step: O + H $\rightarrow$ OH, was studied to represent O-H bond-forming reactions in O-containing intermediates, be it for OH, OOH, HOOH or H_2O formation. Calculations of the activation energies for both O-O bond breaking and O-H bond forming reactions were performed for each of the different transition metal substrates. The intersection of the activation energy curves as a function of O binding energy for both O-O bond breaking and O-H bond forming reactions coincided with the values calculated for the Pt(111) surface, which was considered to be the benchmark catalyst with optimal ORR activity (Zhang et al. 2005a). Of the investigated Pt_{ML} on the different substrates, the Pt_{ML}on Pd(111) results fell in close proximity to the activation energies calculated for Pt(111). From the experimental measurements of the ORR activity in terms of the kinetic currents obtained from rotating disk electrode (RDE) measurements on the different transition metals substrates, the Pt_{ML} on Pd(111) surface was found to have a higher specific - mass activity than Pt(111) (Zhang et al. 2005a).

From the determination of the position of the d-band center for the Pt_{ML} structure, it was established that for this type of Pt_{ML} structures the d-band center position does not correlate strictly with the amount of strain.This is due to the position of the d-band center for the Pt_{ML} structures not depending only on strain effects but also on the electronic interaction between the Pt_{ML} and its substrate (Zhang et al. 2005a).

Experimentally, from voltammetry and X-ray absorption near edge structure spectroscopy (XANES) measurements, OH adsorption on Pt_{ML} on Pd(111) was shifted to more positive potentials than on Pt(111) (Zhang et al. 2005a). This was interpreted as being due to an enhanced repulsive interaction of OH groups on Pt_{ML} on Pd(111) compared to pure Pt. This observation is similar to that made on mixed-metal Pt monolayer catalysts, further signifying the importance of OH adsorption in relation to ORR activity-enhancement. From DFT calculations, a theoretical explanation by Zhang et al. (2005a) was provided for the experimental observation of OH repulsion on Pt_{ML}on Pd(111). Experimentally, a high ORR activity is linked to a reduced OH coverage on Pt atoms, whilst from DFT calculations, a reduced OH coverage is proposed to be due to enhanced hydrogenation rates (Zhang et al. 2005a). Zhang et al. (2005a) proposed that the hydrogenation rates of all O-containing species should follow a similar trend to the O hydrogenation rate. However, this is a claim which was not verified through supporting calculations, and there is no reason to believe that O hydrogenation should necessarily follow the same hydrogenation rates as other O-containing species, such as OH and OOH, since they are chemically different species and could behave differently in hydrogenation reactions. From the calculations, the OH adsorption energy on Pt_{ML} on Pd(111) was found to be weaker than on Pt(111). From the study, it was concluded that the kinetics of O-O bond breaking steps and the hydrogenation of reactive intermediates have to be facilitated at the cathode, for a good ORR catalyst (Zhang et al. 2005a).

Nilekar and Mavrikakis (2008) continued the study of Zhang et al. (2005a), and included the adsorption of other ORR intermediates. The same transition metal substrates as used in the previous study by Zhang et al. (2005a) were considered. The adsorption energies of the different ORR intermediates were determined, from which a free energy diagram (FED) was constructed, using the equilibrium ($\frac{1}{2}H_2 \rightarrow H^+ + e^-$) to represent proton and electron transfer processes, as proposed by Nørskov et al. (2004). The FED was constructed at the equilibrium potential of 1.23 V and a potential of 0.80 V. The study considered three mechanisms for O_2 dissociation, and the activation energy for O_2 dissociation for each mechanism was determined. Mechanism 1 was the direct dissociation of O_2 to form two adsorbed O atoms, mechanism 2 was O-O dissociation in OOH to form O and OH, and mechanism 3 was O-O dissociation in HOOH to form two adsorbed OH species. In all three mechanisms, the O and OH species were hydrogenated to form water as the final product.

For the different transition metal substrates investigated, the results for Pt_{ML} on Pd(111) were found to result in a higher activity than that of Pt(111). The activity was obtained from a simple microkinetic model explained in detail in the article by Nørskov et al. (2004). Comparing the FED at 1.23 V and 0.80 V, it was observed that at 1.23 V the reaction steps which involve proton and electron transfer have positive free energy values and do not spontaneously occur. At the equilibrium potential of 1.23 V, the activity of all five surfaces, i.e. Pt_{ML} on Pd(111), Pt_{ML} on Ru(0001), Pt_{ML}on Ir(111), Pt_{ML}on Rh(111), Pt_{ML}on Au(111) and Pt(111) was the same. On lowering the potential to 0.80 V, the free energies of some of the elementary reaction steps involving proton and electron transfer are reduced and change from positive to negative, and

some of the steps can occur spontaneously, these elementary reaction steps can then compete with the potential independent reactions (i.e. reactions not involving electron transfer). The activation energies for the O-O dissociation reactions were lower at the lower operating potential than at the high operating potential. For both 1.23 V and 0.80 V operating voltages, the hydrogenation step of OH to form water was the step which was endergonic due to having the most positive Free energy change on the FED. At the operating potential of 0.80 V, this reaction step becomes less endergonic (Nilekar and Mavrikakis, 2008).

For the best ORR catalyst of the systems considered by Zhang et al. (2005a) and Nilekar and Mavrikakis (2008) which is Pt_{ML} on Pd(111), a small difference in the calculated activation energy for O-O bond-breaking and O-H bond forming reactions was obtained (Nilekar and Mavrikakis, 2008). For surfaces where a large difference in the calculated activation energy for O-O bond-breaking and O-H bond-forming elementary reactions steps was calculated, e.g. Pt_{ML} on Ir(111), a reduction in ORR activity relative to the activity of Pt(111) was obtained. From the FED of the different surfaces, it was concluded that for systems with a strong O adsorption energy, the rate is limited by bond-making steps involving H-addition to an O-containing reaction intermediate, e.g. Pt_{ML} on Pd(111) (Nilekar and Mavrikakis, 2008; Stamenković et al. 2006). For surfaces with a weaker O adsorption energy, the activity is determined by O-O bond-breaking events be it in O_2, OOH or HOOH; an example of a surface where this occurs is Pt_{ML} on Ir(111) (Nilekar and Mavrikakis, 2008; Stamenković et al. 2006).

The study further deduced that for a good ORR catalyst there must be an optimal balance between O-O bond breaking activity and O-H bond forming activity.

1.10.4 ORR activity-enhancement on Pt alloy surfaces with modified electronic and geometric properties relative to Pt(111)

Hyman and Medlin (2007) studied O, O_2, OOH, OH and H_2O adsorption on PtMPt 'sandwich' structures, to investigate the ligand effect on the adsorption of the ORR intermediates. They also studied the adsorption of the ORR intermediates on strained Pt(111) surfaces to investigate the effect of strain. Furthermore they investigated the combined ligand and geometric effect, by considering Pt-skin structures on: $Pt_3Co(111)$, $Pt_3Ni(111)$ and $Pt_3Fe(111)$ and Pt pseudomorphic overlayers on Co(111), Ni(111) and Fe(111). The pseudomorphic overlayers means the top layer is Pt only and the underneath layers consist of the base metal. Hyman and Medlin (2007) concluded that the adsorption energies of the intermediates correlate with each other except for the adsorption energy of atomic oxygen (O) on the PtMPt 'sandwich' structures and the Pt pseudomorphic structures . The adsorption energies correlate such that the difference in adsorption energies calculated on the PtMPt surfaces relative to Pt(111) follows the same trend. For example, if the difference in the O_2 adsorption energy on PtMPt relative to Pt(111) is 0.20 eV, the difference in adsorption energy of, e.g. OH for PtMPt and Pt can be related to the difference in O_2 adsorption strength on the two surfaces. Hyman and Medlin (2007) concluded that the poor correlation between the O adsorption energy and that of the other ORR intermediates, renders the O adsorption energy an imprecise activity descriptor for the ORR. This observation contradicts the proposal by Xu et al. (2004), that O is a good activity descriptor for the ORR. The contradiction can be considered to be an indication that using only one species, O, as an ORR activity descriptor is not sufficient to describe the complete ORR mechanism, since other ORR intermediates may not follow the same reactivity trends as O. Instead, Hyman and Medlin (2007) proposed that the adsorption energy of OH is the most likely important factor in determining a surface's resistance to inhibition of the ORR, while O and O_2 adsorption energies help determine the kinetically limited rates.

Compressive strain due to the reduction in the Pt-Pt bond distance was argued to be the primary mechanism of OH destabilization on Pt/Pt_3M surfaces (Hyman and Medlin, 2007). Hyman and Medlin (2007) argued in favour of compressive strain destabilizing O and O_2 adsorption on Pt/Pt_3M surfaces. It was discovered through calculations that overly-strained surfaces are likely to be unsuitable ORR catalysts, due to severe destabilization of O_2 (Hyman and Medlin, 2007). Except for Pt(111), the d-band center by itself was found not to be predictive of the adsorption energy trends, due to the uneven redistribution of the d-band induced by the ligand effects (Hyman and Medlin, 2007; Kitchin et al. 2004). Moreover, adsorption on surfaces with

both strain and ligand effects present cannot be predicted based on separate consideration of the effects, since they cannot easily deconvoluted when both effects are present at a catalyst surface (Kitchin et al. 2004).

For surfaces with a weak ligand effect such as Pt/Pt_3M surfaces, Hyman and Medlin (2007), proposed that adsorption energy shifts can be approximated based on the changes in the Pt-Pt bond distances. Strain also affects the distribution of states near the Fermi level. The states near the Fermi level are important, since they determine the availability of electrons for bonding, and the availability of unoccupied states that determine the interaction with the adsorbate's antibonding states (Hyman and Medlin, 2007; Stamenković et al. 2006).

1.10.5 Summary of reviewed literature

From the reviewed literature it emerges that ORR activity-enhancement can be achieved in two different modes:

1. ORR activity-enhancement on Pt-skin structures, due to the electronic interaction which is a result of lattice strain and the ligand effect on Pt induced by the substrate alloy or transition metal substrate.
2. ORR activity-enhancement on mixed-metal PtM surface structures due to inhibition of OH accumulation on Pt sites.

From the review it is evident that ORR activity-enhancement depends on both the geometric and electronic effects present in the alloy catalyst surface. The O adsorption energy is essential as an ORR activity descriptor, as it is linked to the rate determining steps, but knowledge of the O adsorption energy on its own is not sufficient to explain the observed activity improvements of certain surfaces, such as Pt-skin structures. Moreover, understanding OH adsorption on the surface is important, since the OH adsorption strength is an important factor in determining a surface's resistance to inhibition of the ORR. A different OH adsorption behavior is seen on Pt-skin structures and on mixed-metal monolayer PtM structures: on Pt-skin structures a weakened OH adsorption strength relative to the pure Pt(111) surface is observed whilst a stronger OH adsorption strength on the alloying element M relative to Pt(111) is observed on the mixed-metal monolayer PtM surface. The difference leads to the suggestion of different ORR activity-enhancement modes on the two different types of surfaces. In addition, low OH coverages are linked to ORR activity-enhancement experimentally, justifying the need to understand OH adsorption behavior on the catalyst surface.

From the reviewed literature it also emerges that a good ORR catalyst must strike a balance between bond-breaking activity (O-O bond scission) and bond-forming activity (O-H) at the fuel cell operating potential.

The predominant approach based on the surveyed literature has been to use the O adsorption strength as the ORR activity descriptor, meaning that ORR performance is assumed predictable from the O adsorption strength without considering the adsorption of other intermediates. This approach has been shown to fail on surfaces such as Pt-skin structures. The trend in the literature has been to extend the calculation of the activation energy of O-O dissociation in O_2, to extend it to O-O bond dissociation in OOH and HOOH since it is proposed that O-O bond dissociation steps are the most important likely rate-determining steps in the ORR reaction mechanism.

The complete characterization of the ORR mechanism on Pt alloys remains minimal, hence there is a need to study the other elementary reaction steps. The activation energies of all other possible elementary reaction steps need to be determined in order to assess what effect they have on the ORR activity-enhancement. With the activation energies for the different elementary reaction steps calculated, the role of the alloying element M in the alloy in relation to ORR activity-enhancement can be determined and compared to ORR activity on the pure Pt catalyst.

1.11 Aims of the study

The aim of the study is to gain knowledge from first principle calculations of how the oxygen reduction reaction activity-enhancement is achieved on the $Pt_3Co(111)$ surface as has been experimentally observed by Stamenković et al. (2002). The study also seeks to provide insight into the role contributed by Co within Pt_3Co in attaining the ORR activity improvement over a Pt-only catalyst.

To address the aims of the study, a number of key questions have been formulated that will be addressed in the study. The key questions are:

1. How do the different ORR intermediates interact with the $Pt_3Co(111)$ surface, and what is the strength of adsorption of the ORR intermediates on the $Pt_3Co(111)$ surface in comparison to adsorption on the Pt(111) surface?
2. How does the presence of Cobalt on the $Pt_3Co(111)$ surface affect the adsorption of the ORR intermediates, in comparison to adsorption on the pure Pt(111) surface?
3. What are the activation energies for the different elementary reaction steps on the $Pt_3Co(111)$ surface, and how do they compare to those calculated on a pure Pt(111) surface?
4. Which reaction steps are likely rate determining for the ORR on the Pt_3 Co(111) surface?

From the surveyed literature the following hypotheses have been postulated for the present study. The alloying element Cobalt is expected to lead to:

1. Ease of O_2 dissociation on the alloy surface with lower activation barriers than on Pt.
2. Selective stabilization of O-containing intermediates.
3. Selective lowering of the activation energies of certain elementary reaction steps. The affected reaction steps are therefore important in determining the rate of the ORR.

1.12 Thesis outline

The thesis in divided into chapters, each focussing on a different subject. The first chapter reviews the literature and presents the research aims of the present study. Chapter 2 presents a background to density functional theory, the computational methodology to be followed in the study, as well as the model validation for the $Pt_3Co(111)$ surface. In chapter 3 the adsorption results for the various ORR intermediates are presented. Chapter 4 focuses on the coadsorption of the different reactants. The activation energy calculations for the elementary reaction steps are presented in Chapter 5. Chapter 6 provides concluding remarks from the present study.

1.13 List of References

Adzic, R.R. and Wang, J.X. 1998. 'Configuration and site of O_2 adsorption on the Pt(111) electrode surface.' *Journal of Physical Chemistry B* 102: 8988-8993.

Arenz, M., Schmidt, T.J., Wandelt, K., Ross, P.N. and Markovic, N.M. 2003. 'The oxygen reduction reaction on thin palladium films supported on a Pt(111) electrode.' *Journal of Physical Chemistry B* 107: 9813-9819.

Balbuena, P.B., Altomare, D., Agapito, L. and Seminario, J.M. 2003. 'Theoretical analysis of oxygen adsorption on Pt-based clusters alloyed with Co, Ni, or Cr embedded in a Pt matrix.' *Journal of Physical Chemistry B* 107: 13671-13680.

Chen, J., Lim, B., Lee, E.P. and Xia, Y. 2009. 'Shape-controlled synthesis of platinum nanocrystals for catalytic and electrocatalytic applications.' *Nano Today* 4: 81-95.

Christoffersen, E., Liu, P., Ruban, A., Skriver, H.L. and Nørskov, J.K. 2001. 'Anode materials for low-temperature fuel cells: a density functional theory study.' *Journal of Catalysis* 199: 123-131.

Chiodo, L., Sala, F.D., Pellegrino, T., Cingolani, R. and Manna, L. 2009. 'An *ab initio* study of the magnetic-metallic $CoPt_3$-Au interfaces.' *Journal of Condensed Matter* 21: 015001-015014.

Chorkendorff, I. and Niemantsverdriet, J.W. 2007. *Concepts of modern catalysis and kinetics*. 2nd ed. Wiley-VCH Verlag GmbH & Co KGaA: Weinheim Germany.

Fouda-Onana, F. and Savadogo, O. 2009. 'Study of O_2 and OH adsorption energies on Pd-Cu alloys surface with quantum chemistry approach.' *Electrochimica Acta* 54: 1769-1776.

Gasteiger, H.A., Kocha, S.S., Sompalli, B. and Wanger, F. T. 2005. 'Activity benchmarks and requirements for Pt, Pt-alloys and non-Pt oxygen reduction catalysts for PEMFCs.' *Applied Catalysis B: Environmental* 56: 9-35.

Gewirth, A.A. and Thorum, M.S. 2010. 'Electroreduction of dioxygen for fuel cell applications: Materials and challenges.' *Inorganic Chemistry* 49: 3557-3566.

Hagen, J. 2006. *Industrial Catalysis-A practical approach*. Wiley-Vch.Verlarg GmbH & Co. KGA: Weinheim Germany, pp 295-313.

Hansen, M. and Anderko, K. 1958. *Constitution of binary alloys*. 2nd Edition. MaGraw-Hill: New York.

Hyman, M.P. and Medlin, J.W. 2005. 'Theoretical study of the adsorption and dissociation of oxygen on Pt(111) in the presence of homogeneous electric fields.' *Journal of Physical Chemistry B* 109: 6304-6310.

Hyman, P.M. and Meldin, J.W. 2007. 'Effects of electronic structure modifications on the adsorption of oxygen reduction reaction intermediates on model Pt(111) alloy surfaces.' *Journal of Physical Chemistry C* 111: 17052-17060.

International Energy Agency. 2004. *Hydrogen and Fuel Cells: Review of National R&D Programs*. OECD Publishing: Paris, pp 23-25.

Jalan, V. and Taylor, E.J. 1983. 'Importance of interatomic spacing in catalytic reduction of oxygen in phosphoric acid.' *Journal of Electrochemical Society* 130: 2299 - 2302.

Karlberg, G.S., Rossmeisl, J. and Nørskov, J.K. 2007. 'Estimations of electric field effects on the oxygen reduction reaction based on the density functional theory.' *Physical Chemistry Chemical Physics* 9: 5158-5161.

Kitchin, J.R., Nørskov, J.K., Barteau, M.A. and Chen, J.G. 2004. 'Modification of the surface electronic and chemical properties of Pt(111) by subsurface 3d transition metals.' *Journal of Chemical Physics* 120: 10240-10246.

Kristian, N., Yu, Y., Lee, J.M., Liu, X. and Wang, X. 2010. 'Synthesis and characterization of Co_{core}-Pt_{shell} electrocatalysts prepared by spontaneous replacement reaction for oxygen reduction reaction.' *Electrochimica Acta* 56: 1000-1007.

Larminie, J. and Dicks, A. 2003. *Fuel cell systems explained*. 2nd Edition. Wiley: Chichester West Sussex, pp. 1-5.

Løvvik, O.M. 2005. 'Surface segregation in palladium based alloys from density- functional calculations.' *Surface Science* 583: 100-106.

Lytle, F.W. 1976. 'Determination of d-band occupancy in pure metals and supported catalysts by measurement of the L_{III} X-ray absorption threshold.' *Journal of Catalysis* 43: 376-379.

Michaelides, A. and Hu, P. 2001. 'Catalytic water formation on Platinum: a first-principles study.' *Journal of American Chemical Society* 123: 4235-4242.

Mattsson, A.E., Schultz, P.A., Desjarlias, M.P., Mattsson, T.R. and Leung, K. 2005. ' Designing meaningful density functional theory calculations in material science - a primer.' *Modelling and Simulation in Materials Science and Engineering* 13: R1-R3.

Marković, N.M., Gasteiger, H.A. and Ross, P.N. 1996. 'Oxygen reduction on platinum low-index single crystal surfaces in alkaline solution: rotating ring disk$_{Pt(hkl)}$ studies.' *Journal of Physical Chemistry* 100: 6715-6721.

Marković, N.M. and Ross, P.N. 1999. *Wieckonski Ed. International Electrochemistry: Theory, Experiment and Applications.* Marcel Dekker: New York, p. 821

Mukerjee, S., Srinivasan, S., Soriaga, M.P. and McBreen, J. 1995a. 'Role of structural and electronic properties of Pt and Pt alloys on electrocatalysis of oxygen reduction : An in situ XANES and EXAFS investigation.' *Journal of Electrochemical Society* 142: 1409-1422.

Mukerjee, S., Srinivasan, S., Soriaga, M.P. and McBreen, J. 1995b. 'Effects of preparation conditions of Pt alloys on their electronic, structural, and electrocatalytic activities for oxygen reduction reaction- XRD, XAS, and electrochemical studies.' *Journal of Physical Chemistry* 99: 4577-4589.

Mustain, W.E. and Prakash, J. 2007. 'Kinetics and mechanism for the oxygen reduction reaction on ploycrystalline cobalt- palladium electrocatalysts in acid media.' *Journal of Power Sources* 170: 28-37.

Nilekar, A.U. and Mavrikakis, M. 2008. 'Improved oxygen reduction reactivity of platinum monolayers on transition metal surfaces.' *Surface Science* 602: L89-L94.

Nørskov, J.K., Rossmeisl, J., Logadottir, A., Lindqvist, L., Kitchin, J.R., Bligaard, T. and Jónsson, H. 2004. 'Origin of the overpotential for oxygen reduction at a fuel cell cathode.' *Journal of Physical Chemistry B* 108: 17886-17892.

Paffett, M.T., Beery, J.G. and Gottesfeld, S. 1988. 'Oxygen reduction at $Pt_{0.65}Cr_{0.35}$, $Pt_{0.2}Cr_{0.8}$ and roughened Platinum.' *Journal of Electrochemical Society* 135: 1431-1436.

Paulus, U.A., Wonkam, A., Scherer, G.G., Schmidt, T.J., Stamenković, V., Radmilovic, V., Marković, N.M. and Ross, P.N. 2002a. 'Oxygen reduction on carbon-supported Pt-Ni and Pt-Co alloy catalysts.' *Journal of Physical Chemistry B* 106: 4181-4191.

Paulus, U.A., Wonkam, A., Scherer, G.G., Schmidt, T.J., Stamenković, V., Radmilovic, V., Marković, N.M. and Ross, P.N. 2002b. 'Oxygen reduction on high surface area Pt-based alloy catalysts in comparison to well defined smooth bulk alloy electrodes.' *Electrochimica Acta* 47: 3787-3798.

Pillay, D., Johannes, M.D., Garsany, Y. and Swider-Lyons, K.E. 2010. 'Poisoning of Pt_3Co electrodes: A combined experimental and DFT study.' *Journal of Physical Chemistry C* 114: 7822-7830.

Ramirez-Caballero, G., Hirunsit, P. and Balbuena, P.B. 2010. 'Shell-anchor-core structures for enhanced stability and catalytic oxygen reduction activity.' *Journal of Chemical Physics* 133: 134705-134713.

Ruban, A.V., Skriver, H.L. and Nørskov, J.K.1999. 'Surface segregation energies in transition-metal alloys.' *Physical review B* 59: 15990-16000.

Seminario, J.M., Agapito, L.A., Yan, L. and Balbuena, P.B. 2005. 'Density functional theory study of adsorption of OOH on Pt-based bimetallic clusters alloyed with Cr, Co and Ni.' *Chemical Physics Letters* 410: 275-281.

Sha, Y., Yu, T., Liu, Y., Merinov, B. and Goddard III, W.A. 2010. 'Theoretical study of solvent effects on the platinum-catalysed oxygen reduction reaction.' *Journal of Physical Chemistry Letters* 1: 856-861.

Sha, Y., Yu, T.H., Merinov, B.V., Shirvanian, P. and Goddard III, W.A. 2011. 'Oxygen hydration mechanism for the oxygen reduction reaction at Pt and Pd fuel cell catalysts.' *Journal of Physical Chemistry Letters* 2: 572-576.

Shi, Z., Zhang, J., Liu, Z.S., Wang, H. and Wilkinson, D.P. 2006. 'Current status of ab initio quantum chemistry for oxygen electroreduction on fuel cell catalysts.' *Electrochimica Acta* 51: 1905-1916.

Stamenković, V., Mun, B.S., Mayrhofer, K.J.J., Ross, P.N., Marković, N.M., Rossmeisl, J., Greely, J. and Nørskov, J.K. 2006. 'Changing the activity of of electrocatalysts for oxygen reduction by tuning the surface electronic structure.' *Angew Chem. Int. Ed.* 45: 2897-2901.

Stamenković, V., Schmidt, T.J., Ross, P.N. and Marković, N.M. 2003. 'Surface segregation effects in electrocatalysis: kinetics of oxygen reduction reaction on ploycrystalline Pt_3Ni alloy surfaces.' *Journal of Electroanalytical Chemistry* 554: 191-199.

Stamenković, V., Schmidt, T.J., Ross, P.N. and Marković, N.M. 2002. 'Surface composition effects in electrocatalysis : kinetics of oxygen reduction on well defined Pt_3Ni and Pt_3Co alloy surfaces.' *Journal of Physical Chemistry B* 106: 11970-11979.

Toda, T., Igarashi, H., Uchida, H. and Watanabe, M. 1999. 'Enhancement of the electroreduction of oxygen on Pt alloys with Fe, Ni and Co.' *Journal of Electrochemical Society* 146: 3750-3756.

Toda, T., Igarashi, H., and Watanabe, M. 1998. 'Role of electronic property of Pt and Pt alloys on electrocatalytic reduction of oxygen.' *Journal of Electrochemical Society* 145: 4185-4188.

Wang, J.X., Marković, N.M. and Adzic, R.R. 2004. 'Kinetic analysis of oxygen reduction on Pt(111) in acid solutions: intrinsic kinetic parameters and anion adsorption effects'. *Journal of Physical Chemistry B* 108: 4127-4133.

Xu, Y., Ruban, A.V. and Mavrikakis, M. 2004. 'Adsorption and dissociation of O_2on Pt-Co and Pt-Fe alloys.' *Journal of American Chemical Society* 126: 4717-4725.

Zhang, J., Vukmirovic, M., Mavrikakis, M. and Adzic, R.R. 2005a. 'Controlling the catalytic activity of platinum-monolayer electrocatalysts for oxygen reduction with different substrates.' *Angew. Chem. Int. Ed.* 44: 2132-2135.

Zhang, J., Vukmirovic, M.B., Sasaki, K., Nilekar, A.U., Mavrikakis, M. and Adzic, R.R. 2005b. 'Mixed-metal Pt monolayer electrocatalysts for enhanced oxygen reduction kinetics.' *Journal of American Chemical Society* 127: 12480-12481.

Chapter 2

Methodology and model validation

2.1 Computational Chemistry

The properties of materials are ultimately determined by the interactions of electrons and nuclei (Mattson et al. 2005). The fundamental description of these interactions requires quantum mechanics. The electronic structure is described by the time-independent Schrödinger Equation (TISE) (Greely et al. 2002), which is presented below:

$$H\Psi = E\Psi \tag{2.1}$$

The various variables in the equation are explained below:

- H is the Hamiltonian i.e. the total energy operator
- E is the total energy of the system.
- Ψ is the wavefunction, believed to be a function of space, and containing all knowable information about the system under study (Greely et al. 2002).

Solution of the Schrödinger Equation provides useful information about the system which includes the following (Greely et al. 2002):

1. Probability distributions for all particles within a particular configuration.
2. Energetic information about a particular particle configuration.

The Time-Independent Schrödinger Equation is simplified by the Born-Oppenheimer approximation. The Born-Oppenheimer approximation is based on the fact that electrons move much faster than the nuclei (owing to the heavier nuclear mass), therefore the electrons are allowed to relax (move about) while the nuclei positions are kept constant (Atkins and de Paula, 2006). The Born-Oppenheimer approximation allows the TISE to be split into nuclear and electronic structure calculations which are performed separately (Greely et al. 2002). The TISE for which the nuclear-nuclear interactions are kept constant and separated out of the Hamiltonian, results in the Electronic Schrödinger Equation (Gokhale et al. 2004).

The electronic structure of the electron gas is determined by the solution of the Electronic Schrödinger Equation, and the total energy from this Electronic Schrödinger Equation is interpreted as the potential energy for the nuclei (Greely et al. 2002). The solution of the nuclear structure for different nuclear arrangement, results in the construction of the potential energy surface (PES) for the nuclei (Greely et al. 2002). In carrying out chemical analysis, the ground state potential energy surface is of interest (Gokhale et al. 2002). Due to the extreme difficulty of solving the electronic structure for a given nuclear configuration, a large number of schemes

have been developed that are based on the solution of the Electronic Schrödinger Equation in terms of one-electron orbitals (Greely et al. 2002).

Two quantum mechanical methods for solving the TISE are discussed next. The two methods are:

1. The Hartree Fock Self-Consistent Field (HFSCF) method.
2. Density Functional Theory (DFT) method.

2.1.1 Hartree Fock Self - Consistent Field (HFSCF)

In this quantum mechanical method the following crucial assumption is made:

The electrons are independent particles. Thus the focus is on one electron and to establish the potential it feels as a function of the nuclei and the average potential of all other remaining electrons.

In this model the full many-electron wavefunction for the system is written as a determinant of one-electron wavefunctions (molecular orbitals). The number of one-electron orbitals is equal to the number of electrons in the system (Greely et al. 2002). The full wavefunction in this method is constructed so as to be antisymmetric with respect to electron exchange (Greely et al. 2002). The effect of the electron exchange, known as the exchange interaction, is that each electron generates a surrounding hole which electrons with the same spin avoid (Atkins and de Paula, 2006). The hole is known as the Fermi hole. Since the Hartree Fock Theory makes use of determinantal wavefunctions, the electron exchange energy is explicitly incorporated in it (Atkins and de Paula, 2006).

The full TISE is separated into many one-electron wavefunction equations, of which each is represented by the equation:

$$-\frac{\hbar^2}{2m}\nabla^2\Psi + \nu\Psi = \varepsilon\Psi \tag{2.2}$$

where $\hbar$ is Planck's constant divided by 2π, m is the rest mass of an electron, ∇^2 is the Laplacian, ν is an effective one-electron potential energy operator and ε is a one-electron energy eigenvalue.

The one-electron potential energy operator (ν) is calculated or obtained from the exact electrostatic attraction between the nuclei and the electrons and from an average electron-electron electrostatic interaction energy (Greely et al. 2002). The TISE separated into one electron equations as in equation 2.2 is iteratively solved until self-consistency is achieved. The iterative scheme employed in self consistently solving the equation is outlined below (Greely et al., 2002):

1. An initial guess is made for the one-electron wavefunctions which are normally expressed as a linear combination of basis functions.
2. The initial wavefunction estimate is followed by calculation of an average electron-electron interaction energy. This is dependent on all the one-electron orbitals.
3. The calculation of the average electron-electron interaction energy results in the determination of the interaction energy i.e. ν in equation 2.2.
4. The calculated interaction energy ν is used in equation 2.2 to solve for the one-electron orbitals.
5. The above 4 steps are repeated until orbital convergence (self-consistency) is obtained.

Full self consistency in the HFSCF method requires approximately N^4 calculations with N being the number of basis functions used (Greely et al. 2002). The HFSCF method is known to provide inaccurate molecular energies. The poor molecular energies originates from the absence of the explicit inclusion of the electron correlation effects (Greely et al. 2002). Moreover, the correlated motion of electrons due to instantaneous Coulomb repulsion is missing in the Hartree Fock Theory. The only correlation effects are those imposed by the antisymmetric wavefunction form and a neglect of other correlation energies can result in very poor energy predictions (Greely et al. 2002).

Ways of dealing with the shortcomings of the HFSCF method: Due to the shortcomings of the HFSCF method the following methods have been developed to improve on the HFSCF technique (Greely et al. 2002):

Configuration Interaction (CI) methods : This method makes use of unoccupied (virtual) states to account for correlation effects. The method uses similar techniques to those employed in the HFSCF method with additional unoccupied one-electron wavefunctions used to construct the total wavefunction. Excited electron configurations are incorporated into the wavefunction. The CI method results in accurate results compared to HFSCF method results, but these accurate results are obtained at an extreme computational cost. This is because CI methods require more than N^7 calculations per basis function as opposed to N^4 required in the HFSCF approach.

Quantum Monte Carlo techniques (QMC) : This method utilizes random sampling approaches to calculate the energy for many-electron systems. The QMC techniques can be divided into two methods:

- Variational Monte Carlo method
- Diffusion Monte Carlo method

Variational Monte Carlo method: In this method random sampling is used to evaluate integrals that arise naturally during CI methods.

Diffusion Monte Carlo method: In this technique the Schrödinger Equation is reformulated into an integral Green's function form. The Green's function is then approximated by successive Monte Carlo samplings.

The QMC techniques are computationally demanding. The advantages of using the QMC techniques include:

1. Possibility of obtaining exact solutions of the TISE.
2. They are well suited to describe systems where electronic interactions are important, e.g. superconductors and systems where Van der Waals forces play a significant role.

The computational burden of the exact calculation of correlation effects makes it highly desirable to use an approximate scheme for evaluating such effects (Greely et al. 2002). One such approximate scheme is the Density Functional Theory (DFT).

2.1.2 Density Functional Theory (DFT)

In the density functional theory (DFT) method the total energy of a system is calculated from the electron density distribution. The central concept in DFT is the relationship between the total energy and electron density (Gokhale et al. 2004). The electron density is a much easier quantity to deal with since it is only a function of the three spatial coordinates.

DFT is based on the Hohenberg-Kohn Theorem, which states that the electron density determines the ground state wavefunction and all other electronic properties of the system (Hohenberg and Kohn, 1964). The correct ground state electron density is the one that produces the

minimum energy (Hohenberg and Kohn, 1964). Presented in an alternate form, the Hohenberg-Kohn Theorem can be stated simply as: the energy (E) is a unique functional of the electron density, $(\rho(r))$ (Gokhale et al. 2004). Symbolically the theorem is stated as:

$$E = f[\rho(r)] \tag{2.3}$$

Or:

$$E[\rho(r)] \tag{2.4}$$

The ground state energy functional in DFT is represented as follows :

$$E\left[\rho(r)\right] = \int V_{ext}(r)\rho(r)dr + F\left[\rho(r)\right] \tag{2.5}$$

Taking a closer look at the ground state energy functional $E\left[\rho(r)\right]$ expression, $\int V_{ext}(r)\rho(r)dr$ represents the interaction of electrons with an external potential $V_{ext}(r)$. This term is the Coulomb interaction between electrons and nuclei and may readily be determined. The term $F\left[\rho(r)\right]$ in the expression is the sum of the kinetic energy of electrons and inter-electronic interactions. This is the part of the functional expression that is unknown.

The Hohenberg-Kohn Theorem does not provide the functional needed to determine the energy from the electron density, but only states that such a functional exists. The exact exchange and correlation contributions to the functional remains unknown.

In order to find a practical way to solve a system of interacting electrons, the Kohn-Sham formulation was proposed providing a computational scheme for applying the Hohenberg-Kohn theorem (Kohn and Sham, 1965). Practically, the functional is reformulated in Kohn-Sham theory such that the unknown parts are collected in the exchange-correlation term. The energy functional $F\left[\rho(r)\right]$ is approximated by the following equation :

$$F\left[\rho(r)\right] = E_{KE}\left[\rho(r)\right] + E_H\left[\rho(r)\right] + E_{xc}\left[\rho(r)\right] \tag{2.6}$$

where $E_{KE}[\rho(r)]$, is the kinetic energy of the electrons, $E_H[\rho(r)]$ is the Hartree electrostatic energy, which arises from classical interaction between charge densities, and $E_{xc}[\rho(r)]$ is the exchange-correlation functional term.

In the Kohn-Sham formulation instead of solving the real complicated system of interacting electrons in an external potential $V_{ext}(r)$, a much simpler but equivalent fictitious system of non-interacting Kohn-Sham particles in an effective potential $V_{eff}(r)$ is solved for (Mattsson et al. 2005). The non-interacting system is set out such that $V_{eff}(r)$ results in a ground state electron density of the non-interacting system, which is the same electron density as that for the interacting electron system in an external potential $V_{ext}(r)$ (Taylor and Heinonen, 2002). The Kohn-Sham equations need to be solved self-consistently. The self consistency cycle for solving the Kohn-Sham equations involve the following steps:

1. Assume an initial density, this provides an initial estimate of $V_{eff}(r)$.
2. $V_{eff}(r)$ is used to solve for the wavefunction of the single-particle states.
3. Calculation of the new electron density, which provides a new $V_{eff}(r)$.
4. Steps 2-3 are repeated until self-consistency is attained, i.e. until the input and output density in one iteration are within the tolerated convergence limit.

Figure 2.1 illustrates the steps in a self-consistency cycle for solving the Kohn-Sham equations.

The Kohn-Sham equations recast the intractable complexity of the detailed many-body interactions into a computationally manageable single particle effective potential via the exchange-correlation functional (Mattsson et al. 2005). The exchange-correlation energy functional $E_{xc}\left[\rho(r)\right]$ provides knowledge about electron-interactions beyond the Hartree term (Taylor and Heinonen, 2002).

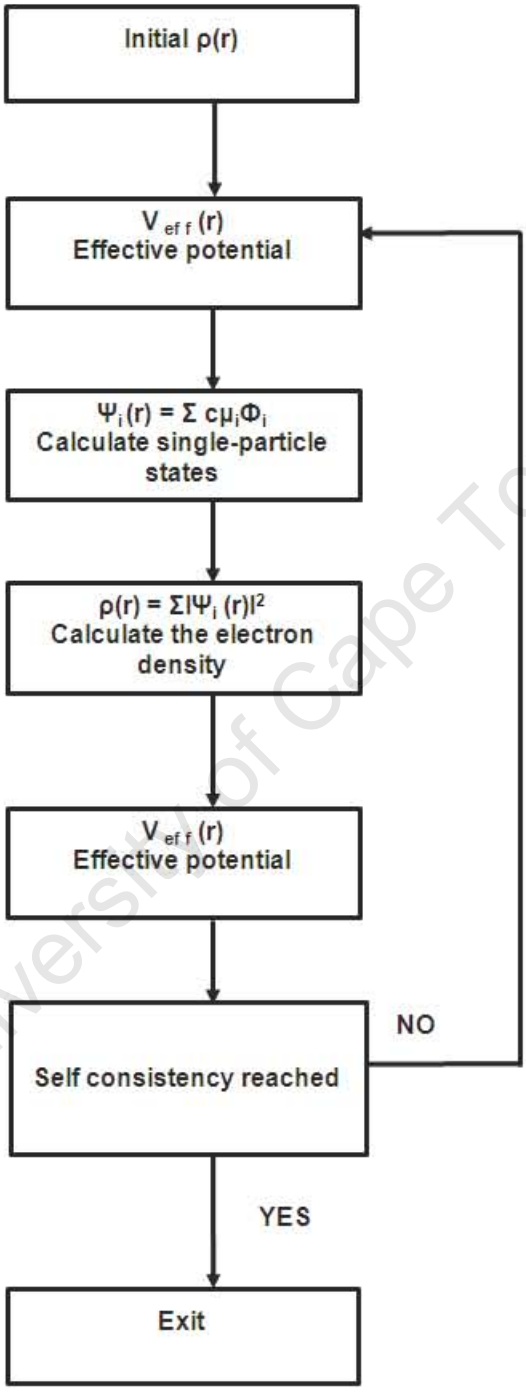

Figure 2.1: Self-consistency loop for solving of the Kohn-Sham equations in the Density Functional Theory technique (adapted from van Helden (2009) and Taylor and Heinonen (2002)).

The variation of the exchange-correlation energy with respect to density leads to:

$$\nu_{xc}\left[\rho\right] \equiv \frac{\partial \varepsilon_{xc}\left[\rho\right]}{\partial \rho(r)} \tag{2.7}$$

The Kohn-Sham formalism is exact if the exact exchange-correlation potential, $\nu_{xc}(\rho)$, can be found (Taylor and Heinonen, 2002). The exchange-correlation term is unknown in reality and there is no known systematic way of finding or deriving it (Shi et al. 2006). Therefore, an approximate functional must be proposed. Due to the approximated exchange-correlation term, the exact electron density is not obtained (Shi et al. 2006).

Exchange-correlation functional: The different exchange-correlation functionals within the DFT approach can be classified according to a 'Jacobs Ladder'. Figure 2.2 illustrates 'Jacob's Ladder' which classifies the functionals into rungs: the functionals in the higher rungs on the ladder are computationally demanding and more complex than the lower-rung functionals.

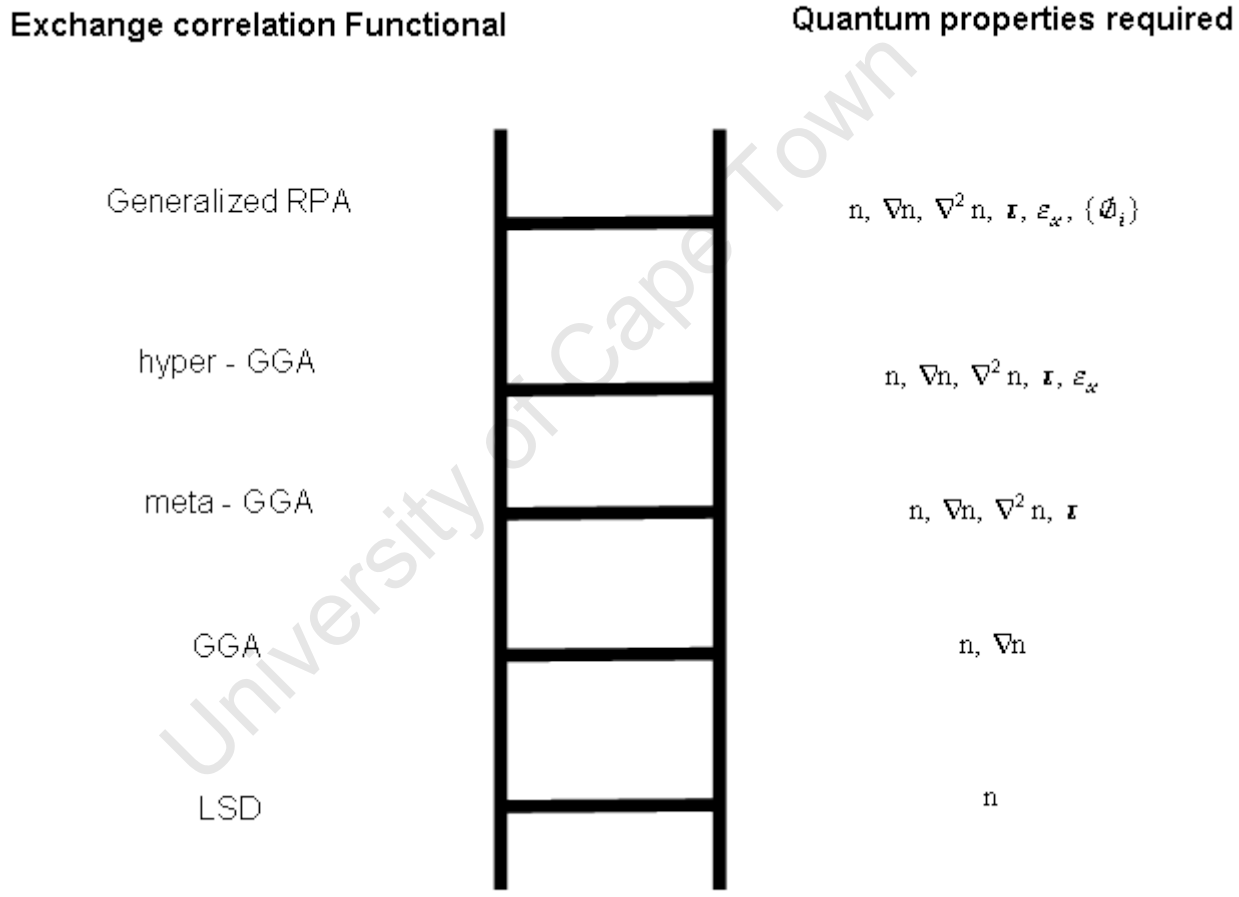

Figure 2.2: Jacob's Ladder for classifying the exchange-correlation energy functionals (adapted from Swart (2008) and Perdew et al. (2005))

The first rung of functionals is the Local Spin Density (LSD) approximation which is represented as :

$$E_{xc}^{LSD}[n_{\uparrow}, n_{\downarrow}] = \int d^3 r n(r) \varepsilon_{xc}^{unif}(n_{\downarrow}(r), n_{\uparrow}(r)) \tag{2.8}$$

where $\varepsilon_{xc}^{unif}(n_{\uparrow,}n_{\downarrow})$ is the exchange-correlation energy per particle of an electron gas with uniform spin densities $n_{\uparrow}$ and $n_{\downarrow}$ (Perdew et al. 2005). When applied, the LSD approach suffers from an inaccurate description of chemical bonding which overestimates bond energies, underestimates lattice parameters, underestimates the exchange energy and overestimates the correlation energy (Taylor and Heinonen, 2000).

The second rung of functionals on Jacob's Ladder is the generalized gradient approximation (GGA). For this method, the exchange-correlation energy functional depends not only on the electron density (n) but also on the electron density gradient (∇n). The GGA approximation of the exchange-correlation energy is represented as:

$$E_{xc}^{GGA}[n_{\downarrow},n_{\uparrow}] = \int d^3r n\varepsilon_{xc}^{GGA}(n_{\uparrow}, n_{\downarrow}, \nabla n_{\uparrow}, \nabla n_{\downarrow}) \tag{2.9}$$

where $\varepsilon_{xc}^{GGA}(n_{\uparrow}, n_{\downarrow}, \nabla n_{\uparrow}, \nabla n_{\downarrow})$ is the exchange-correlation energy per particle of an electron gas with spin densities $n_{\uparrow}$ and $n_{\downarrow}$ and density gradients $\nabla n_{\uparrow}$ and $\nabla n_{\downarrow}$. A wide range of GGA functional are in use and include the common functionals PW91 (Perdew et al. 1992), PBE (Perdew et al. 1996), revPBE (Zhang and Yang, 1998) and RPBE (Hammer et al. 1999). The PBE functional is designed such that it mimics the PW91 functional, whilst being of a simpler functional form and of fewer parameters. The PBE functional is designed to satisfy only exact conditions which are energetically significant, the features of PW91 omitted in PBE are the correct second order gradient coefficient for the exchange energy and the correlation energy in low varying limits, and the correct non-uniform scaling of the exchange energy in limits where the reduced gradients tend to infinity (Perdew et al. 1996).

The difference between revPBE and PBE is with the parameter κ in the exchange enhancement factor $F_x(s)$ that has been changed for revPBE to improve the description of atomic total energies and molecular atomization energies (Hammer et al. 1999; Zhang and Yang, 1998). The parameter κ appears in the exchange energy functional. For PBE κ = 0.804 and for revPBE κ = 1.245. The difference between the RPBE and PBE functionals is in the choice of the mathematical form for the exchange energy enhancement factor (Hammer et al. 1999). The revPBE and RPBE predict chemisorption energies better than PBE and PW91, whilst they are worse at predicting other physical properties such as lattice parameters and surface energies relative to the PW91 and PBE functional (Hammer et al. 1999).

The third rung of functionals in Jacob's Ladder represents the meta-GGA functionals. For these functionals, the kinetic energy density of the occupied Kohm-Sham orbitals is added to the electron density and electron density gradients in approximating the exchange-correlation energy. The exchange-correlation energy for the meta-GGA is approximated as:

$$E_{xc}^{MGGA}[n_{\uparrow}, n_{\downarrow}] = \int d^3r n\varepsilon_{xc}^{MGGA}(n_{\uparrow}, n_{\downarrow}, \nabla n_{\uparrow}, \nabla n_{\downarrow}, \nabla^2 n_{\uparrow}, \nabla^2 n_{\downarrow}, \tau_{\uparrow}, \tau_{\downarrow}) \tag{2.10}$$

where $\nabla^2 n_{\uparrow}$ and $\nabla^2 n_{\downarrow}$ are the Laplacian of the spin-densities and $\tau_{\uparrow}$ and $\tau_{\downarrow}$ are the Kohn-Sham orbital kinetic energy densities.

$$\tau_{\sigma}(r) = \frac{1}{2}\sum \mid \nabla\phi_{i\sigma}(r) \mid^2 \tag{2.11}$$

with $\phi_{i\sigma}(r)$ being the occupied Kohn-Sham orbitals. Two of the meta-GGA functionals developed are the PKZB functional (Perdew et al. 1999 a) and the TPSS functional (Tao et al. 2003). The PKZB functional has one empirical parameter fitted to atomization energies in its exchange part, whereas the TPSS functional does not include any empirical parameters.

The fourth rung of functionals in Jacob's Ladder represents the hyper-GGA functionals. For these functionals the exact exchange-energy-density is added to the electron density, the electron density gradient and the kinetic energy density of the occupied Kohn-Sham orbitals. The exchange-correlation energy of the hyper-GGA functional is approximated as:

$$E_{xc}^{HGGA}[n_{\uparrow}, n_{\downarrow}] = \int d^3r n\varepsilon_{xc}^{HGGA}(n_{\uparrow}, n_{\downarrow}, \nabla n_{\uparrow}, \nabla n_{\downarrow}, \nabla^2 n_{\uparrow}, \nabla^2 n_{\downarrow}, \tau_{\uparrow}, \tau_{\downarrow}, \epsilon_{x\uparrow}, \epsilon_{x\downarrow}) \tag{2.12}$$

where

$$\varepsilon_{x\sigma}(r) = -\frac{1}{2n_{\sigma}(r)}\int d^3r' \frac{\mid \sum \phi_{i\sigma}^{*}(r)\phi_{i\sigma}(r') \mid^2}{\mid r' - r \mid} \tag{2.13}$$

Examples of semi-empirical hyper-GGA's include the commonly used hybrid functionals such as B3LYP and PBE0. This functionals are constructed by mixing a fixed fraction of exact exchange

with a GGA exchange and the local hybrids (Jaramillo et al. 2003). The hyper-GGA can be accurate for molecules and inhomogeneous solids, but are however theoretically less ideal since they do not satisfy any exact constraints that GGAs do satisfy (Perdew et al. 2005). Thus they are considered not to be any better than the GGAs.

The fifth rung of functionals in Jacob's Ladder represents the generalized random phase approximation (RPA). For this functional, all the Kohn-Sham orbitals are used, i.e. the occupied and unoccupied orbitals. The random phase approximation avoids the need for the electron gas data and also accounts for the long range van der Waals attraction between non-overlapped electron densities (Perdew et al. 2005). The fifth rung functionals are not yet practical for general use, since they require huge basis sets and thus are computationally expensive.

2.2 Bulk model optimisation

While setting up a DFT simulation, several choices need to be made to ensure that the model predictions are comparable to the experimentally determined values. The choices which need to be made while performing a calculation are the following (Mattsson et al. 2005):

1. Exchange-correlation functional
2. Pseudopotential
3. Brillouin zone sampling (k-point sampling)
4. Basis set sufficiency

The choice of the exchange-correlation functional determines the physical accuracy of the calculation, while the Brillouin zone sampling and the basis set sufficiency controls the numerical aspects or convergence of the calculation (Mattsson et al. 2005). The pseudopotentials represent the description of electron-ion interactions.

2.2.1 Exchange-correlation functional

The exchange-correlation functional choice determines how the Kohn-Sham (KS) equations are formulated and solved. Once the choice of the exchange-correlation functional is made e.g. LSD, GGA or hybrid, the accuracy of the theory is fixed (Mattsson et al. 2005).

2.2.2 Pseudopotentials

In the pseudopotential approach only the valence electrons are included in the calculation, while the inert core electrons are not explicitly treated, but are replaced by an effective core potential. There are several methods of generating pseudopotentials, such as the generalized norm-conserving pseudopotentials of Hellmann (Hellmann, 1935), softer pseudopotentials by Troullier-Martins (Troullier and Martins, 1991) and Vanderbilt's non-norm-conserving ultra-soft pseudopotentials (USSP) (Vanderbilt, 1990) as well as the Projector Augmented Wave function (PAW) pseudopotentials (Kresse and Joubert, 1999: Blöch, 1994). In principle, the result of a DFT calculation should not be affected by using pseudopotentials instead of all-electron potentials, however in practice replacing the core electrons with an effective core potential is never perfect (Mattsson et al. 2005).

2.2.3 Brillouin zone sampling

The treatment of the electronic structure for periodic systems can take advantage of translational symmetry through Bloch's theorem. By utilizing Bloch's theorem, a problem with an infinite number of atoms and electronic states is transformed into a problem handling a finite number of atoms and electronic states in a translationally invariant unit cell (Mattsson et al. 2005). The translationally invariant unit cell has an infinite number of wave vectors (k-points) in the Brillouin zone (BZ) (Mattsson et al. 2005).

Computing system properties such as the energy, forces and stresses, density and density of states involves integration over all occupied electronic states. In DFT codes, these integrals are approximated by a finite sampling of k-points (Mattsson et al. 2005). Computational time increases linearly with an increase in the number of k-points, therefore, to reduce computational time special k-point schemes are used. The special k-point schemes use the fewest possible k-points whilst giving the most accurate approximation to the full integration over k-space within the BZ (Mattsson et al. 2005). Examples of the special k-point schemes include: the Chadi-Cohen scheme (Chadi and Cohen, 1973) and the Monkhorst-Pack scheme (Monkhorst and Pack, 1976)

The use of a finite number of k-points rather than the full integration over the Brillouin zone is an approximation, and the k-point sampling can have a profound impact on the computed properties (Mattsson et al. 2005). Thus, the optimal number of k-points need to be determined.

2.2.4 Basis set sufficiency

In plane wave codes the basis set is determined by the chosen energy, i.e. kinetic energy cut-off E_{cut}. The higher the cut-off energy, the larger and better the basis set and the lower the cut-off energy, the smaller and worse the basis set (Mattsson et al. 2005). The higher basis set cut-off energy result in more accurate results, but the higher cut-off energy make the calculations more computationally demanding. Therefore, an optimal basis set cut-off energy needs to be determined in order to avoid compromising the accuracy of the model. In calculations only the plane waves with kinetic energy $E \leq E_{cut}$ are included. The higher kinetic energy plane waves give a better description of the core region around the nuclei, but the chemistry is predominately governed by the valence electrons and in the region of overlap between nuclei. This is why a lower basis set cut-off energy still gives meaningful results.

.

2.3 Bulk optimisation of Pt_3Co

In this section, calculations varying the exchange-correlation functional, k-point sampling and basis set cut-off energy for the bulk unit cell of Pt_3Co are presented.

The spin polarised periodic DFT calculations are performed on a primitive bulk unit cell of Pt_3Co, consisting of one Co atom and three Pt atoms. The bulk Pt_3Co structure is a face centred cubic (fcc) crystal with one Pt atom replaced by a Co atom in the conventional fcc unit cell. The experimental lattice parameter of 3.85 Å (Berg and Cohen, 1972) for Pt_3Co, is used for the k-point and basis set cut-off energy convergence test and as the initial structure in the bulk optimisation of Pt_3Co. The plane wave code VASP (Kresse et al. 1993) is used. The electron-ion interactions are described by the projector augmented wave (PAW) pseudopotentials (Kresse and Joubert, 1999; Blöch, 1994). The Brillouin zone sampling is done using the Monkhorst-Pack method (Monkhorst and Pack,1976). Smearing was performed using the tetrahedron method (Blöchl et al. 1994). For bulk Pt_3Co optimisation calculations for the k-point and plane wave basis set cut-off energy convergence tests the ionic relaxation criterion of 0.03 eV/Å for the forces was used, the force relaxation method used is the conjugate gradient algorithm (Press et al. 1986) and the electronic self consistent iteration parameter for the electronic energy convergence was energy changes below 1×10^{-4} eV. Three GGA functionals for the exchange-correlation terms are investigated, these are: PW91(Perdew et al. 1992), PBE (Perdew et al. 1996) and RPBE (Hammer et al. 1999).

2.3.1 k-point mesh convergence test

To determine the optimal k-point mesh size, the k-point mesh was varied from (10 $\times$ 10 $\times$ 10) to (24 $\times$ 24 $\times$ 24) using the Monkhorst-Pack method (Monkhorst and Pack,1989). The k-point mesh convergence test calculations are performed at a constant plane wave basis set cut-off energy, 30 % higher at 350 eV than the default plane wave cut-off energy specified for Co ($\backsim$270 eV) in the PAW pseudopotential file supplied in the VASP distribution . The 30% is added to the default plane wave cut-off energy of Co specified in the pseudopotential file to ensure that the k-point convergence test is not influenced by the basis set cut-off energy value. The default plane wave cut-off energy of Co was used instead of that of Pt since the default plane wave cut-off energy of Co is higher that that of Pt ($\backsim$231 eV). For Pt and Co, the PAW pseudopotentials supplied in the VASP distribution have the same default plane wave cut-off energy for the GGA-PW91 and GGA-PBE functionals, hence for the three different functionals the plane wave basis set cut-off energy was held constant at the same value of 350 eV. A gamma centred Monkhorst-Pack (Monkhorst and Pack,1976) k-point grid was used. The even number k-point meshes were analyzed separately from the odd number k-point meshes. The k-point mesh was considered to be converged if the difference in total energy of the bulk structure at k-point mesh *n* and subsequent k-point meshes relative to the energy value of the densest k-point mesh was within 1 meV/ (Pt_3Co formula unit) of each other. The k-point mesh convergence test calculations were performed using the GGA method for exchange and correlation, and three different functionals, PW91, PBE and RPBE were investigated.

2.3.1.1 Results and discussion

Figure 2.3 shows the convergence test results for the irreducible k-points for bulk Pt_3Co for the three functionals.

From Figure 2.3 it is observed that for all three functionals investigated at 120 irreducible k-points the convergence criterion of 1 meV/ (Pt_3Co formula unit) is obtained except for odd PBE k-points where the energy difference is not converged exactly to 1 meV but is slightly above. The convergence criterion is obtained for both odd and even k-point meshes for all three functionals at 120 irreducible k-points. Therefore for the functionals PW91, PBE and RPBE, 120 irreducible k-points which corresponds to k-point mesh of (16 $\times$ 16 $\times$ 16) for the even mesh and (15 $\times$ 15 $\times$ 15) for the odd mesh is sufficient to describe bulk Pt_3Co. However, it is also observed from Figure 2.3 that at around 90 irreducible k-points the convergence criterion of 1 meV has been

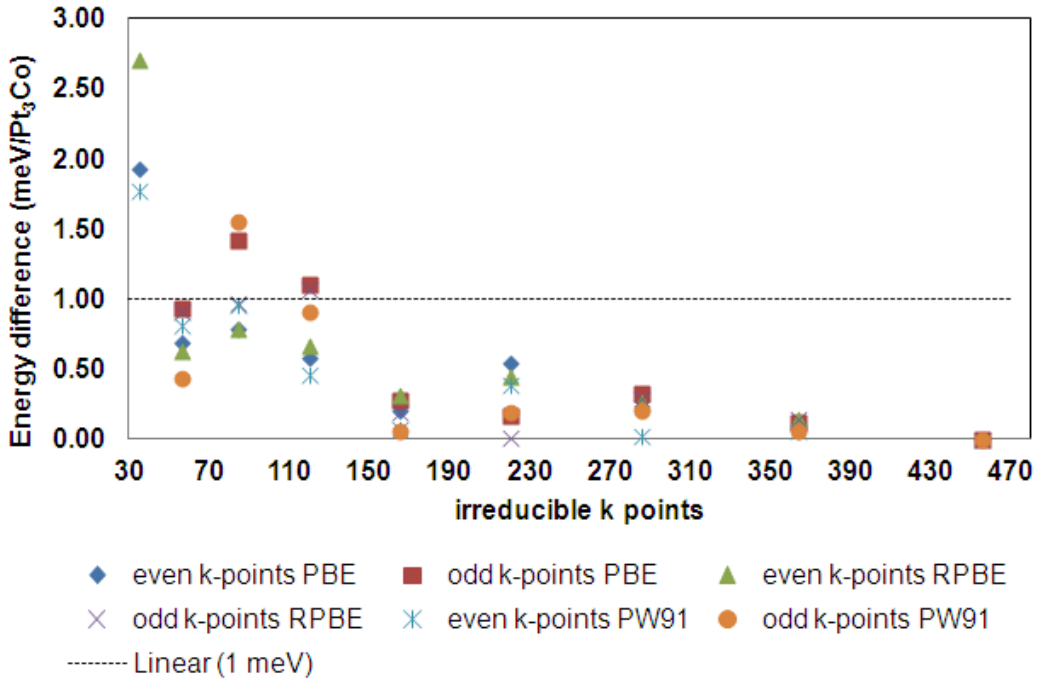

Figure 2.3: Energy difference plotted against irreducible k-points for bulk Pt_3Co for the three functionals, PW91, PBE and RPBE

met for the even k-point meshes for the PBE functional, odd and even k-point meshes for the RPBE functional and for the even k-point meshes for the PW91 functional.

2.3.2 Basis set cut-off energy convergence test

To determine the converged basis set cut-off energy a similar convergence test to that performed for the k-point mesh was followed. The basis set cut-off energy was varied from 250 to 600 eV. The converged basis set cut-off energy was achieved when the difference in total energy of the bulk structure was 1 meV/ (Pt_3Co formula unit) between cut-off energy value *n* and subsequent cut-off energies relative to the highest cut-off energy value used in the calculation. For the basis set cut-off energy convergence test, the k-point mesh was held constant at the converged k-point mesh of ($16 \times 16 \times 16$). The basis set cut-off energy convergence test was repeated for the three GGA functionals, PW91, PBE and RPBE.

2.3.2.1 Results and discussion

Figure 2.4 illustrates the convergence test results for the basis set cut-off energy for describing bulk Pt_3Co for the three functionals: PW91, PBE and RPBE.

From Figure 2.4 it is observed that the basis set cut-off energy is converged for the PW91 functional at 350 eV. For the PBE and RPBE functionals, the basis set cut-off energy is converged at 510 eV to within the convergence criterion of 1 meV/ (Pt_3Co formula unit).

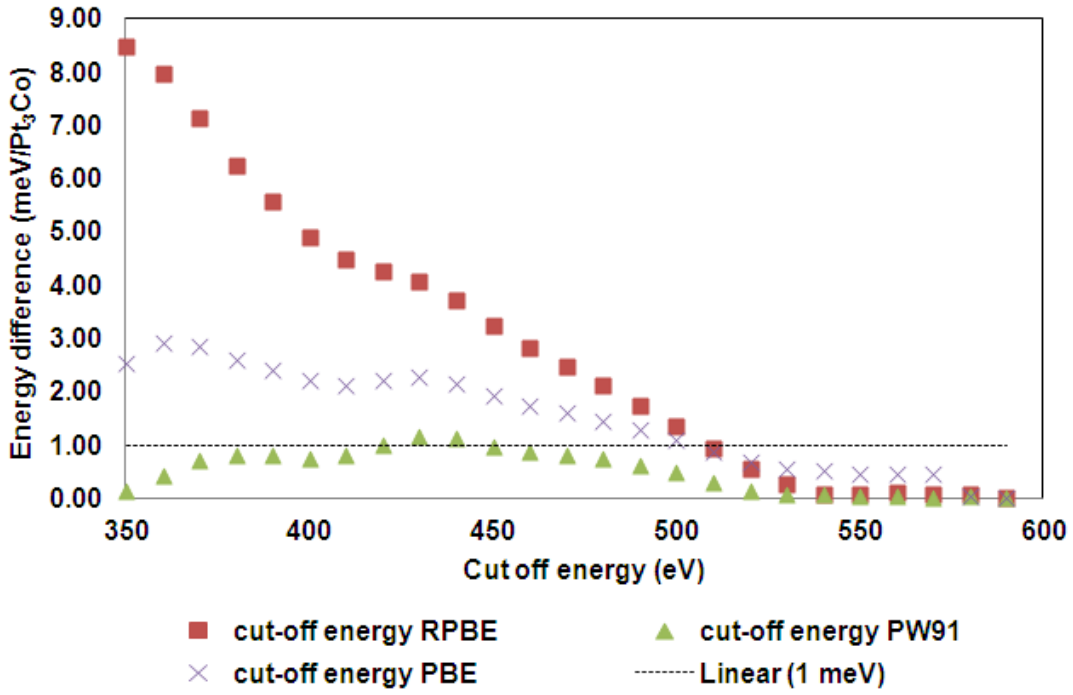

Figure 2.4: Energy difference versus basis set cut-off energy for the three functionals: PW91, PBE and RPBE.

2.3.3 Lattice parameter optimisation

A series of calculations was performed at a k-point mesh of (16 $\times$ 16 $\times$ 16) and a basis set cut-off energy of 510 eV, to generate a set of volume and energy data in order to determine the equilibrium bulk lattice parameter of Pt_3Co. The lattice parameter was varied at $\pm$ 0.05 Å about the experimental lattice parameter value 3.85 Å (Berg and Cohen, 1972) of Pt_3Co, at 0.01 Å intervals, to obtain the energy versus volume data. The volume and energy data was fitted to the Birch-Murnaghan (Birch, 1947; Murnaghan, 1944) equation of state to determine the bulk modulus (B) and the equilibrium volume (V) of the unit cell, from which the equilibrium lattice constant ***a*** can be determined. The Birch-Murnaghan equation is as follows:

$$E(V) = E_0 + \frac{9V_0B_0}{16}\{[\left(\frac{V_0}{V}\right)^{2/3} - 1]^3 B_0^{'} + [\left(\frac{V_0}{V}\right)^{2/3} - 1]^2[6 - 4\left(\frac{V_0}{V}\right)^{2/3}]\} \tag{2.14}$$

where E_0 is the minimum energy, B_0 is the bulk modulus, V_0 is the volume at the minimum energy and $B_0^{'}$ is the bulk modulus pressure derivative.

The determination of the bulk modulus (B_0) and the equilibrium volume (V_0) of the unit cell was repeated for the three GGA functionals: PW91, PBE and RPBE.

Figure 2.5 shows the curves obtained from the energy and volume data for the functionals PW91, PBE and RPBE together with the 3^{rd} order polynomials fitted through the data. The fitted polynomials are used to calculate the lattice parameter from the V_0 and the bulk modulus. The calculated V_0 and the bulk modulus obtained from the fitted polynomials are used as initial approximations for V_0 and B_0 for the Birch-Murnaghan equation of state.

From the fitted polynomials through the energy and volume data, the minimum energy-point on the curve is located. The equilibrium lattice parameter is calculated from the equilibrium volume that results in the minimum energy. The minimum energy is located by calculating both the 1^{st}

and the 2^{nd} derivatives of the polynomial function, fitted through the energy and volume data. A minimum corresponds to a value where the 1^{st} derivative is equal to zero and the second derivative is positive. The bulk modulus is calculated from:

$$B(E,V) = V\frac{d^2E}{dV^2} \tag{2.15}$$

The energy and volume data are used to regress for the constants in the Birch-Murnaghan equation of state. An automatic lattice parameter optimisation via a volume relaxation calculation was also performed to determine the converged lattice parameter using the converged k-point mesh and the basis set cut-off energy and the experimental equilibrium lattice parameter as an initial guess. The ionic relaxation criterion of 0.03 eV/Å for the forces acting on the atoms within the unit cell and the electronic energy convergence was set at energy changes below 1×10^{-4} eV for the automatic volume relaxation calculation. The converged lattice parameter from the automatic optimization was compared to the lattice parameter obtained from the equilibrium volume, calculated using the Birch-Murnaghan equation. The lattice parameters from both the Birch-Murnaghan equation and the automatic lattice parameter optimization were in agreement with each other to within 0.01Å. The converged lattice parameters from the automatic volume relaxation obtained for the different functionals are presented in Table 2.1.

2.3.4 Magnetic moment determination of Pt_3Co

The local magnetic moment of Co and Pt atoms within bulk Pt_3Co structure was determined using the Bader method (Bader, 1990) for charge partitioning as developed for the VASP code by the Henkelman group (Tang et al. 2009; Sanville et al. 2007; Henkelman et al. 2006) using the determined lattice parameter from the automatic volume relaxation calculation. To determine the local magnetic moment of Pt and Co the core charge density file and the valence charge density file are added together to give the total charge file. The total charge file includes the total charge density (spin up + spin down) and the spin charge density (spin up - spin down). The spin charge density is subtracted from the total charge which contains both the total charge density and the spin charge density resulting in the net spin charge density. The Bader method is then applied to the net spin charge density and the resulting charge density partitioning in this case corresponds to the magnetic moment.

2.3.5 Choice of the functional best describing bulk Pt_3Co

Table 2.1 summarizes the reported calculated and experimental properties of Pt_3Co. The reported calculated and experimental values are used to assess the predictions of the properties of Pt_3Co obtained, in the present study, and to aid in the choice of the functional best describing bulk Pt_3Co.

As shown in Table 2.1, the lattice parameters predicted by the various functionals in the present study, are: PW91: 3.90 Å, PBE: 3.89 Å, and RPBE: 3.91 Å. The lattice parameter is predicted close to the experimental value of 3.85 Å (Berg and Cohen, 1972), for all the functionals. The PW91 lattice parameter is 1.3 % higher than the experimental lattice parameter, PBE overestimates the lattice parameter by 1.0 % relative to the experimental lattice parameter, and the RPBE functional overestimates the lattice parameter by 1.6 % relative to the experimental lattice parameter. All three functionals perform similarly in terms of accuracy of the prediction of the lattice parameter.

The next property to consider, in order to choose the functional that best describes the bulk properties of Pt_3Co, is the local magnetic moment of the Co and Pt atoms within the bulk Pt_3Co unit cell. Comparing the calculated magnetic moment of Co and Pt obtained in the present study to the experimentally measured values, it is evident that the calculated values overestimate the experimentally measured moments. The overestimation of the calculated magnetic moments on Co and Pt is common in reported calculations of Pt_3Co, can be seen in Table 2.1. A possible explanation of the observed overestimation by the GGA method in calculating local magnetic

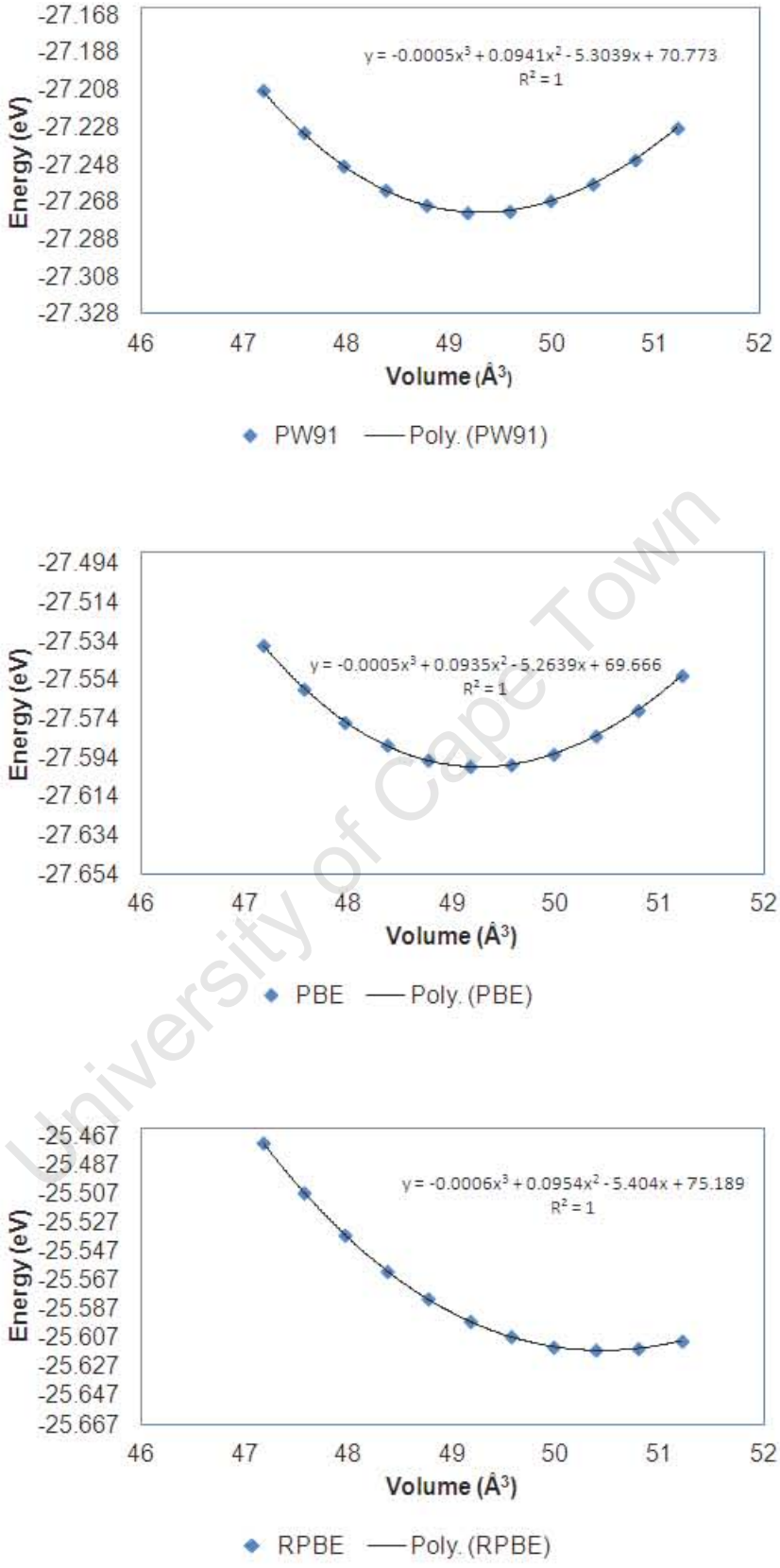

Figure 2.5: Plots of the energy and volume data for the functionals: PW91, PBE and RPBE, showing the 3^{rd} order polynomials fitted through the data, for the bulk structure optimization of Pt_3Co.

Table 2.1: Summary of the reported calculated and experimental bulk properties of Pt_3Co and the results obtained in the present study

Source	Package	Functional	Pseudo-Potentials	a (Å)	M(μ_B)	B (GPa)
Theory						
Koote et al (1991)		LDA			μ_{Co} = 1.69 μ_{Pt} = 0.27	
Galanakis et al (2000)		LDA			μ_{Co} = 1.82 μ_{Pt} = 0.22	
		GGA			μ_{Co} = 1.89 μ_{Pt} = 0.24	
Xu et al (2004)	Dacapo	GGA - PW91	PAW	3.92	μ_{Co} = 1.84 μ_{Pt} = 0.16	
Roques et al (2005)	VASP	GGA - PW91	USSP	3.91		
Ma and Balbuena (2008)	VASP	GGA - PW91	PAW	3.89		
Hirunsit and Balbuena (2009)	VASP	GGA - PBE	PAW	3.89		
Chiodo et al (2009)	PWSCF	LDA - PW91		3.82	μ_{Co} = 1.74 μ_{Pt} = 0.45	
		GGA - PW91			μ_{Co} = 1.93 μ_{Pt} = 0.55	
Kumar et al (2009)	WIEN2K	FPLAPW			μ_{Co} = 1.76 μ_{Pt} = 0.31	
Rajagopalan (2010)	WIEN2K	FPLAPW			μ_{Co} = 1.97 μ_{Pt} = 0.31	257
Pillay et al (2010)	VASP	GGA - PW91	PAW	3.89		
Experimental						
Berg and Cohen (1972)				3.85		
Menzinger and Paoletti (1966)					μ_{Co} = 1.64 μ_{Pt} = 0.26	
Present work	VASP	GGA - PW91	PAW	3.90	μ_{Co} = 1.97 μ_{Pt} = 0.33	224
		GGA - PBE	PAW	3.89	μ_{Co} = 1.98 μ_{Pt} = 0.34	227
		GGA -RPBE	PAW	3.91	μ_{Co} = 2.06 μ_{Pt} = 0.36	203

moments on Co and Pt is provided by Galanakis et al. 2000, who state that the overestimation is due to the fact that for 3d ferromagnets, the GGA produces an atomic-like description of the hybrid orbitals between the Pt 5d orbitals and the 3d orbitals of the base metal, the consequence of which is a slight overestimation of the magnetic moments (Galanakis et al. 2000).

The magnetic moments of Co and Pt calculated using the RPBE functional are higher than the experimentally determined values of 1.64 μ_B for Co and 0.26 μ_B for Pt (Menzinger and Paoletti, 1996) by 38.5 % and 25.6 % for Co and Pt respectively. The RPBE functional overestimates the magnetic moments of Co and Pt more than the PBE and PW91 functionals. The magnetic moment prediction of Co and Pt, obtained with the PW91 and PBE functionals are similar, as can be seen in Table 2.1. The magnetic moment prediction of Co from the PW91 functional is 20.1 % higher than the experimental value of 1.64 μ_B, while the PBE functional predicts a magnetic moment of Co that is 20.7 % higher than the experimental value. The PW91 functional prediction of the local magnetic moment of Pt is 26.9% higher than the experimental local magnetic moment of Pt within bulk Pt_3Co at 0.26 μ_B. The local magnetic moment prediction of Pt by the PBE functional is 30.8 % higher than the experimentally determined value of 0.26 μ_B. Both the PW91 and PBE functionals predict the local magnetic moment of Co to within the same accuracy of 20 % above the experimental value. For the local magnetic moment prediction of Pt, the PW91 prediction is an overestimate of 26.9 % of the experimentally determined value, whilst the PBE functional prediction is an overestimate of 30.8 %.

The bulk modulus prediction is not used as a criterion for determining the functional best describing the bulk properties of Pt_3Co, since no published sources for the experimentally determined value for the bulk modulus are available.

Both PW91 and PBE overestimates the magnetic moment of Co and Pt relative to the experimental magnetic moments. Therefore either the PW91 or PBE functional could be chosen as the functional to proceed with. However, the PW91 functional is slightly better at predicting the magnetic moment of Pt than the PBE functional. Therefore the PW91 functional is chosen over the PBE functional since overall it best predicts the properties of Pt_3Co relative to the PBE and the RPBE functionals. Therefore, the GGA-PW91 functional is the functional of choice to proceed with for the rest of the calculations to be performed on $Pt_3Co(111)$ in the present study.

2.4 Surface structure optimisation of $Pt_3Co(111)$

The optimisation of the $Pt_3Co(111)$ surface was performed on a 4-layer slab with all the slab layers relaxed, each layer had 4 atoms with one Co atom and 3 Pt atoms. The surface structure optimisation calculations were performed in a (1×1) supercell within the full symmetry of the surface cell. However, in the present study and in the literature this (1×1) supercell is referred to as a (2×2) unit cell. The cell is referred to as a (2×2) unit cell due to its similar appearance to a typical (2×2) (111) unit cell for a material which has a fcc crystal structure. The optimised PW91 lattice parameter of 3.90 Å was used for the surface optimisation calculations. For the k-point and basis set cut-off energy convergence calculations the vacuum gap was set as 10 Å, the vacuum gap was later then checked if it is sufficient at 10 Å at the converged k-point and basis set cut-off energy value for a 4-layer slab. The PW91 functional was used to describe the exchange-correlation energy terms. The structural optimisation calculation was continued until the forces acting on the atoms within the unit cell fell below 0.03 eV/Å, the force relaxation method used is the conjugate gradient algorithm (Press et al. 1986), and the electronic energy convergence was set to a convergence parameter of energy changes below 1×10^{-4} eV. The present study is limited to the (111) surface of Pt_3Co with the same concentration as the bulk. No attempt will be made to investigate the surface segregation of either Pt or Co due to the presence of adsorbates on the surface.

2.4.1 k-point mesh convergence test

To determine the converged k-point mesh needed for the $Pt_3Co(111)$ surface, the k-point mesh was varied from ($5 \times 5 \times 1$) to ($23 \times 23 \times 1$). For surface structure optimisation, one k-point

was used for the direction perpendicular to the slab since the reciprocal lattice vector in this direction is much shorter than the other two reciprocal lattice vectors. The gamma-centred Monkhorst-Pack mesh was used for the k-point sampling. The converged k-point mesh was attained when the difference in total energy between k-point mesh *n* and subsequent denser meshes relative to the highest k-point mesh energy was $\leq$1 meV/ (Pt_3Co formula unit). The k-point mesh convergence test was performed at a constant basis set cut-off energy of 350 eV which is 30 % higher than the default plane wave cut-off energy of Co ($\backsim$270 eV) as specified in the PAW pseudopotential file.

2.4.1.1 Results and discussion

In Figure 2.6 the energy difference is plotted against the number of irreducible k-points for determining the converged k-point mesh for describing $Pt_3Co(111)$.

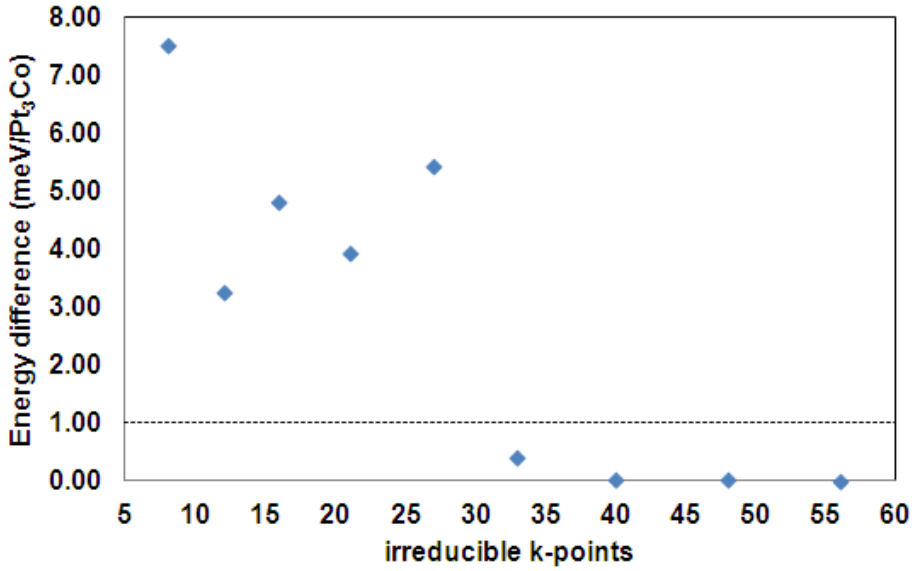

Figure 2.6: Plot of energy difference against number of irreducible k-points for determining the converged k-point mesh for $Pt_3Co(111)$

From Figure 2.6 it is observed that the energy is converged to within 1 meV/Pt_3Co for 33 irreducible k-points which corresponds to a k-point mesh of ($17 \times 17 \times 1$).

2.4.2 Basis set cut-off energy convergence test

The convergence test for the plane wave basis set cut-off energy was performed by varying the basis set cut-off energy from 300 to 900 eV. The converged plane wave basis set cut-off energy was determined by using a 1 meV/ (Pt_3Co formula unit) difference in total energy between the highest basis set cut-off energy value used, and the basis set cut-off energy at *n* and subsequent basis set cut-off energy values. The basis set cut-off energy convergence test was performed at a constant converged k-point mesh of ($17 \times 17 \times 1$).

2.4.2.1 Results and discussion

In Figure 2.7 the basis set cut-off energy convergence test results for the $Pt_3Co(111)$ surface are presented.

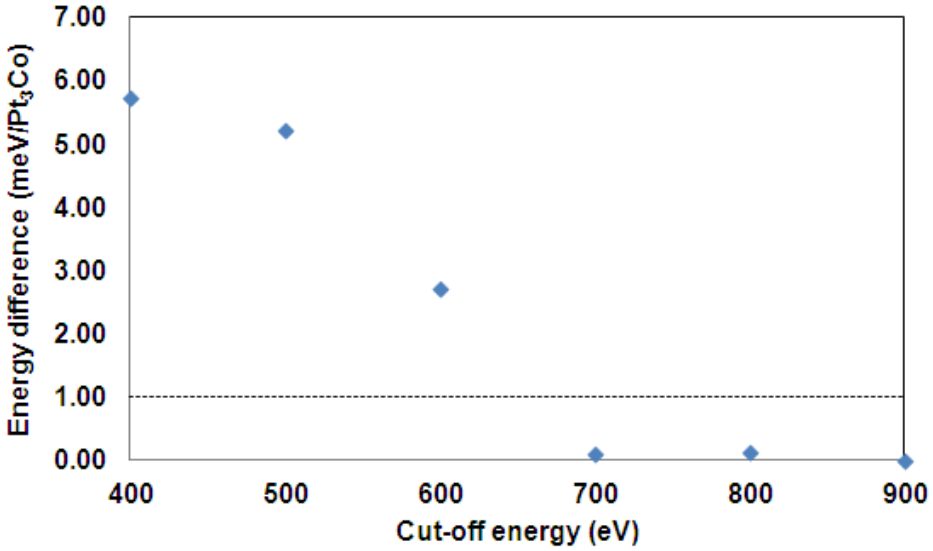

Figure 2.7: Plot of the energy difference as a function of the basis set cut-off energy for the convergence test for describing the $Pt_3Co(111)$ surface

From Figure 2.7 it is observed that the energy is converged to within the 1 meV / Pt_3Co for a basis set cut-off energy in the range between 600 eV and 700 eV.

2.4.3 Vacuum gap convergence test

The converged vacuum gap was determined by varying the vacuum gap from 7 Å to 17 Å. The converged vacuum gap was determined using a convergence criterion of 1 meV/ Pt_3Co difference in total energy between the 17 Å vacuum gap calculation and the vacuum gap energy of *n* and subsequent vacuum gaps. The vacuum gap convergence test was performed using the converged k-point mesh of ($17 \times 17 \times 1$) and the converged basis set cut-off energy of 650 eV. The basis set cut-off energy was determined to converge in the range 600 - 700 eV, 650 eV was chosen since it is half way between 600 - 700 eV.

2.4.3.1 Results and discussion

In Figure 2.8 a plot of the energy as a function of the vacuum gap for the $Pt_3Co(111)$ surface is shown.

From Figure 2.8 it is observed that the vacuum gap is converged to within 1 meV/ Pt_3Co criterion at a vacuum gap of 13 Å. The vacuum gap of 10 Å is within the convergence criterion, but is not chosen since only after a vacuum gap of 13 Å does the energy difference level off below 1 meV, in addition the 13 Å vacuum gap is chosen to accommodate the adsorbates on the surface. Although a 13 Å vacuum gap is used, the 10 Å vacuum gap used for the k-point and basis set cut-off energy convergence is unlikely to affect the accuracy of the determined converged k-points and the basis set cut-off energy.

A calculation of O_2 adsorption atop a Co atom at a vacuum gap of 20 Å was performed, this calculation was used to assess how the adsorption energy of O_2 varies with the vacuum gap. O_2 adsorption atop a Co atom was used as a probe for adsorption energy as a function of the vacuum gap, since O_2 in this configuration is projected into the vacuum. The optimal vacuum gap without adsorbates on the surface is determined as 13 Å. The adsorption energy of O_2 atop a Co atom at a vacuum gap of 13 Å is 0.317 eV and at a vacuum gap of 20 Å, the adsorption energy of O_2 is 0.326 eV. The 0.009 eV difference in the O_2 adsorption energy at the two

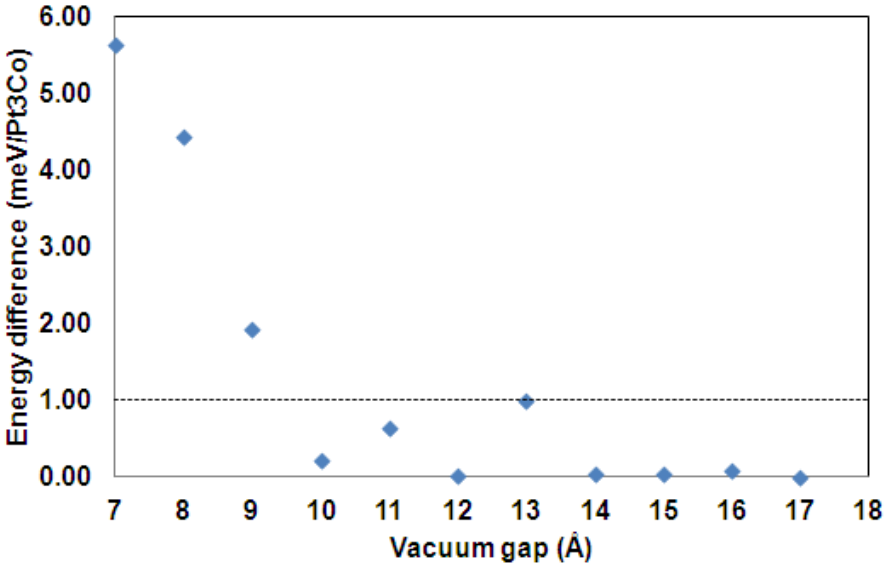

Figure 2.8: Plot of energy difference versus vacuum gap for vacuum gap convergence test for $Pt_3Co(111)$ surface

vacuum gaps, is indicative that the adsorption energy of O_2 atop a Co atom is converged to less than 0.01 eV which is below the accuracy of DFT. Thus, the chosen optimal vacuum gap of 13 Å is still sufficient in the presence of adsorbates on the surface, which point vertically into the vacuum.

2.4.4 Slab thickness optimisation

The variation of the O_2 adsorption energy at 0.25 ML coverage in a (2×2) surface unit cell with varying slab thickness was used as a test to determine the optimal slab thickness. A convergence criterion of 0.01 eV difference in the O_2 adsorption energy for the different slab thicknesses relative to the 6-layer slab with 3-layers free is used to determine the optimal slab thickness.The optimal slab thickness was determined by varying the slab thickness from 3 to 6 layers, and for each slab thickness the top two layers of the slab and the adsorbate were relaxed. The adsorbate O_2 was adsorbed on only one side of the slab, the corresponding electrostatic potential resulting from the dipole created upon adsorption was corrected for using the dipole correction method (Neugebauer and Scheffler, 1992) as implemented in the VASP code (Kresse and Furthmüller, 2010). The structural optimisation calculation was continued until the forces acting on the atoms fell below 0.03 eV/Å, the force relaxation method used is the conjugate gradient algorithm (Press et al. 1986), and the electronic energy convergence was set to a convergence parameter of energy changes below 1×10^{-4} eV. A test calculation was also performed on a 6-layer slab with the top three layers relaxed, this was to assess whether the O_2 adsorption energy is affected by the number of relaxed layers. The optimal slab thickness was determined by plotting $\triangle E_{ads}$ against the slab thickness, and the slab thickness where the convergence criterion is attained is considered as the optimal slab thickness. To determine the optimal slab thickness $\triangle E_{ads}$ at different slab thicknesses was determined. $\triangle E_{ads}$ is defined as the difference between the O_2 adsorption energy for slab *n*, where *n* is 3, 4, 5 and 6 , and the O_2 adsorption energy for the 6 layer slab with the top 3 layers relaxed. The adsorption energy of O_2 is determined as follows:

$$E_{ads} = E_{slab+O2} - E_{O2(gas)} - E_{Cleanslab} \tag{2.16}$$

where $E_{slab+O2}$ is the energy of the slab with O_2 adsorbed, $E_{O2(gas)}$ is the energy of gas phase O_2 and $E_{Cleanslab}$ is the energy of the clean slab without any adsorbate on it.

$\triangle E_{ads}$ is defined as:

$$\triangle E_{ads} = E_{ads-O2-n} - E_{ads-O2-6-3free} \tag{2.17}$$

where $E_{ads-O2-n}$ is the O_2 adsorption energy at slab thickness n and $E_{ads-O2-6-3free}$ is the O_2 adsorption energy for a 6 -layer slab with 3 layers freed.

In the present study the focus will be mostly on energy differences $\triangle$E, i.e. adsorption energies E_{ads}, coadsorption energies E_{coads}, activation energies E_{act} and the heat of reaction $\triangle E_{rxn}$, therefore it is desired to have energy differences converged to within 0.01 eV which is 0.96 kJ mol^{-1}. Thus in order to determine the optimal slab thickness the convergence criterion was set to 0.01 eV differences in the adsorption energy of O_2. In the present study for the adsorption of the diffferent ORR species the pseudopotentials of O and H together with those for Pt and Co will be used. The default plane wave basis set cut-off energy for H is 250 eV and for O is 400 eV as specified in the pseudopotential files supplied with the VASP distribution.

Due to long computational times required for calculating the relaxed structure of O_2 adsorbed on the surface slab for the different slab thicknesses at the determined converged k-point mesh of (17 $\times$17 $\times$ 1) and the basis set cut-off energy at 650 eV, it was decided to perform the calculations at a lower k-point mesh of (12 $\times$ 12 $\times$ 1) and a basis set cut-off energy of 400 eV. A k-point mesh of (17 $\times$17 $\times$ 1) and basis set cut-off energy of 650 eV are referred to as calculations at high settings, and calculations at a k-point mesh of (12 $\times$ 12 $\times$ 1) and a basis set cut-off energy of 400 eV are referred to as calculations at low settings. The lower settings were performed to assess if the same convergence of O_2 adsorption energy to within 0.01 eV would be obtained while using lower settings for the k-point mesh and the basis set cut-off energy. The calculation for the slab optimisation was performed at both high and low settings, and the difference between the two sets of calculations for the same slab thicknesses was determined to assess if there is any significant change in the calculated O_2 adsorption energy at the low settings. A difference in the calculated O_2 adsorption energy between the high and low setting calculations is considered to be insignificant if the difference is $\leq$ 0.01 eV.

2.4.4.1 Results and discussion

In Figure 2.9 a plot of the O_2 adsorption energy as a function of the slab layer thickness for the high (k-point mesh (17 $\times$17 $\times$ 1), $E_{cut-off}$ = 650 eV) and low setting (k-point mesh (12 $\times$ 12 $\times$ 1), $E_{cut-off}$ = 400 eV) calculations is shown.

Figure 2.10 is a plot of $\triangle E_{ads}$ for the low and high-setting calculations for the different slab thicknesses relative to the 6-layer slab with 3 relaxed layers for the low and high settings respectively, i.e. for the low settings $\triangle E_{ads}$ is relative to the 6-layer slab with 3 layers relaxed calculated at the low settings and similarly for the high settings $\triangle E_{ads}$ is relative to the 6-layer slab with 3 layers relaxed calculated at the high settings.

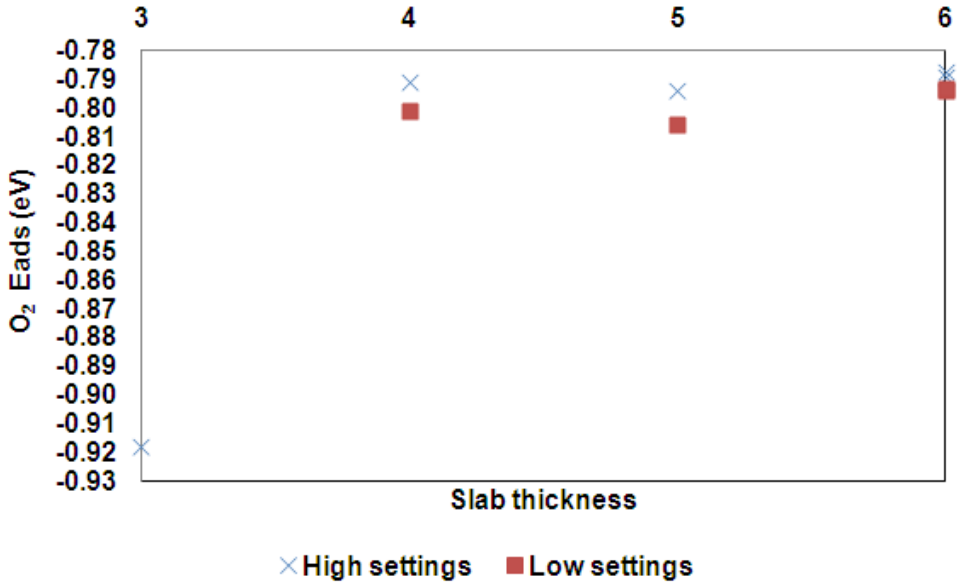

Figure 2.9: Plot of variation of O_2 adsorption energy with varying slab thickness of $Pt_3Co(111)$

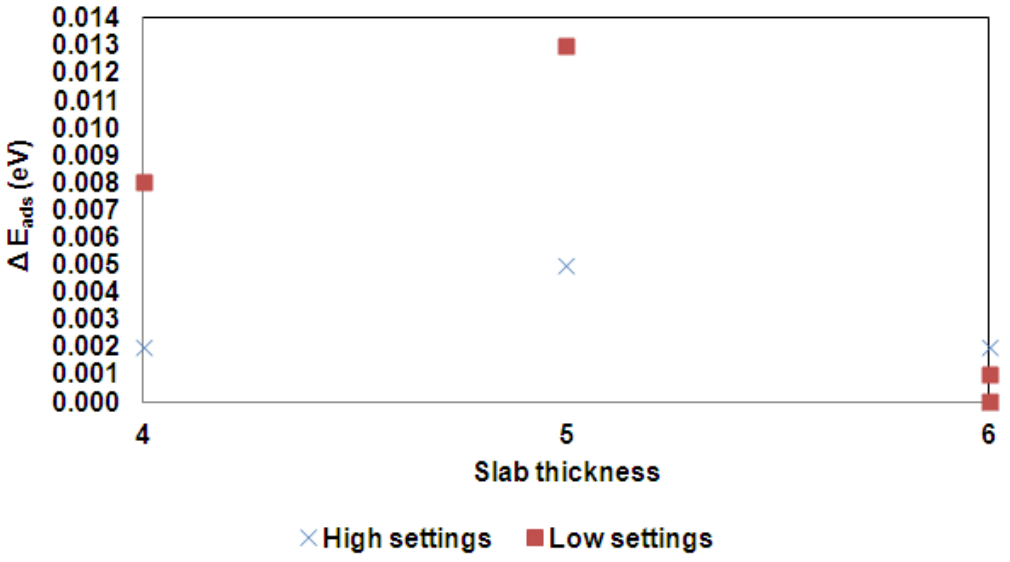

Figure 2.10: Plot of $\triangle E_{ads}$ for the different slab thicknesses of $Pt_3Co(111)$

From Figure 2.10 it is observed that the adsorption energy of O_2 differs by less than 0.01 eV for a 4-layer slab with 2 layers relaxed for both the high and low settings relative to O_2 adsorption energy for a 6-layer slab with 3 layers relaxed , the difference for the low settings is 0.008 eV and 0.002 eV for the high settings. For a 5-layer slab with 2 layers relaxed $\triangle E_{ads}$ for the high settings = 0.004 eV and for the low settings = 0.013 eV and for the 6-layer slab with the top 2 layers relaxed $\triangle E_{ads}$ for high settings = 0.002 eV and for the low settings = 0.001 eV. Therefore,

on a 4-layer slab with the top 2 layers relaxed the adsorption energy of O_2 is converged to within 0.013 eV for the low setting calculations and converged to within 0.004 eV for the high setting calculations. Thus, a 4- layer slab with the top 2 layers relaxed is considered to be sufficient.

Figure 2.11 plots the calculated difference in O_2 adsorption energy between the high and low setting calculations. The difference in O_2 adsorption energy plotted as energy difference in Figure 2.11 is defined as:

$$Energy\_diff = E_{ads-O2-n-high} - E_{ads-O2-n-low} \tag{2.18}$$

where $Energy\_diff$ is the difference in O_2 adsorption energy at slab n between the high and low settings, $E_{ads-O2-n-high}$ is the adsorption energy of O_2 on a slab of thickness n at high settings and $E_{ads-O2-n-low}$ is the adsorption energy of O_2 on a slab of thickness n at low settings.

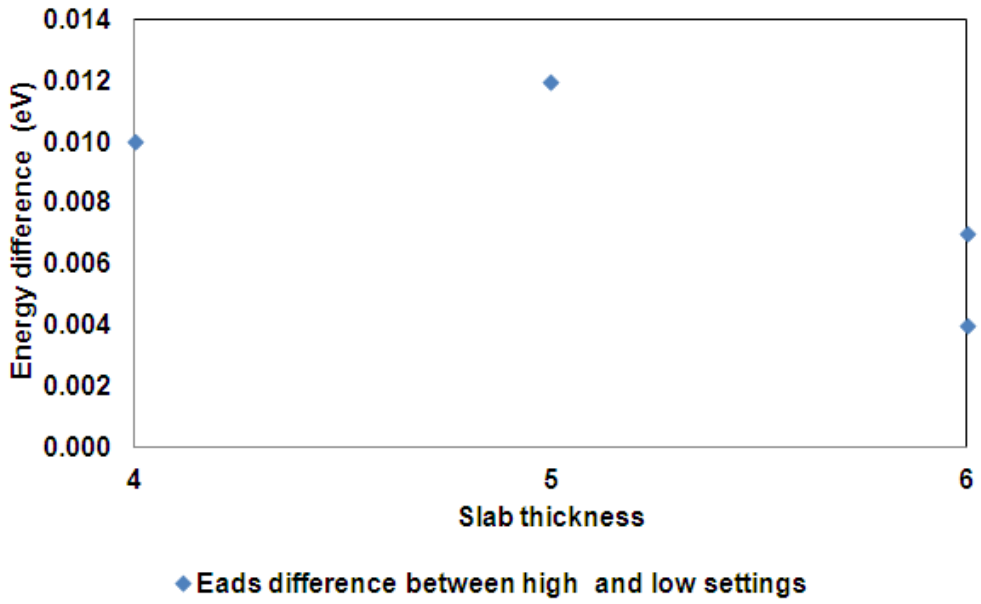

Figure 2.11: Plot of difference in calculated O_2 adsorption energy between high and low setting calculations for corresponding slab thickness

From Figure 2.11, the difference between the calculated adsorption energy of O_2 at the high and low settings are: 0.010 eV for the 4-layer slab, 0.012 eV for the 5-layer slab, 0.007 eV for the 6-layer slab with the top two layers relaxed, and 0.004 eV for the 6-layer slab with the top three layers relaxed. For the 5-layer slab the difference in O_2 adsorption energy between the high and low settings is 0.012 eV, therefore for n $\geq$ 4 the O_2 adsorption energy for the high and low settings is converged to within 0.012 eV/O_2. Therefore, using the low-setting calculations at a k-point mesh of (12 $\times$ 12 $\times$ 1) and a basis set cut-off energy of 400 eV, instead of the high-setting calculations at a k-point mesh of (17 $\times$ 17 $\times$ 1) and a basis set cut-off energy of 650 eV does not significantly affect the calculated O_2 adsorption energy, since the calculated O_2 adsorption energy is converged to within 0.012 eV/O_2 which is 1.16 kJ mol^{-1} O_2.

Based on the results obtained on the section on slab thickness optimisation, the k-point mesh will be (12 $\times$ 12 $\times$ 1) and the basis set cut-off energy will be 400 eV which is the same as the recommended maximum plane wave cut-off energy of O in the pseudopotential file supplied with the VASP distribution. The basis set cut-off energy of 400 eV has been shown not to affect the convergence of the adsorption energy of O_2 to within 0.012 eV/O_2 compared to using a basis set cut-off energy of 650 eV, since O_2 adsorption energy depends on energy differences, and not on total energy. For all the calculations in the present study on the $Pt_3Co(111)$ surface,

the k-point mesh will be (12 $\times$ 12 $\times$ 1) and the basis set cut-off energy set 400 eV. The slab thickness is set at 4 layers with the top 2 slab layers allowed to relax.

2.5 Gas phase molecules

The adsorption energies for the various ORR species will be calculated using the gas phase ORR species as the reference state, hence it is vital to obtain the correct ground state converged energy and properties of the gas phase species.

To calculate the energies and properties of the gas phase species, the gas phase species was placed at the center of a cubic box. The box dimensions were varied from 9 Å to 17 Å, to determine the dimensions of the box giving the converged energies for the gas phase species. The procedure was repeated for the different ORR gas phase species. The total energy of the gas species at each box dimension was subtracted from the total energy of the gas phase at box dimension of 17 Å. The optimal gas phase species energy is obtained when the difference in energy is 0.001 eV relative to the energy of the gas at the highest box dimension of 17 Å. For all the gas phase species the energy converged for a cubic box of dimensions 14 Å $\times$ 14 Å $\times$ 14 Å.

A single k-point at the gamma point is used for the Monkhorst-Pack method (Monkhorst and Pack,1976) for the Brillouin zone sampling. The basis set cut-off energy was set at 400 eV for the gas species optimisation calculations since this value corresponds to the recommended maximum plane wave basis set cut-off energy recommended for O. The plane wave basis set cut-off energy of O is greater than that of H hence why the default plane wave basis set cut-off energy of O is used instead of that of H. The force convergence criterion for determining the converged properties of the gas phase species was forces below 0.01 eV/Å, the force relaxation method used is the conjugate gradient algorithm (Press et al. 1986), and the electronic energy convergence parameter was set to energy changes below 1×10^{-5} eV.

A Hessian matrix was used to calculate the vibrational modes of the gas phase species. The vibrational modes are calculated by numerical differentiation of the forces, through the use of a second order finite difference method (Li and Jensen, 2002). A step size of 0.02 Å in the Cartesian space was used to determine the Hessian matrix.

2.5.1 O_2

The calculated gas phase properties of O_2 are: ν_{O-O} = 1570 cm^{-1}, O-O bond distance = 1.23 Å and bond dissociation energy including the zero point energy corrections = 6.06 eV. The calculated gas-phase properties are in agreement with the experimentally determined values: ν_{O-O} = 1580 cm^{-1} and O-O bond distance = 1.21 Å (Huber and Herzberg, 1979). The calculated dissociation energy is similar to that calculated by Perdew et al. (1996) of 6.20 eV using the same exchange-correlation functional, PW91(Perdew et al. 1992). The experimental bond dissociation energy of O_2 is 498.36 $\pm$ 0.17 kJ mol^{-1} (5.16 eV) (Lide, 2005).

2.5.2 H_2

Calculated gas-phase properties of H_2 are: ν_{H-H} = 4431 cm^{-1} and H-H bond distance = 0.75 Å. The calculated gas phase values are in agreement with the experimentally determined values: ν_{H-H} = 4401 cm^{-1} and H-H bond distance = 0.74 Å (Huber and Herzberg, 1979). The experimental bond dissociation of H_2 is 435.78 kJ mol^{-1} (Lide, 2005). The calculated bond dissociation energy of H_2 is 4.51 eV which is 435.40 kJ mol^{-1} which is in good agreement with the experimental value.

2.5.3 OOH

Calculated gas-phase properties of O_2H are: ν_1= 3474 cm^{-1}, ν_2 = 1379 cm^{-1}, ν_3 = 1126 cm^{-1}, O-H bond distance = 0.98 Å, O-O bond distance = 1.34 Å and $\angle$OOH = 106 º. The calculated gas-phase properties are in agreement with the experimentally determined values: ν_1= 3436 cm^{-1}, ν_2 = 1392 cm^{-1}, ν_3 = 1098 cm^{-1}(Jacox, 1994), O-H bond distance = 0.97 Å, O-O bond distance = 1.33 Å and $\angle$OOH = 104 º (Lubic et al. 1984).

2.5.4 OH

Calculated gas-phase properties for OH are: ν_{O-H} = 3748 cm^{-1} and O-H bond distance = 0.98 Å. The calculated gas-phase properties are in agreement with the experimentally determined values: ν_{O-H} = 3738 cm^{-1} and O-H bond distance = 0.97 Å (Huber and Herzberg, 1979).

2.5.5 HOOH

Calculated gas-phase properties for H_2O_2 are: ν_1= 3688 cm^{-1}, ν_2 = 3686 cm^{-1}, ν_3 = 1393 cm^{-1} , ν_4= 1282 cm^{-1}, ν_5 = 917 cm^{-1}, ν_6 = 370 cm^{-1}, O-H bond distance = 0.96 Å, O-O bond distance = 1.47 Å and $\angle$HOO = 100º. The calculated gas-phase properties are in agreement with the experimentally determined values: ν_1= 3608 cm^{-1}, ν_2 = 3599 cm^{-1}, ν_3 = 1402 cm^{-1} ν_4= 1266 cm^{-1}, ν_5 = 877 cm^{-1}, ν_6 = 371 cm^{-1} (Shimanonchi, NSRDS-NBS 39; Huber and Herzberg, 1979) , O-H bond distance = 0.95 Å, O-O bond distance = 1.48 Å and $\angle$HOO = 95º (Redington et al. 1962).

2.5.6 H_2O

Calculated gas-phase properties of H_2O are: ν_1= 3861 cm^{-1}, ν_2 = 3745 cm^{-1}, ν_3 = 1589 cm^{-1} , O-H bond distance = 0.97 Å and $\angle$HOH = 104 º. The calculated gas-phase properties are in agreement to the experimentally determined values: ν_1= 3756 cm^{-1}, ν_2 = 3657 cm^{-1}, ν_3 = 1595 cm^{-1} (Shimanonchi, NSRDS - NBS; Huber and Herzberg, 1979), O-H bond distance = 0.96 Å and $\angle$HOH = 104 º (Hoy and Bunker, 1979).

Thermodynamic consistency of gas phase species

The prediction of the gas phase thermodynamics in the present study was assessed by calculating the gas phase heat of formation and Gibbs free energy of formation of $H_2O_{(g)}$ and $HOOH_{(g)}$. The equations used to calculate the thermodynamic properties of the species at 298.15 K are presented in Appendix A. The calculated values are compared with the experimentally determined values at 298 K. From Table 2.2, it is observed that the calculated heats of formation and the Gibbs free energy of formation are slightly under-predicted relative to the experimental values. The under-prediction might be due to the prediction in the electronic energy of O_2, whose high-spin ground state is difficult to describe using DFT (Nørskov et al. 2004).

Reaction for the formation of $H_2O_{(g)}$ is:

$$H_{2(g)} + \frac{1}{2}O_{2(g)} \rightarrow H_2O_{(g)} \tag{2.19}$$

Reaction for the formation of $HOOH_{(g)}$ is:

$$H_{2(g)} + O_{2(g)} \rightarrow HOOH_{(g)} \tag{2.20}$$

Table 2.2: Calculated and experimental heats of formation and Gibbs free energy of formation of $H_2O_{(g)}$ and $H_2O_{2(g)}$ at 298.15K

	$\triangle H_f{}^0$ (kJ/mol)		$\triangle G_f{}^0$ (kJ/mol)	
Compound	**Calculated**	**Experimental (Lide, 2005)**	**Calculated**	**Experimental (Lide, 2005)**
$H_2O_{(g)}$	-237.25	-241.83	-208.50	-228.60
$H_2O_{2(g)}$	-133.58	-136.30	-98.14	-105.60

2.6 List of References

Atkins, P. and De Paula, J. 2006. *Atkins physical chemistry*. 8th ed. Oxford University Press:Oxford.

Bader, F. W. 1990. *Atoms in Molecules: A Quantum Theory*. USA: Oxford University Press.

Berg, H. and Cohen, J.H. 1972. 'Long-range order and ordering kinetics in $CoPt_3$.' *Metallurgical Transactions* 3: 1797-1805.

Birch, F. 1947. 'Finite elastic strain of cubic crystals.' *Physical Review* 71: 809-824.

Blöch, P.E.1994. 'Projector augmented-wave method.' *Physical Review B* 50: 17953-17979.

Blöchl, P.E., Jepsen, O. and Anderses, O.K. 1994 'Improved tetrahedron method for Brillouin-zone integrations'. *Physical Review B* 49: 16223-16233.

Chadi, D.J. and Cohen, M.L. 1973. 'Special points in the Brillouin zone.' *Physical Review B* 8: 5747-5753.

Chiodo, L., Sala, F. D., Pellegrino, T., Cingolani, R. and Manna, L. 2009. 'An ab-initio study of the magnetic-metallic $CoPt_3$-Au interfaces.' Journal of Physics: Condensed Matter 21: 015001-015014.

Galanakis, I., Alouani, M. and Dreysse, H. 2000. 'Perpendicular magnetic anisotropy of binary alloys: A total energy calculation.' *Physical Review B* 62: 6475-6484.

Greely, J., Nørskov, J.K. and Mavrikakis, M. 2002. 'Electronic structure and catalysis on metal surfaces.' *Annual Review of Physical Chemistry* 53: 319-348.

Gokhale, A.A., Kandoi, S., Greely, J.P., Mavrikakis, M. and Dumesic, J.A. 2004. 'Molecular-level-descriptions of surface chemistry in kinetic models using density functional theory.' *Chemical Engineering Science* 59: 4679-4691.

Hammer, B., Hansen, L.B. and Nørskov, J.K. 1999. 'Improved adsorption energetics within density-functional theory using revised Perdew-Burke-Ernzehorf functionals'. *Physics Review B* 59: 7413-7421.

Hellman, H. 1935. 'A new approximation method in the problem of many electrons.' *Journal of Chemical Physics* 3: pp. 61.

Henkelman, G., Arnaldson, A., Jònsson, H. 2006. 'A fast and robust algorithm for Bader decomposition of charge density.' *Computional Materials Science* 36: 354-360.

Hirunsit, P. and Balbuena, P.B. 2009. 'Surface atomic distribution and water adsorption on Pt-Co alloys.' *Surface Science* 603: 912-920.

Hohenberg, P. and Kohn, W. 1964. 'Inhomogeneous electron gas.' *Physical Review* 136: B864-B871.

Hoy, A.R. and Bunker, P.R. 1979. 'A precise solution of the rotation Beninding Schrödinger equation for a triatomic molecule with application to the water molecule.' *Journal of Molecular Spectroscopy* 74: 1-8.

Huber, K.P. and Herzberg, G. 1979. *Molecular spectra and molecular structure IV constants for diatomic molecules*. Van Nostrand Reinhold Co.

Hummel, R.E. 1993. *Electronic properties of materials*. 2nd Edition. Springer-Verlag: Berlin, pp. 310.

Jacox, M.E. 1994. 'Vibrational and electronic energy levels of polyatomic transient molecules.' *Journal of Physical Chemistry Reference Data Monograph* 3.

Jaramillo, J., Scuseria, G.E. and Ernzehorf, M. 2003. 'Local hybrid functionals'. *Journal of Chemical Physics* 118: 1068-1073.

Kresse, G. and Hafner, J. 1993. '*Ab initio* molecular dynamics for liquid metals.' *Physical Review B* 47: 558-561.

Kresse, G. and Joubert, D. 1999. 'From ultrasoft pseudopotentials to the projector augmented -wave method.' *Physical Review B* 59: 1758-1775.

Kresse, G and Furthmüller, J. 2010. 'VASP the guide.' http : // cms.mpi.univie.ac.at / VASP/ (last accessed 13 December 2011).

Kohn, W. and Sham, L.J. 1965. 'Self-consistent equations including exchange and correlation effects.' *Physical Review* 140: A1133-A1138.

Koote, A., Haas, C. and de Groot, R.A. 1991. 'The electronic structure of ordered binary Co-Pt compounds.' *Journal of Physical Condensed Matter* 3: 1133-1152.

Kumar, M., Nautiyal, T. and Auluck, S. 2009. 'Magneto-optical properties of transition metal compounds XPt_3(X= V, Cr, Mn, Fe, Co) and X_3Pt (X= Fe, Co).' *Journal of Alloys and Compounds* 486: 60-65.

Lide, D.R. 2005. *CRC handbook of chemistry and physics*. 85^{th} Ed. CRC Press:Boca Roton.

Li, H. and Jensen, J.H. 2002. 'Partial hessian vibrational analysis: the localization of the molecular vibrational energy and entropy.' *Theoretical Chemistry Accounts* 107: 211-219.

Lubic, K.G., Amano, T., Uchara, H., Kawaguehi, K. and Hirota, E. 1984. 'The mol band of the DO_2 radical by difference frequency laser and diode laser spectroscopy: The equilibrium structure of the hydroperoxy radical.' *Journal of Physical Chemistry* 81: pp. 4826.

Ma, Y. and Balbuena, P.B. 2008. 'Surface properties and dissolution trends of Pt_3M alloys in the presence of adsorbates.' *Journal of Physical Chemistry C* 112: 14520-14528.

Mattsson, A.E., Schultz, P.A., Desjarlias, M.P., Mattsson, T.R. and Leung, K. 2005. 'Designing meaningful density functional theory calculations in material science - a primer.' *Modelling and Simulation in Materials Science and Engineering* 13: R1-R3.

Menzinger, F. and Paoletti, A. 1966. 'Magnetic moments and unpaired-electron densities in $CoPt_3$.' *Physics Review B* 143: pp. 365.

Methfessel, M. and Paxton, A.T. 1989. 'High precision sampling for Brillouin-zone integration in metals.' *Physical Review B* 40: 3616-3621.

Monkhorst, H.J. and Pack, J.D. 1976. 'Special points for Brillouin-zone integrations.' *Physical Review B* 13: 5188-5192.

Murnaghan, F.D. 1944. *Proceedings of the National Academy of Science* 30: pp. 244-247.

Neugebauer, J. and Scheffler, M. 1992. 'Adsorbate-substrate and adsorbate-adsorbate interactions of Na and K adlayers on Al(111).' *Physical Review B* 46: 16067-16080.

Nilekar, A.U., Alayoglu, S., Eichhorn, B. and Mavrikakis, M. 2010. 'Preferential CO oxidation in hydrogen : reactivity of core-shell nanoparticles.' *Journal of American Chemical Society Articles.*

Nørskov, J.K., Rossmeisl, J., Logadottir, A., Lindqvist, L., Kitchin, J.R., Bligaard, T. and Jónsson, H. 2004. 'Origin of the overpotential for oxygen reduction at a fuel cell cathode.' *Journal of Physical Chemistry B* 108: 17886-17892.

Perdew, J.P., Burke, K. and Ernzerhof, M. 1996. 'Generalized gradient approximation made simple.' *Physical Review Letters* 77: 3865-3868.

Perdew, J.P., Chevary, J.A., Vosko, S.H., Jackson, K.A., Pederson, M.R., Singh, D.J. and Fiolhais, C. 1992. 'Atoms, molecules, solids and surfaces: applications of the genaralized gradient approximation for exchange and correlation.' *Physical Review B* 46: 6671-6687.

Perdew, J.P., Ruzsinsky, A., Tao, J., Staroverov, V.N., Scuseria, G.E. and Csnoka, G.I. 2005. 'Prescription for the design and selection of density functional approximations: more consistent satisfaction with fewer fits'. *Journal of Chemical Physics* 123: 062201-062209.

Perdew, J.P., Kurth, S., Zupan, A. and Blah, P. 1999. 'Accurate density functional with correct formal properties: a step beyond the generalized gradient approximation'. *Physical Review Letters* 82: 2544-2547.

Pillay, D., Johannes, M.D., Garsany, Y. and Swider-Lyons, K.E. 2010. 'Poisoning of Pt_3Co electrodes: A combined experimental and DFT study.' *Journal of Physical Chemistry C* 114: 7822-7830.

Press, W.H., Flannery, B.P., Teukolsky, S.A. and Vetterling, W.T. 1986. *em Numerical Recipes*. Cambridge University Press: New York.

Rajagopalan, M. 2010. 'Full potential linear augmented plane wave study of the elastic properties of XPt_3(X = V, Cr, Mn, Fe, Co, Ni).' *Physica B* 405: 2516-2518.

Redington, R.L., Oslon, W.B. and Cross, P.C. 1962. 'Studies of hydrogen peroxide: the infra red spectrum and the internal rotation problem.' *Journal of Chemical Physics* 36: 11311-1326.

Roques, J., Anderson, A.B., Murthi, V.S. and Mukerjee, S. 2005. 'Potential shift for OH(ads) formation on the Pt skin on Pt_3Co(111) electrodes in acid.' *Journal of Electrochemical Society* 152: E193-E199.

Sanville, E., Kenny, S.D., Smith, R. and Henkelman, G. 2007. 'Improved grid-based algorithm for Bader charge allocation.' *Journal of Computational Chemitry* 28: 899-908.

Shi, Z., Zhang, J., Liu, Z.S., Wang, H. and Wilkson, D.P. 2006. 'Current status of ab initio quantum chemistry for oxygen electroreduction on fuel cell catalysts.' *Electrochimica Acta* 51: 1905-1916.

Shimanonchi. *Tables of molecular vibrational frequencies :consolidated volume/ NSRDS NBS - 39, 1972*

Swart, J.C.W. 2008. '*A theoritical view on deactivation of Cobalt-based Fischer Tropsch synthesis*.' PhD thesis., University of Cape Town: Cape Town.

Tang, W., Sanville, E., Henkelman, G. 2009. 'A grid-based Bader analysis algorithm without lattice bias.' *Journal of Physics: Condensed Matter* 21: 084204.

Tao, J., Perdew, J.P., Staroverov, V.N. and Scuseria, G.E. 2003. 'Climbing the density functional ladder: nonempirical meta-generalized gradient approximation designed for molecules and solids'. *Physical Review Letters* 91: 146401-146404.

Taylor, P.L. and Heinonen, O. 2002. *A quantum approach to condensed matter physics*. Cambridge University Press: Cambridge, U.K., pp. 182-207.

Troullier, N. and Martins, J.S. 1991. 'Efficient pseudopotentials for plane-wave calculations.' *Physical Review B* 43: 1993 - 2006.

Vanderbilt, D. 1990. 'Soft self-consistent pseudopotentials in a generalized eigenvalue formalism.' *Physical Review B* 41: 7892-7895.

van Helden, P. 2009. *'Initial steps of the Fischer-Tropsch synthesis on Fe(100): The role of hydrogen*.' PhD thesis., University of Cape Town: Cape Town.

Zhang, Y. and Yang, W. 1998. 'Comments on generalized gradient approximation made simple'. *Physical Review Letters* 80:890.

Chapter 3

Adsorption of the oxygen reduction reaction(ORR) intermediates

Introduction

In this chapter the adsorption of the different ORR intermediates, i.e. O_2, O, OOH, OH, HOOH and H_2O is studied on the $Pt_3Co(111)$ surface. Studying adsorption of the individual intermediates is of importance as it provides insight into how the species interact with the surface. Knowledge of how the species interact with the surface subsequently leads to an indication of the reactivity of the species on the surface.

3.1 Computational Method

The adsorption of the different intermediates has been studied on the $Pt_3Co(111)$ surface. The presence of the cobalt atoms in the alloy structure leads to 9 unique high symmetry adsorption sites compared to four on Pt(111). The 9 unique adsorption sites are indicated in Figure 3.1. For each of the intermediates, different adsorption configurations were investigated, and these configurations are presented in the search criterion section for the stable adsorption configurations for each of the intermediates. It is worth mentioning that the investigation of the adsorption configurations in the present study is not exhaustive as some possible configurations were not investigated, however the configurations considered, in the present study, are comprehensive enough such that the role of cobalt on the adsorbate's adsorption behaviour can be determined. Figure 3.1 indicates the unit cell with the 9 unique adsorption sites. The green spheres in Figure 3.1 represent Pt atoms while the maroon spheres represent Co atoms.

Glossary of the adsorption sites considered on the $Pt_3Co(111)$ surface

t_{Pt}: atop a platinum atom

t_{Co}: atop a cobalt atom

b1: bridge between a platinum atom and a cobalt atom

b2: bridge between two platinum atoms, bridging between a cobalt hcp site and a platinum fcc site.

b3: bridge between two platinum atoms, bridging between a cobalt fcc site and a platinum hcp site.

f_{Pt}: fcc site above a platinum atom.

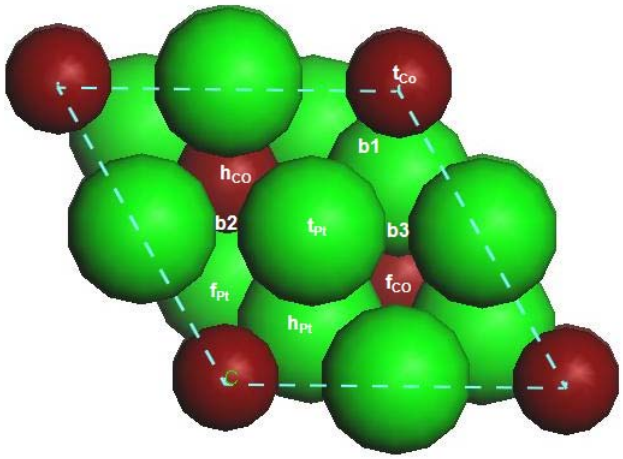

Figure 3.1: $Pt_3Co(111)$ surface with the 9 unique high symmetry adsorption sites. Green spheres represent Pt atoms and the maroon spheres represent Co atoms. The unit cell is a (2 $\times$ 2) surface unit cell

f_{Co}: fcc site above a cobalt atom.

h_{Pt}: hcp site above a platinum atom.

h_{Co}: hcp site above a cobalt atom.

The adsorption of the intermediates has been studied using the plane wave DFT code the Vienna *ab-initio* Simulation Package (VASP) (Kresse et al. 1993). The spin polarized calculations were performed using the generalized gradient approximation (GGA) of the exchange-correlation functional with the PW91 functional (Perdew et al. 1992). The electron-ion interactions are described using the projector augmented wave (PAW) pseudopotentials (Kresse and Joubert, 1999 : Blöch, 1994).

A four layer slab with a vacuum spacing of 13 Å between the surface and its periodic image was used. The adsorbates and the top two layers of the surface were allowed to relax while the bottom two layers were fixed at the optimised bulk positions. The surface was represented using a (2$\times$ 2) periodic cell. The adsorbates were adsorbed on only one side of the slab, the corresponding electrostatic potential resulting from the dipole created upon adsorption was corrected for using the dipole correction method (Neugebauer and Scheffler, 1992) as implemented in the VASP code (Kresse and Furthmüller, 2010). The k-point sampling mesh was generated using the Monkhorst-Pack scheme (Monkhorst and Pack, 1976) with a k-point grid of (12 $\times$ 12 $\times$ 1). The plane wave basis set cut-off energy was set to 400 eV. These parameters were determined as the optimal converged settings as presented in chapter 2. The Methfessel Paxton (Methfessel and Paxton,1989) method was utilised for the electron distribution at the Fermi-level with width σ = 0.20 eV. This value was not optimised but it was used as the recommended value for metals in the VASP user's guide (Kresse and Furthmüller, 2010).

To study the adsorption of the intermediates, 1 molecule of the adsorbate was considered per unit cell. For each adsorbate the adsorption of the species on each of the 9 unique sites, plus the possibility of different high symmetry configurations per site, was investigated. The gas-phase species for each intermediate were used as reference for calculating the adsorption energies. The adsorption energy of the species was calculated using the following equation:

$$E_{\text{ads}} = E_{\text{slab+adsorbate}} - E_{\text{slab}} - E_{\text{gas phase adsorbate}} \tag{3.1}$$

The zero point energy corrections were calculated using the relationship :

$$ZPE = \sum_i \frac{1}{2} h\nu_i \tag{3.2}$$

ν_i represents the different vibrational modes of the adsorbate and h is Planck's constant.. The frequencies are calculated by numerical differentiation of the forces via the use of a second order finite difference method with a step size of 0.02 Å, with subsequent diagonalisation of the Hessian matrix (Li and Jensen, 2002). The calculated frequencies for the adsorption of the ORR species are presented in appendix B. For determination of the vibrational modes only the adsorbate atoms are allowed to move whilst the atoms of the slab are fixed. The adsorption energies with the zero point energy corrections included are calculated as :

$$E_{ads+ZPE} = E_{ads} + \triangle ZPE \tag{3.3}$$

$$\triangle ZPE = E_{\text{ZPE,adsorbate}} - E_{\text{ZPE,gas phase adsorbate}}$$

The force convergence criterion for relaxing the structures was a force below 0.03 eV/Å, the force relaxation method used is the conjugate gradient algorithm (Press et al. 1986), and the energy convergence criterion was energy changes below 1×10^{-4} eV. All the adsorption configurations, presented in this chapter, were confirmed as minima on the potential energy surface. Confirmation of the adsorbates as minima is through the determination of the vibrational modes of the species on the surface, all vibrational modes being positive is an indication of a minimum on the potential energy surface. All reported adsorption energies in the present chapter include the zero-point energy corrections, defined as $E_{ads+ZPE}$, but in the present study the adsorption energies including the zero-point energy corrections will be referred to as E_{ads}.

The Bader charge analysis was performed using the Bader method (Bader, 1990) developed for the VASP code by the Henkelman group (Tang et al. 2009; Sanville et al. 2007; Henkelman et al. 2006). The Bader charge partitioning is performed on the total charge density which is obtained by summing the valence electron density to the core charge density (the structural optimisation calculations were set such that the core charge is also written to file at the end of the structural optimisation). To determine the net charge transfer upon adsorption, the atom-resolved charge of the clean slab + the charge of gas-phase adsorbate was subtracted from the atom-resolved charge of the slab with adsorbate on it. The bader charge transfer is defined as:

$$q_{Bader} = q_{slab+adsorbate} - q_{cleanslab} - q_{gasphase} \tag{3.4}$$

where q_{Bader} is the charge transfer upon adsorption, $q_{slab+adsorbate}$ is the atom resolved charge for the slab with the adsorbate, $q_{cleanslab}$ is the atom resolved charge for the clean slab and $q_{gasphase}$ is the atom resolved charge for the gas phase species. A positive value for the Bader charge transfer indicate charge increase, i.e. a more negative charge on the atom in the adsorbed state than the charge on the atom in the gas phase or in a clean slab with no adsorbate. Similarly, a negative value for the Bader charge transfer indicate a decrease in charge, i.e. a more positive charge on the atom in the adsorbed state than the charge on the atom in the gas phase or in the clean slab with no adsorbate. Therefore, for all the reported Bader charge tranfers, presented in this chapter, a negative value for the Bader charge represent a charge loss and a positive Bader charge transfer represent an increase in charge.

Comparison with adsorption on the Pt(111) surface

Comparison of the lowest energy adsorption configurations of the ORR intermediates on the $Pt_3Co(111)$ surface, is made to the lowest energy configurations of the ORR intermediates obtained on the Pt(111) surface.

The data used for the Pt(111) surface is sourced from the calculations performed by Madala (2012). The lowest energy adsorption geometries obtained on Pt(111) using the PBE functional in the study by Madala (2012) were re-optimised using the PW91 functional for the present study. The same force and energy convergence criteria used for the optimised adsorption geometries on $Pt_3Co(111)$ in the present study were used for determining the optimised adsorption geometries on Pt(111) utilising the PW91 functional. The choice of the lattice parameter, k-point mesh,

slab thickness and vacuum gap used for Pt(111) in the present study is based on the convergence tests done for these parameters on Pt(111) by Madala (2012), which is the source of data for the calculations done on Pt(111). The lattice parameter for Pt(111) was 3.93 Å and a 6-layer slab with the top two layers together with the adsorbate allowed to relax. A vacuum gap of 12 Å was used. The Monkhorst-Pack method (Monkhorst and Pack, 1976) for k-point sampling was used with a k-point mesh of (6×6×1) and the basis set cut-off energy was set at 400 eV. A (2×2) surface unit cell was used for the adsorption of the adsorbate resulting in a coverage of 0.25 ML and adsorption was allowed on only one side of the slab with the dipole correction applied as implemented in the VASP code (Kresse and Furthmüller, 2010) to correct for the resulting electrostatic potential. The Methfessel Paxton (Methfessel and Paxton,1989) method was utilised for the electron distribution at the Fermi-level with width σ = 0.20 eV. The electron-ion interactions were described using the projector augmented plane wave (PAW) pseudopotentials (Kresse and Joubert, 1999; Blöch, 1994).

3.2 Molecular Oxygen (O_2) Adsorption

The first step in the ORR mechanism in proton exchange membrane fuel cells (PEMFC) is proposed to be the adsorption of molecular oxygen on the cathode (Yeh et al. 2009). Thus, investigating the adsorption behaviour of O_2 on the catalyst surface is valuable in providing insights into the first step of the ORR mechanism. Eichler and Hafner (1997) performed DFT studies of O_2 adsorption on Pt(111). Two distinct almost energetically degenerate molecular states of O_2 were identified on Pt(111), one molecular state was a top-bridge-top configuration with a O-O bond length of 1.39 Å and O-O stretching frequency of 850 cm^{-1}. The second molecular state was a top-fcc-bridge configuration with a calculated O-O bond length of 1.43 Å and O-O stretching frequency of 690 cm^{-1}. A top-hcp-bridge configuration with a calculated O-O bond length of 1.42 Å and O-O stretching frequency of 710 cm^{-1} was also reported by Eichler and Hafner (1997).

Xu et al. (2004) also performed DFT studies of O_2 adsorption on Pt_3M alloys and their corresponding Pt-skin structures. The investigated Pt_3M alloys were for M being Co and Fe. The most stable adsorption configurations were a top-bridge-top configuration involving a bridge between Pt-M and top-fcc-bridge configurations. A variety of non-equivalent top-fcc-bridge and top-hcp-bridge configurations of O_2 were obtained on the alloy surface. Relative to Pt(111), O_2 was calculated to adsorb much stronger on Pt_3M structures whilst on the Pt-skin structures on Pt_3M, O_2 adsorbed weaker compared to Pt(111).

Yang et al. (2010) performed DFT studies of O_2 on Pt-skin structure on $Pt_3Ni(111)$. Two unique configurations of O_2 on the Pt-skin on $Pt_3Ni(111)$ were identified, top-bridge-top configuration and top-fcc-bridge configurations. A variety of almost energetically degenerate top-bridge-top configurations were obtained. The top-fcc-bridge configuration was calculated to have a higher O_2 adsorption energy than the top-bridge-top configurations.

From the few cited reported studies of O_2 adsorption on Pt alloys, the most stable O_2 configurations on Pt_3M alloys are the top-bridge-top and top-fcc-bridge configurations.

3.2.1 Search strategy for adsorption configurations of O_2 on $Pt_3Co(111)$

The adsorption of O_2 was probed on the 9 unique high symmetry sites on $Pt_3Co(111)$. For the 3-fold-hollow sites, the different possible configurations of the adsorbate on these sites were explored. The explored configurations in the present study are indicated in Figure 3.2, where the blue circles represents oxygen atoms. Following is a description of the search strategy followed for the different sites.

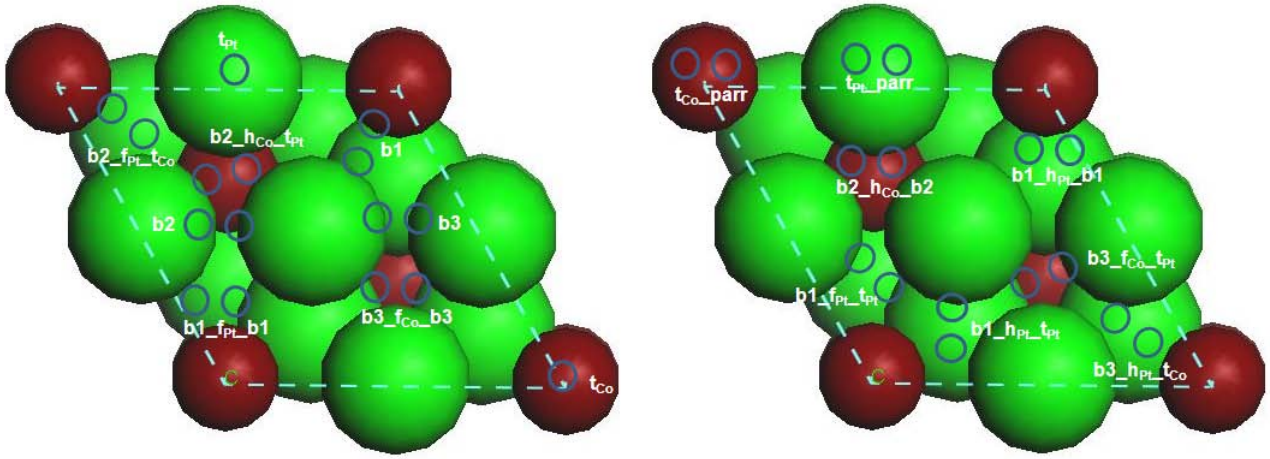

Figure 3.2: Schematic diagram of the different O_2 adsorption configurations explored on Pt_3 Co(111)

For the atop sites, i.e. t_{Co} and t_{Pt} two possible configurations were investigated: the configuration with the O_2 perpendicular to the surface and the configuration with the O-O bond parallel to the surface.

Three possible configurations were explored for O_2 adsorption on the 3-fold-hollow sites based on a Pt atom, viz. f_{Pt} and h_{Pt}. The first configuration was where the oxygen atoms were on the bridge site b1 with the bond axis of the molecule across the 3-fold-hollow sites, e.g. b1_f_{Pt}_b1 and b1_h_{Pt}_b1 as illustrated in Figure 3.2. The second configuration was such that one of the oxygen atoms is atop a Co atom with the other oxygen atom on the bridge site b2 and b3 and the O-O bond axis across the 3-fold-hollow sites, these configurations are represented as b2_f_{Pt}_t_{Co} and b3_h_{Pt}_t_{Co} in Figure 3.2. The third configuration was such that one of the oxygen atoms is on bridge site b1 and the other oxygen atom is atop a Pt atom whilst the O-O bond axis is across the 3-fold-hollow site, configurations b1_f_{Pt}_t_{Pt} and b1_h_{Pt}_t_{Pt} are illustrations of this configuration.

Two possible configurations were explored for O_2 adsorption on the 3-fold-hollow sites based on a Co atom, i.e. f_{Co} and h_{Co}. The first configuration was where both oxygen atoms were on the bridge sites comprising the 3-fold-hollow sites with the O-O bond axis across the 3-fold-hollow site, configuration b3_f_{Co}_b3 and b2_h_{Co}_b2 are illustrations of this configuration. The second configuration was such that one of the oxygen atoms is on a bridge site, i.e. b2 or b3 with the other oxygen atom atop a Pt atom and the O-O bond axis across the 3-fold-hollow site, configurations b3_f_{Co}_t_{Pt} and b2_h_{Co}_t_{Pt} indicated in Figure 3.2 are illustrations of this configuration.

3.2.2 Molecular O_2 adsorption results and discussion

In Table 3.1 the calculated properties of O_2 on the Pt_3Co(111) surface are summarized.

Table 3.1: Calculated adsorption configurations, adsorption energies, O-O bond distance, O-O stretching frequency and the O metal distances for O_2 adsorption on $Pt_3Co(111)$. The calculations are for 0.25 ML coverage of O_2. The data is ordered according to decreasing E_{ads}.

Adsorption configuration	**E_{ads} (eV)**	**d_{O-O} (Å)**	**ν_{O-O} (cm^{-1})**	**d_{O-Co} (Å)**	**d_{O-Pt} (Å)**
b1	-0.97	1.38	865	1.80	2.06
b2_f_{Pt}_t_{Co}	-0.96	1.43	713	1.80	2.18
b1_f_{Pt}_b1	-0.89	1.46	709	2.10	2.09
b1_f_{Pt}_t_{Pt}	-0.88	1.42	773	1.99	2.04, 2.16
b1_h_{Pt}_t_{Pt}	-0.82	1.42	782	1.94	2.03, 2.33
b3	-0.76	1.37	905	-	2.05, 2.07
b3_h_{Pt}_t_{Co}	-0.75	1.40	777	1.81	2.22, 2.25
b2	-0.63	1.36	917	-	2.03, 2.05
b2_h_{Co}_t_{Pt}	-0.63	1.40	829	-	2.05
t_{Co}	-0.30	1.25	1326	1.84	-

Figure 3.3 shows the stable O_2 adsorption configurations on the $Pt_3Co(111)$ surface.

3.2.3 O_2 adsorption configurations

3.2.3.1 Adsorption configurations on 3-fold-hollow sites based on Pt (f_{Pt} and h_{Pt})

For geometrically equivalent sites with the only difference between the sites being that one is a fcc site and the other a hcp site, there is more stretching of the O-O bond length on a f_{Pt} site than on a h_{Pt} site for the same O_2 configuration as is the case for configurations b2_f_{Pt}_t_{Co} and b3_h_{Pt}_t_{Co}. The O-O bond lengths are 1.43 Å and 1.40 Å for the b2_f_{Pt}_t_{Co} and b3_h_{Pt}_t_{Co} configurations, respectively. For both configurations the O-Co distances are almost identical whilst the O-Pt distances are different. The O-Pt distance for configuration b2_f_{Pt}_t_{Co} is 2.18 Å and is lower than the O-Pt distance for configuration b3_h_{Pt}_t_{Co}, which are 2.25 and 2.22 Å.

For the equivalent configurations where one of the oxygen atoms is atop a Pt atom and the other oxygen atom above bridge site b1, i.e. adsorption configurations b1_f_{Pt}_t_{Pt} and b1_h_{Pt}_t_{Pt}, the O-O bond stretch is the same for both the f_{Pt} and h_{Pt} site configurations. The O-O bond length for both configurations was found to be the same despite the difference in the O-Co and O-Pt distances for the two configurations. The O-Co distance for the b1_f_{Pt}_t_{Pt} configuration is 1.99 Å whilst that for the b1_h_{Pt}_t_{Pt} configuration is 1.94 Å, the corresponding O-Pt distances are 2.04 and 2.16 Å for the b1_f_{Pt}_t_{Pt} configuration and 2.03 and 2.33 Å for the b1_h_{Pt}_t_{Pt} configuration.

For the equivalent configurations where the oxygen atoms are above the bridge site b1 and the O-O bond axis across the 3-fold-hollow sites, there was no stable adsorption configuration obtained for the h_{Pt} site while a stable adsorption configuration was obtained on the f_{Pt} site represented as configuration b1_f_{Pt}_b1 in Figure 3.3. The b1_f_{Pt}_b1 configuration was determined to be the configuration with the longest O-O bond length of 1.46 Å and the longest O-Co distance of 2.10 Å.

From the results of O_2 adsorption on the f_{Pt} and h_{Pt} sites it appears that there is no monotonic relationship between the stretching of the O-O bond length and the calculated O - metal distances, e.g. O-Co or O-Pt distances.

3.2.3.2 Adsorption configurations on bridge sites

The most stretched O-O bond length for the bridge site adsorption of O_2 was calculated for the b1 configuration at a distance of 1.38 Å. For the Pt - Pt bridge sites, i.e. b2 and b3, different O-O bond lengths were calculated with the b3 O_2 configuration having a slightly longer O-O bond length of 1.37 Å compared to the 1.36 Å for the b2 configuration.The difference in the

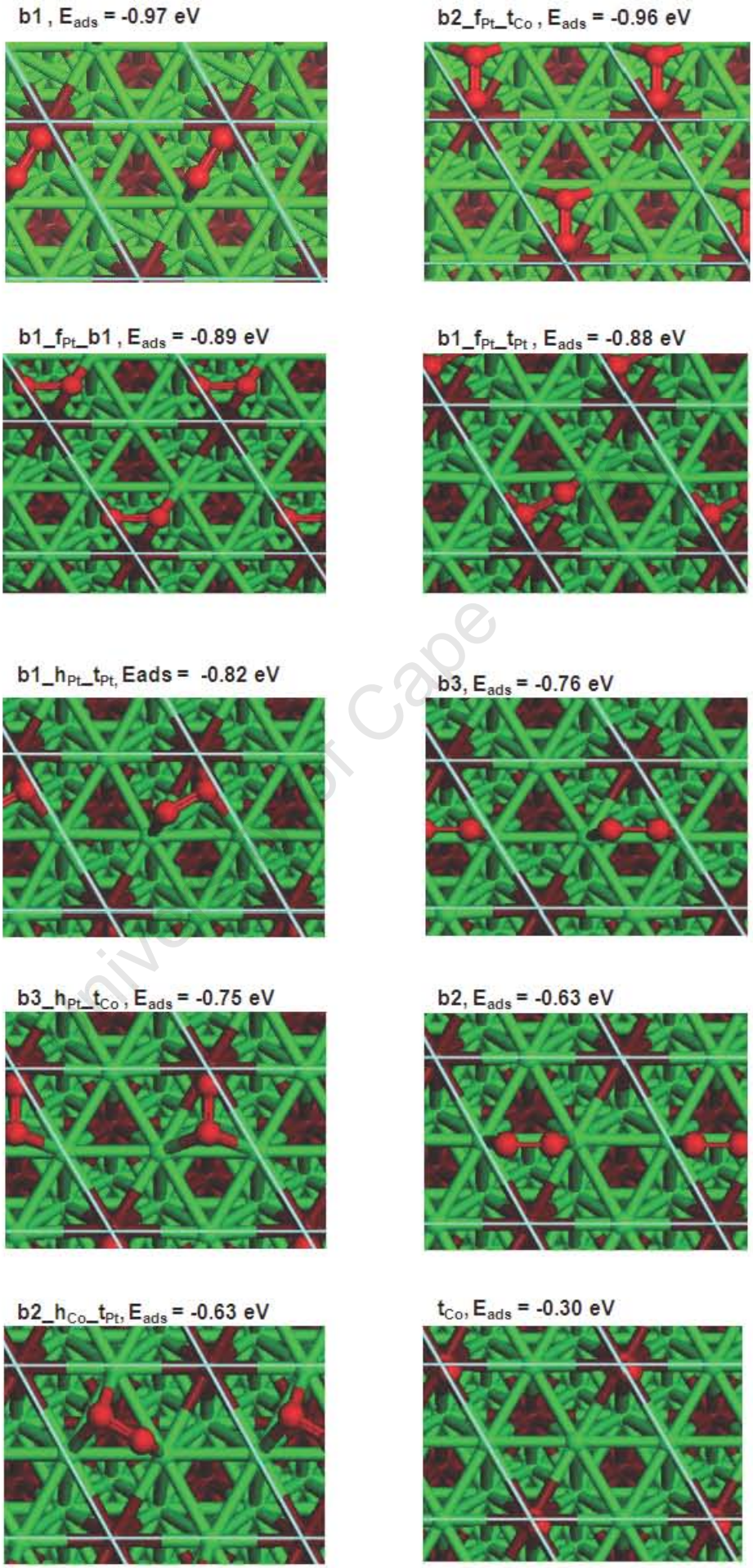

Figure 3.3: Calculated adsorption configurations of O_2 on $Pt_3Co(111)$

calculated O-Pt distances for the bridge sites b2 (2.03 and 2.05 Å) and b3 (2.05 and 2.07 Å) comprising only Pt atoms is an indication that the O_2 molecule does not lie precisely parallel to the surface. The difference in the O-Pt distances for the two configurations might indicate that the O_2 molecule adsorbs on the surface in such a way that one of the oxygen atoms is further away from the surface than the other.

On comparison of the O-Pt distances for b2 and b3 configurations and relating these to the O-O bond stretch it is evident that shorter O-Pt distances do not translate to longer O-O bond lengths. This further strengthens the observation made for O_2 adsorption on the 3-fold-hollow sites based on Pt where there is no correlation between the O-O bond length and the calculated O-Pt or O-Co distances.

The O-O bond lengths of the O_2 bridge configurations are shorter than the O-O bond lengths of the f_{Pt} and h_{Pt} sites. This is an indication that the O-O bond is activated less on the bridge sites compared to activation on the 3-fold-hollow sites.

3.2.3.3 Adsorption configurations on 3-fold-hollow sites based on Co (f_{Co} and h_{Co})

No stable adsorption configurations were obtained for configurations based on the f_{Co} site. The configurations on this site were optimized to final bridge configurations. Of the investigated possible O_2 configurations based on the h_{Co} site, one stable configuration was obtained for the b2_h_{Co}_t_{Pt} configuration. O_2 in this configuration adsorbs with the same O-O bond length of 1.40 Å as the b3_h_{Pt}_t_{Co} configuration. The Co atom in the fcc position appears to destabilize O_2 adsorption on this site, since the final optimized configurations are bridge site configurations. The Co in the hcp position appears to stabilize O_2 adsorption on this site relative to the f_{Co} site, since there is a stable configuration of O_2 on the h_{Co} site.

3.2.3.4 Adsorption configurations on atop sites

No stable O_2 adsorption configuration was obtained atop a Pt atom whereas a stable O_2 adsorption configuration was obtained atop a Co atom. The stable O_2 configuration atop Co is an indication of the stabilizing effect of the surface Co on O_2 adsorption, since subsurface Co destabilizes O_2 as there is no stable adsorption configuration on the f_{Co} site. No stable adsorption configurations were obtained for the O_2 adsorption configurations where both oxygen atoms interact directly with a single metal atom, atop a Pt atom or atop a Co atom, these configurations are identified as t_{Co}-parr and t_{Pt}-parr in Figure 3.2. The t_{Co}-parr configuration optimized to the b3_h_{Pt}_t_{Co} configuration, whilst the t_{Pt}-parr configuration optimized to the b3 configuration. The O_2 molecule adsorbs atop a Co atom with the shortest O-O bond length of all the stable O_2 configurations obtained on the $Pt_3Co(111)$ surface, at O-O bond length of 1.25 Å .

3.2.4 Adsorption energy of O_2 on $Pt_3Co(111)$ for the different configurations

The most stable adsorption configurations for O_2 on the $Pt_3Co(111)$ surface are b1 and b2_f_{Pt}_t_{Co}. The order of the adsorption strength of O_2 for the 3-fold-hollow sites is f_{Pt}> h_{Pt} > h_{Co}. For the bridge site configurations, the order of O_2 adsorption strengths is b1 > b2 > b3.

3.2.4.1 Adsorption energy of O_2 on 3-fold-hollow sites based on Pt (f_{Pt} and h_{Pt})

Comparing similar configurations which differ in that one configuration is based on the f_{Pt} site and the other on the h_{Pt} site , it is observed that the f_{Pt} site is more stable relative to the h_{Pt} site in terms of the adsorption energy of O_2. Using configurations b2_f_{Pt}_t_{Co} and b3_h_{Pt}_t_{Co} as examples the f_{Pt}-based configuration is 0.21 eV more stable than the h_{Pt} site. The difference in energy between equivalent configurations of the f_{Pt} and the h_{Pt} sites is not constant, but depends on the orientation of the O_2 molecule over the 3-fold-hollow site. The difference in energy

between configurations b1_f_{Pt}_t_{Pt} and b1_h_{Pt}_t_{Pt} is 0.06 eV, with the f_{Pt} site configuration being the more stable one; the difference between configurations b2_f_{Pt}_t_{Co} and b3_h_{Pt}_t_{Co} is 0.21 eV with the f_{Pt} site-based configuration the most stable configuration. For configurations b2_f_{Pt}_t_{Co} and b3_h_{Pt}_t_{Co}, the adsorbate is such that one O is atop a surface Co atom as illustrated in Figure 3.3, whilst for configurations b1_f_{Pt}_t_{Pt} and b1_h_{Pt}_t_{Pt} the adsorbate is such that one O is bonded to a Co-Pt bridge site and is shared between a Co and Pt atom unlike the case for b2_f_{Pt}_t_{Co} and b3_h_{Pt}_t_{Co} where one O is atop a Co atom. Figure 3.3 illustrates the adsorption configuration for b1_f_{Pt}_t_{Pt} and b1_h_{Pt}_t_{Pt} and indicates the different orientation to that of configurations b2_f_{Pt}_t_{Co} and b3_h_{Pt}_t_{Co}. In configurations b1_f_{Pt}_t_{Pt} and b1_h_{Pt}_t_{Pt} the adsorbate is such that one O is shared between a Co and Pt atom as in the bridge site b1. Therefore it appears that the adsorbate O_2 is strongly stabilized when one of the O's is atop a surface Co atom rather than when one of the O's is shared between Co and Pt atoms.

Configuration b1_f_{Pt}_b1 is calculated to be the third most stable configuration; it is also the configuration which results in the most activated O-O bond at a O-O bond length of 1.46 Å. For the corresponding configuration on the h_{Pt} site, i.e. b1_h_{Pt}_b1 there was no stable adsorption configuration obtained, since the final optimized configuration was a bridge site configuration. No stable f_{Co} configurations were obtained since the final optimized configurations were bridge site configurations.

3.2.4.2 Adsorption energy of O_2 for bridge site configurations

Of the three different bridge site configurations, bridge site b1 configuration is the most stable adsorption configuration. The bridge site b1 configuration is also the most strongly adsorbed configuration of all the stable O_2 configurations on the $Pt_3Co(111)$ surface, with an adsorption energy of 0.97 eV. This is albeit the b2_f_{Pt}_t_{Co} configuration having a similar adsorption energy at 0.96 eV. The O_2 molecule is stabilized by coordinating directly to a surface Co atom through one of its oxygen atoms directly coordinated to a surface Co atom. The two remaining bridge sites comprise only Pt atoms, and these two bridge sites possess different, less stable, adsorption energies for the adsorbate O_2. The b3 configuration is 0.13 eV more stable than the b2 configuration. Comparing the adsorption energy of the Pt-Co bridge configuration to that of the Pt-Pt bridge configurations, i.e. b2 and b3, it can be deduced that the Co atom interacting with the O_2 molecule provides stabilization for the adsorption of the adsorbate. The O_2 molecule on b1 is stabilized by 0.34 eV relative to the b2 configuration and by 0.21 eV relative to the b3 configuration.

3.2.4.3 Adsorption energy of O_2 for the 3-fold-hollow sites based on Co

Of the investigated configurations on the 3-fold-hollow sites based on Co only one stable configuration was obtained, this configuration is the b2_h_{Co}_t_{Pt} configuration. The adsorption energy of this configuration is -0.63 eV, this adsorption energy is identical to that of bridge site b2. The O_2 adsorbed on the b2_h_{Co}_t_{Pt} configuration has a longer O-O bond length of 1.40 Å than the b2 configuration with a O-O bond length of 1.36 Å. The subsurface Co atom at the 3-fold-hollow site position appears not to play a direct role in the adsorption energy of O_2 over this site relative to b2, since the adsorption energy is identical to that of bridge site b2. O_2 adsorption is less stable on the h_{Co} site than adsorption at the f_{Pt} or h_{Pt} site, this indicates that subsurface Co appears to destabilise O_2 relative to subsurface Pt at the 3-fold-hollow sites, the destabilization of O_2 on the subsurface Co at the 3-fold-hollow sites is to the extent that on the f_{Co} site there is no stable O_2 adsorption geometry.

3.2.4.4 Adsorption energy of O_2 on atop sites

O_2 was least stable adsorbed perpendicularly atop a Co atom with an adsorption energy of -0.30 eV. No stable adsorption sites were obtained atop a Pt atom. With only one of the oxygen atoms atop a surface Co atom and the other oxygen atom not bonded directly to any surface metal atom, this orientation is the least stable for O_2 adsorption on the surface and this manifests itself as a comparatively low adsorption energy.

3.2.5 O-O stretching frequencies for the different O_2 adsorption configurations

In Figure 3.4 the O-O stretching frequency is plotted as a function of the O-O bond length for the various O_2 adsorption configurations.

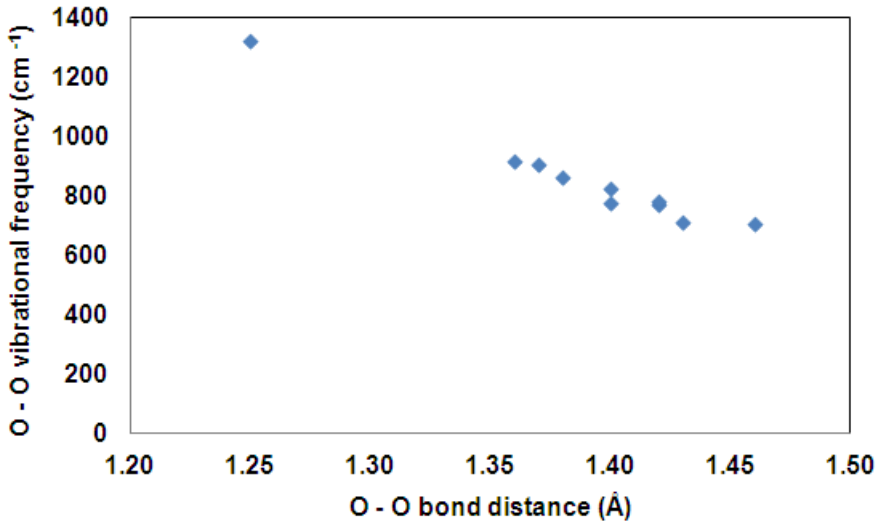

Figure 3.4: Calculated O-O stretching frequencies plotted as a function of the O-O bond length for the different identified stable adsorption configurations of O_2 on $Pt_3Co(111)$

From Figure 3.4, which illustrates the correlation between the O-O stretching frequency and the O-O bond lengths it is observed that a near-linear relation exists between the two variables. Upon the adsorption of O_2 on the surface, for all the 10 unique adsorption configurations, it is evident that the O_2 molecule is activated on the surface, and this activation is manifested by the stretching of the O-O bond length relative to the calculated O-O bond length of gas phase O_2. (The calculated O-O bond length is 1.23 Å for gas-phase O_2 and the calculated O-O stretching frequency is 1570 cm^{-1}). From Table 3.1 the O-O bond lengths of all the unique configurations are greater than 1.23 Å and the O-O stretching frequencies are lower than 1580 cm^{-1}. The lengthening of the O-O bond is indicative of weakening of the O-O bond and this bond-weakening manifests itself as a shift to lower frequencies for the O-O stretching.

Comparing the O-O stretching frequencies for the different configurations, it is observed that the configurations based on the f_{Pt} site correspond to the lowest O-O stretching frequencies and the most stretched O-O bond distances. Therefore, the O_2 molecule is activated most while adsorbed in configurations based on the f_{Pt} site. The O_2 molecule is least activated upon adsorption directly atop a Co atom, as indicated by the highest O-O stretching frequency and the shortest O-O bond distance. For bridge site configurations, the O_2 molecule is activated most for adsorption on bridge site b1 between a Co and a Pt atom, as evidenced by the lower O-O stretching frequency relative to other bridge site configurations. Comparing the Pt-only bridge sites, i.e. b2 and b3, the O-O stretching frequency is lowered most for the b3 configuration, hence the b3 configuration is slightly more activated than the b2 configuration, which has a 0.01 Å less-stretched O-O bond distance relative to that of the b3 configuration.

Figure 3.5 is a plot of the calculated O-O stretching frequency plotted as a function of the adsorption energy of O_2. It can be seen that there is no clear monotonic correlation between the O-O stretching frequency and the adsorption energy of O_2. Therefore, a strong interaction between the O_2 molecule and the surface which is represented by the stable adsorption energy is not expected to lead to a lower activation barrier for the dissociation of O_2 on the surface. The

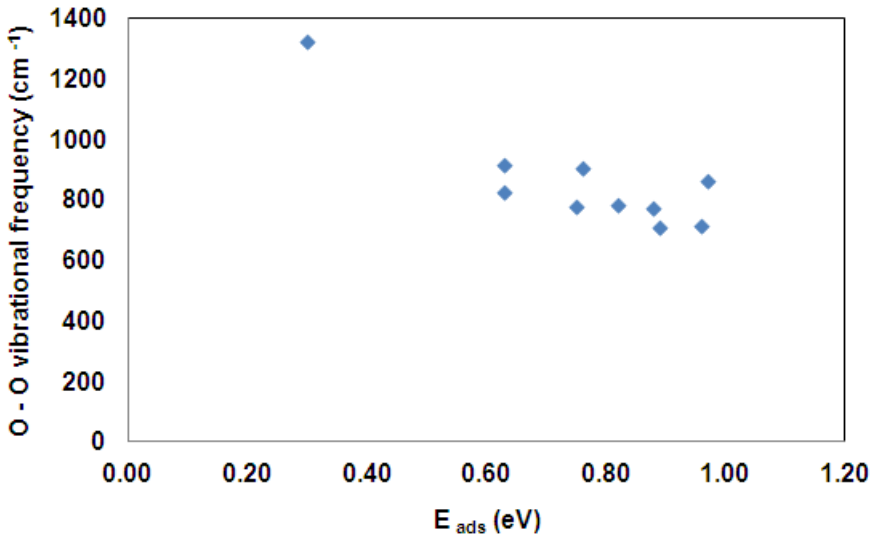

Figure 3.5: Plot of the calculated O-O stretching frequency as a function of the adsorption energy of O_2 for the different configurations of O_2 on $Pt_3Co(111)$

assumption here is that a lower vibrational frequency may possibly produce facile dissociation of O_2 through the lowering of the expected activation energy for dissociation.

3.2.6 Bader charge analysis

In Table 3.2 the calculated charge redistribution upon adsorption of O_2 on the $Pt_3Co(111)$ surface for each of the 10 identified configurations of O_2 adsorption is presented. The table includes the charge redistribution on the adsorbed O_2, the first layer platinum atoms, and the cobalt atom in the first layer.

Table 3.2: Bader charge transfer to the atoms upon adsorption of O_2 on $Pt_3Co(111)$ determined through the Bader method of charge partitioning

Adsorption	**Bader Charge (e^-)**					
Configuration	**O**	**O**	**Pt**$_{surf1}$	**Pt**$_{surf2}$	**Pt**$_{Surf3}$	**Co**$_{surf}$
b1	0.32	0.31	-0.33	-0.07	-0.07	-0.18
b2_f$_{Pt}$_t$_{Co}$	0.36	0.39	-0.27	-0.26	-0.07	-0.20
b1_f$_{Pt}$_b1	0.45	0.42	-0.30	-0.29	-0.06	-0.26
b1_f$_{Pt}$_t$_{Pt}$	0.43	0.35	-0.34	-0.27	-0.06	-0.18
b1_h$_{Pt}$_t$_{Pt}$	0.33	0.42	-0.32	-0.21	-0.06	-0.19
b3	0.30	0.27	-0.31	-0.31	-0.03	-0.04
b3_h$_{Pt}$_t$_{Co}$	0.33	0.37	-0.22	-0.23	-0.06	-0.19
b2	0.28	0.27	-0.30	-0.29	-0.02	-0.05
b2_h$_{Co}$_t$_{Pt}$	0.32	0.35	-0.32	-0.22	-0.21	-0.04
t$_{Co}$	0.32	0.06	-0.05	-0.04	-0.04	-0.19

On average the charge transferred from the surface Co atom is in the range 0.18 to 0.20 e^- for configurations involving coordination to a surface Co atom. All configurations but b3, b2 and b2_h$_{Co}$_t$_{Pt}$ configurations involve coordination to a surface Co atom. The only exception where 0.26 e^- charge is transferred from the surface Co atom is for configuration b1_f$_{Pt}$_b1. For this configuration both oxygen atoms are bonded to bridge site b1 involving the same Co atom, this

configuration is illustrated in Figure 3.3. For configurations not involving direct coordination to a surface Co atom a small amount of charge of 0.04 e^- is transferred from the surface Co atom.

For all adsorption configurations of O_2 there is charge transferred to the oxygen molecule upon adsorption. From the calculated charge transfer to the adsorbed O_2 molecule it is inferred that the Bader method as utilized in the present study is accurate to within $\pm$ 0.03 e^-, this is due to the difference in charge between the two oxygen atoms which are in symmetrically equivalent enviroments for configurations b1_f$_{Pt}$_b1 and b3. The two oxygen atoms for these two configurations are on equivalent sites, i.e. for configuration b1_f$_{Pt}$_b1 both oxygen atoms are bonded to site b1 and for configuration b3 both oxygen atoms are atop Pt atoms hence it would be expected that the charge assignment for the two oxygen atoms should be the same for these two configurations.

The charge transferred to the oxygen atom for configurations where one of the oxygen atoms is atop a Co atom is in the range 0.32 to 0.33 e^-except for the b2_f$_{Pt}$_t$_{Co}$ configuration where a higher charge of 0.36 e^- is transferred to the oxygen atom. The charge transferred to the oxygen atom atop a Co atom is listed in the first column of charge transferred to atomic O in Table 3.2. Configurations involving an oxygen atom atop a Co atom are : b1, b2_f$_{Pt}$_t$_{Co}$, b3_h$_{Pt}$_t$_{Co}$ and t$_{Co}$. For configurations where one of the oxygen atoms is on bridge site b1 higher charge (0.45 and 0.43 e^-) is transferred to the oxygen atom except for configuration b1_h$_{Pt}$_t$_{Pt}$ where the charge transferred to the oxygen atom on b1 is similar to that for an oxygen atom atop a Co atom.

The second column of charge transferred to atomic O in Table 3.2 represents the charge transferred mostly to an oxygen atom atop a Pt atom. The charge transferred to the oxygen atom atop a Pt atom ranges from 0.27 - 0.35 e^-. The exception is where 0.42 e^- charge is transferred to the oxygen atom atop a Pt atom for configuration b1_h$_{Pt}$_t$_{Pt}$. The lowest charge transfer to the oxygen atom is for the O_2 molecule aligned parallel to the bridge sites b2 and b3. The charge transfer to the oxygen atom on a bridge site involving two Pt atoms is higher (0.39 and 0.37 e^-) than when the oxygen atom is atop a Pt atom. Configurations where the oxygen atom is coordinated to a Pt-only bridge site are b2_f$_{Pt}$_t$_{Co}$ and b3_h$_{Pt}$_t$_{Co}$.

The Pt surface atoms in Table 3.2 are listed such that the Pt atoms directly interacting with the adsorbate are listed first. On average 0.22 to 0.33 e^- charge is transferred from the surface Pt atoms in direct contact with the adsorbate. Pt$_{surf3}$ represents the Pt surface atom not directly coordinated to the adsorbate. It is evident from the calculated charges that there small charge, less than 0.1 e^-, transferred from Pt$_{surf3}$ surface atoms except for the b2_h$_{Co}$_t$_{Pt}$ configuration where the adsorbate interacts with all three surface Pt atoms within the unit cell.

The charge transferred from the surface Pt atoms to the adsorbate is higher than the charge transferred from the surface Co atoms for all configurations.

The adsorption configurations in Table 3.2 are arranged in descending order of the O_2 adsorption energies and from the calculated Bader charge transfer to the adsorbate it is evident that there is no clear correlation between the amount of charge transferred to the adsorbate and the O_2 adsorption energy. Figure 3.6 is a plot of the O_2 adsorption energy as a function of charge transferred to the O_2 adsorbate which shows the same lack of correlation.

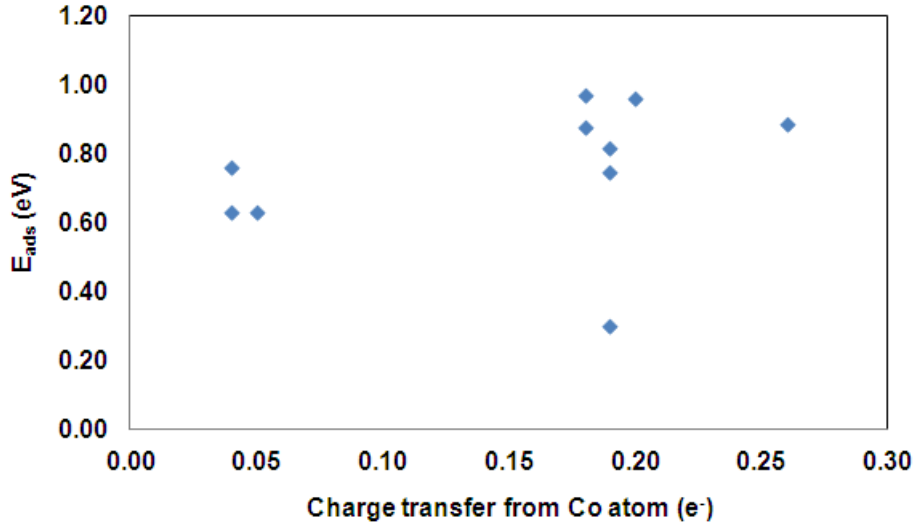

Figure 3.6: Plot of calculated adsorption energy of O_2 as a function of the calculated charge transfer to O_2 on $Pt_3Co(111)$

3.2.7 Comparison with O_2 adsorption on Pt(111)

The lowest energy O_2 configuration obtained on the Pt(111) surface reported by Madala(2012) is a top-fcc-bridge configuration, with an adsorption energy of -0.63 eV calculated with the PW91 functional. The O-O bond for the lowest energy O_2 configuration is 1.40 Å and the O-O stretching frequency is 818 cm^{-1}. Therefore, on the $Pt_3Co(111)$ surface the adsorption strength of the lowest energy O_2 configuration is stronger than on the Pt(111) surface by 0.33 eV and the O-O bond is activated more. The two lowest energy O_2 configurations obtained on the $Pt_3Co(111)$ surface, in the present study, are equivalent to the stable geometries obtained on the Pt(111) surface by Eichler and Hafner (1997). The two stable geometries obtained on the Pt(111) surface are the bridge geometry and the top-fcc-bridge geometry.

3.2.8 Comparison with previous studies of O_2 adsorption on $Pt_3Co(111)$

No experimental literature on O_2 adsorption on the $Pt_3Co(111)$ surface was obtained, hence the results of O_2 adsorption on the $Pt_3Co(111)$ surface obtained in the present study will be compared to other DFT studies.

In order to assess the consistency of the calculated adsorption energies of O_2 on $Pt_3Co(111)$ in the present study, a comparison is made with a previous study of O_2 adsorption on $Pt_3Co(111)$. Xu et al. (2004) investigated O_2 adsorption on $Pt_3Co(111)$ using a 4 layer slab with the top two layers and the adsorbate allowed to relax. The calculations were performed with the GGA - PW91 functional at a surface coverage of 0.25 ML of O_2, the same parameters were used in the present study. Comparing the adsorption configurations of O_2 obtained in the study of Xu et al. (2004) using the DACAPO code and those of the present study there is agreement on the unique adsorption configurations of O_2 in both studies. The same non-stable adsorption configurations were obtained in the present study as reported by Xu et al. (2004), e.g. no stable adsorption configurations were obtained for configurations b3_f$_{Co}$_t$_{Pt}$, b3_f$_{Co}$_b3 and b2_h$_{Co}$_b2.

There is a difference in energy between the adsorption energies of O_2 for the different configurations calculated in the present study and those reported by Xu et al. (2004). The difference in energy is not consistent but depends on the type of O_2 configuration. The adsorption energies of the present study are all more stable than those reported by Xu et al. (2004). Xu et al.

(2004) report two degenerate adsorption configurations to within 0.01 eV, i.e. b1 and b2_f$_{Pt}$_t$_{Co}$ with an adsorption energy of -0.92 eV, the same degenerate configurations are obtained in the present study and these configurations are 0.05 eV and 0.04 eV respectively more stable than those reported by Xu et al. (2004).

The adsorption energies of O_2 on site b2 and b3 in the present study are 0.10 eV and 0.11 eV more stable than those reported by Xu et al. (2004), the reported values by Xu et al. (2004) are b2 = -0.53 eV and b3 = -0.65 eV. The difference in adsorption energy for configurations based on the f$_{Pt}$ site is in the range 0.11 to 0.19 eV whilst the difference for the adsorption energies based on the h$_{Pt}$ site is 0.08 eV. The difference for the h$_{Co}$ based configuration is 0.15 eV. The same trend reported by Xu et al. (2004) of the f$_{Pt}$ based configurations being more stable than the h$_{Pt}$ based configuration is observed in the present study.

The difference in the adsorption energies of the present study and that of Xu et al. (2004) is probably primarily due to the use of different pseudopotentials; in the study by Xu et al. (2004) the calculations were performed using the ultrasoft pseudopotentials, whilst for the present study the projector augmented wave (PAW) method of the pseudopotentials is utilized. Other possible sources of the difference in the calculated adsorption energies is that in the study conducted by Xu et al. (2004), the Brillouin zone was sampled at 18 special Chadi-Cohen k-points, while for the present study the Monkhorst-Pack scheme for the Brillouin zone sampling at a k-point density grid of 12 $\times$ 12 $\times$ 1 corresponding to 74 irreducible k-points is used. Moreover, in the study by Xu et al.(2004) a plane wave basis cut-off of 25 Ry (340 eV) was used whilst for the present study the basis set cut-off energy is set to 400 eV, this could have also led to the difference in the calculated adsorption energies. Another feasible reason for the discrepancy is the omission of zero-point vibrational energy corrections in the study by Xu et al.(2004).

On comparing the amount of charge transferred to adsorbed O_2 on $Pt_3Co(111)$ to that transferred to O_2 adsorbed on Pt(111) reported by Qi et al. (2008), there is significantly a high amount of charge transfer to O_2 on $Pt_3Co(111)$ compared to that on Pt(111). On Pt(111) Qi et al. (2008) report the calculated charge on O_2 adsorbed on the bridge site as 0.07 e^-, and 0.09 e^- for O_2 adsorbed on the top - fcc - bridge configuration. In the present study the amount of charge transferred to O_2 on the bridge sites varies from 0.55 - 0.63 e^- whilst for the 3-fold-hollow site configurations the charge varies from 0.67 - 0.87 e^-. Nevertheless, the amount of charge transferred to adsorbed O_2 on $Pt_3Co(111)$ and on Pt(111) is not high enough such that the surface-adsorbed O_2 can be classified as a true integer anion (Qi et al. 2008).

3.3 Atomic oxygen (O)

Atomic oxygen adsorption is considered an important parameter as a descriptor of surface reactivity, hence as an activity descriptor for the oxygen reduction reaction (ORR) (Stamenković et al. 2006). Stamenković et al. (2006); Zhang et al. (2005) and Nørskov et al. (2004) have argued that atomic oxygen strength of adsorption is a crucial parameter in a surfaces activity to catalyze the ORR, as it is linked to the rate determining step, with too strong O adsorption energy proposed to lead to the rate being limited by O and OH removal, as the surface will be oxidized, while for the case of too weak atomic O adsorption energy, the rate is proposed to be limited more likely by electron and proton transfer to adsorbed molecular oxygen.

Zhang et al. (2005) proposed the use of O adsorption strength as an indicator of a surfaces reactivity, due to it being a simple species, and probably the species which interacts more strongly with the surface than any other ORR intermediate. Hence, O adsorption is believed to be most sensitive to surface property changes (Zhang et al. 2005). From theoretical studies it has been observed that the most stable adsorption site for atomic oxygen is the 3-fold-hollow fcc site on most transition metal (111) surfaces (Ford et al. 2010; Nørskov et al. 2004).

The study of O adsorption is also vital, since O adsorption can be used to provide insight into the mechanisms of the ORR which occur on a metal surface.

3.3.1 Search strategy for atomic O adsorption configurations on $Pt_3Co(111)$

The adsorption of atomic O was investigated on the 9 unique high symmetry sites, Figure 3.7 illustrates the 9 unique sites explored. For the 3-fold-hollow sites the atomic oxygen atom was placed in the center of the 3-fold-hollow site. For bridge site configurations atomic oxygen was placed equidistant between the two atoms constituting the bridge. A geometry optimisation calculation was performed for atomic O on the 9 unique sites with the atomic O and the top two layers of the slab allowed to relax.

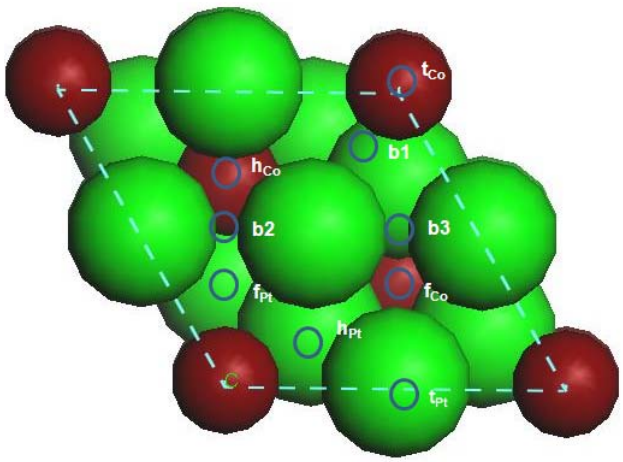

Figure 3.7: Schematic diagram of the adsorption configurations of atomic O explored on the $Pt_3Co(111)$ surface

3.3.2 Atomic oxygen (O) adsorption results and discussion

Table 3.3 presents a summary of results for the adsorption of atomic oxygen on $Pt_3Co(111)$.

Table 3.3: Calculated: adsorption sites, adsorption energy, and the O-metal distances for atomic O adsorption on $Pt_3Co(111)$ at 0.25 ML atomic O coverage. The adsorption energies are calculated relative to gas phase atomic O. The adsorption energies in parenthesis are calculated relative to $\frac{1}{2}$ $O_{2(g)}$

Adsorption site	**E_{ads}(eV)**	**d_{O-Pt} (Å)**	**d_{O-Co}(Å)**
f_{Pt}	-4.62 (-1.59)	2.07, 2.07	1.86
h_{Pt}	-4.38 (-1.35)	2.08, 2.08	1.86
f_{Co}	-3.88 (-0.85)	2.06, 2.06, 2.06	-
h_{Co}	-3.80 (-0.76)	2.08, 2.08, 2.08	-

Figure 3.8 is an illustration of the stable adsorption sites for atomic O on the surface.

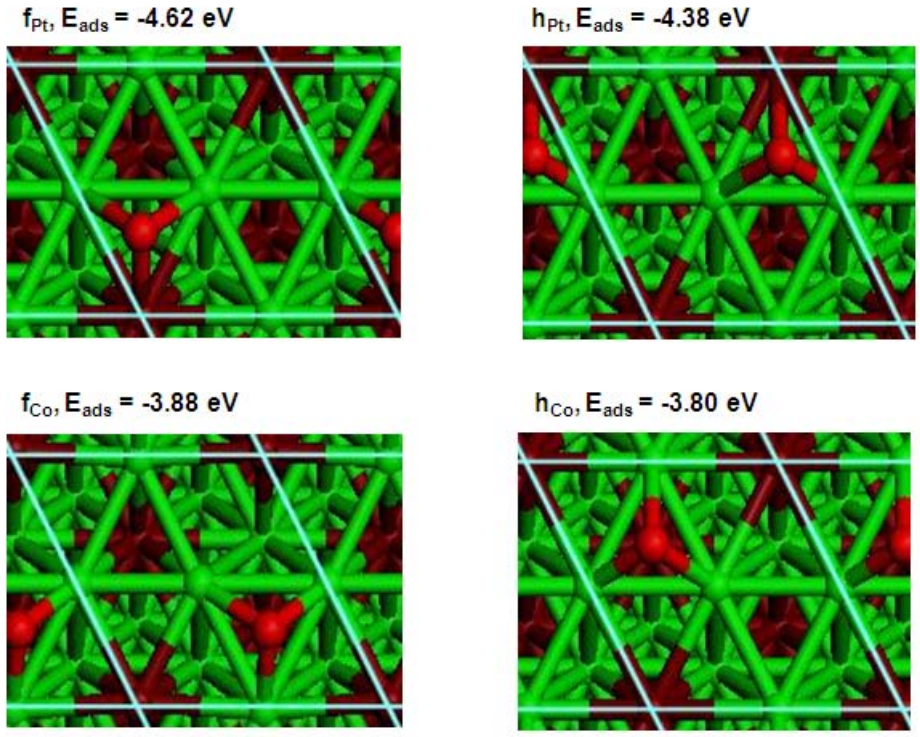

Figure 3.8: Calculated adsorption configurations of atomic O adsorption on $Pt_3Co(111)$

3.3.2.1 Atomic oxygen adsorption configurations on $Pt_3Co(111)$

Of the investigated adsorption sites for atomic oxygen, the adsorbate is stable on the 3-fold-hollow sites only. For the other investigated sites, i.e. atop a Pt atom, atop a Co atom and on the three bridge sites, no stable adsorption configurations were obtained. The calculated O-metal distances for the four stable 3-fold-hollow site configurations are almost identical as they range from 2.06 to 2.08 Å for the O-Pt distances and 1.86 Å for the O-Co distances.

3.3.2.2 Adsorption energy of atomic oxygen on $Pt_3Co(111)$

The surface Co atom directly coordinated to adsorbed atomic oxygen stabilises the adsorption energy of atomic oxygen more relative to the stabilisation from a subsurface Co atom.The adsorption energy of atomic oxygen on the f_{Pt} site is more stable than adsorption on the f_{Co} site by 0.74 eV. For the 3-fold-hollow hcp sites the h_{Pt} site is more stable than the h_{Co} site by 0.58

eV. The adsorption energy of atomic oxygen is more stable for the 3-fold-hollow sites above a subsurface Pt atom (f_{Pt} and h_{Pt}) compared to those above a subsurface Co atom (f_{Co} and h_{Co}).

On comparing the adsorption energy of atomic oxygen for the sites f_{Pt} and h_{Pt}, it can be seen from Table 3.3 that the f_{Pt} site is 0.24 eV more stable than the h_{Pt} site. These two 3-fold-hollow sites are identical in that the 3-fold-hollow site comprises two surface Pt atoms and a Co atom. The adsorption energy of atomic oxygen on the f_{Co} site is 0.08 eV more stable than on the h_{Co} site. The f_{Co} and the h_{Co} sites are similar in that the 3-fold-hollow site comprise three surface Pt atoms. From the calculated energy difference between the fcc and hcp sites, it is observed that there is a higher difference in energy between the fcc and the hcp sites for the 3-fold-hollow sites consisting of a surface Co atom. For the 3-fold-hollow sites not consisting of a surface Co atom but of a subsurface Co atom the difference in adsorption energy between the fcc and the hcp site is small.

3.3.2.3 Bader charge analysis

Table 3.4 is a summary of the calculated charge redistribution upon adsorption of atomic oxygen on $Pt_3Co(111)$ for the different unique adsorption configurations.

Table 3.4: Bader charge transfer to the atoms upon adsorption of atomic O on $Pt_3Co(111)$, calculated with the Bader method of charge partitioning

	Bader charge (e^-)				
Site	**O**	**Pt**$_{surf1}$	**Pt**$_{surf2}$	**Pt**$_{surf3}$	**Co**$_{surf}$
f_{Pt}	0.84	-0.33	-0.33	-0.04	-0.20
h_{Pt}	0.83	-0.30	-0.30	-0.04	-0.19
f_{Co}	0.77	-0.29	-0.28	-0.28	-0.03
h_{Co}	0.74	-0.28	-0.27	-0.29	-0.02

There is more charge transferred to atomic oxygen adsorbed on the 3-fold-hollow sites based on Pt, i.e. f_{Pt} and h_{Pt} than on those based on Co, viz. f_{Co} and h_{Co}. 0.84 e^- charge is transferred to the f_{Pt} configuration and 0.83 e^- charge is transferred to atomic oxygen adsorbed on the h_{Pt} site. The corresponding 3-fold-hollow sites based on Co have 0.77 e^- and 0.74 e^- charge transferred to the f_{Co} and the h_{Co} configurations respectively.

The charge transfer from the surface Pt atoms coordinated to the adsorbate is in the range 0.28 to 0.33 e^-. The highest charge transfer of 0.33 e^- corresponds to charge transferred from the surface Pt atoms for atomic oxygen adsorbed on the f_{Pt} site. The low charge transfer of 0.28 e^- corresponds to atomic oxygen adsorbed on the h_{co} site. The charge transferred from the surface Co atoms is lower than that transferred from surface Pt atoms. The charge transferred from surface Co atoms coordinated to the adsorbate is in the range 0.19 to 0.20 e^-. For configurations where the adsorbate is not coordinated to a surface Co atom, e.g. f_{Co} configuration, a small charge less than 0.10 e^- is transferred from the surface Co atoms. This charge is low such that it is considered to be of minimal influence.

3.3.2.4 Comparison with adsorption on Pt(111)

The lowest energy O adsorption site is over the fcc site on the Pt(111) surface from the results by Madala(2012). The calculated PW91 adsorption energy of the lowest energy O geometry on the Pt(111) surface is -4.17 eV. On the $Pt_3Co(111)$ surface the adsorption energy of the lowest energy O geometry is stabilized by 0.45 eV compared to the adsorption energy of the lowest energy O geometry on Pt(111) whilst O on f_{Co} and h_{Co} is less stable than on Pt(111) by approximately 0.30 eV and 0.40 eV, respectively. This suggests that subsurface Co destabilises O adsorption relative to Pt(111) where fcc and hcp sites also consist of Pt atoms in the surface layer.

3.3.2.5 Comparison with previous studies of atomic oxygen (O) adsorption on $Pt_3Co(111)$

No experimental literature on O adsorption on the $Pt_3Co(111)$ surface was obtained, hence the results of O adsorption on the $Pt_3Co(111)$ surface obtained in the present study will be compared to other DFT studies.

A comparison of the adsorption energy of atomic oxygen calculated in the present study and previous reported adsorption energies of atomic oxygen on the $Pt_3Co(111)$ surface is made to assess the consistency of the calculated adsorption energies of the present study. The reported adsorption energies of atomic oxygen in the present study are lower by 0.19 to 0.26 eV relative to those reported by Ma and Balbuena (2008). The h_{Pt} calculated atomic oxygen adsorption energy for the present study is 0.19 eV lower than that reported by Ma and Balbuena (2008) whilst the highest deviation at 0.26 eV is for the h_{Co} site configuration. The results of the present study follow the same trend as that reported by Ma and Balbuena (2008) where the order of atomic oxygen adsorption energies is $f_{Pt} > h_{Pt} > f_{Co} > h_{Co}$.

The possible primary sources of the difference in the calculated adsorption energies of atomic oxygen for the two studies are: In the study of Ma and Balbuena (2008) (VASP) tighter convergence parameters were used than in the present study. The ionic relaxation was set at a force convergence criterion of 10^{-4} eV/Å whilst for the present study it is set at 0.03 eV/Å, the electronic self consistent iteration parameter was set at energy changes below 10^{-5} eV while for the present study it is set at 10^{-4} eV. Other minor possible sources of the difference between the calculated atomic oxygen adsorption energies is that the reported values by Ma and Balbuena (2008) were for calculations performed with a plane wave basis set cut off energy of 350 eV whilst for the present study the basis set cut off energy is set at 400 eV. In the study of Ma and Balbuena (2008) a Monkhorst Pack scheme at a k-point mesh of ($8 \times 8 \times 1$) was used whilst in the present study a k-point mesh of ($12 \times 12 \times 1$) is utilized. The reported values by Ma and Balbuena (2008) were for calculations performed using the GGA - PBE functional whilst for the present study the GGA - PW91 functional is used. The different functionals are ideally not expected to lead to any difference in the calculated adsorption energies since they are identical by construction (Mattson et al. 2005) but it appears that there is a possibility that the two functionals result in different calculated adsorption energies.

Comparing the results of the present study for atomic oxygen adsorption with those reported by Xu et al. (2004), the calculated adsorption energies for the present study are also higher than those reported by Xu et al. (2004). For the adsorption energies of atomic oxygen on the f_{Co} and h_{Co} sites the difference is 0.08 eV and 0.06 eV whilst for the sites f_{Pt} and h_{Pt} the differences are 0.27 eV and 0.24 eV. The same order of atomic oxygen adsorption energies of $f_{Pt} > h_{Pt} > f_{Co} > h_{Co}$ reported by Xu et al. (2004) is also obtained in the present study.

The difference between the calculated adsorption energies of the present study and that of Xu et al. (2004) are probably due to the same causes as those cited for the difference in the calculated adsorption energies of O_2 between the present study and that of Xu et al. (2004).

3.4 OH adsorption

The strength of OH adsorption is equally important as the adsorption strength of atomic oxygen in determining a surface's activity for the oxygen reduction reaction (Nørskov et al. 2004). The adsorption strength of OH has also been identified as an important parameter in determining a surface's resistance to inhibition of the ORR, as experimental evidence has suggested that OH inhibits the ORR (Hyman and Medlin, 2007). OH is suggested to be a poison that blocks the surface sites from O_2 on Pt, and the presence of the alloying element in the alloy is proposed to lower OH coverage on Pt atoms, thereby leaving these sites free for O_2 adsorption and the ORR to occur (Zhang et al. 2005).

OH adsorption has also been linked to the rate determining step: in a DFT study of the ORR on $Pt_3Ni(111)$ and Pt(111), Rossmeisl et al. (2008) argued that an intermediate adsorption strength of OH corresponds to the highest catalytic activity for the ORR. Pt was proposed to be rate limited by a too strong OH adsorption strength, and Pt_3Ni a too weak OH adsorption strength, suggesting that an intermediate adsorption strength of OH is desirable. Hydrogenation reactions of OH have also been linked to the rate determining step, with the hydrogenation of OH to form H_2O having high reaction barriers (Zhang et al. 2005). Therefore, studying the adsorption behaviour of OH on a surface can provide insight into how the ORR proceeds and the most likely rate determining steps can be identified. Ford et al. (2010) performed DFT studies of OH adsorption on a series of transition metal (111) facets, and the most stable adsorption configuration for OH adsorption was found to be either a bridge-tilted configuration or a top-tilted geometry, with the preferred configuration on Pt being the bridge-tilted geometry.

3.4.1 Search strategy for stable OH adsorption configuration on $Pt_3Co(111)$

The investigated configurations for OH adsorption on $Pt_3Co(111)$ are illustrated in Figure 3.9. The configurations include vertical and parallel orientations. For the vertical configurations the H atom was directed out of the plane of the surface while for the parallel configurations the O and H atoms were in the same plane parallel to the surface. All the investigated configurations of OH were such that the O atom is directly coordinated to the surface. Configurations where the H atom is coordinated directly to the surface were not investigated. In a DFT study of OH adsorption on the Pt-skin on $Pt_3Co(111)$, OH was observed to coordinate via the O to the surface (Roques et al. 2005). Similarly, in a DFT study of OH adsorption on a series of transition metal (111) facets, OH was observed to adsorb or coordinate to the surface through O (Ford et al. 2010).

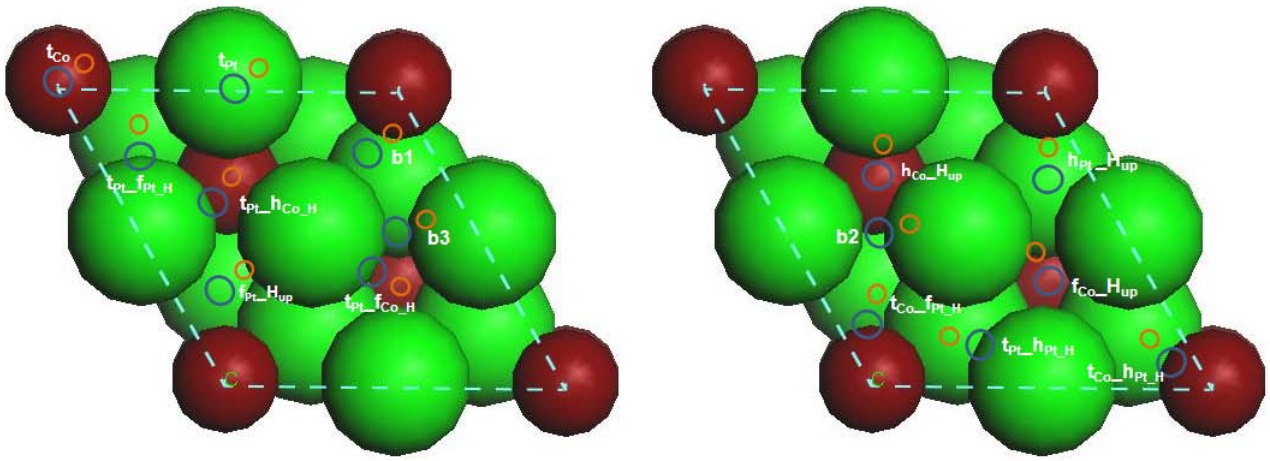

Figure 3.9: Schematic diagram of the adsorption configurations of OH on $Pt_3Co(111)$ investigated. The large blue circles represents O, the small orange denotes H.

Three bridge site configurations were investigated, i.e. b1, b2 and b3, and on each bridge site configuration the O atom was coordinated to the bridge site while the H atom was directed away from the surface. Two atop site configurations were investigated with the OH directly atop a Pt atom and atop a Co atom, respectively. For the 3-fold-hollow sites based on a Pt atom, viz. f_{Pt} and h_{Pt}, three possible configurations were explored. In the first set, identified as configurations f_{Pt}_H_{up} and h_{Pt}_H_{up} in Figure 3.9, the configurations are such that the O atom is above a 3-fold-hollow site with the H atom directed up into the vacuum. The second set of configurations, identified as t_{Pt}_f_{Pt-H} and t_{Pt}_h_{Pt-H} in Figure 3.9, are such that the O atom is atop a Pt atom with the H atom in the same plane as the O, parallel to the surface and directed over the 3 - fold -hollow site. The third set of configurations represented as t_{Co}_f_{Pt-H} and t_{Co}_h_{Pt-H} in Figure 3.9 were such that the O atom is atop a Co atom with the H atom in the same plane as the O, parallel to the surface and directed over the 3-fold-hollow site.

For the case of the 3-fold-hollow sites based on Co, viz. f_{Co} and h_{Co}, two sets of configurations were investigated. The first set of configurations represented as f_{Co}_H_{up} and h_{Co}_H_{up} in Figure 3.9 were such that the O atom is above the 3-fold-hollow site with the H atom directed up into the vacuum. The second set of configurations, i.e. t_{Pt}_f_{Co-H} and t_{Pt}_h_{Co-H} shown in Figure 3.9 were such that the O atom is atop a Pt atom with the H atom in the same plane as the O atom, parallel to the surface and directed over the 3-fold-hollow site.

Two atop configurations atop a Co atom and atop a Pt atom were investigated in which the O atom was atop the metal atom with the H atom directed vertically up into the vacuum.

3.4.2 OH adsorption results and discussion

Table 3.5 summarises the calculated adsorption properties of OH on Pt_3Co (111).

Table 3.5: Calculated: adsorption configurations, adsorption energy, the O-H bond distance, The O-metal distances and the tilt angle of OH adsorbed on Pt_3Co(111). The reported results are for a 0.25 ML coverage of OH. The adsorption energy is relative to gas phase OH.

Adsorption Configuration	**E_{ads}(eV)**	**d_{O-H} (Å)**	**d_{O-Co} (Å)**	**d_{O-Pt} (Å)**	**tilt θ (^{0})**
b1	-2.58	0.98	1.96	2.24	47
t_{Co-a}	-2.56	0.98	1.80	-	48
t_{Co-b}	-2.55	0.98	1.80	-	59
f_{Pt}	-2.49	0.97	1.98	2.26	87
b2-a	-2.37	0.98	-	2.19	48
b3-a	-2.31	0.98	-	2.21	22
b2-b	-2.30	0.98	-	2.18	22
t_{Pt-b}	-2.22	0.98	-	2.02	19
t_{Pt-a}	-2.20	0.98	-	2.08	21
b3-b	-2.09	0.98	-	2.19	48

Figure 3.10 indicates the unique adsorption configurations of OH on Pt_3Co(111).

3.4.2.1 OH adsorption configurations on Pt_3Co(111)

Of the investigated starting configurations of OH on the Pt_3Co(111) surface, the final adsorbed configuration is either a bridge or an atop OH configuration. The only exception to this is the starting configuration f_{Pt}, where the final optimized configuration is a OH molecule with the oxygen atom over the 3-fold-hollow fcc site and the atomic H sticking vertically up into the vacuum.

There is a variation in the stability of the bridge-bonded configurations depending on which site the atomic H is directed over. An illustration of this effect can be seen in Figure 3.10 for configurations b3-a and b3-b. The site over which the atomic H of the OH is directed does not

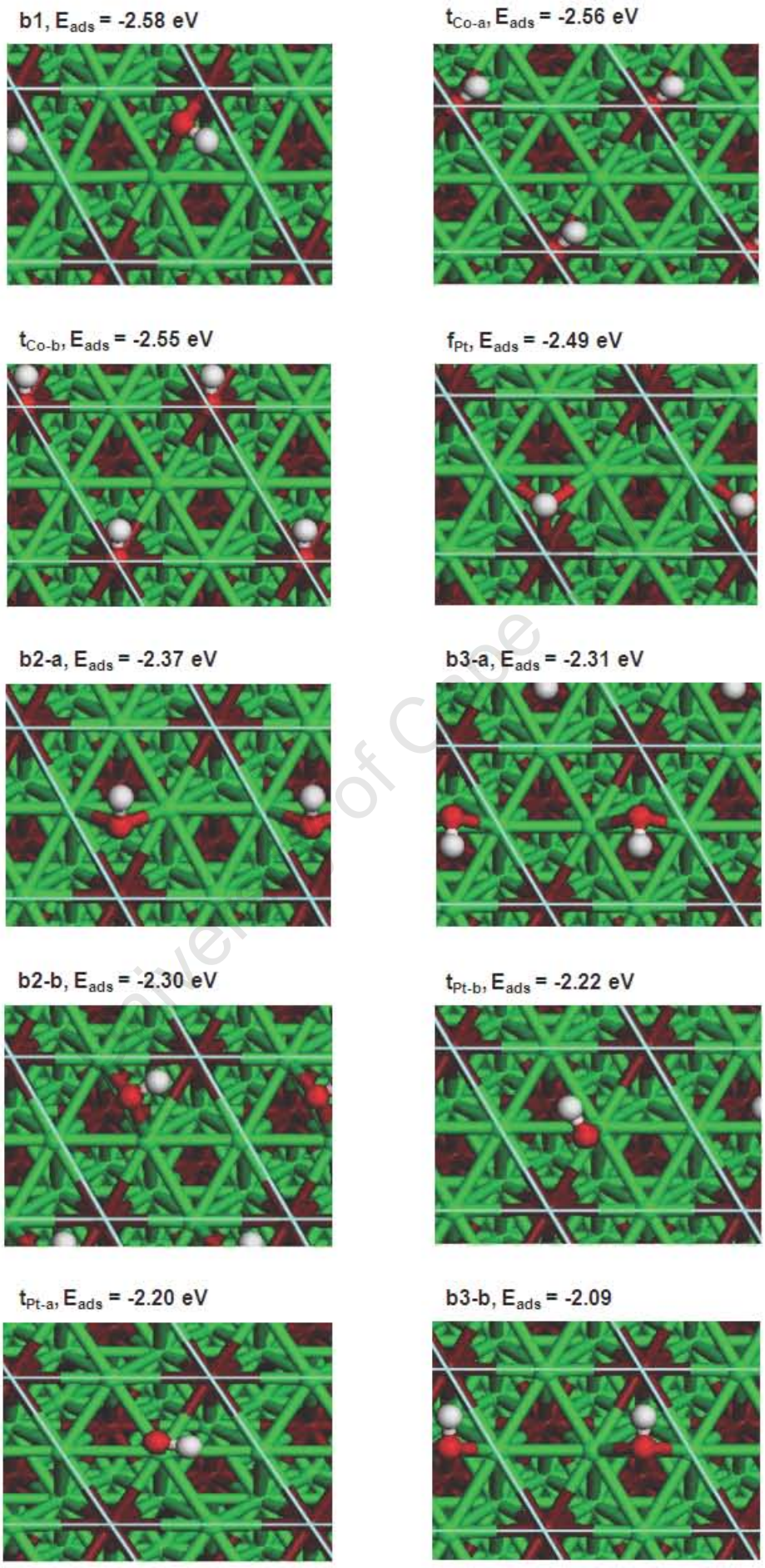

Figure 3.10: Calculated adsorption configurations of OH on $Pt_3Co(111)$

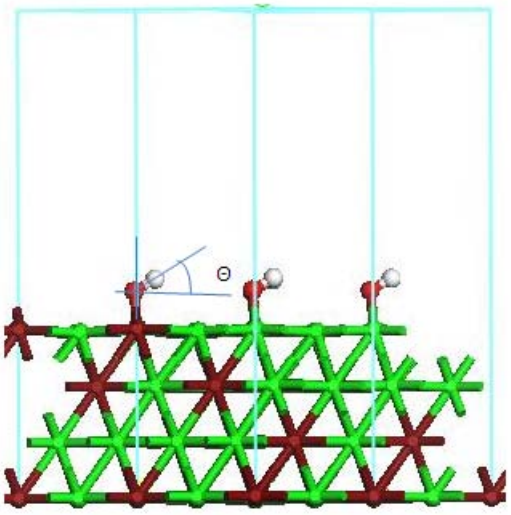

Figure 3.11: Illustration of the tilt angle for OH adsorption on $Pt_3Co(111)$

affect the the O-M (oxygen-metal) distance; the O-M distances for b2-a and b2-b are 2.19 Å and 2.18 Å, respectively. The same type of pattern is observed for bridge site configurations b3-a and b3-b with O - M distances of 2.21 Å and 2.19 Å. However, the tilt angle of the OH molecule from a plane parallel to the surface depends over which site the atomic H of OH is directed; for atomic H directed over the hcp 3-fold-hollow site the tilt angle is 48 ^{o} such as for configurations b2-a and b3-b and for atomic H over the fcc 3-fold-hollow site the tilt angle is 22 ^{o} such as for configurations b2-b and b3-a.

For atop configurations, two variations of the top configurations are obtained. The two atop Pt configurations are t_{Pt-a} and t_{Pt-b}, likewise the two atop Co configurations are t_{Co-a} and $t_{Co-b.}$

For all the unique adsorption configurations of OH on $Pt_3Co(111)$, the O-H bond length is identical at 0.98 Å. The O-H bond length on the surface is comparable to the calculated O-H bond length of 0.99 Å for gas-phase OH.

3.4.2.2 OH adsorption energy on $Pt_3Co(111)$

The strongest adsorption energies for OH adsorption are calculated for the configurations where there is direct coordination of the adsorbate through O to the surface Co atom. Such configurations are b1, f_{Pt}, t_{Co}-a and t_{Co}-b and the difference in adsorption energy between these three configurations excluding f_{Pt} is below 0.03 eV, which for calculation purposes can be considered to be energetically degenerate.

For bridge site configurations based on bridge site b2, i.e. b2-a and b2-b, the adsorption energy is dependent on which site atomic H is directed over. There is a 0.07 eV difference in adsorption energy between configuration b2-a and b2-b. For configuration b2-a, atomic H is directed over the h_{Co} site whereas for configuration b2-b atomic H is directed over the f_{Pt} site. Therefore, for bridge site b2 adsorption for OH, the subsurface Co atom on the h_{Co} position appears to stabilize OH adsorption more strongly compared to the subsurface Pt atom on the f_{Pt} position. For bridge site configurations based on bridge site b3, i.e. b3-a and b3-b the difference in adsorption energy of 0.22 eV between the two configurations is greater than that for the b2 configurations. For configuration b3-a, atomic H is directed over the f_{Co} site and for configuration b3-b atomic H is directed over the h_{Pt} site. Thus, based on the results of the present study it can be tentatively concluded that for OH adsorption on bridge site b3 the subsurface Co atom on the f_{Co} position has a stronger stabilizing effect on the adsorption energy of OH relative to the subsurface Pt atom in the h_{Pt} position.

The adsorption energy of OH atop a Pt atom is almost independent of the orientation of atomic H of OH. In configuration t_{Pt}-a atomic H is directed along bridge site b3, whilst for configuration

t_{Pt}-b, atomic H is directed along bridge site b2. Despite the difference in the orientations of the two configurations the difference in adsorption energy is only 0.02 eV. This energy difference is low hence the adsorption geometries can be considered as energetically degenerate.

3.4.2.3 Bader charge analysis

Table 3.6 summarises the calculated charge transferred to and from the different atoms upon adsorption of OH on $Pt_3Co(111)$.

Table 3.6: Bader charge transfer to the atoms upon adsorption of OH on $Pt_3Co(111)$ calculated using the Bader charge partition method

Adsorption	**Bader charge (e^-)**				
Configuration	**OH**	**Pt**$_{surf1}$	**Pt**$_{surf2}$	**Pt**$_{surf3}$	**Co**$_{surf}$
b1	0.53	-0.23	-0.07	-0.11	-0.15
t_{Co-a}	0.38	-0.10	-0.04	-0.08	-0.25
t_{Co-b}	0.43	-0.04	-0.03	-0.06	-0.26
f_{Pt}	0.52	-0.20	-0.20	0.00	-0.19
b2-a	0.46	-029	-0.20	-0.04	-0.04
b3-a	0.41	-0.22	-0.21	0.02	-0.05
b2-b	0.42	-0.24	-0.24	-0.02	0.00
t_{Pt-b}	0.40	-0.35	-0.05	0.00	-0.05
t_{Pt-a}	0.41	-0.36	-0.03	-0.04	-0.04
b3-b	0.46	-0.28	-0.21	-0.03	-0.02

Comparing the charge transferred from the surface atoms to the adsorbate for the atop configurations, it is evident that there is more charge transfer from the Pt atoms directly interacting with the adsorbate than when a surface Co atom is interacting with the adsorbate. For configurations t_{Pt}-a and t_{Pt}-b in which the adsorbate interacts with a surface Pt atom, the charge transferred from the Pt atoms is 0.36 e^- and 0.35 e^- for the two configurations, respectively, whereas for configurations t_{Co}-a and t_{Co}-b the charge transferred from the surface Co atom is 0.25 e^- and 0.26 e^- respectively. Despite higher charge donation from the surface Pt atoms compared to surface Co atoms for the atop configurations, the ontop configurations atop Co atoms have higher or more stable adsorption energies than those atop Pt atoms. Thus a higher adsorption energy does not correlate linearly with the amount of charge donated to the adsorbate.

The charge donated from the surface Co atoms for configurations where the adsorbate is not coordinated to a surface Co atom is small, less than 0.05 e^-.

The charge difference on OH, i.e. charge on OH, between the two b2 OH configurations b2-a and b2-b, is less than 0.10 e^-. The difference is low hence the charge transferred to the two configurations is considered to be the same to within the accuracy of the Bader partitioning method used. For the b3 OH configurations, the difference between b3-a and b3-b is 0.05 e^- which is also low rendering the two configurations to be of the same charge transfer, to within the accuracy of the Bader partitioning method used. For the t_{Co} based configurations, the configuration with atomic H directed over the f_{Pt} site (t_{Co}-b) has 0.05 e^- more charge transferred to the OH than for configuration t_{Co}-a. Similarly the charge difference is low hence the two configurations are considered to be the same, to within the accuracy of the Bader partitioning method used, in regard to the charge transferred to the adsorbed OH.

Configurations b1 and f_{Pt} have the highest charge transferred to the adsorbed OH with 0.53 e^- and 0.52 e^- respectively. For configuration b1 the adsorbate is coordinated to one Pt and one surface Co atom, whereas for the f_{Pt} configuration the adsorbate is coordinated to two surface Pt atoms and a Co atom. The coordination for these two configurations explain why there is higher charge transferred to the adsorbate. For the other configurations the adsorbate is either coordinated to a single Pt or Co atom or to two Pt atoms such as for b2 and b3 configurations.

3.4.2.4 Comparison with OH adsorption on Pt(111)

The lowest energy configuration of OH, i.e. the most stable OH configuration on the Pt(111) surface from the results by Madala(2012) is a bridge site. The adsorption strength of the lowest OH configuration on the Pt(111) surface is -2.21 eV. The O-H bond is 0.98 Å. The O-H bond obtained on the Pt(111) surface is the same as that obtained on the $Pt_3Co(111)$ surface. The lowest energy adsorption of OH on the $Pt_3Co(111)$ surface has an adsorption energy of -2.58 eV, hence on the $Pt_3Co(111)$ surface OH is 0.37 eV more stable relative to adsorption on the Pt(111) surface. On Pt bridge sites on $Pt_3Co(111)$ OH is more stable than on Pt(111). It is only atop Pt atoms on $Pt_3Co(111)$ where the stability of OH is similar to that on Pt(111).

3.4.2.5 Comparison with previous studies for OH adsorption on $Pt_3Co(111)$

No experimental literature on OH adsorption on the $Pt_3Co(111)$ surface is available, thus comparisons are only made to theoretical studies.

A comparison of the calculated adsorption properties of OH in the present study with reported adsorption properties of OH on $Pt_3Co(111)$ is done to assess the consistency of the adsorption energy of OH in the present study. The calculated OH adsorption energies in the present study are less stable than the DFT values reported by Tian and Anderson (2008). Tian and Anderson (2008) report the two stable adsorption configurations of OH being atop a Co atom and atop a Pt atom on $Pt_3Co(111)$. The calculated adsorption energy for OH atop a Co atom for the present study is 0.22 eV less stable than that reported by Tian and Anderson (2008). The calculated adsorption energy of OH atop a Pt atom in the present study is 0.16 eV less stable than that reported by Tian and Anderson (2008). The calculated O-Pt distances are similar; for the present study the O-Pt distance is 2.02 Å, whilst that reported by Tian and Anderson (2008) is 2.03 Å. Both studies report the same O-H distance of 0.98 Å. For OH adsorbed atop a Co atom a O-Co distance of 1.80 Å is calculated in the present study, whilst Tian and Anderson (2008) report a O-Co distance of 1.82 Å.

The difference in the calculated OH adsorption energy between the present study and those reported by Tian and Anderson (2008) might be primarily due to a different ionic relaxation criterion for the force convergence. For the present study an ionic relaxation criterion of 0.03 eV/Å for the forces is used, while in the study by Tian and Anderson (2008) an ionic relaxation criterion of 0.01 eV/Å was used. Another possible source of the difference in the adsorption energies is the use of a different Monkhorst-Pack scheme for the k-points, in the study of Tian and Anderson (2008) a k-point mesh of ($5 \times 5 \times 1$) was used whilst for the present study the k-point mesh is set at ($12 \times 12 \times 1$). In both studies the plane wave basis set cut-off energy is set to 400 eV, the projector augmented wave (PAW) pseudopotentials are utilized and the OH adsorption is studied at a coverage of 0.25 ML. The exchange-correlation energy is described by the GGA-PW91 functional in both studies and the VASP code is used. There is no mention of zero-point energy (ZPE) corrections for the study by Tian and Anderson (2008) hence the possible ommission of the ZPE corrections might be one of the sources of the discrepancies.

3.5 OOH adsorption

Besides the direct dissociation of O_2, the other ORR mechanism is proposed to be the hydrogen assisted O_2 dissociation on the Pt(111) surface. In the hydrogen-assisted O_2 dissociation the hydrogen activates O_2 to form OOH, the OOH can then dissociate to form O_{ads} and OH_{ads} or further be hydrogenated to form HOOH (Sha et al. 2011). The hydrogen-assisted O_2 dissociation has been calculated to proceed with a lower activation barrier than direct dissociation of O_2, hence it was concluded to be the dominant pathway on Pt(111) by Sha et al. (2011). Ford et al. (2010) performed DFT studies of the adsorption of OOH on different (111) facets of transition and noble metal surfaces, and found the most stable configuration of OOH as the configuration where OOH is bonded to a single metal atom on Pd and Pt, or two metal atoms on Cu, Ag and Au. For Pd and Pt, OOH was observed to bond through its non-hydrogenated O, with the OH end slightly tilted away from the surface.

Hyman and Medlin (2007) also performed DFT studies of OOH adsorption on a Pt(111) surface, and found the most stable adsorption configuration to be on a bridge site. The adsorption behaviour and decomposition of the radical OOH are important to study, since OOH plays an essential role in determining pathways of the ORR (Balbuena et al. 2006). The activation barrier for OOH formation compared to the barrier for O_2 dissociation are suggested to dictate whether the ORR proceeds via the direct O_2 dissociation route or by hydrogen-assisted O_2 dissociation. Moreover, the activation barrier for OOH dissociation relative to the barrier for the further hydrogenation of OOH to form HOOH can also affect the ORR pathway followed.

3.5.1 Search strategy for OOH adsorption configurations on $Pt_3Co(111)$

In order to determine the adsorption configurations of OOH on $Pt_3Co(111)$, only the configurations which are parallel to the surface were investigated, as these type of stable configurations have been reported in calculations of OOH adsorption on Pt(111) (Ford et al. 2010). Parallel configurations are configurations where the O-O bond of the OOH is parallel to the surface, whilst for vertical configurations the O-O bond is perpendicular to the surface. Vertical configurations are not considered in the present study. Figure 3.12 is an illustration of the different possible starting configurations of OOH investigated on $Pt_3Co(111)$.

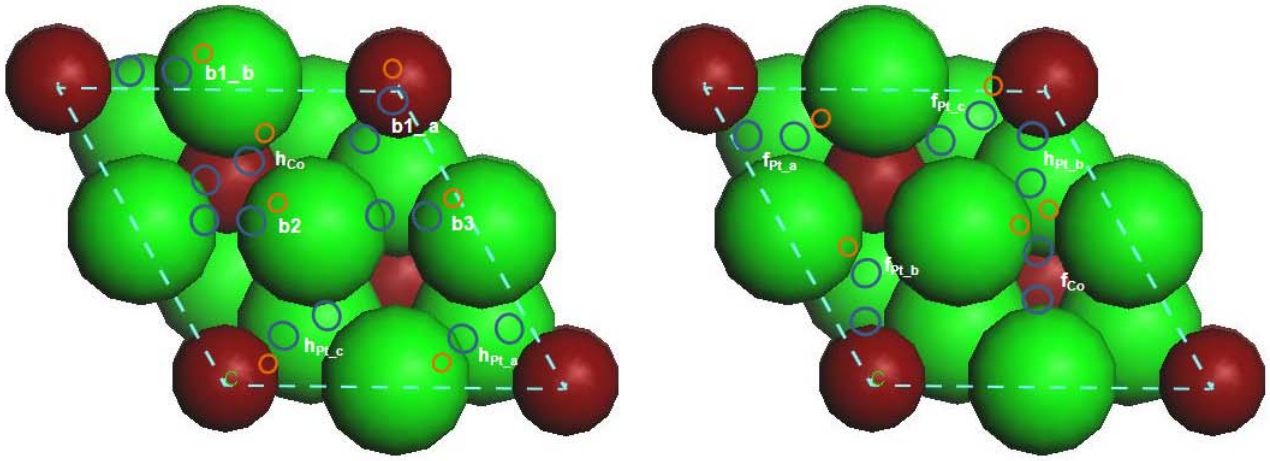

Figure 3.12: Schematic diagram for the different possible adsorption configurations of OOH on $Pt_3Co(111)$

Two possible configurations were investigated for bridge site b1, viz. b1-a and b1-b illustrated in Figure 3.12 , for b1-a the OH-end of the OOH molecule is atop a Co atom whereas configuration b1-b is such that the OH-end of the OOH molecule is atop a Pt atom.

For the 3-fold-hollow sites based on Pt, i.e. f_{Pt} and h_{Pt} three sets of possible configurations were investigated. For the first set, indicated as f_{Pt-a} and h_{Pt-a}, the OH-end of the molecule

is atop a Pt atom while the unhydrogenated O atom is on bridge site b1 with the O-O bond axis over the 3-fold-hollow site. The second set of configurations represented as f_{Pt-b} and h_{Pt-b} in Figure 3.12 were such that the unhydrogenated O atom is atop a Co atom while the OH-end is on bridge site b2 and b3 for f_{Pt-b} and h_{Pt-b} respectively, and the O-O bond axis across the 3-fold-hollow site. The third set of configurations, represented by configurations f_{Pt-c} and h_{Pt-c} in Figure 3.12, were such that the unhydrogenated O atom is on bridge site b2 and b3 for configurations f_{Pt-c} and h_{Pt-c}, respectively, while the OH-end is atop a Co atom and the O-O bond axis across the 3-fold-hollow site.

For the 3-fold-hollow sites based on Co, viz. f_{Co} and h_{Co} only one set of configurations was investigated. For both f_{Co} and h_{Co}, the configuration was such that the unhydrogenated O atom is atop a Pt atom while the OH-end is on bridge site b2 and b3 for the f_{Co} and h_{Co} configurations respectively. The O-O bond axis sits across the 3-fold-hollow site.

Bridge site configurations based on b2 and b3 were investigated with the configurations where the unhydrogenated O atom was atop a Pt atom while the OH-end is also atop a Pt atom with the O-O bond axis parallel to the bridge site.

3.5.2 OOH adsorption results and discussion

In Table 3.7 a summary of the adsorption properties of OOH upon adsorption on $Pt_3Co(111)$ is presented.

Table 3.7: Calculated: adsorption configurations, adsorption energy, O-O bond distances, O-H bond distance, O-O stretching frequency, OOH angle and the O-metal distances for OOH adsorption on $Pt_3Co(111)$. Calculations are for 0.25 ML coverage of OOH. The adsorption energy is relative to gas phase OOH.

Adsorption site	**E_{ads}(eV)**	**d_{O-O}(Å)**	**d_{O-H} (Å)**	**ν_{O-O} (cm^{-1})**	**$\angle$OOH (^{o})**	**d_{O-M}(Å)**
b1	-1.37	1.51	0.99	636	101	2.07 (Co)
						2.05 (Pt)
b2	-1.20	1.49	0.99	698	101	2.05 (Pt)
b3	-1.10	1.47	0.99	758	101	2.05 (Pt)

Figure 3.13 illustrates the unique stable adsorption configurations of O_2H on the $Pt_3Co(111)$ surface.

3.5.2.1 OOH adsorption configurations on $Pt_3Co(111)$

Of the investigated starting configurations of OOH adsorption on $Pt_3Co(111)$, only the bridge site configurations resulted in stable adsorption configurations for OOH. The 3-fold-hollow sites based on Pt, f_{Pt} and h_{Pt}, were not calculated stable adsorption sites for OOH since the OOH molecule dissociated into atomic oxygen and OH while adsorbed on these sites. The dissociation of OOH upon adsorption on these sites was investigated by varying the starting distance of the OOH from the surface. Upon performing a geometry optimisation calculation for the different starting distances the final optimized geometry was the dissociated product of atomic oxygen and OH. The starting configurations of OOH on the 3-fold-hollow sites based on Co, f_{Co} and h_{Co} did not dissociate but optimised to bridge site configurations.

The b1 configuration has the most stretched O-O bond length at 1.51 Å compared to the O-O bond length of 1.49 Å for the b2 configuration and 1.47 Å for configuration b3. In the b1 configuration the adsorbate is directly coordinated to a surface Co atom via the hydrogenated oxygen end of the molecule. A similar type of configuration to the b1 site was also investigated where the hydrogenated oxygen end of the molecule was atop a Pt atom, upon geometry optimization the final configuration was a dissociated OOH molecule. This indicates that the stability of OOH on bridge site b1 is dependent on which atom, i.e. a Pt or Co atom, the hydrogenated

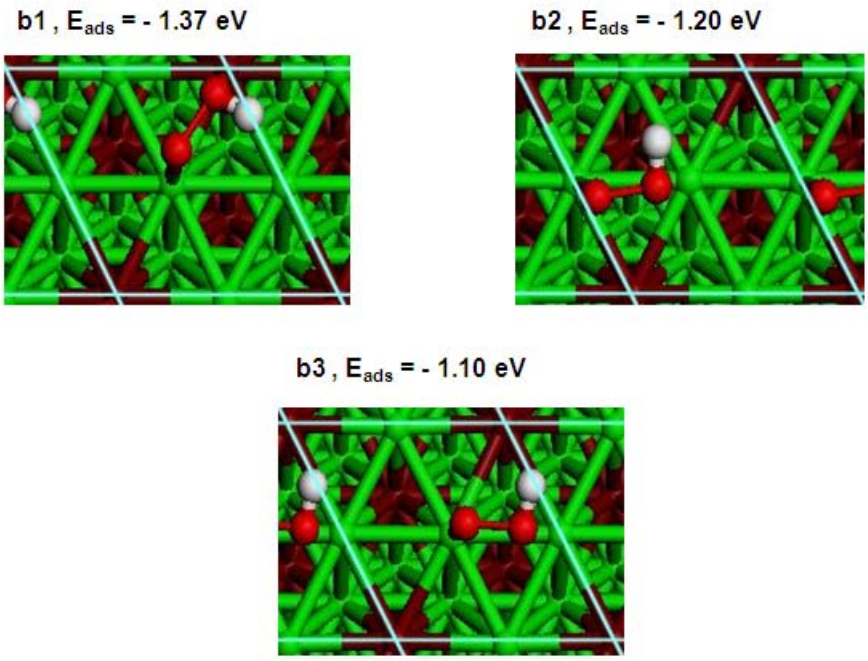

Figure 3.13: Calculated adsorption configurations of OOH on $Pt_3Co(111)$

oxygen-end of the molecule is interacting with. The calculated difference of 0.02 Å for the O-O bond lengths for configurations b2 and b3, despite the two bridge sites comprising Pt atoms only, can be ascribed to the different orientations of the adsorbate on the two bridge sites. For configuration b2, the orientation of the adsorbate is such that the atomic H of the OOH molecule is directed above bridge site b2 while configuration b3 is such that atomic H is directed above bridge site b1. For both configurations b2 and b3 the O-O bond axis of the OOH is not aligned perfectly parallel to the bridge site but the O-O bond axis is slightly in a tilted orientation on the bridge site.

The same O-H bond distance of 0.99 Å was calculated for the three different bridge site configurations of OOH. The same OOH angle of 101 ^{o} was calculated for all the three unique bridge site configurations. The O - M distances for configurations b2 and b3 are identical at 2.05 Å whilst b1 configuration has a O-Co distance of 2.07 Å and a O-Pt distance of 2.05 Å. Therefore, for the b1 configuration the OOH molecule is not aligned perfectly parallel to the surface, but the hydrogenated oxygen end of the molecule is slightly lifted off from the surface compared to the unhydrogenated oxygen end.

3.5.2.2 OOH adsorption energy on $Pt_3Co(111)$

The OOH adsorption energy is more stable for the b1 configuration than for the b2 and b3 configurations. The b1 configuration is 0.17 eV more stable than the b2 configuration and 0.27 eV more stable than configuration b3. The difference in adsorption energy between b1 and the other bridge site configurations is indicative of the interaction with the surface Co atom stabilizing OOH. This leads to a highly stable adsorption energy of OOH on b1 relative to adsorption on b2 and b3.

3.5.2.3 O-O stretching frequency of OOH on $Pt_3Co(111)$

Comparing the calculated O-O stretching frequency of OOH for the three configurations, the O-O stretching frequency is lowered most for configuration b1, with a calculated stretching mode

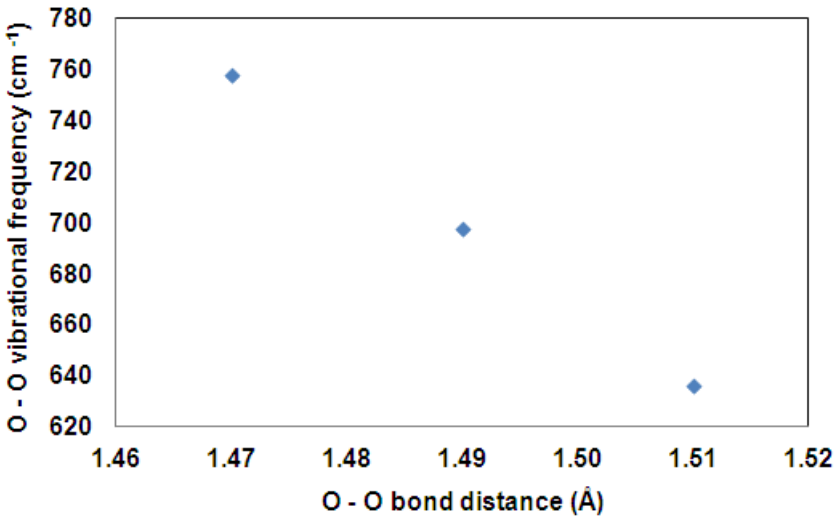

Figure 3.14: Plot of O-O stretching frequency as a function of the O-O bond length for OOH adsorption on $Pt_3Co(111)$

of 636 cm^{-1}. The O-O stretching frequency is highest for configuration b3 at 758 cm^{-1}. Comparing the O-O bond lengths and the O-O stretching frequency for the three configurations, it is observed that the lower the O-O stretching frequency, the longer the O-O bond length. Therefore the O-O bond length is weakened most for configuration b1, and the bond weakening manifests itself as a stretching of the O-O bond length and lowering of the O-O stretching frequency. From Figure 3.14 which shows the relation between the O-O stretching frequency and the O-O bond length, it is observed that there is a linear correlation between the O-O stretching frequency and the O-O bond length.

3.5.2.4 Bader charge analysis

Table 3.8 summarises the calculated charge transfer to and from the atoms upon adsorption of OOH on the $Pt_3Co(111)$ surface.

Table 3.8: Calculated Bader charge transfer to the atoms upon adsorption of OOH on $Pt_3Co(111)$ calculated with the Bader method of charge partitioning

	Bader charge (e^-)					
Adsorption site	**O1**	**OH**	**Pt_{surf1}**	**Pt_{surf2}**	**Pt_{surf3}**	**Co_{surf}**
b1	0.27	0.22	-0.32	0.00	0.00	-0.09
b2	0.26	0.15	-0.31	-0.17	0.00	-0.04
b3	0.25	0.14	-0.33	-0.11	0.00	-0.04

Table 3.8 is arranged such that O1 represents the charge difference on the unhydrogenated oxygen atom of the OOH molecule, and OH represents the charge difference on the hydrogenated oxygen end of OOH. Pt_{surf1} represents the Pt atom coordinated to the unhydrogenated oxygen end of OOH while Pt_{surf2} represents the Pt atom coordinated to the hydrogenated oxygen end of OOH. For all three unique configurations there is higher charge transfer to the unhydrogenated oxygen relative to the hydrogenated oxygen atom. For the bridge site configurations based on Pt atoms only, i.e. b2 and b3 the difference in charge between the two oxygen atoms of OOH is 0.11 e^- while for configuration b1 the difference is 0.05 e^-.

From Table 3.8 it is also observed that for all the three unique configurations, higher charge, in the range of 0.31 to 0.33 e^- is transferred from the Pt atom above which is the unhydrogenated oxygen of OOH molecule. For the Pt atoms directly coordinated to the hydrogenated oxygen atom, lower charge in the range 0.11 to 0.17 e^- is transferred from these surface atoms. The Pt surface atom not directly coordinated to the adsorbate has no net charge transferred from or to it.

The total charge transferred to the adsorbate is obtained by summing the charge on the two oxygen atom and the OH. The highest charge of 0.49 e^- is transferred to the adsorbate for the b1 configuration. The least charge is transferred to configurations b3, with 0.39 e^- charge transferred to the adsorbate. The charge transferred to OOH for configuration b3 is 0.10 e^- less than that transferred to configuration b1.

The charge transferred from the surface Co atoms is low, with the charge transfer being 0.09 e^- for configuration b1. Configuration b1 is such that the adsorbate is directly coordinated to a surface Co atom. For the b2 and b3 configurations, the charge transferred from the surface Co atoms is 0.04 e^-, this value is too low for the charge transfer from the Co atoms to be of meaningful contribution.

3.5.2.5 Comparison to adsorption of OOH on the Pt(111) surface

The lowest energy adsorption configuration of OOH obtained on the Pt(111) surface is the bridge configuration from the results by Madala(2012), with an adsorption energy of -1.12 eV calculated with the PW91 functional. The O-O bond of OOH on the Pt(111) surface is 1.46 Å and the O-H distance is 0.99 Å. The O-H distance is the same on the Pt(111) surface and the Pt_3Co(111) surface, whilst on the Pt_3Co(111) surface the O-O bond is longer than on the Pt(111) surface. On the Pt_3Co(111) surface, OOH adsorption is 0.25 eV more stable than on the Pt(111) surface. b2 consisting of only Pt atoms on Pt_3Co(111) is also more stable than the lowest energy structure on Pt(111) by 0.08 eV.

3.5.2.6 Comparison with previous studies for OOH adsorption

No experimental literature on the adsorption of OOH on the Pt_3Co(111) surface is available, hence comparison is made only to theoretical studies.

The adsorption configurations of OOH on Pt_3Co(111) in the present study are compared to the reported adsorption configurations on Pt(111) and other 5d transition metal surfaces.. Ford et al. (2010) reports OOH dissociation into O and OH on Rh, Ir and Ni (111) facets. In the present study, OOH dissociated into OH and O while adsorbed on the f_{Pt}, h_{Pt}, f_{Co} h_{Co} sites and the b1 site if O is directed to Co and the other OH end is atop Pt. The adsorption configurations of OOH on the bridge sites on Pt_3Co(111) reported for the present study are similar to the adsorption configurations reported by Ford et al. (2010) on Pt(111).

3.6 HOOH adsorption

Despite the lack of consensus with regard to the mechanism of the ORR, the four electron O_2 reduction reaction must involve both the breaking of the O-O bond, whether it be in O_2, OOH or HOOH, and O-H bond formation (Zhang et al. 2005). Therefore, the study of the behaviour and decomposition of HOOH is vital since HOOH has as essential role to play in determining pathways of the ORR (Balbuena et al. 2006). If the dissociation of HOOH proceeds with high activation barriers and is disfavored, then the final product of the ORR will be HOOH, not the desired product H_2O. HOOH production in Proton Exchange Membrane Fuel Cells (PEMFC) also has detrimental effects on the performance of the cell; HOOH has the potential for generating radicals that degrade the polymer (Balbuena et al. 2006). The proposed membrane degradation mechanisms are based on the decomposition of HOOH into $\cdot$OH or $\cdot$OOH radicals which attack any H-containing terminal bonds present in the polymer; the presence of foreign elements aggravates the production of HOOH (Balbuena et al. 2006). The dissociation of HOOH on the electrocatalyst is proposed to produce strongly adsorbed OH radicals which have been postulated to occupy sites that would otherwise be available for further increase in the O_2 reduction current (Balbuena et al. 2006). It has been proposed by Ford et al. (2010) that alloying platinum with cobalt, chromium or nickel should be useful in readily dissociating OOH hence avoiding the initial formation of HOOH.

Ford et al. (2010) performed DFT studies of HOOH adsorption on metal (111) surfaces and observed the trans configuration of the adsorbate to be the preferred configuration on the surface, with one oxygen atom atop a metal atom and one hydrogen atom pointing towards the surface.

3.6.1 Search strategy for HOOH adsorption configuration on $Pt_3Co(111)$

Figure 3.15 is an illustration of the different investigated configurations for HOOH adsorption on the $Pt_3Co(111)$ surface. The adsorption of HOOH was investigated on the 9 unique high symmetry sites identified on $Pt_3Co(111)$. To determine the adsorption configurations of HOOH on the surface, vertical and parallel configurations were investigated. Vertical configurations are configurations where the O-O bond axis of HOOH is perpendicular to the surface, this configuration was investigated for the atop site configurations. The parallel configuration is the configuration where the O-O bond axis of HOOH is parallel to the surface.

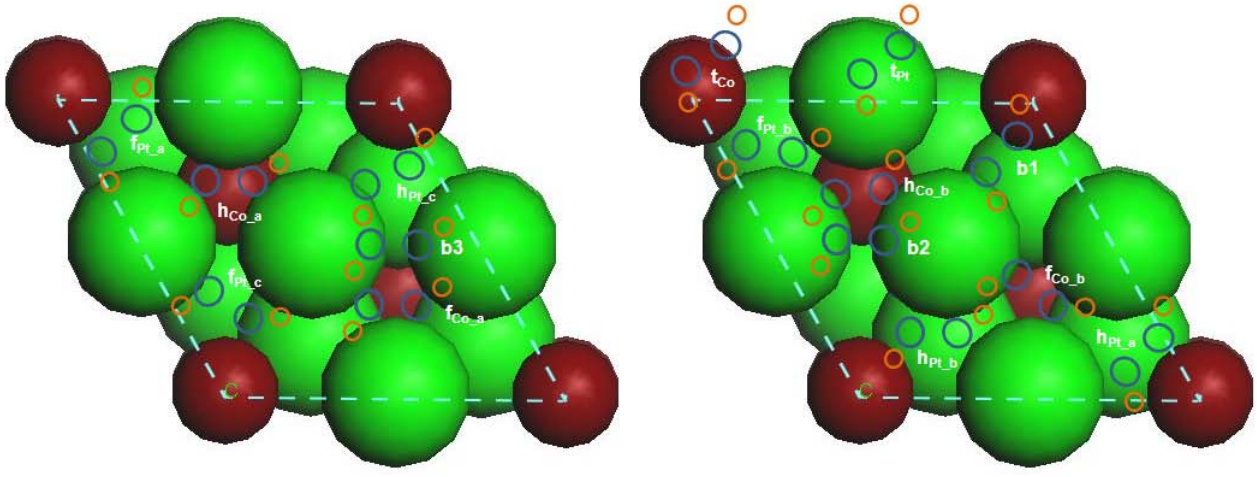

Figure 3.15: Schematic diagram of the adsorption configurations of HOOH investigated on $Pt_3Co(111)$

Two atop configurations were investigated, one atop a Co atom and the other atop a Pt atom. In both configurations one OH end is atop the metal atom while the other OH end is directed away from the surface. Three bridge site configurations, i.e. b1, b2 and b3 were investigated and in

all configurations the OH ends of HOOH were atop metal atoms while the O-O bond axis was aligned parallel to the bridge sites.

For 3-fold-hollow sites based on Pt, f_{Pt} and h_{Pt} sites, three possible configurations were investigated. In the first set of configurations represented as f_{Pt-a} and h_{Pt-a} in Figure 3.15 the configurations were such that the OH ends of HOOH were on the bridge sites b1, whilst the O-O bond axis was over the 3-fold-hollow site. For the second configurations, i.e. f_{Pt-b} and h_{Pt-b} in Figure 3.15, the configurations were such that one OH-end is above site b1 while the other OH-end was above bridge site b2 and b3 for f_{Pt-b} and h_{Pt-b}, respectively, with the O-O bond axis over the 3-fold-hollow site. The third set of configurations illustrated as configurations f_{Pt-c} and h_{Pt-c} in Figure 3.15 were such that one OH end was atop a Pt atom while the other OH end was above bridge site b1 with the O-O bond axis over the 3-fold-hollow sites.

For 3-fold-hollow sites based on Co, f_{Co} and h_{Co} sites, two possible configurations were investigated. In the first set of configurations represented as f_{Co-a} and h_{Co-a} in Figure 3.15 the configurations were such that the OH ends of the HOOH molecule are above Pt-only bridge sites, i.e. b2 for f_{Co-a} and b3 for h_{Co-a}, whilst the O-O bond axis is over the 3-fold-hollow sites. The second set of configurations represented as configurations f_{Co-b} and h_{Co-b} in Figure 3.15 were such that one OH end was atop a Pt atom while the other OH end is above a bridge site, i.e. b2 for configuration f_{Co-b} and b3 for configuration h_{Co-b}, whilst the O-O bond axis was over the 3-fold-hollow sites.

3.6.2 HOOH adsorption results and discussion

3.6.2.1 HOOH adsorption configurations on $Pt_3Co(111)$

In Table 3.9 the calculated adsorption properties of HOOH upon adsorption on $Pt_3Co(111)$ are presented.

Table 3.9: Calculated: adsorption configurations, adsorption energy, O-O bond distance, O-H bond distance, O-O stretching frequency, OOH bond angles, O-metal distances and the tilt angle for HOOH adsorption on $Pt_3Co(111)$. The calculations are for 0.25 ML coverage of HOOH. The adsorption energy is relative to gas phase HOOH.

Adsorption site	**E_{ads}(eV)**	**d_{O-O}(Å)**	**d_{O-H} (Å)**	**ν_{O-O} (cm^{-1})**	**$\angle$OOH (^{o})**	**d_{O-M}(Å)**	**tilt θ (^{o})**
t_{Co-a}	-0.51	1.49	1.00	774	100	2.12 (Co)	32
t_{Co-b}	-0.52	1.48	1.00	779	99	2.12 (Co)	30
t_{Pt-a}	-0.28	1.47	1.00	862	100	2.49 (Pt)	22
t_{Pt-b}	-0.28	1.47	1.00	869	100	2.49 (Pt)	21

Figure 3.16 is an illustration of the unique adsorption configurations of HOOH identified on $Pt_3Co(111)$.

Of the investigated possible starting configurations of HOOH on $Pt_3Co(111)$ the final optimised configurations were either atop a Pt or Co atom. The HOOH configuration on the surface is such that one OH-end of HOOH is closer to the surface with the atomic oxygen closer to the surface and coordinated to a surface atom. The other OH-end of the molecule is further away from the surface with the O-O bond of the molecule at an angle to the plane parallel to the surface. Figure 3.17 illustrates the O-O bond angle relative to a plane parallel to the surface. The HOOH adsorption configurations are such that the atomic H of the OH-end further away from the surface is directed down towards the surface whilst the atomic H of the OH closer to the surface is pointing away from the surface.

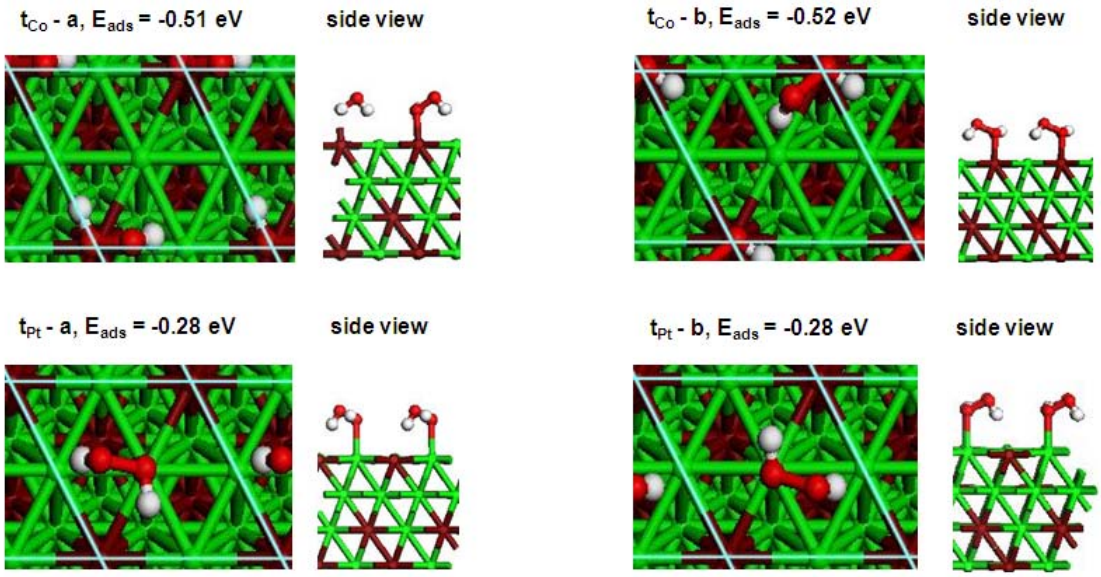

Figure 3.16: Calculated adsorption configurations of HOOH on $Pt_3Co(111)$

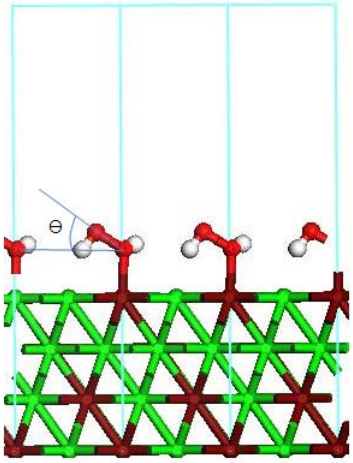

Figure 3.17: Illustration of the angle of the O-O bond relative to a plane parallel to the surface. The angle θ is the tilt angle in Table 3.9

From the sampled adsorption sites only two sites were identified to be stable sites for HOOH, i.e. atop a Pt atom or atop a Co atom. For each site there are two possible configurations which are energetically degenerate, the different possible configurations are obtained through rotating the molecule about the surface-O axis.

For the starting configurations based on the h_{Pt}, f_{Co} and h_{Co} sites, the HOOH optimised to the type of geometries presented in Figure 3.16.

For starting configurations based on the f_{Pt} site there are no stable HOOH configurations obtained on this site, the final configuration was the dissociated product of two OH's. The HOOH on the f_{Pt} site optimised to the state of two OH species irrespective of the starting distance of the HOOH from the surface. For HOOH furthest away from the surface, the initial O-M distances investigated were 2.38 Å and 2.32 Å and for the adsorbate close to the surface, the initial O-M distances investigated were 2.01 Å and 1.91 Å.

For the two HOOH atop Co configurations, the geometrical properties are identical except that for the t_{Co-a} configuration the O-O bond length is slightly longer at

1.49 Å compared to 1.48 Å for the t_{Co-b} configuration. The difference between the ν_{O-O}, O-M distances, ∠OOH and the tilt angles are very small to signify any meaningful structural difference between the two configurations by symmetry.

Similarly, for HOOH adsorption atop a Pt atom, the two configurations have identical properties as can be seen from Table 3.9. For both configurations of HOOH atop a Pt and atop a Co atom, the two configurations, viz. t_{Co-a} and t_{Co-b} for HOOH atop a Co atom, and t_{Pt-a} and t_{Pt-b} for HOOH atop a Pt atom, the two configurations are obtained through rotation about the metal-O axis.

3.6.2.2 HOOH adsorption energy on $Pt_3Co(111)$

The adsorption energy of HOOH is stronger for adsorption atop a Co atom than atop a Pt atom. The adsorption configurations atop a Co atom are 0.24 eV more stable than those atop a Pt atom, this represents almost twice the adsorption stability atop the Pt atoms. Despite there being two different configurations atop a Co atom, i.e. t_{Co-a} and t_{Co-b} the two configurations can be considered energetically degenerate with adsorption energies of -0.51 eV and -0.52 eV. The same observation is made for the configurations atop a Pt atom, the two different configurations , viz. t_{Pt-a} and t_{Pt-a} are energetically degenerate with an adsorption energy of -0.28 eV.

3.6.2.3 O-O stretching mode for HOOH on $Pt_3Co(111)$

The O-O stretching frequency for HOOH is lowered more for configurations atop a Co atom than for configurations atop a Pt atom relative to the O-O stretching frequency of gas-phase HOOH. From Table 3.9, the difference in the calculated O-O stretching frequency despite the same O-O bond lengths for t_{Pt-a} and t_{Pt-b} can be regarded as an indication of the uncertainty in the calculated frequencies.

From the calculated O-O stretching frequencies presented in Table 3.9, it is observed that the frequency of the O-O stretch is lower atop a Co atom by approximately 100 cm^{-1} compared to the O-O stretching frequency atop a Pt atom. The difference in the O-O stretching frequency of approximately 100 cm^{-1} despite the similar O-O bond lengths, atop a Co atom the O-O bond length is 1.49 Å, whilst atop a Pt atom the O-O bond length is 1.47 Å.

3.6.2.4 Bader charge analysis

Table 3.10 is a summary of the calculated charge transferred to and from the atoms during adsorption of HOOH on $Pt_3Co(111)$.

Table 3.10: Calculated Bader charge transfer to the atoms upon adsorption of HOOH on $Pt_3Co(111)$ calculated through the Bader method of charge partitioning

	Bader charge (e^-)				
Adsorption site	**HOOH**	**Pt_{surf1}**	**Pt_{surf2}**	**Pt_{surf3}**	**Co_{surf}**
t_{Co} - a	0.08	0.00	0.02	0.05	-0.15
t_{Co} - b	0.06	0.06	0.00	0.02	-0.15
t_{Pt} - a	0.00	-0.12	0.03	0.08	0.00
t_{Pt} - b	0.02	-0.02	0.00	-0.03	0.02

The configurations atop Co atoms have higher charge (0.08 e^- and 0.06 e^-) transferred to the oxygen atom closer to the surface relative to the charge (0.00 and 0.02 e^-) transferred to configurations atop a Pt atom. The configurations atop a Co atom correspond to the highest charge transferred from the metal atom above which the oxygen atom of the HOOH is directed.

For configurations atop a Co atom, t_{Co-a} and t_{Co-b}, the charge transferred from the Co directly coordinated to the adsorbate is 0.15 e^- whereas for configurations atop a Pt atom, t_{Pt-a} and t_{Pt-b} the charge transferred from the surface atom coordinated to the adsorbate is 0.12 e^- and 0.02 e^- for the two configurations, respectively.

For configurations atop a Pt atom the charge transferred to the adsorbate is small; for t_{Pt-a} there is no net charge transferred to the adsorbate within the error limits of the Bader method as determined in the present study and for t_{Pt-b} 0.02 e^- is transferred to the adsorbate. This value of the charge transfer to configuration t_{Pt-b} falls within the error range.

The Bader charge redistribution upon HOOH adsorption on $Pt_3Co(111)$ as determined in the present study indicates that the charge redistribution is too small to be meaningful, i.e. below 0.10 e^- except for configurations where charge is transferred from surface Co atoms with the adsorbate atop the Co atoms. Therefore, no meaningful conclusion about the role of net charge transfer on the adsorption of HOOH on the $Pt_3Co(111)$ surface can be drawn from the Bader charge partitioning results for HOOH adsorption in the present study.

3.6.2.5 Comparison with HOOH adsorption on the Pt(111) surface

The lowest energy configuration of HOOH adsorbed on the Pt(111) surface from the results by Madala(2012) is a trans-isomer of HOOH with one OH-end bonded atop a Pt atom and the other OH-end further away from the surface, with the H directed towards the surface. The calculated adsorption strength and geometric parameters of HOOH on the Pt(111) surface in the present study using the PW91 functional are: E_{ads}= -0.29 eV, O-O bond length = 1.47 Å, O-H bond length = 1.00 Å and ν_{O-O} = 852 cm^{-1}. The lowest energy configuration of HOOH on the $Pt_3Co(111)$ surface is 0.23 eV more stable compared to adsorption on the Pt(111) surface. The O-O and the O-H bond distances are identical on the $Pt_3Co(111)$ and Pt(111) surfaces. The O-O stretching frequency is lowered more on the $Pt_3Co(111)$ surface than on the Pt(111) surface relative to the O-O stretching frequency of gas-phase HOOH. The adsorption energy of HOOH atop Pt on $Pt_3Co(111)$ is similar to within 0.01 eV to adsorption of HOOH on Pt(111).

3.6.2.6 Comparison with previous studies for HOOH adsorption

No literature on the experimental adsorption of HOOH on the $Pt_3Co(111)$ surface could be obtained, hence comparison is made to theoretical studies only.

The adsorption configurations of HOOH on $Pt_3Co(111)$ in the present study are compared to the reported adsorption configurations on Pt(111) and other 5d transition metal surfaces since to the best of our knowledge there is no published work on HOOH adsorption on $Pt_3Co(111)$. The stable adsorption configurations of HOOH on $Pt_3Co(111)$ are identical to the adsorption configurations reported by Ford et al. (2010) on Cu(111), Pd(111), Ag(111) and Au(111). The configuration of the adsorbed HOOH is a trans isomer of HOOH with one oxygen of the molecule directly bonded atop a metal atom and the hydrogen atom on the OH end of the molecule furthest away from the surface directed towards the surface. The adsorption energy of HOOH was found to be weak on Cu(111), Pd(111), Pt(111), Ag(111) and Au(111) compared to the adsorption energy of the other ORR intermediates, O_2, O, OH, OOH and H_2O (Ford et al. 2010). The same observation of HOOH being weakly adsorbed relative to the other ORR intermediates is made in the present study on $Pt_3Co(111)$.

3.7 H_2O adsorption

The study of water adsorption on metal surfaces is of importance and is required in order to understand how water responds to an applied electrochemical field and how water dissociates, and also provides knowledge of the stability and structure of water clusters that may form on the surface (Michaelides et al. 2003). Michaelides et al. (2003) performed DFT studies on the adsorption of a monomer of water on close packed transition metal surfaces, and observed that the preferred adsorption site for water is on the ontop sites with the water molecule nearly parallel to the surface. DFT studies have indicated that the interaction between a water molecule and a metal surface is dominated by the chemical bonding between the oxygen lone pairs of the water and the electronic states of the metal (Hirunsit and Balbuena, 2009). The adsorption energy of the water molecule on the metal surface has been postulated to be affected by the surface atoms of the metal substrate due to the localisation of the bond in the contact region (Hirunsit and Balbuena, 2009). Water adsorption energy on Pt skin structures on Pt-Co substrates has been studied and the adsorption energy of water on Pt-skin structures was found to increase or decrease depending on the concentration of the subsurface cobalt atoms (Roques and Anderson, 2005).

3.7.1 Search strategy for H_2O adsorption configuration on $Pt_3Co(111)$

The investigated configurations for H_2O adsorption on $Pt_3Co(111)$ are illustrated in Figure 3.18. For all the investigated configurations of H_2O on the surface only the configurations where the hydrogen atoms are parallel to the surface with H_2O coordinated to the surface via the oxygen atom were considered. The configurations where H_2O coordinates to the surface through the hydrogen with the hydrogen atoms directed towards the surface were not investigated since this orientation was found not to be stable on Pt-Co alloys (Hirunsit and Balbuena, 2009). The configurations with the H's initially coordinated directly to the surface resulted in configurations with the hydrogen atoms directed away from the surface upon a geometry optimisation calculation (Hirunsit and Balbuena, 2009). No bridge site configurations were investigated, since Hirunsit and Balbuena (2009) did not obtain any stable bridge site configurations for H_2O adsorption on the PtCo(111) surface .

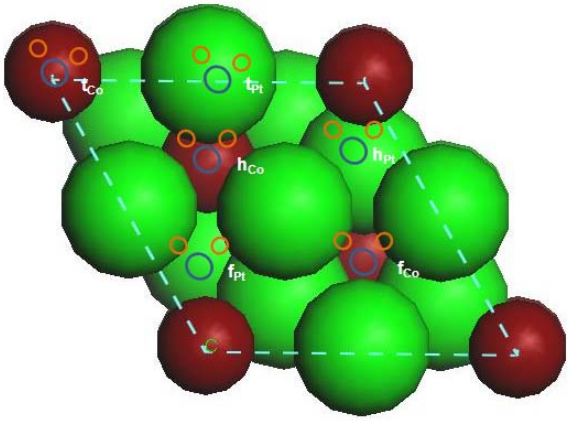

Figure 3.18: Schematic diagram of the adsorption configurations of H_2O on $Pt_3Co(111)$ investigated

Two starting atop configurations were investigated, one atop a Co atom and the other atop a Pt atom. The configurations were such that the O atom of H_2O was directly atop a metal atom while the H atoms were parallel to the surface in the same plane as the oxygen atom.

The adsorption configuration of H_2O was also investigated on four different 3-fold-hollow sites, i.e. f_{Pt}, h_{Pt}, f_{Co} and h_{Co}. For all the 3-fold-hollow sites investigated the configurations were

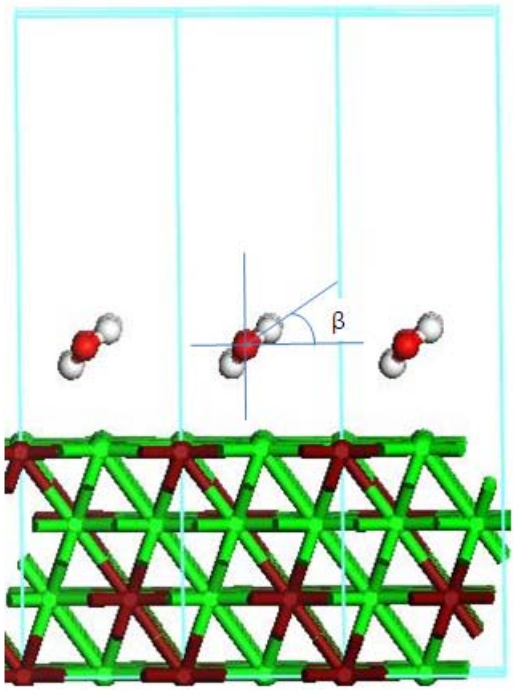

Figure 3.19: Illustration of the tilt angles of H_2O upon adsorption on $Pt_3Co(111)$

such that the O atom of the H_2O molecule was over the 3-fold-hollow site while the H atoms were in the same plane as the O atom and parallel to the surface.

3.7.2 H_2O adsorption results and discussion

Table 3.11 summarises the adsorption properties of optimised H_2O on the $Pt_3Co(111)$ surface.

Table 3.11: Calculated: adsorption configurations, adsorption energy, O-H bond distance, O-metal distance, H_2O stretching frequencies and the tilt angles of the hydrogen atoms upon H_2O adsorption on $Pt_3Co(111)$. The calculations are for a surface coverage of 0.25 ML of H_2O and the adsorption energies are relative to gas phase H_2O.

Adsorption							
Configuration	**E_{ads}(eV)**	**d_{O-H} (Å)**	**d_{O-M} (Å)**	**ν (cm^{-1})**	**$\angle$HOH (^{o})**	**β_1 (^{o})**	**β_2 (^{o})**
t_{Co-a}	-0.35	0.98	2.20	3662, 3559,	105	6	6
				1551			
t_{Co-b}	-0.35	0.98	2.18	3669, 3564,	105	6	5
				1552			
t_{Pt-a}	-0.14	0.98	2.55	3746, 3615,	105	8	3
				1567			
t_{Pt-b}	-0.14	0.98	2.59	3752, 3591,	105	-10	11
				1568			

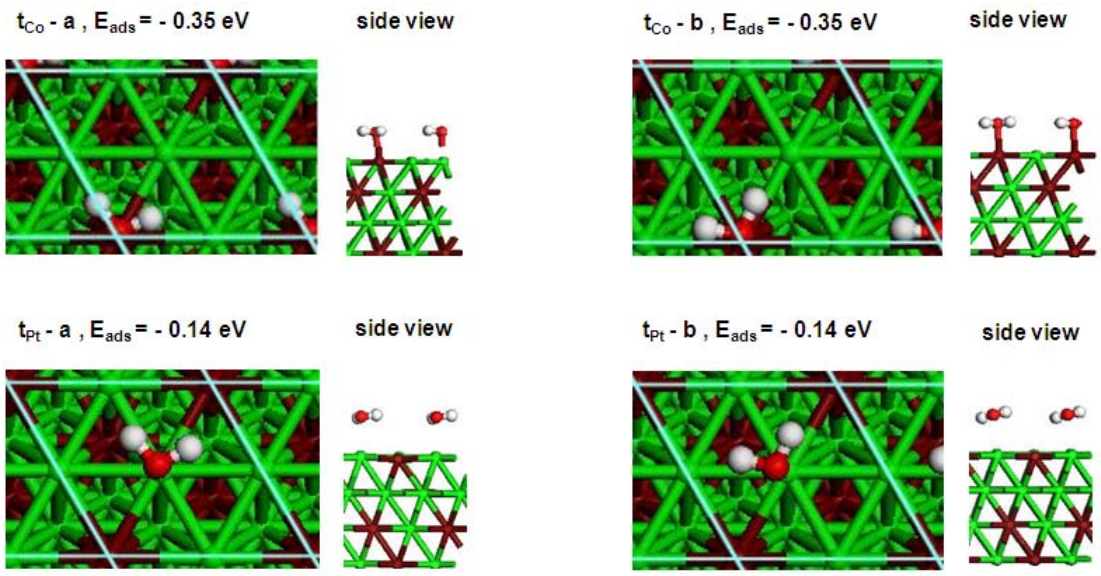

Figure 3.20: Calculated adsorption configurations of H_2O on $Pt_3Co(111)$

3.7.2.1 Adsorption configurations of H_2O on $Pt_3Co(111)$

Only two sites out of the six investigated for H_2O adsorption on $Pt_3Co(111)$ were found to be stable adsorption sites for H_2O. The two preferred adsorption sites are atop a Co atom and atop a Pt atom. For both adsorption atop a Pt and atop a Co atom there are two configurations of H_2O on these sites.

The geometrical properties of the two optimised H_2O configurations atop a Co atom are identical as can be seen in Table 3.11. This indicates that the two configurations atop a Co atom are equivalent.

The two configurations atop a Pt atom are identical except for the tilt angles of the two H atoms of the H_2O molecule. For configuration t_{Pt-b}, one of the H atoms is tilted towards the surface, the H tilted towards the surface is represented by a negative tilt angle of -10 ^{o}. Figure 3.21 shows configuration t_{Pt-b}, indicating the tilted H_2O adsorption configuration.

3.7.2.2 Adsorption energy of H_2O on $Pt_3Co(111)$

The calculated adsorption energy of H_2O atop a Co atom is -0.35 eV whilst the adsorption energy atop a Pt atom is -0.14 eV. The strength of adsorption of H_2O atop a Co atom is more than twice the strength of adsorption atop a Pt atom. Therefore the adsorption energy of H_2O is stabilised more atop Co atoms than atop Pt atoms on $Pt_3Co(111)$. The two Co configurations, viz. t_{Co-a} and t_{Co-b}, are energetically degenerate, the same energy degeneracy is observed for the two Pt configurations. The energy degeneracy of the two configurations for Co and Pt geometries indicates that the adsorption energy of H_2O is insensitive to rotation about the M-O bond. This is observed for the t_{Co} configurations which are equivalent despite a slight difference in their geometries around the t_{Co} site. This observation is indicative of the likely free rotation of H_2O atop a Co atom, due to the high degree of symmetry at the t_{Co} site.

3.7.2.3 Frequencies of adsorbed H_2O on $Pt_3Co(111)$

The calculated stretching frequencies of H_2O on the $Pt_3Co(111)$ surface indicates that the stretching frequencies of H_2O are lowered more for configurations atop a Co atom relative to the gas phase H_2O frequencies. The calculated gas phase frequencies are: 3861, 3745 and 1589 cm^{-1}**.** The higher red shifting of the stretching frequencies for H_2O atop a Co atom than

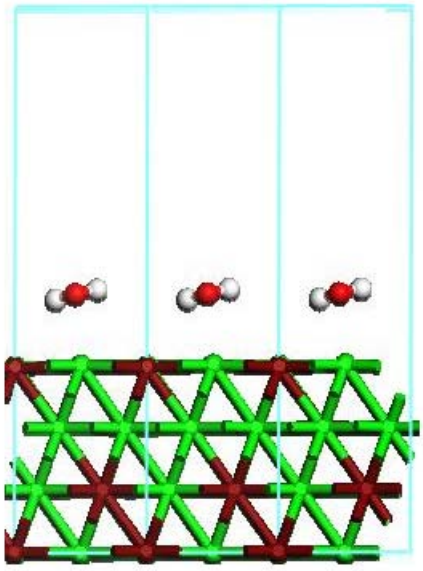

Figure 3.21: Adsorption configuration t_{Pt}-b of H_2O on $Pt_3Co(111)$ illustrating one of the atomic H facing towards the surface

atop a Pt atom relative to gas phase H_2O can be considered to be an indication that the H_2O molecule is activated more atop a Co atom. The activation of the H_2O molecule manifests itself as the lowering of the stretching modes of the O-H bonds. The activation of H_2O atop a Co atom is higher than atop a Pt atom despite the same O-H bond distances, thus the activation of H_2O does not manifest itself as a stretching of the O-H bond length.

3.7.2.4 Bader charge analysis

Table 3.12 summarises the calculated charge transfer to and from the atoms upon adsorption of H_2O on $Pt_3Co(111)$.

Table 3.12: Calculated Bader charge transfer for the atoms for H_2O adsorption on $Pt_3Co(111)$, calculated with the Bader charge partition method.

	Bader charge				
Geometry	**H_2O**	**Pt_{surf1}**	**Pt_{surf2}**	**Pt_{surf3}**	**Co_{surf}**
t_{Pt}	0.00	-0.10	-0.05	0.06	0.01
t_{Co}	0.00	0.02	0.06	0.05	-0.14

From Table 3.12, for H_2O atop a Pt atom the Pt atom directly coordinated to the oxygen of H_2O loses 0.10 e^- charge. There is no net charge transferred to H_2O but the charge might be transferred to the nearby surface Pt atoms as they are calculated to have charge gain in the present study. Upon adsorption of H_2O atop Pt there appears to be a likely repulsive interaction leading to charge loss from the Pt atom bonding to H_2O.

For H_2O adsorbed directly above a Co atom there is more charge transferred from the Co atom than for the case where the H_2O is bonded atop a Pt atom. The charge transferred from the Co may be accepted by the surface Pt atoms as they gain charge. From the Bader charge analysis, within the limitations of the accuracy of the Bader method, there appears to be no net charge transfer to or from the adsorbate. Similarly for H_2O adsorption atop Co also there appears to be a likely repulsive interaction leading to charge loss from the Co atom.

3.7.2.5 Comparison with H_2O adsorption on the Pt(111) surface

The lowest energy H_2O configuration obtained on the Pt(111) surface from the results by Madala(2012) is H_2O atop a Pt atom. The adsorption energy of the lowest energy H_2O configuration on the Pt(111) surface calculated with the PW91 functional is -0.15 eV. The OH bond length of H_2O on the Pt(111) is 0.98 Å. The lowest energy configuration on the $Pt_3Co(111)$ surface is 0.20 eV more stable than the lowest energy H_2O on the Pt(111) surface. H_2O adsorption atop Pt on $Pt_3Co(111)$ is similar to within 0.01 eV to adsorption of the lowest energy structure on Pt(111), this indicates that Co within $Pt_3Co(111)$ does not change the adsorption energy of H_2O atop Pt sites relative to Pt(111). The O-H bond lengths of H_2O are the same on the $Pt_3Co(111)$ surface and the Pt(111) surface.

3.7.2.6 Comparison with previous studies of H_2O adsorption on $Pt_3Co(111)$

No literature on the experimental adsorption of H_2O on the $Pt_3Co(111)$ surface is available, hence comparisons will only be made to theoretical studies.

A comparison is made between the calculated adsorption properties of H_2O in the present study and previous reported adsorption properties to assess the consistency of the adsorption of H_2O in the present study. Comparing the adsorption energy of H_2O calculated in the present study to that reported by Tian and Anderson (2008), the adsorption energies of the present study without zero point energy corrections are comparable to those reported by Tian and Anderson (2008). In the study by Tian and Anderson (2008) it is not specified whether ZPE corrections were added to the adsorption energies, but agreement of the uncorrected adsorption energies of the present study and the values reported by Tian and Anderson (2008), suggests that the reported values by Tian and Anderson (2008) do not include ZPE corrections. Atop a Pt atom the adsorption energy is -0.20 eV and the same value is reported by Tian and Anderson (2008), for H_2O atop a Co atom a value of -0.42 eV is calculated in the present study while Tian and Anderson (2008) reports -0.47 eV. The H_2O adsorption energies in Table 3.11 are adsorption energies including the zero point energy corrections. The non-zero point energy corrected adsorption energies for H_2O for the present study are not included in Table 3.11.

The calculated O-Co distances in both studies are identical, for the present study the O-Co distance is 2.18 Å whilst that reported by Tian and Anderson (2008) is 2.19 Å. The O-Pt distances reported in both studies are similar; in the study by Tian and Anderson (2008) the reported O-Pt distance is 2.63 Å whilst for the two atop H_2O configurations in the present study the O-Pt distances are 2.55 Å and 2.59 Å. The same O-H distance of 0.98 Å is calculated in the present study as is reported by Tian and Anderson (2008).

For H_2O atop a Co atom the tilt angles β_1 and β_2 in the present study are lower than those reported by Tian and Anderson (2008); for both H_2O atop Co configurations in the present study β_1 and β_2 are identical at 6 ^{o} whereas the reported values by Tian and Anderson (2008) are β_1 = 8.9 ^{o} and β_2 = 9.3 ^{o}. For H_2O atop a Pt atom, Tian and Anderson (2008) report β_1 = 0.3 ^{o} and β_2 = 4.2 ^{o}, in the present study the tilt angles calculated for the two H_2O atop a Pt atom configurations are different. For configuration t_{Pt}-a, β_1 = 8 ^{o} and β_2 = 3 ^{o} ,while for configuration t_{Pt}-b, β_1 = -11 ^{o} and β_2 = 10 ^{o}.

The possible source of the difference in the calculated tilt angles in the present study and in that of Tian and Anderson (2008) is the different relaxation criteria for the forces acting on the adsorbate. Tian and Anderson (2008) used a force relaxation criterion of 0.01 eV/Å whilst in the present study the force relaxation criterion is set to 0.03 eV/Å. Therefore, in the present study the forces acting on the relaxed adsorbate could be higher than those of the relaxed adsorbate reported by Tian and Anderson (2008), possibly leading to slight differences in the orientation of the hydrogen atoms of H_2O.

3.8 H adsorption

Zhang et al. (2005) and Sha et al. (2011) have emphasised that including H adsorption for ORR adsorption species is not meant to imply that under ORR conditions H is adsorbed on the surface, but adsorbed H (H_{ads}) is used to trace the energy needed for activating O-containing species to accomplish a hydrogen addition to O-containing species. Similarly in the present study including H_{ads} is not implying that hydrogen is adsorbed on $Pt_3Co(111)$ under ORR conditions but it is included to trace the energy for the process of electron and proton transfer ($H^+ + e^-$). Nørskov et al. (2004) proposed the equilibrium reaction ($H^+ + e^-$) $\rightleftharpoons \frac{1}{2}H_{2-ads}$, hence ($H^+ + e^-$) can be represented by H_{ads}, indicating that the chemical potential of H_{ads} can be related to the process ($H^+ + e^-$).

The search criterion used for determining the unique H adsorption geometries on $Pt_3Co(111)$ was similar to that used for the unique adsorption geometries of O adsorption on $Pt_3Co(111)$.

3.8.1 Results and discussion

Table 3.13 summarises the adsorption properties of H adsorption on $Pt_3Co(111)$.

Table 3.13: Calculated: adsorption sites, adsorption energy, and the H-metal distances for atomic H adsorption on $Pt_3Co(111)$ at 0.25 ML atomic H coverage. The adsorption energies are calculated relative to gas phase atomic H. The adsorption energies in parenthesis are relative to $\frac{1}{2}$ $H_{2(g)}$

Adsorption site	**E_{ads}(eV)**	**d_{O-Pt} (Å)**	**d_{O-Co}(Å)**
f_{Pt}	-2.68 (-0.42)	1.80, 1.80	2.04
h_{Pt}	-2.63 (-0.37)	1.80, 1.80	2.00
h_{Co}	-2.63 (-0.37)	1.85, 1.86, 1.89	-
f_{Co}	-2.61 (-0.35)	1.85, 1.85, 1.85	-
t_{Pt}	-2.57 (-0.31)	1.57	-

Figure 3.22 shows the unique adsorption geometries for H adsorption on $Pt_3Co(111)$.

6 unique adsorption geometries for H adsorption were obtained on $Pt_3Co(111)$ and they are shown in Figure 3.22. A stable adsorption geometry of H atop Pt was obtained whilst there was no stable adsorption geometry atop Co on $Pt_3Co(111)$.

The most stable adsorption site for H adsorption is the f_{Pt} site with an adsorption energy of -2.68 eV and the least stable adsorption site is atop Pt with an adsorption energy of -2.57 eV. The adsorption energy for the other 3-fold-hollow sites, i.e. h_{Pt}, h_{Co} and f_{Co} are -2.63 eV and -2.61 eV respectively. The adsorption energies indicate that H adsorption on the f_{Pt} site is preferred over the h_{Pt} and the h_{Co} sites by 0.05 eV and 0.07 eV over the f_{Co} site. The small differences in energy between the adsorption energy of H at the h_{Co} and h_{Pt} of 0.05 eV and 0.07 eV at the f_{Co} site relative to the f_{Pt} site indicates that H might easily diffuse between the four different 3-fold-hollow sites with a small diffusion barrier.

Comparing H adsorption at the f_{Pt} and f_{Co} sites, it is observed that there is a difference of 0.07 eV between H adsorption at a fcc site where H is bonded directly to a surface Co atom (i.e. f_{Pt} site) and where H is not bonded to a surface Co atom at the fcc site (i.e. f_{Co} site). There is no difference in the adsorption energy for H between the h_{Pt} and the h_{Co} sites, H is not bonded to a surface Co atom at the hcp site for adsorption at the h_{Co} site. The difference between the most stable adsorption site and the least stable adsorption site for H adsorption on $Pt_3Co(111)$ is 0.11 eV, this also indicates a likely low diffusion barrier between the two sites.

The surface Co atom stabilises H adsorption only at the f_{Pt} site since for the hcp site the adsorption energy for H at the h_{Co} and h_{Pt} site is the same, this is despite the later being bonded directly to a surface Co atom and the former not bonded directly to a surface Co atom.

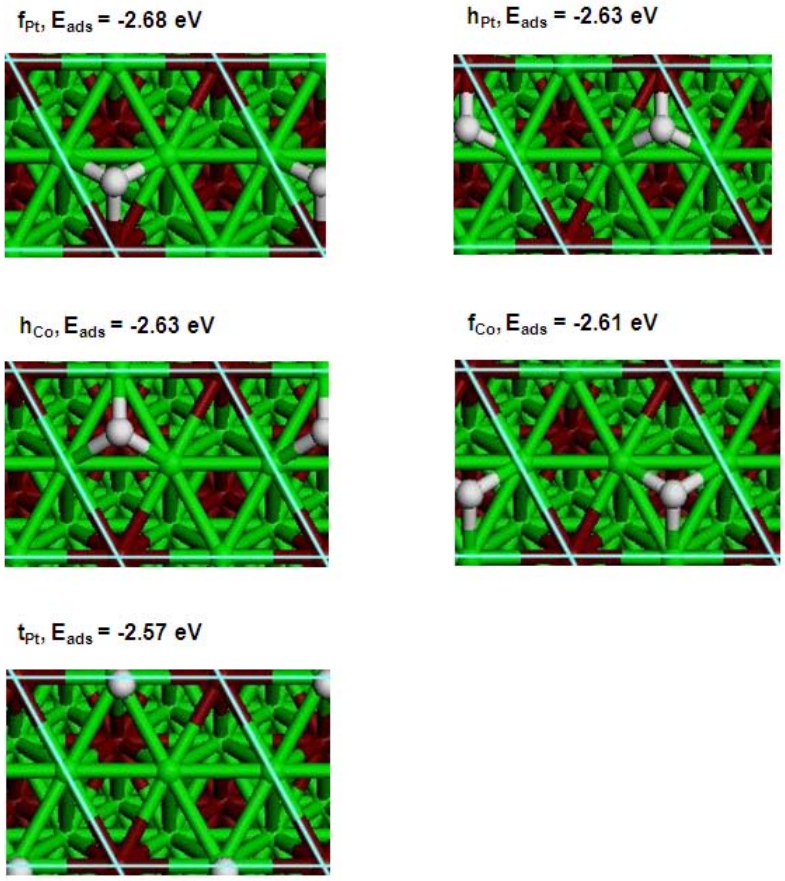

Figure 3.22: Calculated adsorption configurations of atomic H adsorption on $Pt_3Co(111)$

3.8.2 Bader analysis

Table 3.14 summarises the calculated charge transfer to and from the atoms upon adsorption of H on $Pt_3Co(111)$.

Table 3.14: Calculated Bader charge redistribution on the atoms upon adsorption of atomic H on $Pt_3Co(111)$, calculated with the Bader method of charge partitioning

	Bader charge (e^-)				
Site	**H**	**Pt**$_{surf1}$	**Pt**$_{surf2}$	**Pt**$_{surf3}$	**Co**$_{surf}$
f_{Pt}	0.14	-0.04	-0.03	-0.02	-0.04
h_{Pt}	0.12	-0.04	-0.03	-0.02	-0.03
h_{Co}	0.08	-0.02	-0.03	-0.02	-0.05
f_{Co}	0.06	-0.02	-0.01	-0.01	-0.03
t_{Pt}	0.06	-0.03	-0.02	-0.02	-0.04

From the Bader analysis results presented in Table 3.14 it is observed that there is more charge donated to H bonded to a surface Co atom than at adsorption sites where H is not bonded to a surface Co atom. Sites where H is bonded to a surface Co atom are f_{Pt}, h_{Pt}. The charge donated to adsorbed H i.e. equal to the sum of the charge lost by the surface Co and Pt atoms to within $\pm$ 0.02 e^- except for H adsorption at sites h_{Co} and t_{Pt} where there is more charge than $\pm$ 0.02 e^- lost by the surface atoms than is gained by adsorbed H. For adsorption sites h_{Co}, f_{Co} and t_{Pt} adsorbed H is not bonded to a surface Co atom but there is charge lost from the surface Co atom, this charge might be donated to nearby surface Pt atoms or subsurface Pt atoms. No correlation is found between the the highest charge transfer from the surface Co atom and the

highest charge gain to adsorbed H, e.g. the highest charge loss from the surface Co atoms of 0.05 e^- corresponds to 0.08 e^- charge gained by adsorbed H which is not the highest charge transferred to adsorbed H.

3.8.3 Comparison with H adsorption on Pt(111)

On Pt(111) the same observation has been made of a rather flat potential energy surface for H adsorption with the fcc site having a 0.10 eV preference over the other high symmetry sites (Michaelides and Hu (2001); Kandoi et al. (2004)). The calculated adsorption energy for H at the most stable site, i.e. fcc is -2.62 eV on Pt(111). This value is 0.06 eV lower than the most stable adsorption site for H of -2.68 eV on $Pt_3Co(111)$.

No reported experimental and theoretical results on H adsorption on $Pt_3Co(111)$ are available hence no comparison is made to the results of the present study to published results.

3.9 Conclusions

Table 3.15 summarises the adsorption results of the lowest energy configurations of the ORR intermediates on the $Pt_3Co(111)$ and Pt(111) surfaces.

Table 3.15: Summary of the adsorption properties of the low energy configurations of the ORR intermediates on the Pt_3 Co(111) surface and the Pt(111) surface. The bracketed values are the Pt(111) surface results.

Species	**E$_{ads}$ (eV)**	**$\triangle$E$_{ads}$ (eV)**	**d$_{O-O}$ (Å)**	**d$_{O-H}$ (Å)**	**ν_{O-O} (cm^{-1})**
O_2	-0.96 (-0.63)	-0.33	1.43 (1.40)	-	713 (818)
O	-4.62 (-4.17)	-0.45	-	-	-
OOH	-1.37 (-1.12)	-0.25	1.51 (1.46)	0.99 (0.99)	636 (766)
OH	-2.58 (-2.21)	-0.37	-	0.98 (0.98)	-
H_2O	-0.35 (-0.15)	-0.20	-	0.98 (0.98)	-
HOOH	-0.52 (-0.29)	-0.23	1.48 (1.47)	1.00 (1.00)	779 (852)

The following conclusions are drawn, based on the results and discussion for the adsorption of the various ORR intermediates:

For all the ORR intermediates, the lowest energy configurations, viz. most stable configurations are those where the adsorbate is directly bonded to a surface Co atom.

The order of the adsorption of the ORR intermediates on the $Pt_3Co(111)$ surface is O > OH > OOH > O_2 > HOOH > H_2O. The same pattern of the adsorption strength of the ORR intermediates is preserved on the Pt(111) surface.

For all the ORR intermediates species, the adsorption strength of the lowest energy geometries is more exothermic on the $Pt_3Co(111)$ surface than on the Pt(111) surface.

For adsorbates with the O-O bond, i.e. O_2, OOH and HOOH, the O-O bond stretching frequencies of the most activated geometries follow the order OOH < O_2 < HOOH. However, the order of the O-O bond lengths is OOH > HOOH > O_2. The same order of the O-O stretching frequencies of the species having the O-O bond is also preserved on the Pt(111) surface. On the Pt(111) surface the order of the O-O bond lengths is HOOH > OOH > O_2. The O-O bond

lengths of OOH and O_2 on the $Pt_3Co(111)$ surface are longer than the bond lengths for the species adsorbed on the Pt(111) surface. For the HOOH species, the O-O bond length on both the $Pt_3Co(111)$ surface and the Pt(111) surface are identical.

The O-O stretching frequencies on the Pt(111) surface are higher than the frequencies on the $Pt_3Co(111)$ surface. The longer O-O bond lengths of O_2 and OOH on the $Pt_3Co(111)$ surface, together with the lower O-O stretching frequencies relative to those calculated on the Pt(111) surface is indicative that the O-O bond is activated more on the $Pt_3Co(111)$ surface. For the HOOH species, the activation of the O-O bond on the $Pt_3Co(111)$ surface relative to the Pt(111) surface, manifests itself as a lowering of the O-O stretching frequency only, but does not involve the O-O bond stretch.

For species with the O-H bond, the O-H bond distances are the same on both the $Pt_3Co(111)$ and Pt(111) surfaces. Thus, the O-H bond interaction with the surface, for both the $Pt_3Co(111)$ and Pt(111) surfaces is considered to be identical.

The type of site and the configuration of the lowest energy geometry on the Pt_3 Co(111) surface is the same type of site and configuration for the lowest energy geometry on the Pt(111) surface for all the ORR intermediates. The site and geometry preferences for the ORR intermediates on the $Pt_3Co(111)$ surface and the Pt(111) surface are : O_2 adsorption is the bridge and the top-fcc-bridge configurations, O prefers the fcc site, OOH prefers the bridge site, OH prefers the bridge site, H_2O prefers the atop site and HOOH prefers the top-bridge configuration.

3.10 List of references

Bader, F. W. 1990. *Atoms in Molecules: A Quantum Theory*. USA: Oxford University Press.

Balbuena, P.B., Calvo, S.R., Lamas, E.J., Salazar, P.F. and Seminario, J.M. 2006. 'Adsorption and dissociation of H_2O_2 on Pt and Pt-alloy clusters and surfaces.' *Journal of Physical Chemistry B* 110: 17452-17459.

Blöch, P.E.1994. 'Projector augmented-wave method.' *Physical Review B* 50: 17953-17979.

Eichler, A. and Hafner, J. 1997. 'Molecular precussors in the dissociative adsorption of O_2 on Pt(1 1 1).' *Physical Review Letters* 79: 4481-4484.

Ford, D.C., Nilekar, A.U., Xu, Y. and Mavrikakis, M. 2010. 'Partial and complete reduction of O_2 by hydrogen on transition metal surfaces.' *Surface Science* 604: 1565-1575.

Henkelman, G., Arnaldson, A., Jònsson, H. 2006. 'A fast and robust algorithm for Bader decomposition of charge density.' *Computional Materials Science* 36: 354-360.

Hirunsit, P. and Balbuena, P.B. 2009. 'Surface atomic distribution and water adsorption on Pt-Co alloys.' *Surface Science* 603: 912-920.

Hyman, P.M. and Meldin, J.W. 2007. 'Effects of electronic structure modifications on the adsorption of oxygen reduction reaction intermediates on model Pt(111) alloy surfaces.' *Journal of Physical Chemistry C* 111: 17052-17060.

Kandoi, S., Gokhale, A.A., Grabow, L.C., Dumesic, J.A. and Mavrikakis, M. 2004. 'Why Au and Cu are more selective than Pt for preferential oxidation of CO at low temperature.' *Catalysis Letters* 93: 93-100.

Kresse, G. and Hafner, J. 1993. '*Ab initio* molecular dynamics for liquid metals.' *Physical Review B* 47: 558-561.

Kresse, G. and Joubert, D. 1999. 'From ultrasoft pseudopotentials to the projector augmented -wave method.' *Physical Review B* 59: 1758-1775.

Kresse, G and Furthmüller, J. 2010. '*VASP the guide*.' http : // cms.mpi.univie.ac.at / VASP/ (last accessed 13 December 2011).

Lide, D.R. 2008. *CRC handbook of chemistry and physics : a ready - reference book of chemical and physical data*. 88^{th} Edition. CRC Press: Boca Raton.

Li, H. and Jensen, J.H. 2002. 'Partial hessian vibrational analysis: the localization of the molecular vibrational energy and entropy.' *Theoretical Chemistry Accounts* 107: 211-219.

Ma, Y. and Balbuena, P.B. 2008. 'Surface properties and dissolution trends of Pt_3M alloys in the presence of adsorbates.' *Journal of Physical Chemistry C* 112: 14520-14528.

Madala, T. 2012 (In preparation). *Reaction pathways for the formation of hydrogen peroxides in fuel cells: a DFT study*, MSc. Thesis., University of Cape Town: Cape Town.

Mattsson, A.E., Schultz, P.A., Desjarlias, M.P., Mattsson, T.R. and Leung, K. 2005. 'Designing meaningful density functional theory calculations in material science-a primer.' *Modelling and Simulation in Materials Science and Engineering* 13: R1-R3.

Methfessel, M. and Paxton, A.T. 1989. 'High precision sampling for Brillouin-zone integration in metals.' *Physical Review B* 40: 3616-3621.

Michaelides, A. and Hu, P. 2001. 'Catalytic water formation on Platinum: A first principles study.' *Journal of American Chemical Society* 123: 4235-4242.

Michaelides, A., Ranea, V.A., de Andres, P.L. and King, D.A. 2003. 'General model for water monomer adsorption on close packed transition and noble metal surfaces.' *Physical Review Letters* 90: 216102-216104.

Monkhorst, H.J. and Pack, J.D. 1976. 'Special points for Brillouin-zone integrations.' *Physical Review B* 13: 5188-5192.

Nørskov, J.K., Rossmeisl, J., Logadottir, A., Lindqvist, L., Kitchin, J.R., Bligaard, T. and Jónsson, H. 2004. 'Origin of the overpotential for oxygen reduction at a fuel cell cathode.' *Journal of Physical Chemistry B* 108: 17886-17892.

Perdew, J.P., Burke, K. and Ernzerhof, M. 1996. 'Generalized gradient approximation made simple.' *Physical Review Letters* 77: 3865-3868.

Perdew, J.P., Chevary, J.A., Vosko, S.H., Jackson, K.A., Pederson, M.R., Singh, D.J. and Fiolhais, C. 1992. 'Atoms, molecules, solids and surfaces: applications of the genaralized gradient approximation for exchange and correlation.' *Physical Review B* 46: 6671-6687.

Pillay, D., Johannes, M.D., Garsany, Y. and Swider-Lyons, K.E. 2010. 'Poisoning of Pt_3Co electrodes: A combined experimental and DFT study.' *Journal of Physical Chemistry C* 114: 7822-7830.

Press, W.H., Flannery, B.P., Teukolsky, S.A. and Vetterling, W.T. 1986. *em Numerical Recipes*. Cambridge University Press: New York.

Qi, L., Qian, X. and Li, J. 2008. 'Near neutrality of an oxygen molecule adsorbed on a Pt(111) surface.' *Physical Review Letters* 101: 146101-146104.

Rossmeisl, J., Karlberg, G.S., Jaramillo, T. and Nørskov, J.K. 2008. 'Steady state oxygen reduction and cyclic voltammetry.' *Faraday Discuss* 140: 337-346.

Roques, J. and Anderson, A.B. 2005. 'Cobalt concentration effect in $Pt_{1-x}Co_x$ on the reversible potential for forming OH_{ads} from H_2O_{ads} in acid solution.' *Surface Science* 581: 105-107.

Roques, J., Anderson, A.B., Murthi, V.S. and Mukerjee, S. 2005. 'Potential shift of OH(ads) formation on the Pt skin on $Pt_3Co(111)$ electrodes in acid.' *Journal of Electrochemical Society* 152: E193-E199.

Sanville, E., Kenny, S.D., Smith, R. and Henkelman, G. 2007. 'Improved grid-based algorithm for Bader charge allocation.' *Journal of Computational Chemistry* 28: 899-908.

Sha, Y., Yu, T.H., Merinov, B.V., Shirvanian, P. and Goddard, W.A. 2011. 'Oxygen hydration mechanism for the oxygen reduction reaction at Pt and Pd fuel cell catalysts.' *Journal of Physical Chemistry Letters* 2: 572-576.

Stamenković, V., Mun, B.S., Mayrhofer, K.J.J., Ross, P.N., Marković, N.M., Rossmeisl, J., Greely, J. and Nørskov, J.K. 2006. 'Changing the activity of electrocatalysts for oxygen reduction by tuning the surface electronic structure.' *Angew Chem. Int. Ed*. 45: 2897-2901.

Tang, W., Sanville, E., Henkelman, G. 2009. 'A grid-based Bader analysis algorithm without lattice bias.' *Journal of Physics: Condensed Matter* 21: 084204.

Tian, F. and Anderson, A.B. 2008. 'Theoretical study of early steps in corrosion of Pt and Pt/Co alloy electrodes.' *Journal of Physical Chemistry C* 112: 18566-18571.

Xu, Y., Ruban, A.V. and Mavrikakis, M. 2004. 'Adsorption and dissociation of O_2 on Pt-Co and Pt-Fe alloys.' *Journal of American Chemical Society* 126: 4717-4725.

Yang, Z., Wang, J. and Yu, X. 2010. 'The adsorption, diffusion and dissociation of O_2 on Pt-skin $Pt_3Ni(111)$.' *Chemical Physics Letters* 499: 83-88.

Yeh, K.Y., Wasileski, S.A. and Janik, M.J. 2009. 'Electronic structure models of oxygen adsorption at the solvated electrified Pt(111) interface.' *Physical Chemistry Chemical Physics* 11: 10180-10117.

Zhang, J., Vukmirovic, M., Mavrikakis, M. and Adzic, R.R. 2005. 'Controlling the catalytic activity of platinum - monolayer electrocatalysts for oxygen reduction with different substrates.' *Angew. Chem. Int. Ed*. 44: 2132-2135.

Chapter 4

Coadsorption of the ORR intermediates

Introduction

In this chapter the coadsorption of reactants that form the various ORR intermediates is investigated. The coadsorption studies are important, since for the reactants to react they must be in close proximity on the surface. In this chapter, the structures of the coadsorbates on the surface, and the interactions between the coadsorbed species, are presented.

Owing to the multiple possibilities of coadsorbed states, only a few select coadsorbed states will be used for reactions involving the adsorbates. To study the reactions involving the different ORR intermediates, a subset of the stable adsorbates for each species is used. The study is focused on making a comparison of the activation energies for the reactions of each species while reacting from a Co based pathway and a Pt based pathway. Co based pathways are pathways where the reaction involves a species bonded to a surface Co atom whilst Pt based pathways involve the species reacting from a site where it is not bonded to a surface Co atom.

Therefore, the study is not entirely exhaustive in terms of the considered coadsorbed states hence it does not exclude the possibility that even lower energy reaction pathways and coadsorbed states might be excluded in the present study.

4.1 Computational method

Spin-polarized calculations were performed using the plane wave DFT code VASP (Kresse et al. 1993). The exchange and correlation energy terms were approximated using the GGA-PW91 functional (Perdew et al. 1992). The basis set cut-off energy was set to 400 eV, and the Brillouin zone sampling method of Monkhorst-Pack (Monkhorst and Pack, 1976) was used with a (12 $\times$ 12 $\times$ 1) k-point mesh. Both the basis set cut-off energy and the k-point mesh were determined through convergence tests for these parameters, as presented in chapter 2. The electron-ion interactions were described using the projector augmented wave (PAW) pseudopotentials (Kresse and Joubert, 1999; Blöch, 1994), as implemented in VASP. To correct for the electron redistribution at the Fermi level, the method of Methfessel-Paxton (Methfessel and Paxton,1989) was used, with a smearing width of σ = 0.20 eV.

The coadsorption of the different reactants for the different elementary reaction steps was studied on a 4-layer slab. The bottom two layers of the slab were fixed at the bulk optimised positions, while the top two layers and the adsorbates were allowed to relax. A vacuum gap of 13 Å was used in the calculations. Coadsorption was studied in a (2$\times$2) surface unit cell. The adsorption of the intermediates was studied on only one side of the slab, with the resulting electrostatic interactions corrected for using the dipole correction (Neugebauer and Scheffler, 1992), as implemented in VASP code (Kresse and Furthmüller, 2010). The force convergence criterion for

relaxing the structures was a force below 0.03 eV/Å, the force relaxation method used is the conjugate gradient algorithm (Press et al. 1986), and the energy convergence criterion was energy changes below 1 $\times$ 10^{-4} eV.

4.1.1 Coadsorption energy

The coadsorption energy of two adsorbates on the surface is calculated from:

$$E_{coads} = E_{slab+A+B} - E_{cleanslab} - E_{gasphaseA} - E_{gasphaseB} \tag{4.1}$$

where $E_{slab+A+B}$ is the energy of the slab with the coadsorbates, $E_{cleanslab}$ is the energy of the clean slab, $E_{gasphaseA}$ is the energy of gas phase adsorbate A and $E_{gasphaseB}$ is the energy of gas phase adsorbate B. In the present study A and B can be the following species; H_2O, O_2, H_2, OH, OOH, HOOH, H and O.

The formation of the coadsorbed state can be represented by the following surface reaction:

A_{ads} + B_{ads} $\Leftrightarrow$ ($A_{ads}B_{ads}$) + Free slab

where A_{ads} is adsorbate A in a (2 $\times$ 2) surface unit cell at 0.25 ML , B_{ads} is adsorbate B in a (2 $\times$ 2) surface unit cell at 0.25 ML and $A_{ads}B_{ads}$ is adsorbates A and B coadsorbed in a (2$\times$2) surface unit cell. The energy of mixing to form the coadsorbed state on the surface is calculated as follows:

$$\triangle E_{mix} = (E_{slab+A+B} - E_{Aads} - E_{Bads} + E_{cleanslab}) \tag{4.2}$$

where E_{Aads}, is the energy of adsorbate A, in its most stable site in a (2 $\times$ 2) surface unit cell at 0.25 ML and E_{Bads} is the energy of adsorbate B defined as for E_{Aads}.

4.1.2 Vibrational analysis

A partial Hessian vibrational analysis (Li and Jensen, 2002) was performed on the adsorbates, whilst the atoms of the slab were not allowed to move. The partial Hessian vibrational analysis is used to calculate the Hessian matrix, from which the vibrations are obtained. Perturbations of 0.02 Å in the Cartesian space were used to calculate the Hessian matrix. The calculated vibrational frequencies are used to calculate the zero point energy (ZPE) corrections. All the coadsorbed configurations are confirmed as minima on the potential energy surface, by determining the vibrational frequencies. For a structure which is a minimum on the potential energy surface, all the vibrational frequencies should be real. The calculated frequencies for the coadsorbed structures are presented in appendix C.

All presented energy values in the present study include zero point energy (ZPE) corrections.

4.1.3 Bader charge analysis

The method of Bader charge partitioning (Bader,1990) developed for the VASP code by the Henkelman group (Tang et al. 2009; Sanville et al. 2007; Henkelman et al. 2006) was used to determine the atom-resolved charge on the coadsorbates.The Bader charge partitioning is performed on the total charge density which is obtained by summing the valence electron density to the core charge density (the structural optimisation calculations were set such that the core charge is also written to file at the end of the structural optimisation). The charge transferred to or from the coadsorbates was determined by subtracting the atom-resolved charge of the clean slab and the gas phase adsorbate from the atom-resolved charge of the slab with the coadsorbates on it. The bader charge transfer is defined as:

$$q_{Bader} = q_{slab+adsorbates} - q_{cleanslab} - q_{gasphase} \tag{4.3}$$

where q_{Bader} is the charge transfer upon coadsorption, $q_{slab+adsorbates}$ is the atom resolved charge for the slab with the coadsorbates, $q_{cleanslab}$ is the atom resolved charge for the clean slab and $q_{gasphase}$ is the atom resolved charge for the gas phase species. A positive charge transfer is indicative of charge gain by a species, and a negative charge transfer is indicative of charge loss from a species.

The charge redistribution, to or from the adsorbates, was calculated to assess if there is an electrostatic attraction or repulsion between the coadsorbates on the catalyst surface.

4.2 Elementary reaction steps of the ORR

Below is a list of the elementary reactions steps investigated in the present study:

O-O bond scission reaction steps

$O_2^* + * \rightarrow 2O^*$

$O_2H^* + * \rightarrow O^* + OH^*$

$H_2O_2{}^* + {}^* \rightarrow 2OH^*$

Hydrogenation reaction steps

$O^* + H^* \rightarrow OH^* + *$

$OH^* + H^* \rightarrow H_2O^* + *$

$O_2^* + H^* \rightarrow O_2H^* + *$

$O_2H^* + H^* \rightarrow H_2O_2{}^* + *$

O-assisted H_2O dissociation

$H_2O^* + O^* \rightarrow 2OH^*$

4.3 Choice of the species to consider for studying the elementary reactions steps

In order to study the elementary reaction steps, the coadsorbed states of the reactants for formation reaction steps, and coadsorbed states for products for the dissociation reactions, have to be studied. From chapter 3, which presented the adsorption of the ORR intermediates, a variety of adsorption configurations for some species was obtained, e.g. 10 configurations for O_2 adsorption and 10 for OH adsorption. In order to determine the possible coadsorbed states, a choice is made of which configurations of the adsorbates will be used in calculations to determine the coadsorbed states, and subsequently to determine the reaction activation barriers for the elementary reaction steps. The configurations are chosen such that different reaction pathways, i.e. pathways involving and not involving a surface Co atom, for the elementary reaction steps can be explored.

4.3.1 O_2 dissociation

To study the possible coadsorbed states for the dissociation of O_2, 5 stable configurations of O_2 were selected from the 10 identified in chapter 3, to study of O_2 dissociation. The 5 chosen configurations are: b2_f_{Pt}_t_{Co}, b1_f_{Pt}_b1, b1_h_{Pt}_t_{Pt}, b3_h_{Pt}_t_{Co} and b2_h_{Co}_t_{Pt} .

Configuration b1 and b2_f_{Pt}_t_{Co} are energetically degenerate. Therefore, at equilibrium the probability of these configurations being occupied is expected to be the same. In reported transition state structures for O_2 dissociation on Pt(111) and Pt-skin on Pt_3Co(111) by Xu et al. (2004), O_2 rotated into the top-fcc/hcp-bridge like structures at the transition state. No top-bridge-top transition state structures were obtained on the Pt(111) and the Pt-skin on Pt_3Co(111) surfaces. Configuration b2_f_{Pt}_t_{Co} is accessed through a rotation or reorientation of the b1 configuration as one of the possible geometries it can adopt prior to dissociation. Therefore, configuration b2_f_{Pt}_t_{Co} is chosen over b1 since b2_f_{Pt}_t_{Co} is one possible geometry that b1 can access prior to dissociation and also due to the more lengthened O-O bond of 1.43 Å relative to 1.38 Å for configuration b1.

Configurations b1_f_{Pt}_b1 and b1_f_{Pt}_t_{Pt} are energetically degenerate, and it is expected that their equilibrium coverages will be the same owing to the same possibility of these type of configurations per unit cell. Configuration b1_f_{pt}_b1 is accessed through a reorientation or rotation of the b1_f_{Pt}_t_{Pt} configuration over the f_{Pt} site. Configuration b1_f_{Pt}_b1 is chosen over b1_f_{Pt}_t_{Pt} due to a more activated O-O bond of 1.46 Å compared to 1.42 Å for b1_f_{Pt}_t_{Pt}; its different configuration of the bridge-fcc-bridge type, and also to investigate what type of transition state structure will result if O_2 dissociates from a different orientation than the top-fcc/hcp-bridge geometry in the f_{Pt} site.

Configurations b1_h_{Pt}_t_{Pt} and b3 are energetically degenerate to within 0.06 eV, with b3 being less stable. On the Pt(111) and Pt-skin on Pt_3Co(111) surfaces, the type of transition state structure accessed is not a top-bridge-top geometry, but is a top-fcc/hcp-bridge geometry (Xu et al. 2004). Therefore, configuration b1_h_{Pt}_t_{Pt} is chosen over the b3 configuration since the O-O bond is more lengthened at 1.42 Å than for b3 at 1.37 Å; configuration b1_h_{Pt}_t_{Pt} is accessed through a rotation or reorientation of configuration b3 over the h_{Pt} site as a possible initial state prior to dissociation.

Configuration b3_h_{Pt}_t_{Co} is chosen to investigate how O_2 dissociates in the h_{Pt} site when one of the oxygen atoms is atop Co, in contrast to O_2 dissociation from b1_h_{Pt}_t_{Pt}, where one of the oxygen atoms is atop Pt, and the other O is only coordinated to Co in a bridged configuration.

b2_h_{Co}_t_{Pt} and b2 configurations are energetically degenerate, and the probability of occupation of both at equilibrium is identical. However, due to a higher number of b2 sites per unit cell compared to the h_{Co} sites, the equilibrium coverage of site b2 is expected to be higher than that of the b2_h_{Co}_t_{Pt} configuration. However, the dissociation of O_2 from b2_h_{Co}_t_{Pt} is included to investigate how the dissociation of O_2 is affected by the absence of a surface Co atom from the site of O_2 dissociation. Configuration b2_h_{Co}_t_{Pt} is chosen over configuration b2; based on greater lengthening of the O-O bond at 1.40 Å relative to 1.36 Å and also due to the assumption that the b2 configuration would have to access the b2_h_{Co}_t_{Pt} geometry as one possible geometry prior to dissociation, based on the type of transition state structures obtained on the the Pt(111) and Pt-skin on Pt_3Co(111) surfaces.

Configuration t_{Co} is the least stable O_2 adsorption structure. It is anticipated that the equilibrium surface coverage of O_2 in this configuration will be the lowest of the other configurations. Therefore, it is anticipated that the dissociation of O_2 from this configuration is least likely to occur, hence the dissociation of O_2 from this configuration will not be explored in the present study. Also, O_2 would likely have to reorientate such that both O-atoms interact with the surface prior to dissociation.

4.3.2 OH

From chapter 3, 10 unique configurations for OH adsorption were identified. To study the possible reaction pathways for OH formation, 5 OH configurations are chosen, from which possible

coadsorbed states of O and H are investigated. The 5 chosen OH configurations are: b1, t_{Pt-a}, b2, b3-a and b3-b.

Configurations b1, t_{Co-a} and t_{Co-b} are energetically degenerate to within 0.03eV with b1 being the most stable, hence there is an almost equal probability of these configurations being equally occupied at equilibrium. However, due to the higher density (6 sites/unit cell) of b1 sites relative to the t_{Co} sites (1 site/unit cell) , it is expected that the actual coverage of the b1 site geometry will be higher than that for the t_{Co} based geometries. Therefore, due to the higher density of the b1 site, the b1 geometry is chosen over the t_{Co} based geometries, and also due to similar adsorption energies; OH atop Co can be displaced to a neighboring b1 site with minimal energy cost.

Configurations t_{Pt-a} and t_{Pt-b} are essentially energetically degenerate, and are related through rotation about the Pt-O bond. In the present study, t_{Pt-a} is chosen for studying OH atop Pt.

b2-a and b2-b configurations are almost energetically degenerate to within 0.07 eV, and the probability of these two geometries being occupied is expected to be similar. The adsorption energy of OH for the two configurations is similar despite the different orientations for H for the two configurations. For b2-a, H is directed over the h_{Co} site, and for b2-b, H is directed over the f_{Pt} site. However, to study OH on site b2, configuration b2-a is chosen since it is the lowest energy geometry.

Configurations b3-a and b3-b have adsorption energies which differ by 0.22 eV, therefore they will have different probabilities of being occupied at equilibrium. Therefore, the two configurations are considered separately, thus coadsorbed states which would form OH in the two different configurations are explored. The dependence of the activation energy on the orientation of H in the two geometries will be investigated, for b3-a, H is directed over the f_{Co} site whilst for b3-b, H is directed over the h_{Pt} site.

OH in configuration f_{Pt} is not considered in the present study. Using as a guide for the search of possible coadsorbed states on the $Pt_3Co(111)$ surface, the transition state structure for OH formation from O+H and the transition state structure for H_2O formation from OH+H on the Pt(111) surface, it is assumed that the f_{Pt} geometry is obtained from OH formed on a bridge followed by reorientation or rotation to the f_{Pt} site. On the Pt(111) surface the transition state structure for OH is O on the bridge site and H in the off-top position tilted in a direction towards the O (Ford et al. 2010; Kandoi et al. 2004; Michaelides and Hu, 2001). The transition state structure for H_2O formation on the Pt(111) surface is OH atop Pt and H in the off-top position tilted towards the OH (Ford et al. 2010; Michaelides and Hu, 2001). Therefore, based on the observations made on the Pt(111) surface, OH is likely to be formed on the bridge and top sites and for H_2O formation, OH will be on the ontop site prior to reaction with H. Hence, it is assumed that OH would be formed on the bridge or top sites and would access the f_{Pt} geometry through a reorientation or rotation step.

4.3.3 OOH

All 3 unique OOH configurations identified in chapter 3 are considered for the pathways forming OOH, and for the dissociation pathways of OOH.

4.3.4 HOOH

The configurations of HOOH chosen to study OH atop Co and Pt are t_{Co-b} and t_{Pt-a}.

The two atop Co configurations differ through their orientation on the surface. The two configurations are energetically degenerate, indicating that the probability of both geometries being occupied at equilibrium is the same. However, the two configurations could be formed through different pathways which would access different energy transition states leading to different activation energies. Therefore, the two atop Co configurations could be formed from different coadsorbed states of OOH and H, but for the purposes of the current study which is to compare the Co and Pt based pathways and not necessarily to find the lowest energy coadsorbed state

and the lowest energy tranistion state structures, only the t_{Co-b} configuration is used to study the reactions of HOOH bonded atop a surface Co atom.

Similarly, for the atop Pt configurations, the t_{Pt-a} configuration is used to study the reactions of HOOH bonded atop a Pt surface atom. The same rationale for choosing only one configuration to study reactions of HOOH atop Co is used for selecting the configuration atop Pt.

4.3.5 H_2O

The configurations chosen to study H_2O atop Co and Pt are t_{Co-b} and t_{Pt-a}.

The two H_2O atop Co configurations are related through rotation about the O-M axis, which result in different surface geometries which may be formed through different transition states with different activation energies. The two H_2O configurations atop Co imply that the two configurations could be formed from different coadsorbed states of OH and H resulting in different transition state energies. For the purposes of the present study which is to compare the reactions of H_2O from Co and Pt based pathways only one configuration t_{Co-a} is selected to study the reactions of H_2O bonded atop a surface Co atom.

Based on the same rationale used for H_2O atop Co, configuration t_{Pt-a} is selected to study the reactions of H_2O bonded atop a surface Pt atom.

4.4 Procedure for determining the coadsorbed configurations

Bond stretching is used as an initial guess to determine a possible coadsorbed configuration in the vicinity of the site where a species or adsorbate is adsorbed. The coadsorbed configurations, obtained through bond stretching, represent possible coadsorbed configurations, which will be used for the CI-NEB calculations to study possible reaction pathways, and determine activation barriers for the elementary ORR reaction steps. The assumption made in using bond stretching to identify coadsorbed states, is that the main motion contributing to the reaction coordinate is bond stretching with minor rotation and diffusion.

Hydrogenation steps

As an initial estimate to the coadsorbed state for bond formation reaction steps, i.e. OOH formation, OH formation, H_2O formation and HOOH formation, one O-H bond of OOH, OH, H_2O and HOOH is stretched, and the stretched structure is allowed to relax through a geometry optimization calculation. The resulting coadsorbed structure, after the structural relaxation calculation, is then taken as the coadsorbed structure which is used to study the reaction pathway forming the initially stretched adsorbate, as discussed in chapter 5.

O-O bond scission steps

Similarly, for bond dissociation elementary reaction steps, i.e. O_2 dissociation, OOH dissociation and HOOH dissociation, the O-O bond is stretched, followed by relaxation of the stretched structure via a geometry optimization calculation. The resulting coadsorbed structures are taken as possible dissociation products of the initially stretched adsorbates. The coadsorbed states are used to investigate the reaction pathways, which would proceed via the obtained coadsorbed states, to determine the dissociation reaction activation energies, as discussed in chapter 5.

O-assisted H_2O dissociation reaction step

For coadsorbed H_2O with O, only one coadsorbed state of H_2O atop Co is considered, and similarly only one coadsorbed state of H_2O atop Pt is considered. Other possible coadsorbed states do exist but are not explored in the present study, since the aim is to compare Co and Pt based reaction pathways cognisant of the fact that lower energy pathways than those investigated might exist.

For H_2O atop Co coadsorbed with O, a coadsorbed state in which H_2O and O are in close proximity is desired. The desired coadsorbed state of H_2O atop Co with O should be such that the assumed product which they form of two OH species, should be on sites close to the sites occupied by the reactants. Sites which O could occupy are: f_{pt}, h_{Pt}, f_{Co} and h_{Co}. The sites f_{Pt} and h_{Pt} are not available for occupation by O in the (2×2) cell, since it is anticipated that if occupied by O, this would result in crowding of the adsorbates, as the adsorbates share the Co atom to which H_2O is coordinated to in the (2×2) cell which is expected to result in an unstable coadsorbed state. The remaining sites are the h_{Co} and f_{Co} sites. Therefore, the investigated initial structure of coadsorbed H_2O atop Co atom with O, used to investigate the formation of OH atop Co and OH on site b2 as the possible product state, is H_2O atop Co and O over the h_{Co} site.

For H_2O atop Pt, the desired coadsorbed state of H_2O with O is one with O in close proximity to H_2O, which would result in the product of two OH species, atop Pt atoms, in the vicinity of the starting reactant site of H_2O atop Pt. The sites which could be occupied by O are: f_{Pt}, h_{Pt} and f_{Co}. The f_{Pt} and h_{Co} sites are inaccessible to occupation by O, due to the hydrogen atoms of H_2O directed over these sites. The hydrogen atoms block access to these sites. The remaining sites for occupation by O, is the h_{Pt} site and the f_{Pt} site further away. The investigated initial structure of coadsorbed H_2O atop Pt with O, forming two OH species atop Pt , close to the site occupied by H_2O on a Pt atom, is H_2O atop Pt with O over the h_{Pt} site. The two coadsorbed OH species atop neighboring Pt atoms are illustrated in section 4.5.

4.5 Results and discussion

4.5.1 Coadsorbed atomic oxygen

Table 4.1 summarizes results for coadsorbed O's on $Pt_3Co(111)$, at a surface coverage of 0.5 ML.

Table 4.1: Calculated coadsorption energies of O's, the $\triangle E_{mix}$ upon coadsorption, and the sites occupied by coadsorbed O's . E_{coads} is calculated relative to $O_{2(g)}$

Dissociating geometry	O1 site	O2 site	$\triangle E_{mix}$(eV)	E_{coads}(eV)
b2_f_{Pt}_t_{Co}	t_{Co}	h_{Co}	1.74	-1.45
b1_f_{Pt}_b1	h_{Pt}	h_{Pt}	0.98	-2.20
b1_h_{Pt}_t_{Pt}	f_{Pt}	f_{Pt}	0.42	-2.76
b3_h_{Pt}_t_{Co}	t_{Co}	f_{Co}	1.73	-1.46
b2_h_{Co}_t_{Pt}	f_{Pt}	f_{Pt}	0.42	-2.76

Figure 4.1 shows the starting geometries from which the O_2 used to locate the coadsorbed O's by stretching the O-O bond, and the final position of the two O's on the $Pt_3Co(111)$ surface, obtained in this way.

4.5.1.1 Coadsorption structures

The structures of coadsorbed atomic oxygen shown in Figure 4.1 do not mean to imply that the dissociation of O_2 in a particular site to 2O's will result in the coadsorbed structures shown here,

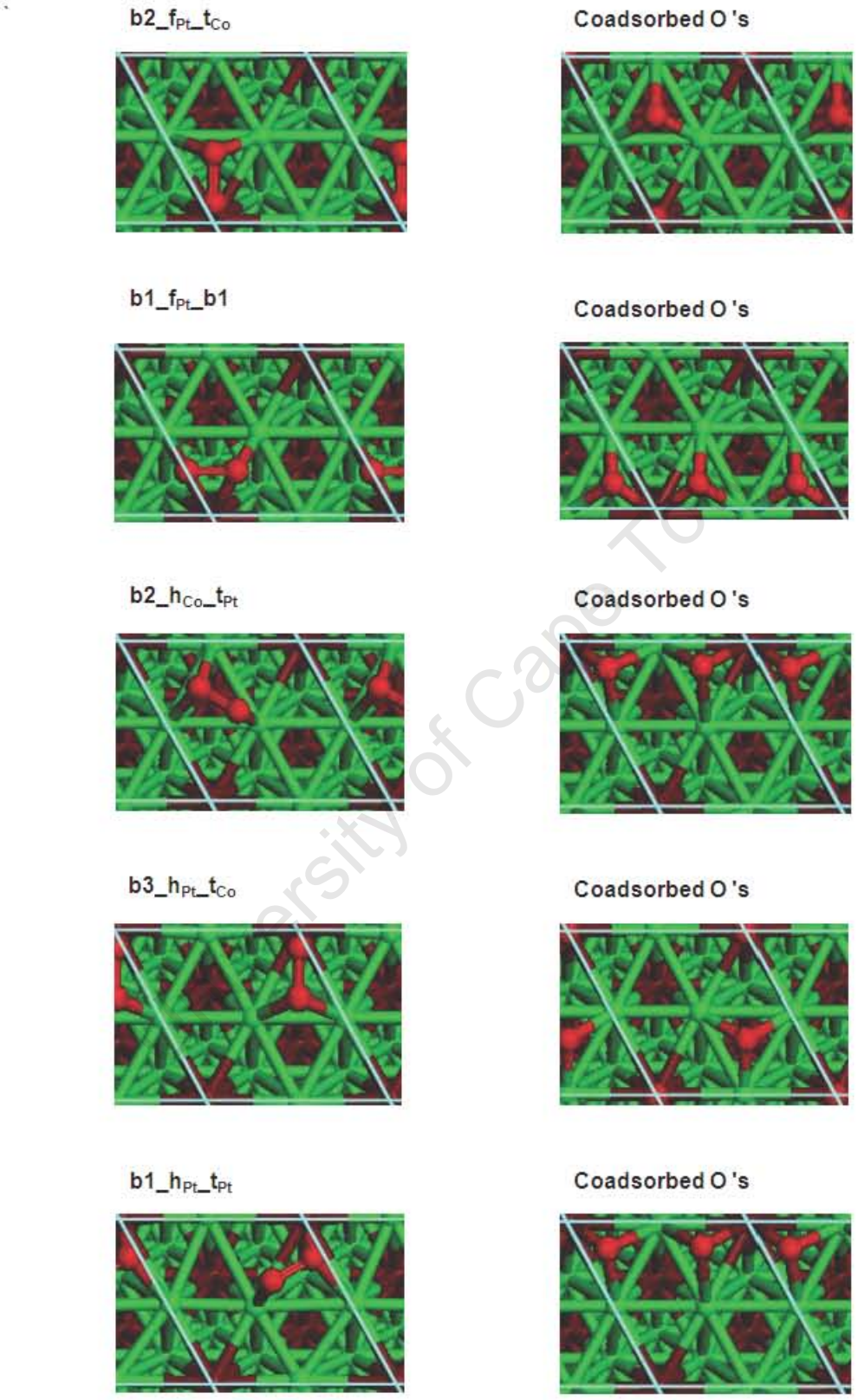

Figure 4.1: Starting O_2 structures, and the final optimised coadsorbed O structures.

which are obtained by stretching the O-O bond of O_2 in that site. The coadsorbed structures obtained here are only used to set up the CI-NEB calculations, to locate possible transition states. Rotation and reorientation of the reactants is allowed such that the final product need not necessarily be the one shown for each site here.

For the investigated coadsorbed structures of O, two types of structures are identified. Type I is a coadsorbed state where one O is atop a Co atom and the other O is over a 3-fold-hollow site, based on a Co atom, i.e. h_{Co} and f_{Co} site. Type II coadsorbed state is where both O's are adsorbed over 3-fold-hollow sites. Upon coadsorption of two O's, the ontop site on a Co atom becomes a stable site for O adsorption. For O adsorption at a coverage of 0.25 ML, separately adsorbed in a (2×2) surface unit cell, the ontop site atop Co was identified not to be a stable adsorption site for O. The vibrational analysis of type I coadsorbed state yielded no imaginary frequencies indicating that this type of coadsorbed state is a minimum on the potential energy surface.

For the type II coadsorbed state, both O's occupy equivalent 3-fold-hollow sites based on a Pt atom, i.e. either the f_{Pt} or h_{Pt} site. The two O's on equivalent sites are separated by a 3-fold-hollow site.

4.5.1.2 Coadsorption energy and $\triangle E_{mix}$

The coadsorption energies of the type I coadsorption state of O's is the least stable. This is in part due to adsorption in the h_{Co} or f_{Co} sites, which are least stable, and also in part due to one O being atop Co. O atop Co at 0.25 ML was found to be an unstable site. The difference in the coadsorption energy, of the coadsorbed state of O atop a Co atom and O over the h_{Co} site, and O atop a Co atom and O over the f_{Co} site is 0.01 eV. The difference in the coadsorption energies, of the coadsorbed state structures, is less than the difference of 0.08 eV in adsorption energy of the h_{Co} or f_{Co} at 0.25 ML. The similarity in coadsorption energies between the coadsorbed states, indicates that in the presence of O atop Co on the surface, the site preference for O adsorption over the h_{Co} or f_{Co} sites is effectively identical.

The two coadsorbed states that involve O atop a Co atom, have the most endothermic $\triangle E_{mix}$. The high endothermic $\triangle E_{mix}$ values indicate that the coadsorbed state of O atop a Co atom and O over a 3-fold-hollow site based on a Co atom, i.e. h_{Co} and f_{Co} sites, are least stable states relative to two O's occupying the most stable f_{Pt} site, at a coverage of 0.25 ML.

The type II coadsorption states of O's have the most stable coadsorption energies. The coadsorption energy of the coadsorbed state with O's occupying the most stable f_{Pt} site for O adsorption is the most stable at -2.76 eV. For O's occupying the h_{Pt} site, which is the second most stable site for O adsorbed at 0.25 ML, the coadsorption energy is lower at -2.20 eV relative to the coadsorption energy of two O's at 0.5 ML coverage, with the O's occupying the f_{Pt} site.

From the investigated coadsorbed state of two O's, it is observed that coadsorbing O's on equivalent f_{Pt} sites on the surface is mildly endothermic, compared to coadsorbing O's on equivalent h_{Pt} sites on the surface. The endothermic $\triangle E_{mix}$ values, indicate that the system with the two O's coadsorbed, is less stable relative to two O's adsorbed separately over the f_{Pt} site, in separate (2×2) surface unit cells at 0.25 ML surface coverages.

All the calculated $\triangle E_{mix}$ values are endothermic. This indicates that the O's exhibit repulsive interactions on increasing the coverage from 0.25 ML to 0.5 ML. For the coadsorbed state of the O's occupying the most stable site, i.e. the f_{Pt} site, the $\triangle E_{mix}$ value is 0.42 eV. For the other coadsorbed states, the repulsive interactions which are partly due to O occupying less stable sites are greater, with the coadsorbed states involving O atop a Co atom having $\triangle E_{mix}$ value of 1.73 eV.

4.5.1.3 Bader analysis for atomic oxygen at 0.5 ML

Table 4.2 summarizes the calculated charge transferred to the coadsorbed species as determined by the method of Bader charge partitioning.

Table 4.2: Calculated Bader charge transfer to coadsorbed O's on the $Pt_3Co(111)$ surface. The values in italics represent the charge transferred to the adsorbates at 0.25 ML coverage, in the same site they occupy in the coadsorbed configuration.

Dissociating geometry	q_{O1} (e^-)		O1 site	q_{O2} (e^-)		O2 site
b2_f_{Pt}_t_{Co}	0.54	-	t_{Co}	0.71	*0.74*	h_{Co}
b1_f_{Pt}_b1	0.78	*0.83*	h_{Pt}	0.78	*0.83*	h_{Pt}
b1_h_{Pt}_t_{Pt}	0.78	*0.84*	f_{Pt}	0.78	*0.84*	f_{Pt}
b3_h_{Pt}_t_{Co}	0.54	-	t_{Co}	0.74	*0.77*	f_{Co}
b2_h_{Co}_t_{Pt}	0.78	*0.84*	f_{Pt}	0.78	*0.84*	f_{Pt}

For all the coadsorbed states the coadsorbed O's have charge transferred to them, indicating that they are negatively charged. Therefore, Coulomb repulsions between the coadsorbed O's will be present and are expected to result in the coadsorbed state being less favourable than the separate state of O adsorbed at 0.25 ML. The coadsorbed states with one O atop Co have the least amount of charge transferred to the O, with 0.54 e^- transferred to the O atop Co.

The charge transfer to O in the f_{Pt} site in the coadsorbed state is 0.06 e^- higher than the amount of charge transfer to O in the f_{Pt} site at 0.25 ML. Similarly, the difference in charge transfer to O in the coadsorbed state in the h_{Co}, h_{Pt} and f_{Co} sites are 0.03 e^-, 0.05 e^- and 0.03 e^-, respectively, relative to charge transfer to O at 0.25 ML in the same sites. Therefore, there is no meaningful change in charge transferred to O in the coadsorbed state relative to charge transfer to O at 0.25 ML in the same sites as those occupied in the coadsorbed state.

4.5.2 Coadsorbed O_2 and H

In Table 4.3, a summary of the results of coadsorbed O_2 and H on $Pt_3Co(111)$ is presented.

Table 4.3: Calculated coadsorption energies of coadsorbed O_2 and H, the $\triangle E_{mix}$ upon coadsorption, and the sites occupied by O_2 and H in the coadsorbed state. E_{coads} is calculated relative to $O_{2(g)}$ and $\frac{1}{2}$ $H_{2(g)}$

Product geometry	O_2 site	H site	$\triangle E_{mix}$ (eV)	E_{coads}(eV)
b1	b1	t_{Pt}	0.34	-1.05
b2	b2	t_{Pt}	0.45	-0.94
b3	b3	t_{Pt}	0.55	-0.84

Figure 4.2 illustrates the coadsorbed configurations of O_2 and H, together with the OOH configurations from which the coadsorbed states are derived from on the $Pt_3Co(111)$ surface.

4.5.2.1 Coadsorption structures

For all the investigated coadsorbed states of O_2 and H, a similar type of coadsorbed state structure was identified, with O_2 on a bridge site and H atop Pt.

4.5.2.2 Coadsorption energy and $\triangle E_{mix}$

The coadsorption of O_2 on b1 and H atop Pt configuration, is more stable relative to the coadsorption of O_2 on b2 and H atop Pt, and O_2 on b3 and H atop Pt. The stabilization in adsorption of O_2 on b1 and H atop Pt, is due to O_2 being coordinated to a surface Co atom. From chapter 3, it was observed that the adsorption of O_2 is stabilized by coordination to a surface Co atom. The difference in coadsorption energy between the configuration with O_2 on b2 and H atop Pt, and

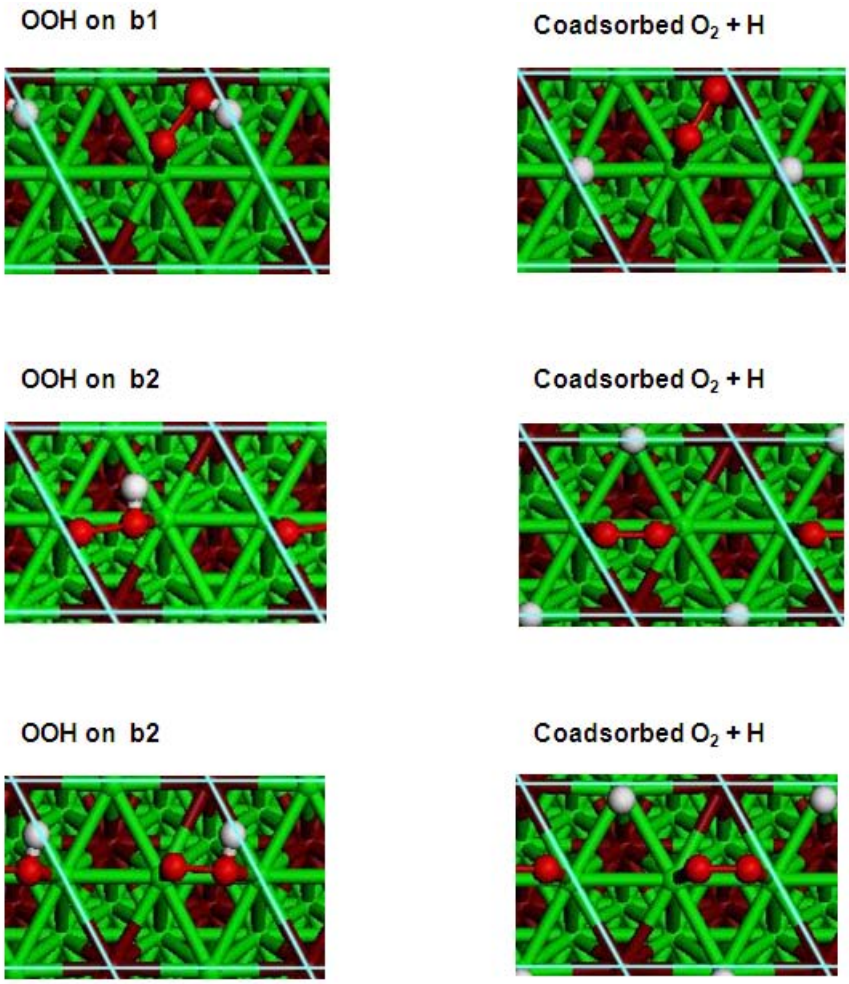

Figure 4.2: Coadsorbed O_2 and H structures, and the OOH structures the coadsorbed states are derived from.

the configuration with O_2 on b3 and H atop Pt is the opposite of the energy difference between O_2 adsorption on site b2 relative to O_2 adsorption on site b3, for O_2 coverage at 0.25 ML.

For all the identified coadsorbed states of O_2 and H, it is observed that the coadsorbed state of O_2 and H is less stable relative to separately adsorbed O_2 in its most stable adsorption site b1, at 0.25 ML, and H in its most stable site f_{Pt}, at 0.25 ML. Therefore, there is an energy cost, i.e. a repulsive lateral interaction that has to be overcome to bring O_2 and H into close proximity prior to reaction to form OOH on the surface. The $\triangle E_{mix}$ values become more endothermic as O_2 is adsorbed on less stable sites, relative to its most stable adsorption site b1, in the coadsorbed state with H atop Pt.

4.5.2.3 Bader analysis for coadsorbed O_2 and H

Table 4.4 summarizes the calculated charge transferred to coadsorbed O_2 and H on the surface, determined using the Bader method of charge partitioning.

Table 4.4: Calculated Bader charge transfer to coadsorbed O_2 and H on the $Pt_3Co(111)$ surface. The values in italics represent the charge transferred to the adsorbates at 0.25 ML coverage, on the same site they occupy in the coadsorbed configuration.

Product geometry	**q$_{O2}$ (e$^-$)**		**O$_2$ site**	**q$_H$ (e$^-$)**		**H site**
b1	0.62	*0.63*	b1	0.03	*0.06*	t_{Pt}
b2	0.57	*0.55*	b2	0.05	*0.06*	t_{Pt}
b3	0.45	*0.57*	b3	0.04	*0.06*	t_{Pt}

In all 3 coadsorbed states, both O_2 and H gain charge indicating that they are negatively charged. An electrostatic repulsive Coulomb interaction will be present as a result of bringing the negatively charged coadsorbates closer to each other in the coadsorbed state. As a consequence of the electrostatic repulsive Coulomb interaction, the coadsorbed state is less favourable than the separate state of O_2 and H in their lowest energy sites in (2×2) surface unit cells.

Charge transfer to O_2 in the coadsorbed state is the same as charge transfer to O_2 at 0.25 ML to within 0.02 e$^-$ for O_2 in sites b1 and b2. For the coadsorbed state with O_2 in site b3, 0.12 e$^-$ more charge is transferred to O_2 in the coadsorbed state relative to charge transfer to O_2 in site b3 at 0.25 ML. For all 3 coadsorbed geometries there is less charge transfer to H in the coadsorbed state relative to charge transfer to H at 0.25 ML.

4.5.3 Coadsorbed OH and O

In Table 4.5, a summary of the results of coadsorbed OH and O on the $Pt_3Co(111)$ surface is presented.

Table 4.5: Calculated coadsorption energies of coadsorbed OH and O, $\triangle E_{mix}$ values for coadsorption, and the sites occupied by O and OH in the coadsorbed state. E$_{coads}$ is calculated relative to OH(g) and $\frac{1}{2}$ $O_{2(g)}$.

Dissociating geometry	**O site**	**OH site**	**$\triangle E_{mix}$ (eV)**	**E$_{coads}$(eV)**
b1	h_{Co}	t_{Co}	0.56	-3.61
b2	h_{Pt}	t_{Pt}	0.65	-3.52
b3	h_{Co}	t_{Pt}	1.66	-2.51

Figure 4.3 illustrates coadsorbed structures of O and OH used to study OOH dissociation on the $Pt_3Co(111)$ surface.

4.5.3.1 Coadsorption structures

For all the investigated coadsorbed states of O and OH, a similar type of coadsorbed structure is obtained with OH atop either a Co or Pt atom, and O over a 3-fold-hollow site. The coadsorbed state of O over the h_{Co} site and OH atop Pt is different to the other coadsorbed structures, in that the O and OH share the same 3-fold site and a Pt atom, whereas for other coadsorbed structures the O and OH are separated by one 3-fold-hollow site. In addition, in the coadsorbed structure with O over the h_{Co} site and OH atop Pt, the OH is in a top tilted configuration.

4.5.3.2 Coadsorption energy and $\triangle E_{mix}$

The coadsorbed state with O over the h_{Co} site and OH atop Co is the most stable coadsorbed state of the structures considered here. The h_{Co} site is the least stable adsorption site for O,

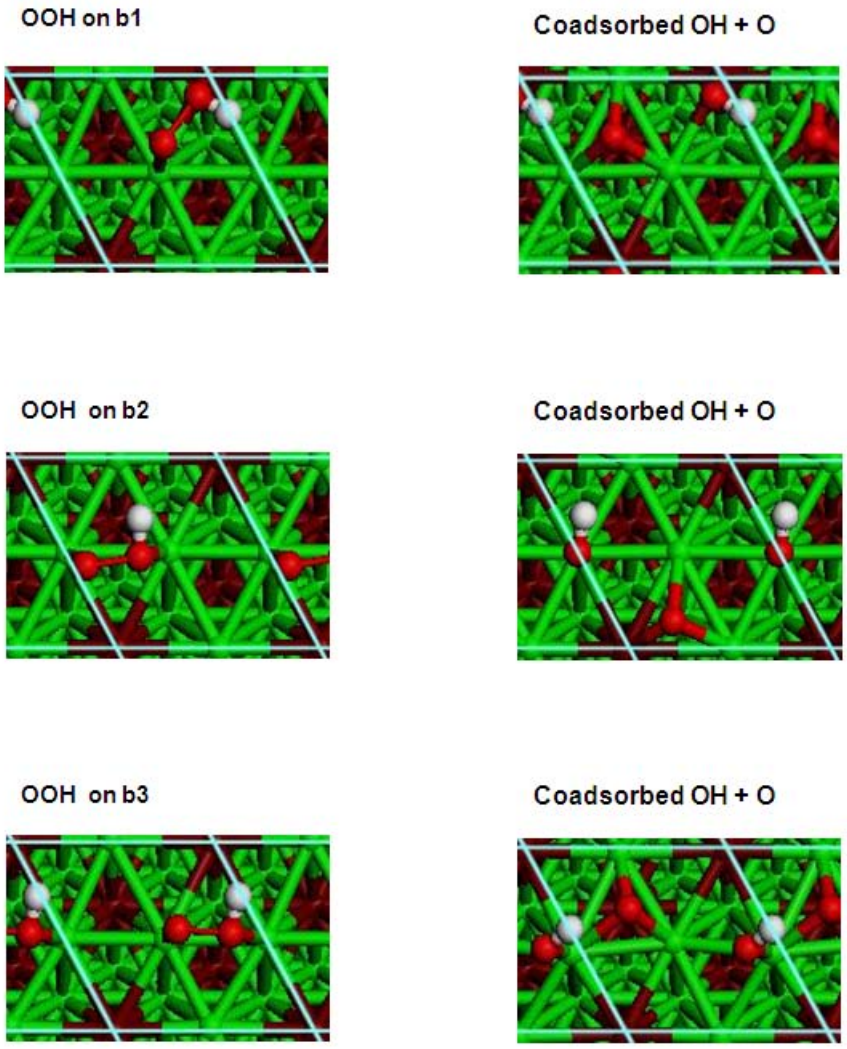

Figure 4.3: Coadsorbed structures of OH and O, and the geometries of OOH from which coadsorbed OH and O structures are derived.

adsorbed at 0.25 ML, and OH atop Co is one of the most stable sites for OH adsorbed at 0.25 ML. The coadsorbed state of O over the h_{Co} site and the tilted-top configuration of OH atop Pt, is the least stable coadsorbed configuration. The destabilization of this coadsorbed state is most likely to be due to the proximity of OH and O, and the sharing of a surface Pt between the OH and O in the coadsorbed state. This is due to O occupying the least stable site for O, separately adsorbed at a coverage of 0.25 ML, in a (2×2) surface unit cell, and OH in a top tilted configuration atop a Pt atom. OH atop a Pt atom is not one of the most stable adsorption sites for OH, separately adsorbed in a (2×2) surface unit cell, at a coverage of 0.25 ML, hence the coadsorbed state of O over the h_{Co} site and OH atop a Pt atom is a least stable configuration.

in comparison, the coadsorption energies of the coadsorbed state with O over the h_{Co} site and OH atop Pt is less stable by 1.01 eV, than the coadsorbed state with O over the h_{Pt} site and OH atop Pt. The b3 derived coadsorbed state is less stable than the b2 derived coadsorbed due to the close proximity between the OH and O species for the b3 derived coadsorbed state.

The $\triangle E_{mix}$ for OH atop Co with O over the h_{Co} site is less endothermic compared to the $\triangle E_{mix}$ for the b2 and b3 derived coadsorbed states. The repulsive lateral interaction between OH atop Co with O over the h_{Co} site is less repulsive since it involves O in the least stable adsorption site, the h_{Co} site, and OH on the stable atop Co site. Whereas for the b2 and b3 derived coadsorbed states, the repulsive lateral interaction energy is higher, partly due to occupation of the least stable adsorption sites by both OH and O species. The b3 derived coadsorbed state

has the most endothermic $\triangle E_{mix}$ indicating a high repulsive lateral interaction between OH and O, which is partly due to the close proximity of OH and O which share a Pt atom.

4.5.3.3 Bader analysis for coadsorbed O and OH

Table 4.6 summarizes the calculated charge transferred to coadsorbed O and OH on the $Pt_3Co(111)$ surface, determined through the Bader method of charge partitioning.

Table 4.6: Calculated Bader charge transfer to coadsorbed O and OH on the $Pt_3Co(111)$ surface. The values in italics represent the charge transferred to the adsorbates at 0.25 ML coverage, on the same site they occupy in the coadsorbed configuration.

Product geometry	**q$_O$ (e$^-$)**		**O site**	**q$_{OH}$ (e$^-$)**		**OH site**
b1	0.73	*0.74*	h_{Co}	1.41	*0.43*	t_{Co}
b2	0.84	*0.83*	h_{Pt}	1.39	*0.41*	t_{Pt}
b3	0.76	*0.74*	h_{Co}	1.36	*0.41*	t_{Pt}

For all the 3 coadsorbed configurations there is charge gain by the O and OH. Thus, these species are negatively charged on the surface resulting in a repulsive Coulomb interaction between the two coadsorbed species. In all coadsorbed configurations there is more charge transferred to OH relative to charge transfer at 0.25 ML; for the b1 and b2 derived coadsorbed states 0.98 e$^-$ more charge is transferred to OH whilst for the b3 derived coadsorbed state 0.95 e$^-$ more charge is transferred to OH. Due to higher charge transfer to OH in the coadsorbed state relative to charge transfer to OH at 0.25 ML, the repulsive Coulomb interactions will be strong between coadsorbed O and OH.

4.5.4 Coadsorbed O and H

In Table 4.7 the results for coadsorbed O and H on $Pt_3Co(111)$ are summarized.

Table 4.7: Calculated coadsorption energies for coadsorbed O and H, the $\triangle E_{mix}$ upon coadsorbing the adsorbates, and the sites occupied by coadsorbed O and H. E_{coads} is calculated relative to $\frac{1}{2}$ $O_{2(g)}$ and $\frac{1}{2}$ $H_{2(g)}$.

Product geometry	**O site**	**H site**	$\triangle E_{mix}$ (eV)	E_{coads}(eV)
b1	f_{Pt}	t_{Pt}	0.19	-1.82
t_{Pt}	f_{Pt}	t_{Pt}	0.19	-1.82
b2	f_{Pt}	f_{Pt}	0.17	-1.85
b3-a	h_{Pt}	t_{Pt}	0.46	-1.55
b3-b	f_{Co}	b2	1.07	-0.94

Figure 4.4 shows coadsorbed O and H structures, and the geometries of OH from which they are derived.

4.5.4.1 Coadsorption structures

From the investigated coadsorbed configurations of O and H, three types of coadsorbed structures of O and H are identified. In the type I structure, O is in a 3-fold-hollow site and H is atop Pt. In type II coadsorbed structures, O is in a 3-fold-hollow site and H is in a 3-fold-hollow site. In type III coadsorbed structures, O is in a 3-fold-hollow site and H is on a bridge site.

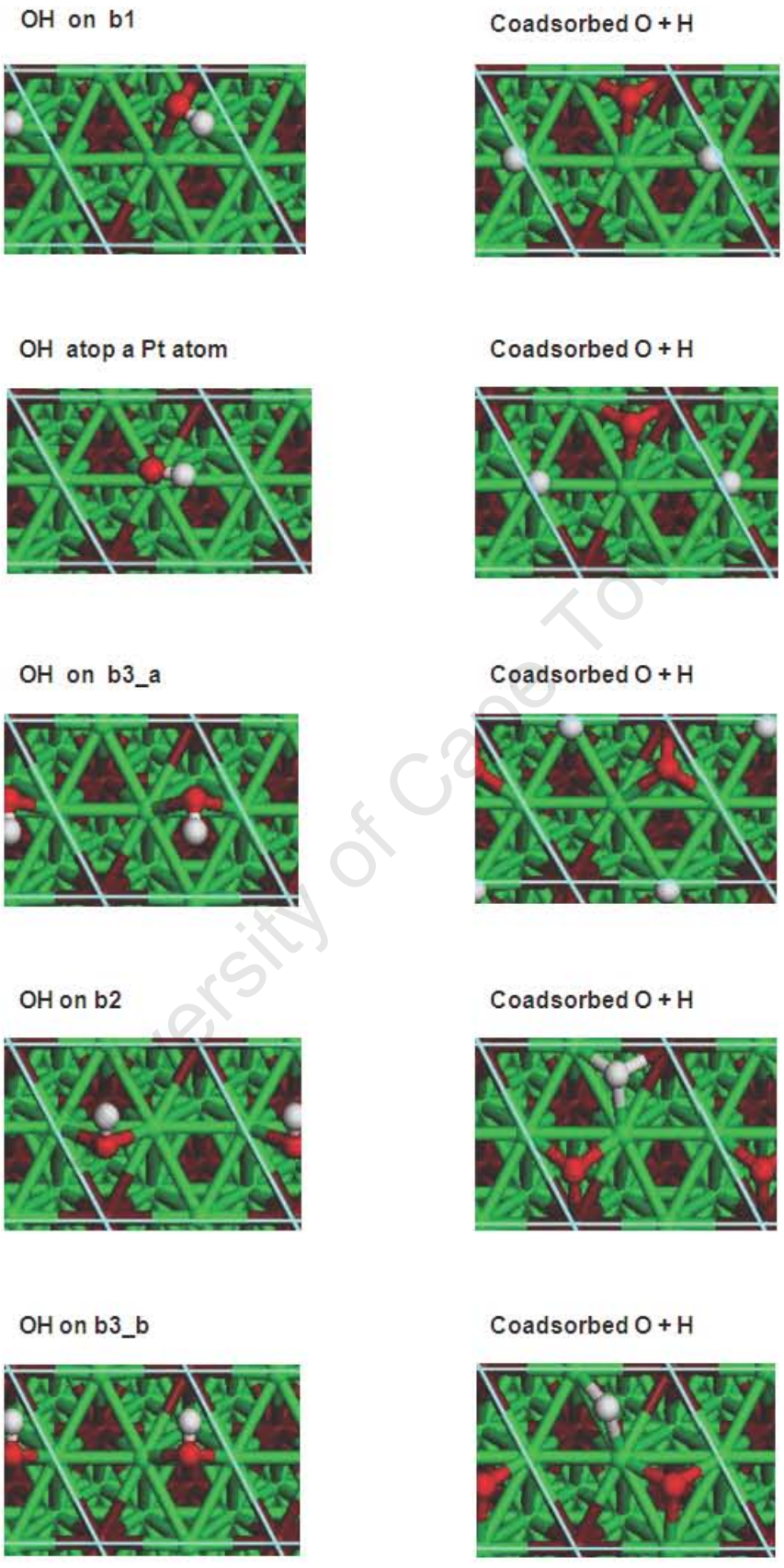

Figure 4.4: Coadsorbed structures of O and H, and structures of OH from which the coadsorbed O and H structures are derived.

4.5.4.2 Coadsorption energy and $\triangle E_{mix}$

The most stable coadsorption energy is for the coadsorbed configuration with O in the f_{Pt} site and H in the f_{Pt} site. The coadsorbed configuration with O in the f_{Pt} site and H atop Pt is 0.02 eV less stable than the most stable configuration. The similarity of the coadsorption energies of type I and type II coadsorption configurations indicates that the adsorption preference of H, on a surface covered with O in the f_{Pt} site is indistinguishable between the f_{Pt} and t_{Pt} sites, compared to a 0.11 eV preference of the f_{Pt} site over the t_{Pt} site for H adsorption at a coverage of 0.25 ML. The coadsorption energy of O with H is also influenced by the location of H relative to O in the coadsorbed state.

Comparing the coadsorption energies of different type I coadsorbed structures, i.e. O over f_{Pt} and H atop Pt, and O over h_{Pt} and H atop Pt, it is observed that the coadsorption energy is dependent on the site occupied by O. Coadsorbing O over the f_{Pt} site, on a surface covered with H atop Pt, is stabilized by 0.27 eV relative to adsorbing O over the h_{Pt} site, on a surface covered with H atop Pt. Type III coadsorbed state structures of O in the f_{Co} and H on site b2 is the least stable coadsorbed state. This coadsorbed state has O in the f_{Co} site, which is the third most stable site for O adsorption, for O adsorbed at 0.25 ML. In addition, this coadsorption configuration has H on site b2, site b2 is not a stable adsorption site for H separately adsorbed at 0.25 ML. Therefore, moving O from its stable f_{Pt} site to the f_{Co} site, and H from the f_{Pt} site to the b2 site, results in a coadsorbed configuration which is much higher in energy, relative to the other coadsorbed states identified here.

The $\triangle E_{mix}$ value of the coadsorbed state of O in the f_{Co} site and H in site b2 is the most endothermic. This indicates that O in the f_{Co} relative to O in the f_{Pt} site, separately adsorbed in a (2×2) surface unit cell, and H in site b2 relative to H in the f_{Pt} site, separately adsorbed in a (2×2) surface unit cell, requires more energy to move the adsorbates to this unstable configuration. This configuration is made unstable by the close proximity between the coadsorbed O and H. Comparing the $\triangle E_{mix}$ for the coadsorbed state of O in the f_{Pt} site and H atop Pt to the coadsorbed state of O in the h_{Pt} site and H atop Pt, it is observed that moving H from its stable site f_{Pt} , in the separately adsorbed state in a (2×2) surface unit cell, costs less energy relative to moving both O and H from their most stable sites in the separately adsorbed state of the adsorbates in a (2×2) surface unit cell, to O in the h_{Pt} site and H atop Pt. For all the investigated coadsorbed states, the calculated $\triangle E_{mix}$ are endothermic, indicating that there is a repulsive lateral interaction between coadsorbed O and H, which needs to be overcome in bringing O and H from their lowest energy sites at 0.25 ML to the coadsorbed state prior to reaction to form OH.

4.5.4.3 Bader analysis for coadsorbed O and H

Table 4.8 is a summary of the calculated charge transferred to coadsorbed O and H, determined through the method of Bader charge partitioning.

Table 4.8: Calculated Bader charge transfer to coadsorbed O and H on the $Pt_3Co(111)$ surface. The values in italics represent the charge transferred to the adsorbates, at 0.25 ML coverage, on the same site they occupy in the coadsorbed configuration.

Product geometry	q_O (e^-)		O site	q_H (e^-)		H site
b1	0.84	*0.84*	f_{Pt}	0.06	*0.06*	t_{Pt}
t_{Pt}	0.84	*0.84*	f_{Pt}	0.04	*0.06*	t_{Pt}
b2	0.83	*0.84*	f_{Pt}	0.11	*0.14*	f_{Pt}
b3-a	0.83	*0.83*	h_{Pt}	0.05	*0.06*	t_{Pt}
b3-b	0.77	*0.77*	f_{Co}	0.06	*0.07*	b2

For all the coadsorbed configurations the charge transfer to O and H is the same to within the calculation error of the Bader method , as the charge transfer at 0.25 ML. Both O and H gain charge and are thus negatively charged, therefore a repulsive electrostatic Coulomb interaction will result from bringing two negatively charged species in close proximity in the coadsorbed state.

4.5.5 Coadsorbed OH and H

In Table 4.9 a summary of the coadsorption results of OH and H on the $Pt_3Co(111)$ surface is presented.

Table 4.9: Calculated coadsorption energies of coadsorbed OH and H, the $\triangle E_{mix}$ for coadsorption, and the sites occupied by OH and H in the coadsorbed state. E_{coads} is calculated relative to $OH(g)$ and $\frac{1}{2}$ $H_{2(g)}$ and $E_{coads}{}^*$ is calculated relative to $H_2O(g)$.

Product geometry	OH site	H site	$\triangle E_{mix}$ (eV)	E_{coads}(eV)	$E^*{}_{coads}$ (eV)
t_{Co}	t_{Co}	t_{Pt}	0.23	-5.03	0.23
t_{Pt}	t_{Pt}	t_{Pt}	0.55	-4.71	0.55

Figure 4.5 shows the coadsorbed state of OH and H, used to study the formation of H_2O atop Co and atop Pt on the $Pt_3Co(111)$ surface.

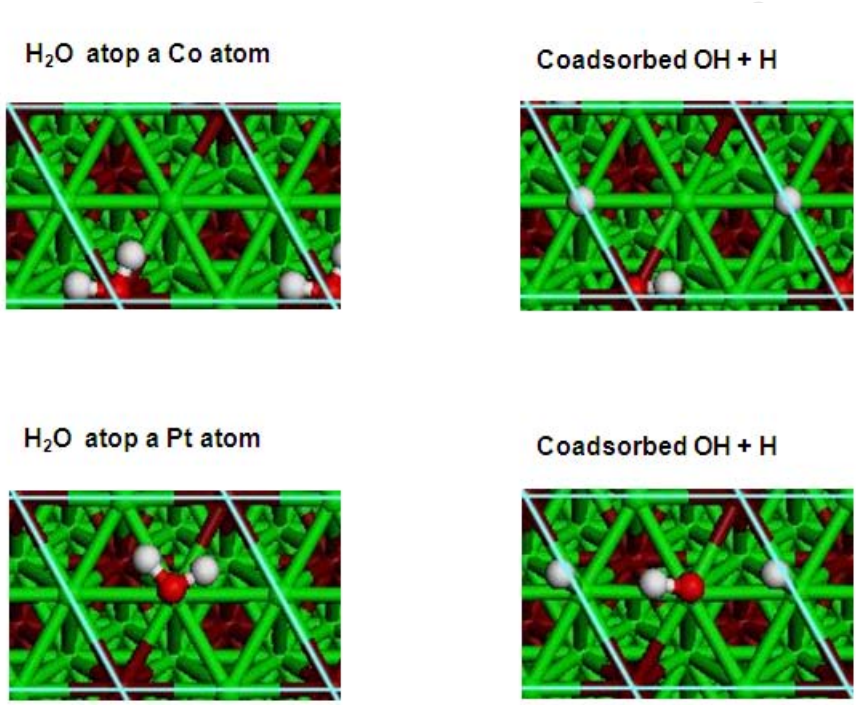

Figure 4.5: Coadsorbed structures of OH and H, and H_2O geometries they are derived from.

4.5.5.1 Coadsorption structures

The coadsorbed structures of OH and H obtained in the present study have H atop Pt and OH either atop Co or Pt.

4.5.5.2 Coadsorption energy and $\triangle E_{mix}$

The coadsorbed configuration of OH atop Co and H atop Pt is more stable than the coadsorbed configuration of OH atop Pt and H atop Pt. Since OH atop Co is the most stable site for OH at 0.25 ML. The energy difference of 0.32 eV between the 2 coadsorbed configurations is essentially equivalent to the adsorption energy difference of 0.34 eV for OH atop Co and atop Pt at

0.25 ML. The coadsorption energies calculated relative to gas phase H_2O are positive indicating that H_2O in the gas phase is more stable than H_2O dissociating into OH and H on $Pt_3Co(111)$.

The $\triangle E_{mix}$ for the H_2O atop Pt derived coadsorbed state is more endothermic than the H_2O atop Co derived coadsorbed state. The increased repulsive lateral interaction for the H_2O atop Pt derived coadsorbed state is partly due to adsorbing OH on the less stable adsorption site atop Pt. For both coadsorbed states, $\triangle E_{mix}$ is endothermic indicating that there is a repulsive lateral interaction energy which needs to be overcome to bring OH and H to the coadsorbed state, from their lowest energy sites at 0.25 ML.

4.5.5.3 Bader analysis for coadsorbed OH and H

Table 4.10 summarizes the calculated charge transferred to OH and H, determined through the method of Bader charge partitioning

Table 4.10: Calculated Bader charge transfer to coadsorbed OH and H on the $Pt_3Co(111)$ surface. The values in italics represent the charge transferred to the adsorbates, at 0.25 ML coverage, on the same site they occupy in the coadsorbed configuration.

Product geometry	**q$_{OH}$ (e$^-$)**		**OH site**	**q$_H$ (e$^-$)**		**H site**
t_{Co}	0.45	*0.43*	t_{Co}	0.07	*0.06*	t_{Pt}
t_{Pt}	0.42	*0.41*	t_{Pt}	0.06	*0.06*	t_{Pt}

For both coadsorbed states there is charge gain by both OH and H, thus these species are negatively charged on the surface. Therefore, there will be a repulsive electrostatic Coulomb interaction between the negatively charged OH and H which are brought close to each other in the coadsorbed state relative to adsorption at 0.25 ML. The charge transfer to both OH and H in the coadsorbed state is the same to within the calculation error of the Bader method, as the charge transfer to OH and H adsorbed at 0.25 ML.

4.5.6 Coadsorbed O and H_2O

In Table 4.11 a summary of the coadsorption results of O and H_2O on the $Pt_3Co(111)$ surface is presented.

Table 4.11: Calculated coadsorption energies of coadsorbed O and H_2O, the $\triangle E_{mix}$ for the formation of the coadsorbed state, and the sites occupied by O and H_2O in the coadsorbed state. E_{coads} is calculated relative to $H_2O_{(g)}$ and $\frac{1}{2}$ $H_{2(g)}$.

H_2O geometry	**H_2O site**	**O site**	**$\triangle E_{mix}$ (eV)**	**E_{coads}(eV)**
t_{Co}	t_{Co}	b2	0.46	-1.48
t_{Pt}	t_{Pt}	h_{Pt}	0.30	-1.64

Figure 4.6 shows coadsorbed H_2O and O geometries used to study O-assisted H_2O dissociation on the $Pt_3Co(111)$ surface.

4.5.6.1 Coadsorption structures

The two types of structures are obtained in the present study. One has H_2O atop Co and O in bridge site b2, and the other H_2O atop Pt and O in the h_{Pt} site.

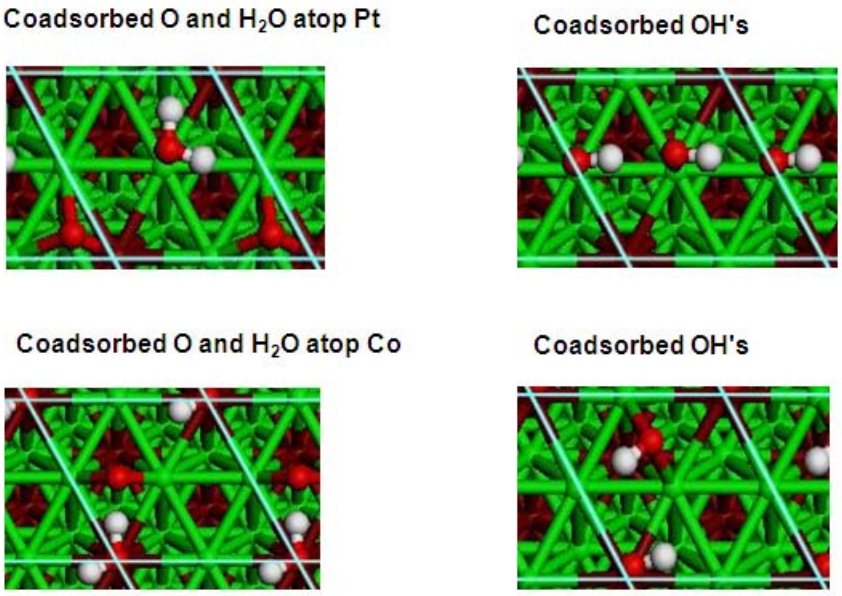

Figure 4.6: Coadsorbed structures of H_2O and O, and the resulting product OH geometries from the possible reaction of coadsorbed O and H_2O on the $Pt_3Co(111)$ surface.

4.5.6.2 Coadsorption energy and $\triangle E_{mix}$

The coadsorbed state with H_2O atop Pt and O in the h_{Pt} site, is more stable by 0.16 eV than the configuration with H_2O atop Co and O in site b2. O in site b2 destabilizes the coadsorbed state of H_2O atop Co coadsorbed with O. This is despite H_2O occupying the most stable site t_{Co}, which is the preferred adsorption site for H_2O, at 0.25 ML. Site b2 was identified as a non-stable adsorption site for O, at 0.25 ML, suggesting that promoting of O to b2 may contribute to destabilizing the system relative to adsorption at lower coverage.

The presence of hydrogen bonding in the coadsorbed state also contributes to the exothermic coadsorption energies.

In the coadsorbed configuration of H_2O atop Pt and O in the h_{Pt} site, H_2O and O occupy sites that are not the most stable sites at 0.25 ML. Despite O and H_2O occupying less stable sites, the coadsorption energy of this coadsorbed configuration, is more favourable than that for the configuration of H_2O atop Co and O in site b2.

Both $\triangle E_{mix}$ for the 2 coadsorbed configurations are endothermic, indicating that a repulsive lateral interaction energy has to be overcome to bring H_2O and O together in the coadsorbed state. The $\triangle E_{mix}$ for H_2O atop Co and O in site b2 is more endothermic partly due to the very close proximity of H_2O and O in site b2 and also due to O being adsorbed in the least stable site.

4.5.6.3 Bader analysis for coadsorbed O and H_2O

Table 4.12 summarizes the calculated charge transfer to, and from, coadsorbed H_2O and O, determined through the Bader method of charge partitioning.

Table 4.12: Calculated Bader charge transfer to and from coadsorbed O and H_2O on the $Pt_3Co(111)$ surface. The values in italics represent the charge transferred to the adsorbates, at 0.25 ML coverage, on the same site they occupy in the coadsorbed configuration.

H_2O geometry	**q_{H2O} (e^-)**		**H_2O site**	**q_O (e^-)**		**O site**
t_{Co}	-0.08	*0.00*	t_{Co}	0.90	-	b2
t_{Pt}	0.40	*0.00*	t_{Pt}	0.39	*0.83*	h_{Pt}

For the t_{Co} H_2O coadsorbed state the H_2O and O have opposite charge signs hence an attractive electrostatic Coulomb interaction will be present between the two coadsorbed species. For H_2O atop Pt coadsorbed state both H_2O and O are negatively charged indicating that there will be a repulsive electrostatic Coulomb interaction between H_2O and O, which needs to be overcome in bringing O and H_2O in close proximity in the coadsorbed state.

For the t_{Co} H_2O coadsorbed state H_2O loses charge whereas at 0.25 ML H_2O atop Co has no charge transferred to or away from it. The O in site b2 has 0.90 e^- charge transferred to it whilst at 0.25 ML O in site b2 is an unstable adsorption site. For H_2O atop Pt coadsorbed state H_2O gains 0.40 e^- charge which is higher than the charge gain at 0.25 ML for H_2O atop Pt. The charge gain by O in the h_{Pt} site in the coadsorbed state is 0.44 e^- lower than charge gain at 0.25 ML.

4.5.7 Coadsorbed OOH and H

Table 4.13 summarises the coadsorption results of O_2H and H on the $Pt_3Co(111)$ surface.

Table 4.13: Calculated coadsorption energy of OOH and H , $\triangle E_{mix}$ for forming the coadsorbed state, and the site preference for OOH and H in the coadsorbed state. E_{coads} is calculated relative to $OOH_{(g)}$ and $\frac{1}{2}$ $H_{2(g)}$

Product geometry	**OOH site**	**H site**	**$\triangle E_{mix}$ (eV)**	**E_{coads}(eV)**
t_{Co}	b1	t_{Pt}	0.20	-1.59
t_{Pt}	b2	t_{Pt}	0.41	-1.38

Figure 4.7 indicates the coadsorbed configurations of OOH and H used to study HOOH formation on the Pt_3Co (111) surface.

4.5.7.1 Coadsorption structures

The coadsorbed structure for OOH and H investigated in the present study is a structure with H atop Pt and OOH on a bridge site.

4.5.7.2 Coadsorption energy and $\triangle E_{mix}$

The t_{Co} HOOH derived coadsorbed state has a more stable coadsorption energy than the t_{Pt} HOOH derived coadsorbed state. This is due to OOH being adsorbed at the b1 site, which is the lowest energy adsorption site at 0.25 ML. The difference in the coadsorption energies is the same to within 0.04 eV as the difference in adsorption energy between OOH in site b1 and b2 for adsorption at 0.25 ML.

Both the $\triangle E_{mix}$ for the 2 coadsorption configurations is endothermic, indicating that a repulsive lateral interaction energy needs to be overcome to bring OOH and H together to the coadsorbed state. The t_{Pt} HOOH derived coadsorbed state has a more endothermic $\triangle E_{mix}$, partly due to adsorbing OOH in the least stable site b2.

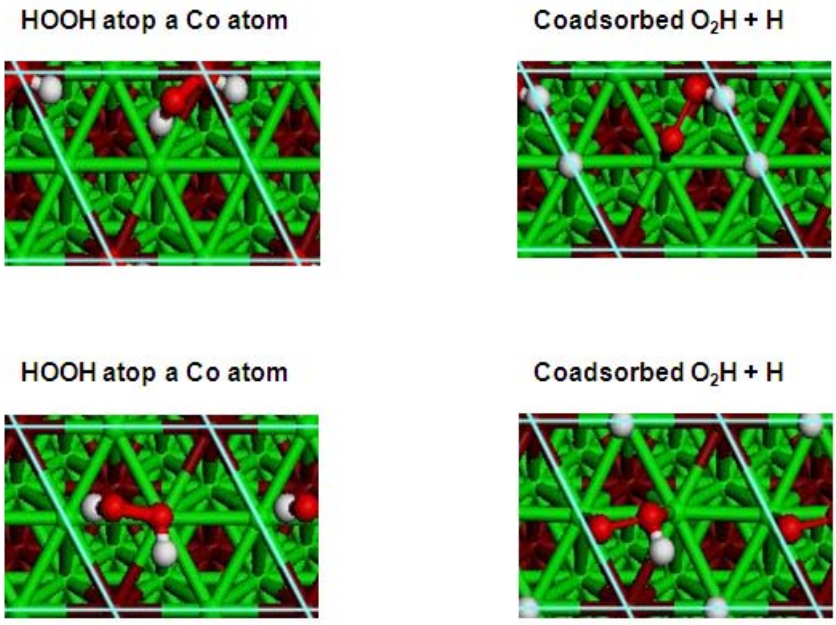

Figure 4.7: Structures of coadsorbed OOH and H, and the HOOH structures from which they are derived.

4.5.7.3 Bader analysis for coadsorbed OOH and H

Table 4.14 summarizes the calculated charge transfer to coadsorbed OOH and H, determined through the Bader method of charge partitioning.

Table 4.14: Calculated Bader charge transfer to coadsorbed OOH and H on the $Pt_3Co(111)$ surface. The values in italics represent the charge transferred to the adsorbates, at 0.25 ML coverage, on the same site they occupy in the coadsorbed configuration.

Product geometry	**q_{OOH} (e^-)**		**O_2H site**	**q_H (e^-)**		**H site**
t_{Co}	1.48	*0.49*	b1	0.12	*0.06*	t_{Pt}
t_{Pt}	1.24	*0.41*	b2	0.02	*0.06*	t_{Pt}

For both coadsorbed states OOH and H gain charge, indicating that they are negatively charged. Therefore, a repulsive Coulomb interaction will be present due to bringing the negatively charged OOH and H in close proximity in the coadsorbed state.

The charge transfer to OOH in the t_{Co} derived coadsorbed state is 0.99 e^- more than the charge transfer at 0.25 ML, similarly 0.83 e^- more charge is transferred to OOH in the t_{Pt} derived coadsorbed state relative to charge transfer at 0.25 ML. The charge transfer to H in the t_{Co} derived coadsorbed state is twice the charge transfer to H at 0.25 ML and the charge transfer to H in the t_{Pt} derived coadsorbed state is $\frac{1}{3}$ of the charge transfer at 0.25 ML.

A strong repulsive Coulomb interaction is expected between the coadsorbed OOH and H, and neighbouring OOH's due to the higher amount of charge transferred to OOH in the coadsorbed state relative to charge transfer at 0.25 ML.

4.5.8 Coadsorbed OH at 0.5 ML

In Table 4.15 a summary of the coadsorption results of two OH species, resulting from stretching the O-O bond of HOOH on the $Pt_3Co(111)$ surface, is presented.

Table 4.15: Calculated coadsorption energy of two OH's coadsorbed, the $\triangle E_{mix}$ for forming the coadsorbed state, and the site preference for the two OH's coadsorbed. E_{coads} is calculated relative to $OH_{(g)}$.

Dissociating geometry	OH1 site	OH2 site	$\triangle E_{mix}$ (eV)	E_{coads}(eV)
t_{Co}	t_{Co}	b2	0.39	-4.77
t_{Pt}	t_{Pt}	t_{Pt}	0.35	-4.81

Figure 4.8 shows coadsorbed OH's structures used to study the dissociation of HOOH on the $Pt_3Co(111)$ surface.

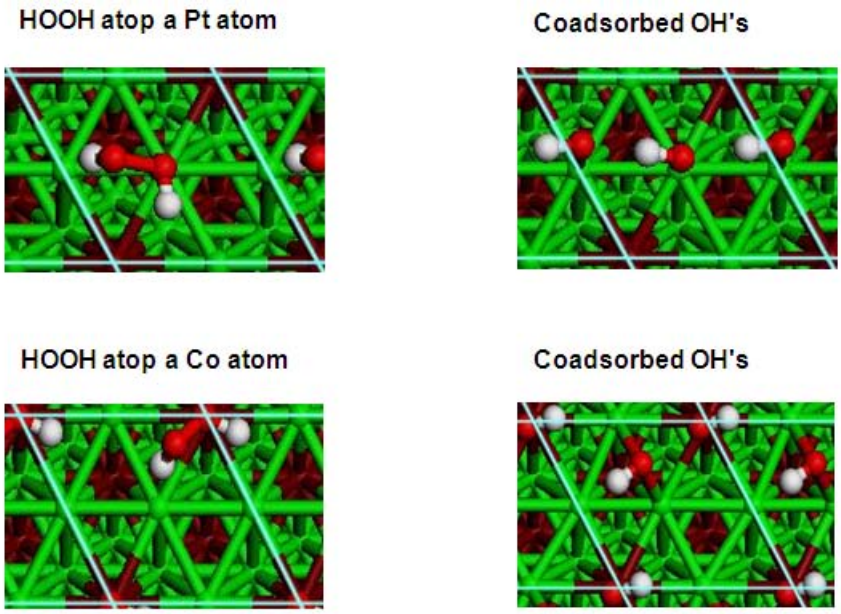

Figure 4.8: Coadsorbed structures of OH's, and the structures HOOH from which the coadsorbed states are derived.

4.5.8.1 Structures of 0.5 ML OH on $Pt_3Co(111)$

From the investigated coadsorption structures which will be used to study the dissociation of HOOH, two different types of coadsorbed configurations are obtained: a coadsorbed configuration with both OH's atop neighbouring Pt atoms, with the H of one OH directed towards the O of the other OH and a O-H approach distance between neighboring OH's of 1.88 Å. A second coadsorbed configuration with one OH atop Co and another OH in site b2 is obtained, with the H of the 2 OH's facing in opposite directions.

4.5.8.2 Coadsorption energies and $\triangle E_{mix}$

The t_{Co} HOOH derived coadsorbed state is less stable than the t_{Pt} site despite having the OH in site t_{Co} and b2 which are stable sites for OH adsorption at 0.25 ML. The source for the less favourable coadsorption energy of the t_{Co} HOOH derived coadsorbed state is likely due to the orientation of the OH's, the H of OH in site b2 is pointing away from the O of OH atop Co. This orientation is likely to destabilise the coadsorbed state of two OH's and not be stabilized by hydrogen bonding as a consequence of the H arrangement.

The $\triangle E_{mix}$ for both coadsorbed configurations is endothermic, indicating that there is a repulsive lateral interaction energy to be overcome to bring the OH's in close proximity to a coverage

of 0.5 ML in the coadsorbed state. The $\triangle E_{mix}$ for the t_{Co} HOOH derived coadsorbed state is slightly more endothermic in part due to the unfavorable orientation of the H of the OH's pointing in opposite directions.

4.5.8.3 Bader analysis for coadsorbed OH at 0.5 ML

Table 4.16 summarizes the calculated charge transferred to coadsorbed OH's, determined using the Bader method of charge partitioning.

Table 4.16: Calculated Bader charge transfer to coadsorbed OH's on the $Pt_3Co(111)$ surface. The values in italics represent the charge transferred to the adsorbates, at 0.25 ML coverage, on the same site they occupy in the coadsorbed configuration.

Dissociating geometry of HOOH	**q_{OH1} (e^-)**		**OH1 site**	**q_{OH2} (e^-)**		**OH2 site**
t_{Co}	0.43	*0.43*	t_{Co}	0.38	*0.42*	b2
t_{Pt}	0.39	*0.41*	t_{Pt}	0.40	*0.41*	t_{Pt}

In both coadsorbed states both OH's gain charge and are thus negatively charged, indicating that a repulsive electrostatic Coulomb interaction will be present due to bringing two negatively charged OH's in close proximity to each other in the coadsorbed state.

The charge transfer to the OH's in the coadsorbed state is the same to within the calculation error in the Bader method, as the charge transfer to OH at 0.25 ML.

4.6 Conclusions

For all the investigated coadsorbed state configurations the calculated $\triangle E_{mix}$ values are positive. This indicates that there is an energy cost associated with bringing the coadsorbates together in a (2×2) surface unit cell, from their most stable adsorption sites at 0.25 ML coverage, in separate (2×2) surface unit cells.

The adsorbates are in general all negatively charged on the surface and thus repulsive Coulomb interactions will be present between the adsorbates in the coadsorbed state. The only exception is H_2O atop Co coadsorbed with O which is positively charged and thus an attractive interaction is expected to be present. Upon coadsorption the density of adsorbates is increased per unit cell and the consequence of the increased coverage is that the lateral interactions between the adsorbates will be stronger. The increase in the repulsive lateral interactions between the adsorbates at the higher coverage in the coadsorbed states, can be linked to the endothermic $\triangle E_{mix}$ values for all the investigated coadsorbed states here. The link is that there is an energy cost to overcome the repulsive lateral interactions between the negatively charged species in close proximity to each other in the coadsorbed state, that is, an energy cost to bring the adsorbates to the coadsorbed state from their lowest energy sites at 0.25 ML.

4.7 List of references

Bader, F. W. 1990. *Atoms in Molecules: A Quantum Theory*. USA: Oxford University Press.

Blöch, P.E. 1994. 'Projector augmented-wave method.' *Physical Review B* 50: 17953-17979.

Ford, D.C., Nilekar, A.U., Xu, Y. and Mavrikakis, M. 2010. 'Partial and complete reduction of O_2 by hydrogen on transition metal surfaces.' *Surface Science* 604: 1565-1575.

Henkelman, G., Arnaldson, A., Jònsson, H. 2006. 'A fast and robust algorithm for Bader decomposition of charge density.' *Computional Materials Science* 36: 354-360.

Kandoi, S., Gokhale, A.A., Grabow, L.C., Dumesic, J.A. and Mavrikakis, M. 2004. 'Why Au and Cu are more selective than Pt for preferential oxidation of CO at low temperature.' *Catalysis Letters* 93: 93-100.

Kresse, G. and Joubert, D. 1999. 'From ultrasoft pseudopotentials to the projector augmented-wave method.' *Physical Review B* 59: 1758-1775.

Kresse, G. and Hafner, J. 1993. '*Ab initio* molecular dynamics for liquid metals.' *Physical Review B* 47: 558-561.

Kresse, G and Furthmüller, J. 2010. '*VASP the guide*.' http : // cms.mpi.univie.ac.at / VASP/ (last accessed 13 December 2011).

Li, H. and Jensen, J.H. 2002. 'Partial hessian vibrational analysis: the localization of the molecular vibrational energy and entropy.' *Theoretical Chemistry Accounts* 107: 211-219.

Methfessel, M. and Paxton, A.T. 1989. 'High precision sampling for Brillouin-zone integration in metals.' *Physical Review B* 40: 3616-3621.

Michaelides, A. and Hu, P. 2001. 'Catalytic water formation on Platinum: A first principles study.' *Journal of American Chemical Society* 123: 4235-4242.

Monkhorst, H.J. and Pack, J.D. (1976). 'Special points for Brillouin-zone integrations'. Physical Review B., 13, pp. 5188-5192.

Neugebauer, J. and Scheffler, M. 1992. 'Adsorbate-substrate and adsorbate-adsorbate interactions of Na and K adlayers on Al(111).' *Physical Review B* 46: 16067-16080.

Perdew, J.P., Chevary, J.A., Vosko, S.H., Jackson, K.A., Pederson, M.R., Singh, D.J. and Fiolhais, C. 1992. 'Atoms, molecules, solids and surfaces : applications of the genaralized gradient approximation for exchange and correlation.' *Physical Review B* 46: 6671-6687.

Press, W.H., Flannery, B.P., Teukolsky, S.A. and Vetterling, W.T. 1986. *em Numerical Recipes*. Cambridge University Press: New York.

Sanville, E., Kenny, S.D., Smith, R. and Henkelman, G. 2007. 'Improved grid-based algorithm for Bader charge allocation.' *Journal of Computational Chemistry* 28: 899-908.

Tang, W., Sanville, E., Henkelman, G. 2009. 'A grid-based Bader analysis algorithm without lattice bias.' *Journal of Physics: Condensed Matter* 21: 084204.

Xu,Y., Ruban, A.V. and Mavrikakis, M. 2004. 'Adsorption and dissociation of O_2 on Pt-Co and Pt-Fe alloys.' *Journal of American Chemical Society* 126: 4717-4725.

Chapter 5

Activation energies of the elementary reaction steps

Introduction

In this chapter the activation energies for the possible elementary reaction steps for the ORR mechanism are determined. The activation energies for the different elementary ORR reaction steps are determined using the coadsorption structures obtained in chapter 4. A brief review of the Climbing Image Nudged Elastic Band (CI-NEB) method used in the present study to determine the activation energies will be presented. The review will first consider the Nudged Elastic Band (NEB) method of locating transition states, on which the CI-NEB method is based.

The review of the NEB and the CI-NEB methods for locating the transition state is based on the following references: Henkelman et al. (2000), Henkelman and Jónsson (2000) and Henkelman (2001).

The NEB method is an efficient method for finding the minimum energy path (MEP) between an initial state and a final state (Mills et al. 1995). The NEB method can be used to determine the reaction path between a known initial state and a known final state. The MEP is determined by setting up a set of replicas (images) of the system between the two minima, i.e. the known initial and final states. The number of images typically ranges between 4 to 20 images between the initial and final states. The images are connected by a spring interaction to ensure continuity of the path.

Each image on the band feels forces due to the spring force and forces due to the potential. The optimization of the band involves minimization of the forces acting on the images which brings the images of the band to the MEP in the NEB method. The total force acting on an image is the sum of the spring force along the tangent to the path and the true force perpendicular to the tangent to the path. An essential feature of the NEB method which distinguishes it from other elastic methods (Gilhan and Wilson, 1992; Czerminski and Elber, 1990; Elber and Karplus, 1987) is the force projection or nudging which ensures the spring forces do not interfere with the convergence of the elastic band to the MEP, and the true force does not affect the distribution of images along the MEP. In the NEB method, the force which is optimised is the component of the true force (due to the potential surface) perpendicular to the tangent of the path, and the spring force parallel to the tangent of the path. The projection of the forces is referred to as nudging.

During NEB calculations the tangent to the path at each image and every iteration during the optimization is required. This is to allow for the decomposition of the true force and the spring force into components parallel and perpendicular to the path. In optimization calculations of the NEB only the parallel component of the spring force and the perpendicular component of the true force are the forces included. The spring force acts along the band to maintain constant spacing between the images, the potential or true forces are allowed to act in all directions perpendicular to the band to ensure that the band comes to rest on the MEP between the two minima.

In NEB calculations the activation energy is estimated from the maximum on the MEP for transitions between the initial and the final states within the harmonic transition state theory (hTST) approximation. A maximum along the MEP is a first order saddle point on the potential energy surface, and the energy of the highest saddle point is used to determine the activation energy. A first order saddle point is a point on a potential energy surface at which the forces are zero and at which there is one negative curvature or unstable mode in the Hessian matrix. The downfall of the NEB method is that it may not find the exact saddle point along the path, and interpolation is often employed to locate the saddle point.

The CI-NEB method is a slight modification to the NEB method. In the CI-NEB method, the image with the highest energy is identified and moved right to the saddle point. In the CI-NEB method the highest energy image is freed of the spring force so that it can move exactly to the saddle point. The highest energy image feels the full force due to the potential with the component along the elastic band inverted. So long as the CI-NEB method converges, the climbing image will converge to the saddle point.

There is no additional computational cost incurred in switching one of the images into a climbing image since all images are relaxed simultaneously. Since the climbing image is not affected by the spring forces, the spacing of the images will be different on each side of the climbing image.

5.1 Computational method

DFT spin-polarised periodic calculations were performed using the plane wave code VASP (Kresse et al. 1993). The PW91 functional (Perdew et al. 1992) was utilized to describe the exchange and correlation energy terms. Projector augmented wave (PAW) pseudopotentials (Kresse and Joubert, 1999; Blöch, 1994) were used to describe the electron-ion interactions. The plane wave basis set cut-off energy was set to 400 eV. The Brillouin zone was sampled using the Monkhorst-Pack scheme (Monkhorst and Pack, 1976**)** with a k-point mesh of (12 $\times$ 12 $\times$ 1). To correct for the electron redistribution at the Fermi level the method of Methfessel-Paxton (Methfessel and Paxton, 1989) was used with a smearing width of σ = 0.2 eV.

The Pt_3Co alloy was represented by a 4 layer slab with 4 atoms per layer. The top two slab layers and the adsorbates were allowed to relax to their lowest energy values, whilst the bottom two layers were fixed at their bulk optimised positions. A vacuum gap of 13 Å was utilized in the calculations. The calculations were performed in a (2 $\times$ 2) surface unit cell. The adsorption of the species was studied on only one side of the slab with the corresponding resulting electrostatic interactions corrected for using the dipole correction (Neugebauer and Scheffler, 1992) as implemented in the VASP code.

The minimum energy paths were calculated using the CI-NEB method (Henkelman et al. 2000). Some reaction pathways were investigated using 8 images of the system, whilst for other reaction pathways 4 images of the system were used between the fixed end points. The highest point along the minimum energy path provides an initial transition state structure for the chosen reaction path. The transition state structure was identified as the highest energy image with total forces less than 0.10 eV $Å^{-1}$. The energy convergence criterion for the electronic relaxation steps was energy changes below 1$\times$ 10^{-5} eV. A Quasi-Newton optimization was then performed on the identified transition state structure to further refine the forces on the structure. The force convergence criterion for the Quasi-Newton optimization was forces below 0.01eV $Å^{-1}$.

The transition state structure was confirmed to be a first order saddle point by performing a partial Hessian vibrational analysis (Li and Jensen, 2002) on the refined transition state structure. For the partial Hessian vibrational analysis, only the adsorbate atoms are allowed to move while the atoms of the slab are not allowed to move. Perturbations of 0.02 Å in the Cartesian space were used to calculate the Hessian matrix. Presence of a single imaginary vibrational frequency for the identified transition state image is confirmation of the transition state.

The activation energy is calculated as the difference in energy between the energy of the optimised state from the Quasi-Newton refinement of the highest energy image determined from

the CI-NEB calculation, and the energy of the initial state (coadsorbed reactant state for formation reactions and the dissociating molecule for dissociation reactions). For the overall activation barriers the activation energy is determined by calculating the energy difference between the optimised transition state from the Quasi-Newton refinement of the highest energy image obtained from the CI-NEB calculation, and the energy of the non-interacting adsorbed state of the reactants in their lowest energy sites at 0.25 ML, for the formation reactions. For the dissociation reactions, the energy of the most stable configuration for the dissociating species is used to determine the overall energy barrier. The zero point energy (ZPE) corrected activation energies are determined by adding the ZPE corrections to the reactant state and the transition state excluding the imaginary frequency and then calculating the energy difference between the transition state and the reactant state. All the presented activation barriers in this chapter include the ZPE corrections. The calculated frequencies for the transition state structures are presented in appendix D.

For the formation reaction steps the direct activation is defined as:

$$E_{act}^{coads} = E_{TS} - E_{react-coads} \tag{5.1}$$

where E_{act}^{coads} is the direct activation energy, E_{TS} is the energy of the transition state and $E_{react-coads}$ is the energy of the reactants in the coadsorbed state.

The overall activation energy for formation reaction steps is defined as:

$$E_{act}^{inf..sep.} = E_{TS} - E_{react-non-interating} \tag{5.2}$$

where $E_{act}^{inf.sep.}$ is the overall activation energy, E_{TS} is the energy of the transition state and $E_{react-non-interacting}$ is the energy of the reactants in their lowest energy site at 0.25 ML in the non-interacting state (i.e. not coadsorbed).

For dissociation reactions the direct activation energy is defined as:

$$E_{act}^{dir.} = E_{TS} - E_{react-site} \tag{5.3}$$

where $E_{act}^{dir.}$ is the direct dissociation activation energy, E_{TS} is the energy of the transition state and $E_{react-site}$ is the energy of the dissociating reactant at the site of dissociation.

The overall dissociation activation energy is defined as:

$$E_{act}^{ovr.} = E_{TS} - E_{react-low} \tag{5.4}$$

where $E_{TS}^{ovr.}$ is the overall dissociation activation energy, E_{TS} is the energy of the transition state and $E_{react-low}$ is the energy of the dissociating reactant at its lowest energy site at 0.25 ML.

For formation and dissociation reaction steps, $\triangle E_{rxn}$ is defined as:

$$\triangle E_{rxn} = (E_{prd,1} + E_{prd,2} + ...) - (E_{react,1} + E_{react,2} + ...) \tag{5.5}$$

For formation reaction steps $E_{prd,1}$, $E_{prd,2}$ are the energy of the products at the site at which they are formed at and $E_{react,1}$, $E_{react,2}$ are the energy of the reactants in their lowest energy sites at 0.25 ML in the non-interacting state (i.e. the separate state not the coadsorbed state).

For dissociation reaction steps $E_{prd,1}$, $E_{prd,2}$ are the energy of the dissociation products at the coadsorbed state and $E_{react,1}$, $E_{react,2}$ are the energy of the dissociating reactants in their lowest energy sites at 0.25 ML.

The activation energies on Pt(111) were calculated using the transition state structures obtained in the study by Madala(2012). In the study by Madala(2012) the PBE functional was used. Calculated activation energies can vary with the functional used hence the need to calculate the activation energies using the PW91 functional for Pt(111) in the present study. The optimised transition state structures obtained with the PBE functional were re-optimised using the PW91 functional for the present study using the same convergence criteria for the forces and energy as those used on $Pt_3Co(111)$ in the present study. The same calculation settings, e.g. k-points, basis set cut-off energy and the PW91 optimised lattice parameter for Pt as those used for the adsorption calculations on Pt(111) presented in chapter 3 were used.

5.2 Results and discussion

5.2.1 O_2 dissociation

Table 5.1 summarizes the calculated activation energies for the O_2 dissociation pathways investigated in the present study.

Table 5.1: O-O stretching frequencies and bond length of the dissociating O_2 species, and the activation energies, the O-O bond length of the transition state structure and the heat of reaction for the dissociation reaction calculated on the $Pt_3Co(111)$ surface.

Configuration	ν_{O-O}**(cm** $^{-1}$**)**	**O-O (Å)**	$E_{act}^{dir.}$**(eV)**	$E_{act}^{ovr.}$**(eV)**	**O-O**$_{TS}$ **(Å)**	$\triangle$**E**$_{rxn}$ **(eV)**
b2_f$_{Pt}$_t$_{Co}$	713	1.43	0.08	0.08	1.78	-0.49
b1_f$_{Pt}$_b1	709	1.46	0.08	0.16	1.71	-1.25
b1_h$_{Pt}$_t$_{Pt}$	782	1.42	0.00	0.09	1.76	-1.80
b3_h$_{Pt}$_t$_{Co}$	777	1.40	0.17	0.39	1.74	-0.50
b2_h$_{Co}$_t$_{Pt}$	829	1.40	0.45	0.79	1.89	-1.80

Figure 5.1 indicates the initial state of the dissociating O_2 molecules, the transition state structures and the dissociation products for the O_2 configurations investigated in the present study.

The transition state structures for O_2 dissociation on the $Pt_3Co(111)$ surface are geometrically similar to those obtained on the Pt(111) surface. The only exception is the transition state structure for O_2 dissociating from configuration b1_f$_{Pt}$_b1. The O_2 dissociation transition state structure calculated on the Pt(111) surface in the present study and by Ford et al. (2010), Xu et al. (2004) and Eichler et al. (2000) are structures of the top-fcc-bridge type, with one O atop a Pt atom and the other O on the bridge site, with the stretched O-O bond across the 3-fold-hollow fcc site.

The transition state structure obtained for O_2 dissociating from the b1_h$_{Pt}$_t$_{Pt}$ orientation is unlikely to be directly connected to the starting orientation, since it would require O_2 to diffuse or rotate through the lowest energy site (i.e. site b1) from a less stable orientation (i.e. b1_h$_{Pt}$_t$_{Pt}$). The obtained transition state is symmetrically equivalent to that obtained for O_2 dissociating at b2_f$_{Pt}$_t$_{Co}$.

The direct and overall activation energies for O_2 dissociating from the f$_{Pt}$ sites are lower than for the h$_{Pt}$ site, excluding O_2 dissociation from the b1_h$_{Pt}$_t$_{Pt}$ orientation whose transition state structure was calculated to be over the f$_{Pt}$ site.

The direct and overall activation energy for O_2 dissociating from the h$_{Co}$ site is higher than the direct and overall O_2 dissociation activation energy for the f$_{Pt}$ and h$_{Pt}$ sites. O_2 dissociating at the h$_{Co}$ site from the b2_h$_{Co}$_t$_{Pt}$ orientation results in a transition state structure with O_2 not bonded directly to a surface Co atom. The subsurface Co at the h$_{Co}$ site appears to lead to higher direct and overall activation energies for O_2 dissociation, since the calculated overall and direct activation energies for O_2 dissociation from sites where there is a surface Co atom present and which access transition states bonded to a surface Co atom have lower direct and overall activation energies.

The difference between the direct and overall activation energies is a measure of the relative stabilities of the O_2 species relative to the lowest energy O_2 structure on $Pt_3Co(111)$ indicating the energy difference between the adsorption energy of O_2 at the site of dissociation and adsorption energy of O_2 at the lowest energy site.

The direct and overall activation energies for O_2 dissociation calculated for the various configurations on $Pt_3Co(111)$ are lower than the direct and overall activation energy of 0.59 eV calculated on the Pt(111) surface in the present study. The only exception is for configuration b2_h$_{Co}$_t$_{Pt}$, for which the overall activation energy is 0.79 eV. On $Pt_3Co(111)$ O_2 dissociation is more facile with an activation energy of 0.08 eV compared to 0.59 eV on Pt(111).Therefore,

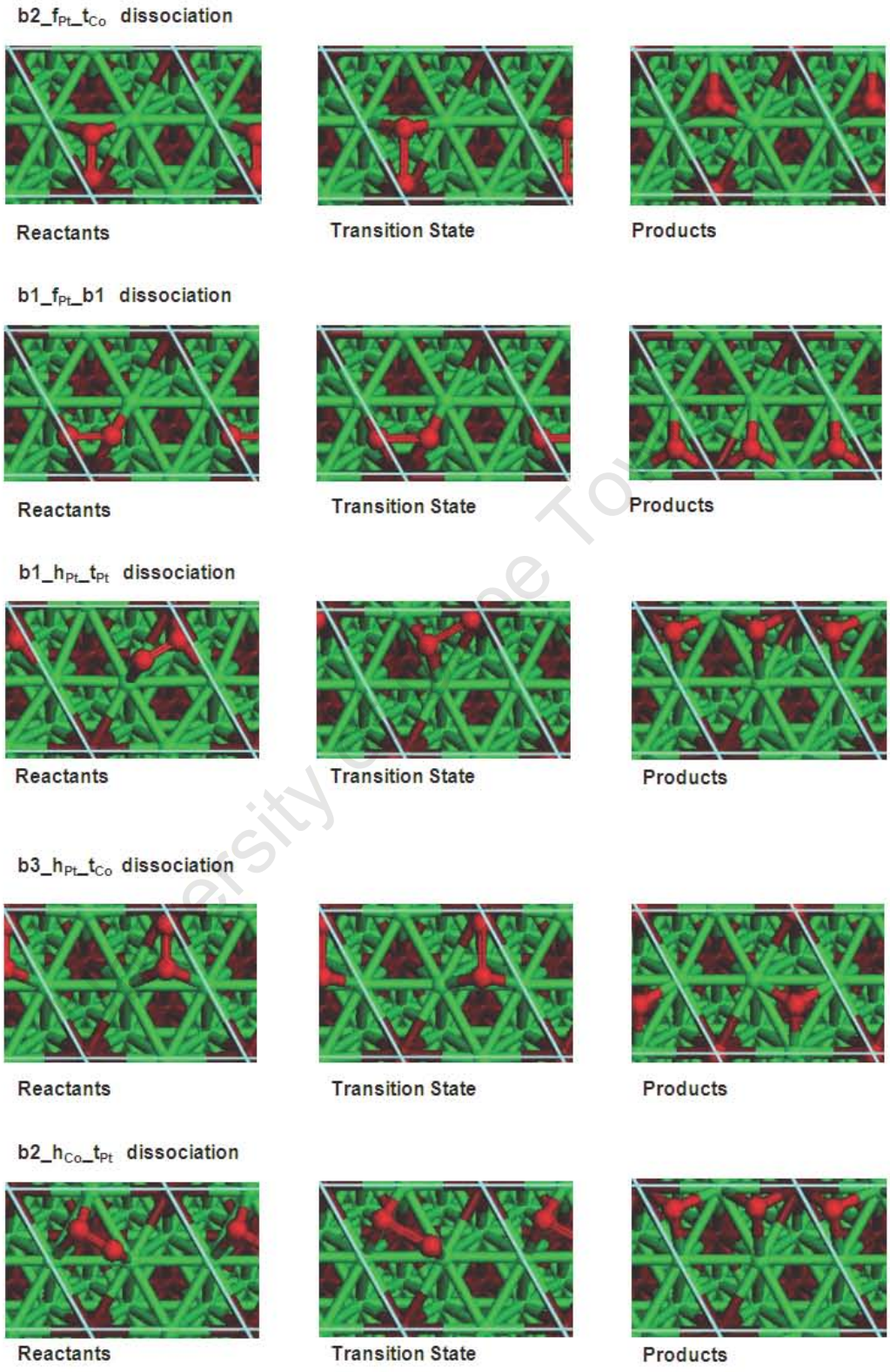

Figure 5.1: Structures of the reactants, transition state structures and the final dissociation products for the dissociation reaction of O_2 on $Pt_3Co(111)$

on the $Pt_3Co(111)$ surface alternative O_2 dissociation pathways exists with lower activation energies than on Pt(111).

Plots of the activation energy for O_2 dissociation E_{act} as a function of the O-O stretching frequency and the dissociative adsorption energy of O_2 ($\triangle$ E) for reaction pathways which access the top-fcc/hcp-bridge type of transition states were made to investigate if there is a relation between the two variables. The O_2 dissociation pathways used to make the plots are for configurations b2_f_{Pt}_t_{Co} , b3_h_{Pt}_t_{Co} and b2_h_{Co}_t_{Pt}. The activation energy for O_2 dissociation (E_{act}) and the dissociative adsorption energy of O_2 used for the plots in Figures 5.2 and 5.3 is defined in the same way as was done for N_2 dissociation on different transition metal surfaces by Logadottir et al. (2001) to investigate if a linear relation exists between the activation energy for N_2 and the dissociative adsorption energy of N_2. The activation energy for dissociation and the dissociative adsorption energy of O_2 are calculated relative to gas phase O_2 hence why negative activation energies for O_2 dissociation are obtained in Figures 5.2 and 5.3. The activation energy for dissociation is calculated from:

$$E_{act} = E_{TS} - E_{gas-phase-O2} - E_{cleanslab} \tag{5.6}$$

where E_{act} is the activation energy for O_2 dissociation, E_{TS} is the energy for the transition state, $E_{gas-phase-O2}$ is the energy of O_2 in the gas phase and $E_{cleanslab}$ is the energy of the clean $Pt_3Co(111)$ slab without any adsorbate. The dissociative adsorption energy of O_2 is calculated from:

$$\triangle E = E_{2O's} - E_{gas-phase-O2} - E_{cleanslab} \tag{5.7}$$

where $\triangle E$ is the dissociative adsorption energy of O_2, $E_{2O's}$ is the energy of the coadsorbed product state of two O's and $E_{cleanslab}$ is the energy of the clean $Pt_3Co(111)$ slab without any adsorbate.

From Figure 5.2 it is observed that there is seemingly a linear relation between the activation energy for O_2 dissociation and the O-O stretching frequency. Higher O-O stretching frequencies correspond to higher activation energies for O_2 dissociation. More data points are required which would confirm if indeed a linear relation exists.

From Figure 5.3 it is observed that there is no apparent linear relation between the activation energy for O_2 dissociation and the dissociative adsorption energy of O_2. More data points would be required to establish whether a linear relation exists or not.

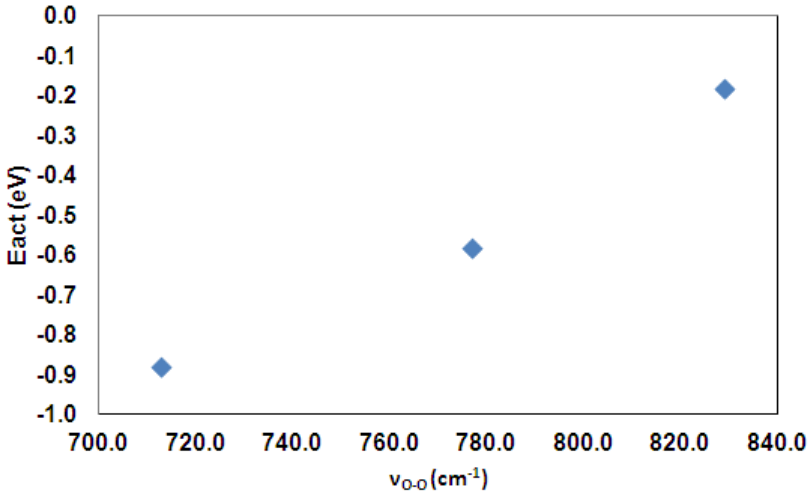

Figure 5.2: Plot of the activation energy for O_2 dissociation against the O-O stretching frequency, for O_2 dissociation on the $Pt_3Co(111)$ surface.

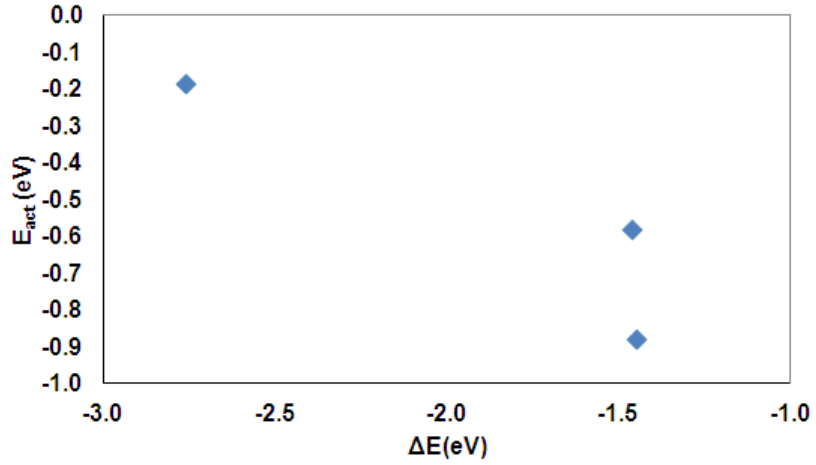

Figure 5.3: Plot of activation energy for O_2 dissociation against the dissociative heat of adsorption of O_2.

From the results presented in Table 5.1 it is observed that the heat of reaction for the dissociation of O_2 resulting in a product with O atop Co and the other O on a 3-fold-hollow site over a Co atom, i.e. h_{Co} or f_{Co} are the least exothermic. The heat of reaction for these reaction pathways are least exothermic partly due to O occupying either the f_{Co} or h_{Co} sites which are less stable sites for O at 0.25 ML and also due to O bonded atop Co. O bonded atop Co was identified not to be a stable adsorption site for O at 0.25 ML. On Pt(111) the reaction energy for the lowest energy reaction pathway for O_2 dissociation is -0.42 eV in the present study. The overall reaction energy for O_2 dissociation on $Pt_3Co(111)$ resulting in the product state of two non-interacting O's at the f_{Pt} site is -2.23 eV whilst the overall reaction energy on Pt(111) resulting in the product state of two non-interacting O's at the fcc site is -1.53 eV.

5.2.2 OOH formation

Table 5.2 summarizes the activation energies and structural parameters characterizing the OOH formation pathways investigated in the present study.

Table 5.2: Calculated activation energies, the O-O bond lengths and the O-H bond lengths of the transition state structures, and the heat of reaction calculated on the $Pt_3Co(111)$ surface.

Product site	E_{act}^{coads}(eV)	$E_{act}^{inf.sep}$(eV)	O-O_{TS} (Å)	O-H_{TS} (Å)	$\triangle E_{rxn}$(eV)
b1	0.23	0.56	1.41	1.48	0.08
b2	0.30	0.75	1.39	1.50	0.25
b3	0.39	0.94	1.42	1.44	0.35

Figure 5.4 illustrates the geometries for the reactants, transition state structure and product structures for investigated reaction pathways for the reaction of atomic H and O_2 to form OOH.

The transition state structure obtained on the $Pt_3Co(111)$ surface in the present study, is similar to the transition state structure on the Pt(111) surface reported by Madala(2012) and Ford et al. (2010), with O_2 on the bridge site and H atop Pt in a tilted direction towards O_2 at the transition state.

The difference in energy between the activation energy calculated relative to the coadsorbed state and the energy relative to O_2 and H separately adsorbed, in their lowest energy sites at

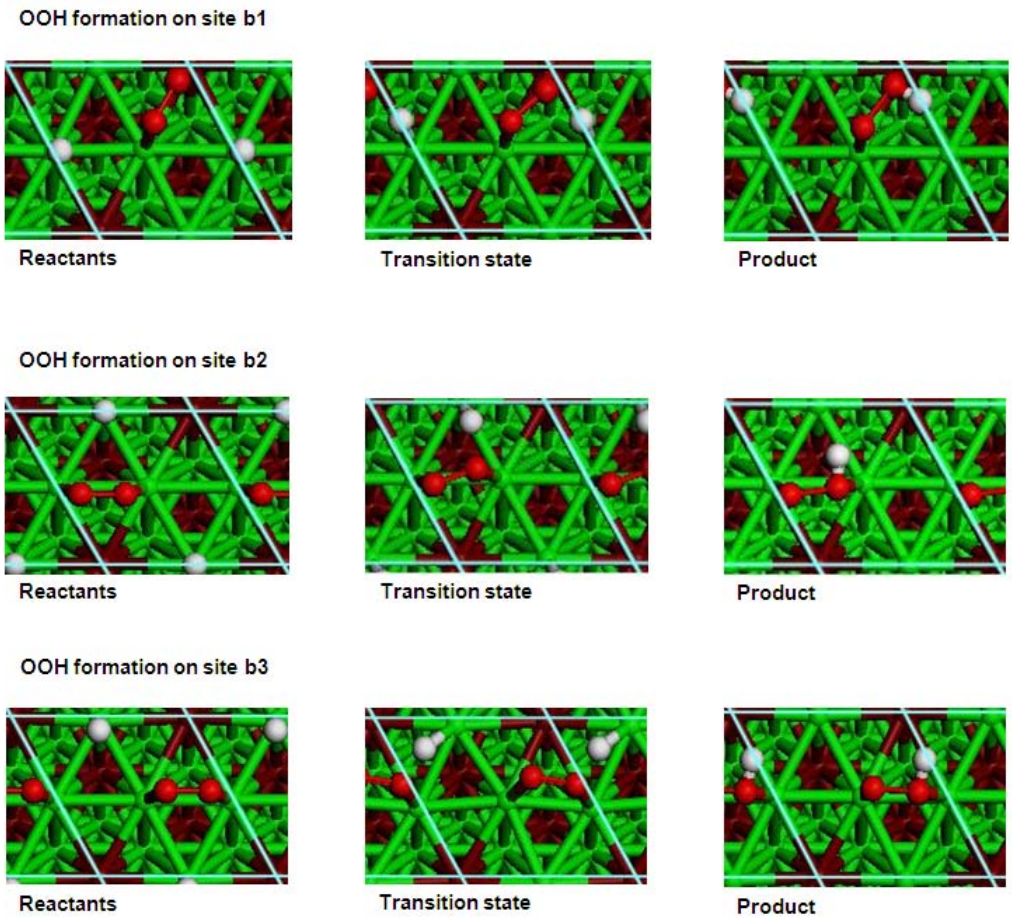

Figure 5.4: Structures for the reactants, transition state and the products for OOH formation from atomic H and O_2 to form on $Pt_3Co(111)$.

0.25 ML, indicates that the coadsorbed states are higher in energy relative to the separated state of O_2 and H as discussed in chapter 4.

The overall activation energies for OOH formation, investigated in the present study, follow the trend b3 > b2 > b1. The pathway forming OOH on site b1 proceeds with the lowest activation energy. This can be linked to the fact that the transition state structure involves bonding to a surface Co atom, and from the adsorption of the ORR intermediates as discussed in chapter 3, it was established that adsorbates coordinated to a surface Co atom are stabilized relative to those not bonded to a surface Co atom. The transition state structures for the formation of OOH on site b2 and b3 do not involve direct bonding to a surface Co atom hence the calculated overall and direct activation energies are higher than that for b1 where the transition state structure is bonded to a surface Co atom. The calculated direct activation energy for the lowest energy pathway for the formation of OOH on the Pt(111) surface is 0.26 eV, the calculated direct activation energy on the Pt(111) surface is 0.03 eV higher than the calculated direct activation energy on the $Pt_3Co(111)$ surface. However, the calculated overall activation energy for the lowest energy pathway for the formation OOH on the $Pt_3Co(111)$ surface is 0.04 eV higher than the calculated overall activation energy on the Pt(111) surface which is 0.52 eV. Therefore, there is a higher lateral repulsive energy which needs to be overcome in order to coadsorb O_2 and H prior to reaction on the $Pt_3Co(111)$ surface than on the Pt(111) surface, which results in a higher overall activation energy for the reaction on the $Pt_3Co(111)$ surface.

The $\triangle E_{rxn}$ for the formation of OOH on b1 is the least endothermic compared to the formation of OOH on site b2 and b3, as can be seen in Table 5.2. OOH is stabilised on site b1 relative to site b2 and b3 hence the low endothermic heat of reaction for the formation of OOH on site

b1 relative to formation on sites b2 and b3. On Pt(111) the reaction energy for OOH formation for the lowest energy reaction pathway is calculated to be -0.17 eV in the present study. On $Pt_3Co(111)$ the heat of reaction for OOH formation is endothermic.

5.2.3 OOH dissociation

Table 5.3 summarizes the activation energies and structural parameters characterizing the OOH dissociation pathways investigated in the present study.

Table 5.3: O-O stretching frequencies and the O-O bond lengths of the dissociating OOH species, the calculated activation energies, the O-O bond lengths of the transition state structures, and the heat of reaction for the dissociation calculated on the $Pt_3Co(111)$ surface.

Reactant site	ν_{O-O}**(cm** $^{-1}$**)**	**O-O (Å)**	$E_{act}^{dir.}$**(eV)**	$E_{act}^{ovr.}$**(eV)**	**O-O**$_{TS}$ **(Å)**	$\triangle$**E**$_{rxn}$
b1	636	1.51	0.05	0.05	1.69	-1.67
b2	698	1.49	0.00	0.17	1.70	-1.59
b3	758	1.47	0.21	0.48	1.79	-0.58

Figure 5.5 indicates the initial states of a dissociating OOH molecule, the transition state structures and the dissociation products for the dissociation pathways of OOH investigated in the present study.

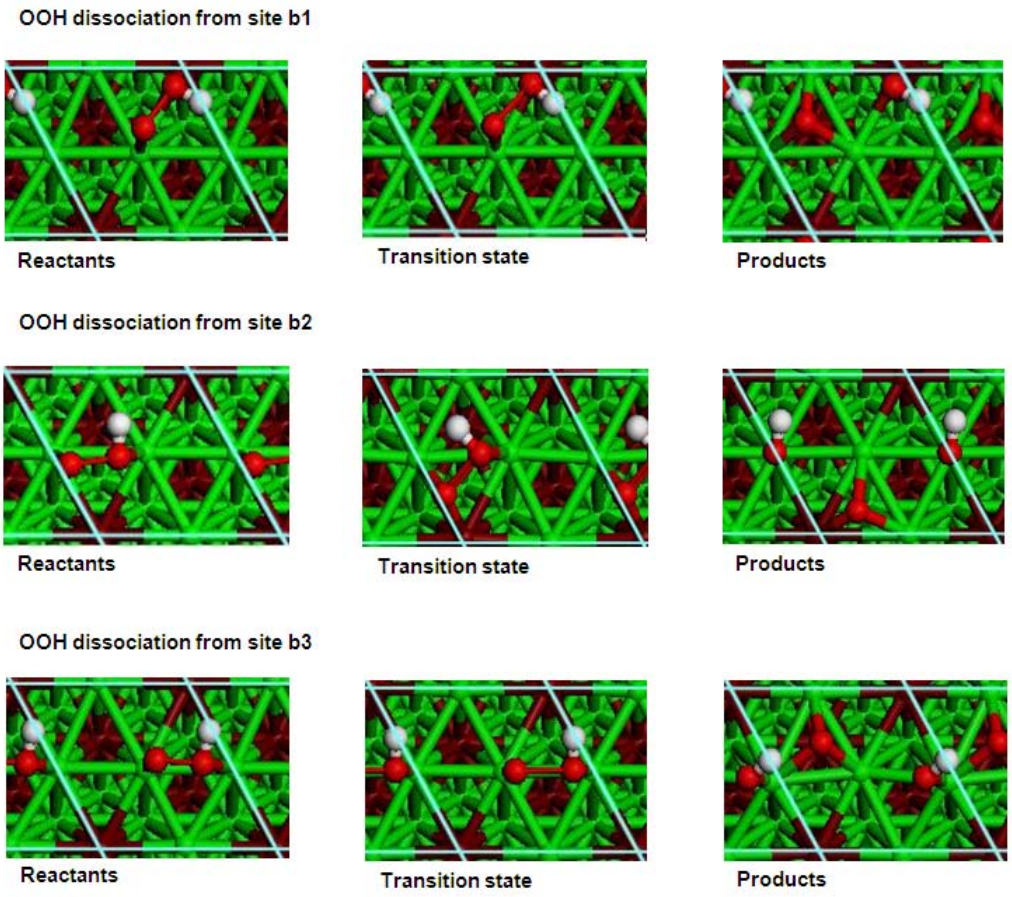

Figure 5.5: Structures of the reactant, transition state and the products for the dissociation pathways of OOH on $Pt_3Co(111)$

The transition state structures for OOH dissociation at sites b1 and b3 are similar to the transition states reported for OOH dissociation on the Pt(111) surface. In the study by Ford et al. (2010) and the present study the transition state has OH atop a Pt atom and O is also atop a Pt atom with the O-O bond aligned along the bridge site. However, the transition state structure for OOH dissociation at site b2 on $Pt_3Co(111)$ is different to that obtained on the Pt(111) surface, but similar to that reported by Ford et al. (2010) for OOH dissociation on a Ag(111) surface, in which OH is atop Pt with O on the bridge site and the O-O bond across the 3-fold-hollow hcp site.

The direct dissociation of OOH from site b2 is barrierless which can be explained by examining the transition state structure. The transition state structure has O-O bond over the f_{Pt} site. For O_2 dissociation on $Pt_3Co(111)$, it was observed that dissociation at the f_{Pt} site is characterised by a low direct activation energy of 0.08 eV as presented in Table 5.1. However, the overall activation energy for dissociating OOH at the b2 site is higher than that of the b1 site, for which the overall activation energy is 0.05 eV.

The transition state structures for OOH dissociating at sites b1 and b2 are bonded to a surface Co atom, whereas that for OOH dissociating at b3 does not involve bonding to a surface Co atom. Therefore, the lower direct and overall dissociation activation energies at sites b1 and b2 can be linked to the surface Co atom stabilizing the energy of the transition state structures.

From the investigated dissociation pathways of OOH, it is observed that the pathway for OOH dissociation at the b1 site proceeds with a lower direct and overall activation energy of 0.05 eV compared to 0.11 eV calculated on the Pt(111) surface in the present study and 0.16 eV reported by Ford et al. (2010). The dissociation pathways from the b2 and b3 sites have higher overall activation energies than on the Pt(111) surface, with overall activation energies of 0.17 eV and 0.48 eV respectively.

For the dissociation of OOH the correlation between the O-O stretching frequency of the dissociation OOH species and the activation energy for dissociation cannot be established based on the results of the present study on $Pt_3Co(111)$ since only two data points are available where the transition state geometries are of the same type. The transition state geometries are of the same type for OOH dissociation at the sites b1 and b3. Similarly, a correlation cannot be reliably established between the $\triangle E_{rxn}$ and the activation energies.

From the heat of reaction for OOH dissociation results presented in Table 5.3 it is observed that the heat of reaction for the dissociation of OOH at sites b1 and b2 is more exothermic than that for OOH dissociation at site b3. The heats of reaction at sites b1 and b2 are more exothermic since the dissociation products are bonded to a surface Co atom whereas for dissociation at site b3 the products are not bonded to a surface Co atom. Dissociation at site b1 is more exothermic than at site b2 because for b1 both O and OH are bonded to surface Co atoms whereas for b2 only O is bonded to a surface Co atom. On Pt(111) the heat of reaction for OOH dissociation for the lowest energy reaction pathway is -1.56 eV.

5.2.4 Hydrogenation of atomic O to form OH

Table 5.4 summarizes the activation energies and structural parameters characterizing the OH formation pathways from O hydrogenation investigated in the present study.

Table 5.4: Activation energies, the O-H bond lengths of the transition state structures, and the heat of reaction for OH formation calculated on the $Pt_3Co(111)$ surface

Product site	E_{act}^{coads}**(eV)**	$E_{act}^{inf.sep}$**(eV)**	**O-H**$_{TS}$ **(Å)**	$\triangle$**E**$_{rxn}$**(eV)**
b1	0.66	0.86	1.46	0.06
b2	1.00	1.16	1.48	0.26
b3-a	1.11	1.57	1.51	0.33
t_{Pt}	0.68	0.87	1.47	0.42
b3-b	0.96	2.03	1.62	0.55

Figure 5.6 illustrates the geometries for the reactants, transition state structure and the product for investigated reaction pathways for the reaction of atomic O and atomic H to form OH.

The transition state structures for OH formation obtained on the $Pt_3Co(111)$ surface are identical to the transition state structures previously reported on the Pt(111) surface. Ford et al. (2010) and Kandoi et al. (2004) reported a transition state structure on the Pt(111) surface with O in a bridge site and H on the top site tilted towards the O. The same transition state structure is obtained on the Pt(111) surface for the present study. The transition state structure for OH formation on site b2 is similar to the structures reported by Kandoi et al. (2004), for OH formation on the Cu(111) and Au(111) surfaces. On Cu(111) and Au(111) surfaces O is in a 3-fold-hollow fcc site and H on a bridge site, while for the formation of OH in b2 on $Pt_3Co(111)$ O is on the f_{Pt} site with H in a top configuration tilted towards O.

The transition state structure for OH formation on site b1 and atop Pt on $Pt_3Co(111)$ are identical. OH on site b1 is adsorbed stronger than atop Pt by 0.36 eV, hence the transition state structure is more likely to be connected to OH on site b1 than OH atop Pt.

The direct activation energy for OH formation on site b1 is the lowest relative to the direct activation energy for OH formation on sites b2 and b3. The direct activation energy for OH formation on site b1 is 0.34 eV lower than OH formation on site b2, 0.45 eV lower than OH formation in site b3 for configuration b3-a and 0.30 eV lower than the activation energy for OH formation in configuration b3-b. The overall activation energy for OH formation on site b1 is the lowest on the $Pt_3Co(111)$ surface with an overall activation energy of 0.86 eV. The trend for the overall activation energies for the formation of OH is similar to the direct activation energy trend except that b3-a and b3-b have exchanged positions. OH in site b1 is directly bonded to a surface Co atom whereas OH in sites b2 and b3 is not directly bonded to a surface Co atom hence pathways forming OH bonded to a surface Co atom occur through lower direct and overall activation energies than pathways for OH formation in sites where OH is not bonded to a surface Co atom.

The activation energies for OH formation on bridge site b3, referenced to O and H separately adsorbed in their lowest energy sites at 0.25 ML, indicates that OH formation in site b3 has the highest activation energies. The overall activation energies for configuration b3-a, b3-b and b2 are higher than that on the Pt(111) surface calculated in the present study which is an overall activation energy of 0.95 eV. The difference between the activation energy for OH formation on b3-b, calculated relative to the coadsorbed state, and that calculated relative to separately adsorbed O and H in their lowest energy sites at 0.25 ML, indicates that there is a repulsive interaction of 1.07 eV which must be overcome to bring O and H from their lowest energy sites at 0.25 ML to the coadsorbed state prior to reaction.

The difference between the overall and the direct activation energies for OH formation are due to the mixing energy needed to coadsorb the reactants prior to reaction as presented in chapter 4.

On the Pt(111) surface the direct activation energy for OH formation for the lowest energy pathway is calculated to be 0.73 eV in the present study and 0.72 eV by Ford et al. (2010)(PW91 functional). The overall activation energy in the present study is calculated as 0.95 eV on the Pt(111) surface and 0.83 eV by Ford et al. (2010). On $Pt_3Co(111)$ the lowest energy pathway for OH formation occurs with a lower direct activation energy of 0.66 eV and an overall activation energy of 0.86 eV. Thus on $Pt_3Co(111)$ the overall activation energy for OH formation is approximately 0.10 eV lower than on the Pt(111) surface.

OH formation on $Pt_3Co(111)$ is endothermic as can be seen from the calculated heat of reaction $\triangle E_{rxn}$ in Table 5.4 for the different pathways. The reaction energy for OH formation on site b1 is the least endothermic compared to OH formation on sites b2, b3 and atop Pt. The reason for the low endothermicity for OH formation in site b1 is due to the stronger adsorption strength of OH in site b1 compared to OH adsorption in sites b2,b3 and atop Pt. On Pt(111) the heat of reaction for the lowest energy reaction pathway is -0.50 eV. On $Pt_3Co(111)$ the heat of formation of OH is endothermic

Plots of the activation energy of OH formation as a function of the adsorption energy of OH were made to investigate if a linear relation exists between the activation energy of OH formation and the adsorption energy of OH. The plots were made using the data for the OH pathways which

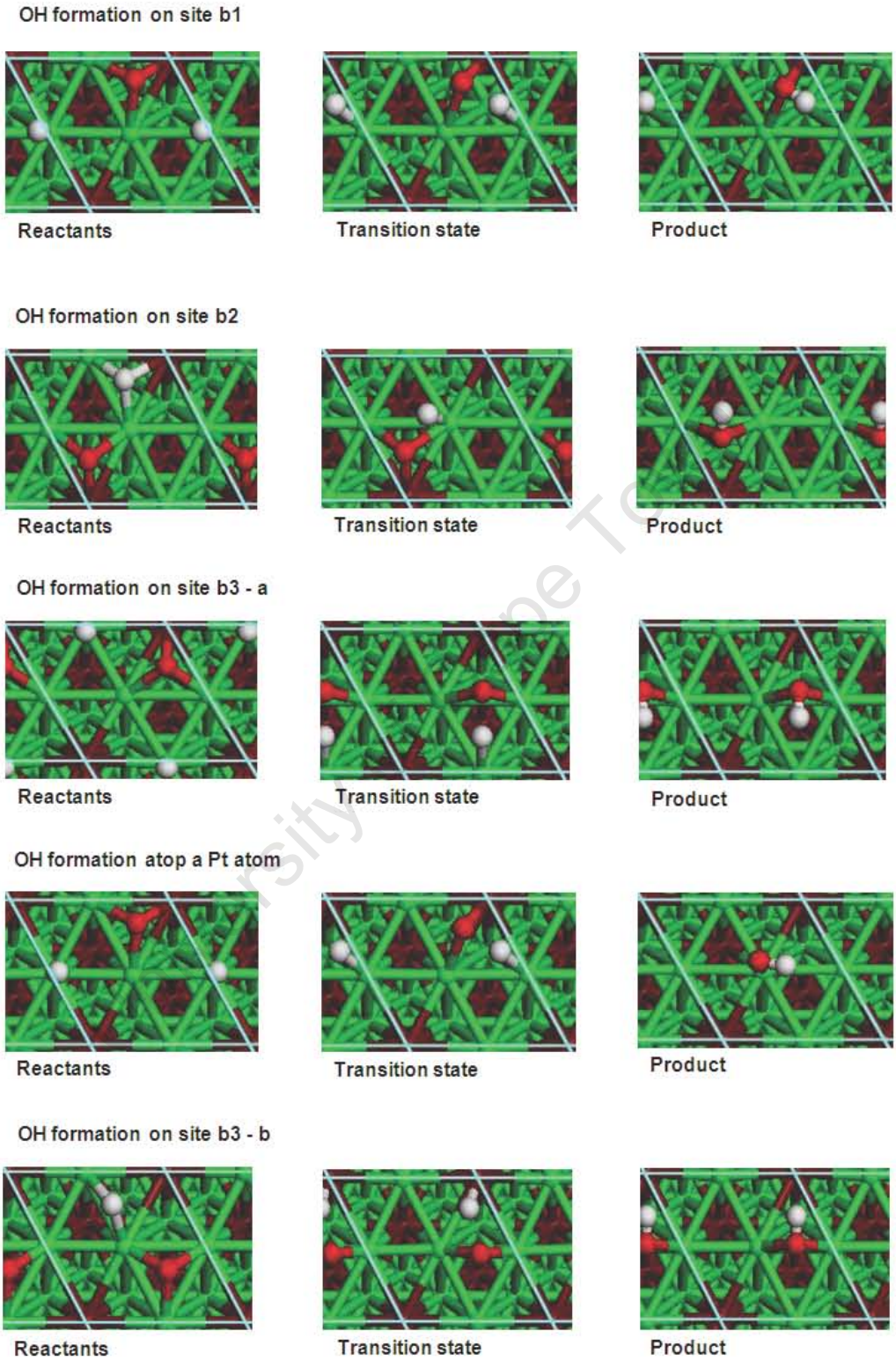

Figure 5.6: Structures for the reactant, transition state and products for the reaction pathway forming OH from the reaction of O and H on Pt_3 Co(111)

accessed the same type of transition state structure with O in the bridge site and H atop Pt tilted towards OH, the OH pathways accessing this type of transition state structures are b1, b3-a and b3-b.

From the plots in Figures 5.7 and 5.8 it is observed that no conclusion can be drawn concerning the linearity of the relation between the activation energy of OH formation and the adsorption energy of OH. In Figure 5.7 the activation energy of OH formation and the adsorption energy of OH are calculated relative to gas phase O_2 and H_2 whereas in Figure 5.8 the activation energy and the adsorption energy of OH are referenced to gas phase H_2O, with water adsorbing dissociatively to form adsorbed OH and H. The trend between E_{act} and $\triangle E$ is the same in Figures 5.7 and 5.8. More data points would be required to assess whether there indeed no linear relation between E_{act} and $\triangle E$ for OH formation.

The activation energy and the adsorption energy of OH were referenced to gas phase H_2O so as to follow the definition used by Michaelides et al. (2003) for studying the Brønsted-Evans-Polanyi relation for reaction steps involving the OH_x species. The calculations for the activation energy for OH formation and the adsorption energy of OH referenced to H_2 and O_2 in the gas phase were performed in order to make a comparison between the cases for the different reference states.

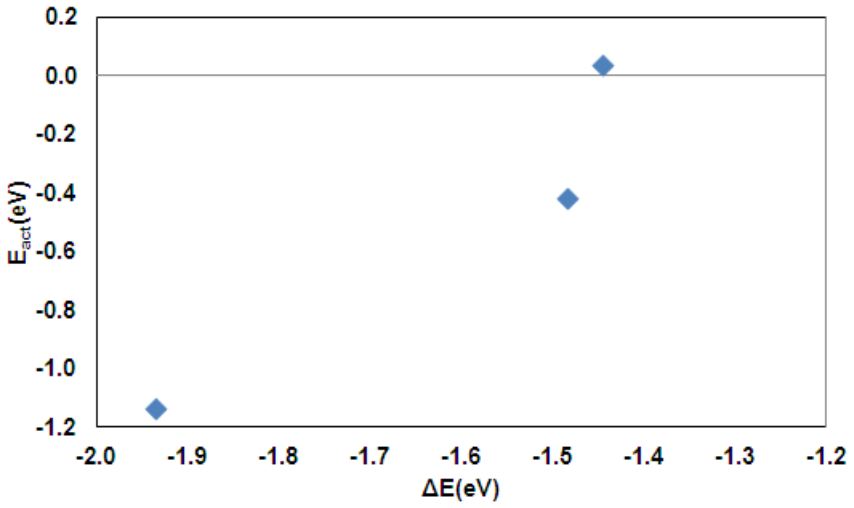

Figure 5.7: Plot of the activation energy of OH formations as a function adsorption energy of OH referenced to O_2 and H_2.

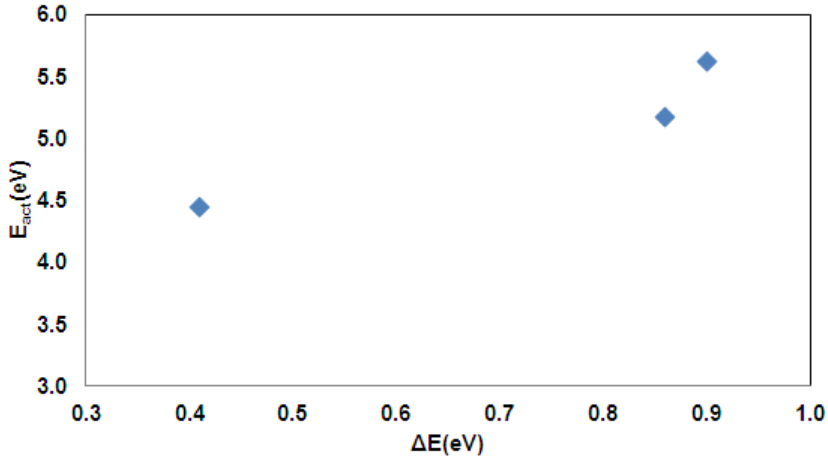

Figure 5.8: Plot of the activation energy for OH formations as a function of the adsorption energy of OH referenced to gas phase H_2O.

5.2.5 Hydrogenation of OH to form H_2O

Table 5.5 summarizes the activation energies and structural parameters characterizing the H_2O formation pathways from OH hydrogenation investigated in the present study.

Table 5.5: Calculated activation energies, the O-H bond lengths of the transition state structures, and the heat of reaction for H_2O formation calculated on the $Pt_3Co(111)$ surface

Product site	E_{act}^{coads}**(eV)**	$E_{act}^{inf.sep}$**(eV)**	**O-H**$_{TS}$ **(Å)**	$\triangle$**E**$_{rxn}$**(eV)**
t_{Co}	0.15	0.38	1.68	-0.35
t_{Pt}	0.16	0.71	1.71	-0.15

Figure 5.9 illustrates the geometries for reactants, transition state and products for the reaction of OH and H to form H_2O atop Co and atop Pt on $Pt_3Co(111)$.

The transition state structures determined for H_2O formation on the $Pt_3Co(111)$ surface are similar to those previously reported for the Pt(111) surface. Ford et al. (2010) and Michaelides and Hu (2001) report a transition state structure on Pt(111) in which OH is on the ontop site and H is on a neighboring ontop site tilted towards the OH.

The direct activation energy for H_2O formation atop Co and Pt on $Pt_3Co(111)$ are the same to within 0.01 eV, with the direct activation energy for H_2O formation atop Pt being higher although not with a significant energy difference.

The reaction pathway for H_2O formation from OH hydrogenation was not investigated in the study by Madala(2012) hence no data was available to calculate the activation energy for H_2O formation on Pt(111) in the present study.

The direct activation energies for H_2O formation atop Co and Pt on $Pt_3Co(111)$ are comparable to the reported direct activation energies for H_2O formation atop Pt on Pt(111) of 0.12 eV by Michaelides and Hu (2001) and 0.14 eV by Kandoi et al. (2004). Reported results by Michaelides and Hu (2001) were for the PW91 functional with the ultrasoft pseudopotentials for the electron-ion interactions and the constraint minimization technique was used to locate the transition states, and the reported results by Kandoi et al. (2004) were for the PW91 functional with the ultrasoft pseudopotentials for the electron-ion interactions and the CI-NEB method was

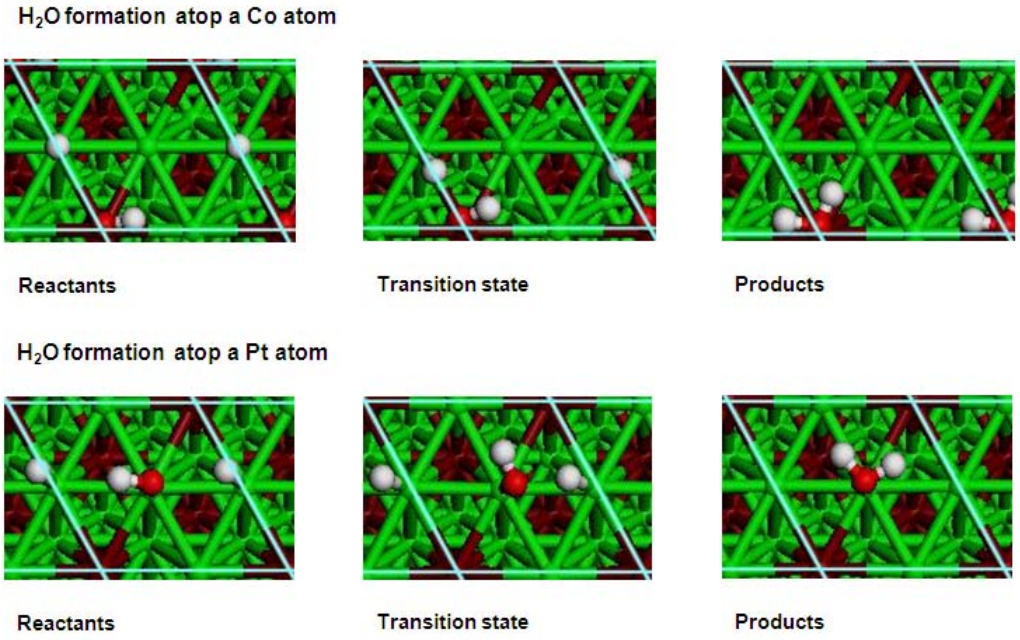

Figure 5.9: Structures of the reactants, transition state and the products for the hydrogenation reaction of OH to form H_2O atop a Co and a Pt atom on $Pt_3Co(111)$.

used to locate the transition states. The direct activation energy for the lowest reaction pathway on $Pt_3Co(111)$, i.e. H_2O formation atop Co is 0.03 eV higher than the value reported by Michaelides and Hu (2001) and 0.01 eV higher than that reported by Kandoi et al. (2004). Thus, there is no significant difference in the direct activation energy for H_2O formation on $Pt_3Co(111)$ whether be it atop Co or Pt and on Pt(111).

However, on comparing the overall activation energies, the overall activation energies reported on Pt(111) are lower than the overall activation energies on $Pt_3Co(111)$. The overall activation energies for the lowest energy pathways on $Pt_3Co(111)$, i.e. H_2O formation atop Co is 0.38 eV which is 0.17 eV higher than the overall activation energy on Pt(111) reported by Michaelides and Hu (2001) and 0.18 eV higher than the value reported by Kandoi et al. (2004). The difference between the overall and the direct activation energies on Pt(111) are 0.05 eV for the results reported by Michaelides and Hu (2001) and 0.04 eV for the results reported by Kandoi et al. (2004), this indicates that less energy is needed to coadsorb OH and H prior to reaction on Pt(111).

On $Pt_3Co(111)$, for the lowest energy pathway more energy for $\triangle E_{mix}$ of 0.23 eV needs to be overcome in order to coadsorb OH and H prior to reaction. The formation of H_2O atop Co is more exothermic than H_2O formation atop Pt on $Pt_3Co(111)$, the higher exothermicity for H_2O formation atop Co is due to H_2O being stabilised more atop Co than atop Pt on $Pt_3Co(111)$. On Pt(111) the heat of reaction for H_2O formation from OH hydrogenation for the lowest energy reaction pathway is calculated as -0.60 eV in the present study.

5.2.6 O-assisted H_2O dissociation

Table 5.6 summarizes the activation energies and structural parameters characterizing the O-assisted H_2O dissociation pathways investigated in the present study.

Table 5.6: Calculated activation energies and the OH-OH distances for the transition state structures for O-assisted H_2O dissociation, and the heat of reaction for O-assisted H_2O dissociation reaction on the $Pt_3Co(111)$ surface.

H_2O site	E_{act}^{coads}**(eV)**	$E_{act}^{inf.sep}$**(eV)**	**OH-OH**$_{TS}$ **(Å)**	$\triangle$**E**$_{rxn}$**(eV)**
t_{Co}	0.38	0.84	2.04	0.46
t_{Pt}	0.61	0.92	3.00	0.77

Figure 5.10 illustrates the geometries of the reactants, the transition state, and the products for the elementary reaction step of O-assisted H_2O dissociation to form OH species, studied on the $Pt_3Co(111)$ surface.

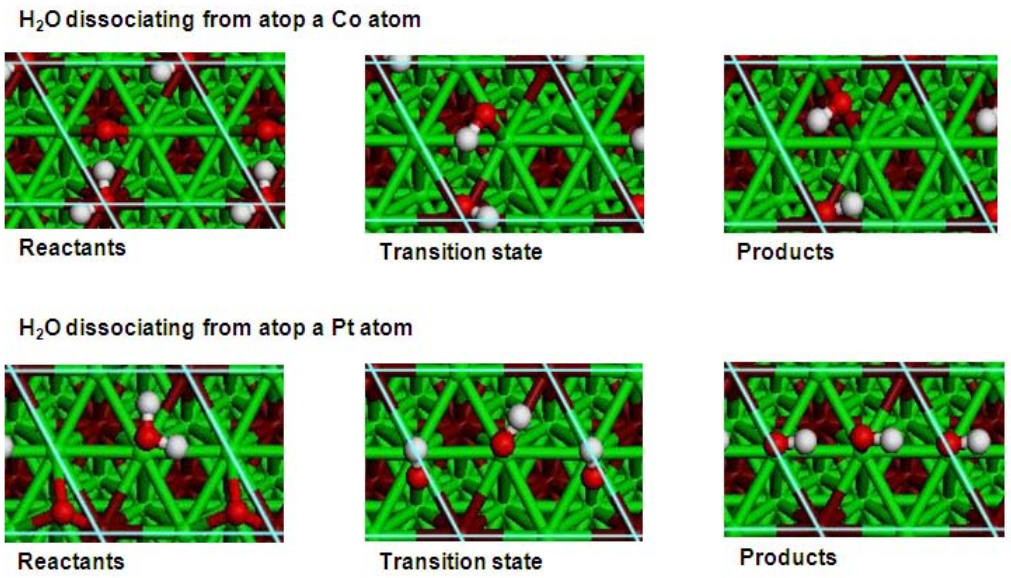

Figure 5.10: Geometries for the reactants, the transition state, and the products for the reaction of O-assisted H_2O dissociation, on the $Pt_3Co(111)$ surface

For both investigated reaction pathways it is observed that the transition state structure is close to the final product structure of two separate OH's. Michaelides and Hu (2001) reported a transition state structure close to the final product for the same reaction on Pt(111). The transition state structure for which the starting position of H_2O is atop Co in the coadsorbed state on $Pt_3Co(111)$, is a configuration similar to that reported by Michaelides and Hu (2001) on Pt(111) in which two pseudo-OH groups are obtained, with one OH on the atop site and the other OH on a bridge site.

The overall activation energy for the O-assisted H_2O dissociation step is 0.84 eV due to the presence of a repulsive lateral interaction of 0.46 eV between H_2O and O in the reactant state. The low direct activation energy of 0.38 eV relative to the coadsorbed state suggests that if a lower energy transition state exists and can be accessed from a lower energy coadsorbed state then a much lower direct activation energy pathway can be obtained.

The activation energy for the coadsorbed state with H_2O atop Pt is 0.61 eV relative to the coadsorbed state, and 0.92 eV relative to the separate state of H_2O in its most stable site and O on its most stable site at 0.25 ML. These results are similar to the activation energies calculated on Pt(111) in the present study, the activation energies are 0.55 eV relative to the coadsorbed state and 0.92 eV relative to the separate state of H_2O in its stable adsorption site and O in its stable adsorption site at 0.25 ML.

The reaction pathway involving H_2O atop Co occurs with lower direct and overall activation energies than the reaction pathway in which H_2O is atop Pt. The differences in the activation

energies may be linked to the differences in the transition state structures for the two pathways, the pathway with H_2O atop Co accesses a transition state which has the structure with the OH bonded atop Co whereas for the pathway starting with H_2O atop Pt the transition state structure is not bonded directly to a surface Co atom. Therefore, the surface Co atom stabilises the transition state structure for the pathway with H_2O atop Co hence resulting in lower overall and direct activation energies.

A comparison of the lowest energy pathways on $Pt_3Co(111)$ for reactions consuming strongly adsorbed O on the surface reveals that the direct activation energy for the reaction O* + H_2O* $\rightarrow$ 2OH* is 0.28 eV lower than the direct activation energy for the reaction O* + H* $\rightarrow$ OH* + *. The overall activation energy for the reaction O* + H_2O* $\rightarrow$ 2OH* on $Pt_3Co(111)$ is 0.84 eV which is lower than the overall activation energy for the lowest energy pathway for the reaction O* + H* $\rightarrow$ OH* + *. The overall activation energies for both reactions are the same to within 0.02 eV, indicating that the both reactions have similar activation energies. The overall activation energies incorporates diffusion effects to get the reactants to the reaction site (i.e. concentration effects are included) whereas the direct activation energies implicitly neglects concentration effects which could also influence the rate of reaction. Therefore, the similar overall activation energies to within 0.02 eV for both reactions can be considered a direct measure that the rate of these 2 types of reactions can be expected to be similar.Thus, O-assisted H_2O dissociation reaction represents an alternative reaction pathway to reacting strongly adsorbed O on the surface in addition to the direct hydrogenation of O to OH.

The heat of reaction for the O- assisted H_2O dissociation reaction is endothermic as can be seen from the reported calculated heat of reaction in Table 5.6. The Co based reaction pathway(i.e. the pathway with H_2O atop Co) is less endothermic than the Pt based pathway (i.e. the reaction pathway with H_2O atop Pt). The surface Co atom stabilises both the reactants and the products for the Co based pathway leading to a less endothermic heat of reaction whereas for the Pt based pathway only the reactants are bonded to a surface Co atom and the products are less stabilised since the product OH species are not directly bonded to a surface Co atom. On Pt(111) the heat of reaction is endothermic with a calculated heat of reaction of 0.50 eV in the present study.

5.2.7 HOOH formation

Table 5.7 summarizes the activation energies and structural parameters characterizing the HOOH formation pathways from OOH hydrogenation investigated in the present study.

Table 5.7: Activation energies, and the O-O bond distances of the transition state structures, the heat of reaction for HOOH formation calculated on the $Pt_3Co(111)$ surface.

Product site	E_{act}^{coads}**(eV)**	$E_{act}^{inf.sep}$**(eV)**	**O-H**$_{TS}$ **(Å)**	$\triangle$**E**$_{rxn}$**(eV)**
t_{Co}	0.39	0.97	1.49	-0.24
t_{Pt}	0.29	0.71	1.48	0.01

Figure 5.11 illustrates the geometries of the reactants, the transition state, and the products for the elementary reaction step for the formation on HOOH, from coadsorbed OOH and H.

The transition state structures for the formation of HOOH, obtained in the present study on $Pt_3Co(111)$, are equivalent to those reported on Pt(111). On Pt(111) Ford et al. (2010) reports a transition state structure in which OOH is on a bridge site and H is atop a Pt atom.

The direct and overall activation energies for HOOH formation for the Co based pathway are higher than those for the Pt based pathway despite HOOH adsorption being more stable atop Co than atop Pt on $Pt_3Co(111)$. A possible reason for the high direct and overall activation energies for HOOH formation for the Co based pathway is due to the close proximity of H and OOH and the orientation of H which is directed away from OOH on the bridge in the transition state structure. The closeness of H and OOH and the orientation of H in the transition state may

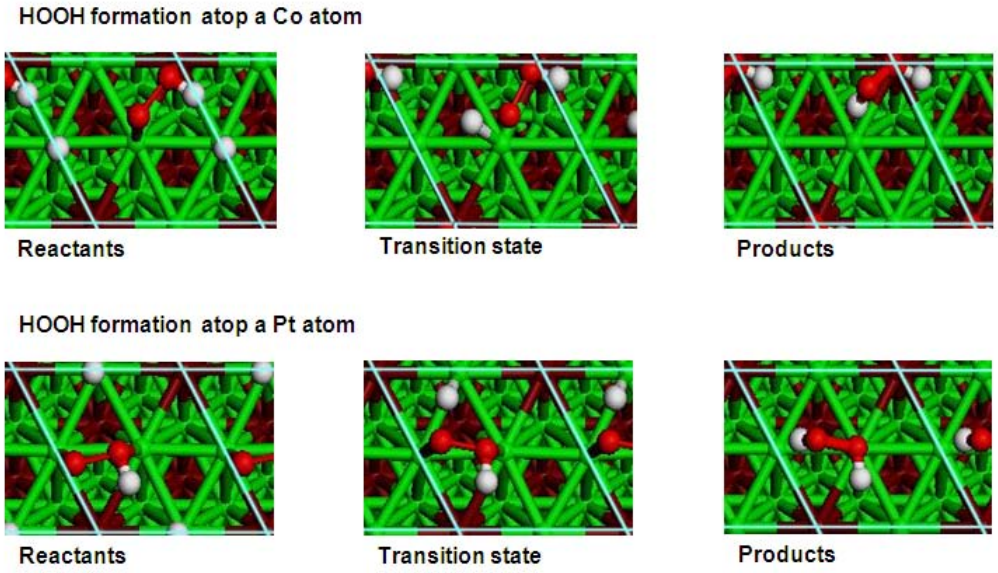

Figure 5.11: Geometries of the reactants, transition state, and the products for the formation of HOOH from coadsorbed OOH and H studied on the $Pt_3Co(111)$ surface.

lead to a higher energy state resulting in a high activation energy, despite OOH being bonded directly to a surface Co atom in the transition state.

The Pt based pathway for HOOH formation on $Pt_3Co(111)$ has the lowest direct and overall activation energies than the Co based pathway.

The direct and overall activation energies for HOOH formation on Pt(111) calculated in the present study are lower than those for the lowest energy pathway on $Pt_3Co(111)$. The activation energies calculated on Pt(111) in the present study of 0.21 eV for the direct activation energy and 0.37 eV for the overall activation energy are comparable to the activation energies reported by Ford et al. (2010) (PW91 functional) of 0.21 eV for the direct activation energy and 0.34 eV for the overall activation energy. From the investigated reaction pathway for HOOH formation obtained in the present study it appears that the HOOH formation on $Pt_3Co(111)$ has higher direct and overall energies than on Pt(111).

The heat of formation for HOOH formation atop Co is more exothermic than HOOH formation atop Pt as shown in the results in Table 5.7. The products for the Co based pathway are more stabilised than for the Pt based pathway, hence the Co based pathway becomes more exothermic than the Pt based pathway. On Pt(111) the lowest energy reaction pathway for HOOH formation is exothermic with the calculated heat of reaction of -0.20 eV in the present study.

5.2.8 HOOH dissociation

Table 5.8 summarizes the activation energies and structural parameters characterizing the HOOH dissociation pathways investigated in the present study.

Table 5.8: The O-O stretching frequencies and the O-O bond lengths of the dissociating HOOH species, the activation energies and the O-O bond lengths of the transition state structure, and the heat of reaction for HOOH dissociation reaction calculated on the $Pt_3Co(111)$ surface.

Reactant site	ν_{O-O}**(cm** $^{-1}$**)**	**O-O (Å)**	$E_{act}^{dir.}$**(eV)**	$E_{act}^{ovr.}$**(eV)**	**O-O**$_{TS}$ **(Å)**	$\triangle$**E**$_{rxn}$**(eV)**
t_{Co}	779	1.48	0.13	0.13	1.87	-1.55
t_{Pt}	862	1.47	0.36	0.59	1.90	-1.58

Figure 5.12 illustrates the geometries of the reactants, the transition state, and the products, for the elementary reaction step of the dissociation of HOOH.

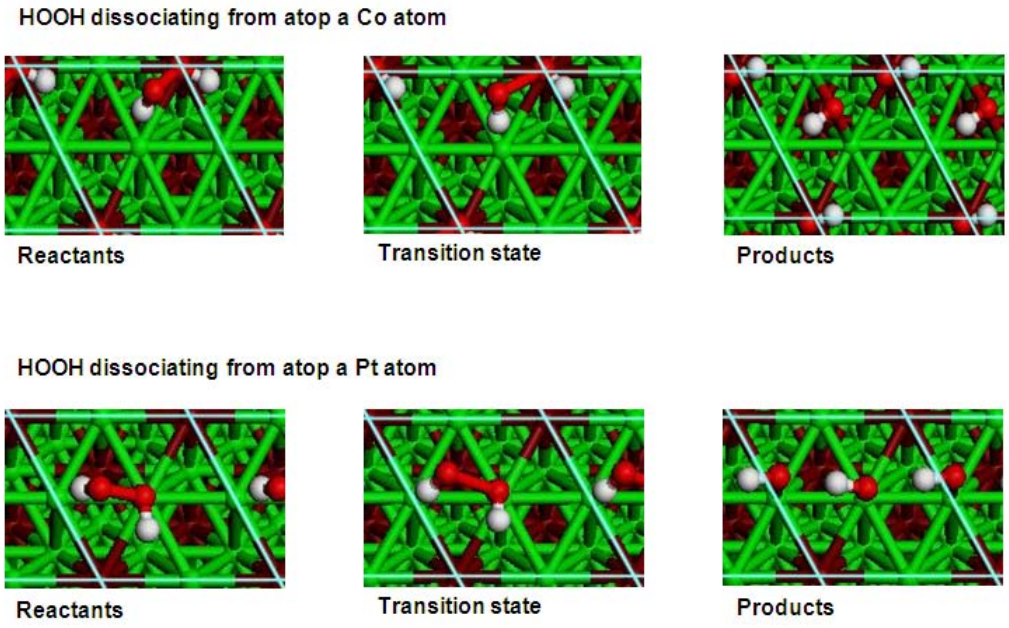

Figure 5.12: Geometries of the reactants, transition state, and the products, for the dissociation of HOOH on $Pt_3Co(111)$

The transition state structures for the dissociation of HOOH investigated in the present study are different from those reported for other transition metal (111) surfaces. Ford et al. (2010) reports a transition state structure with the two OH's atop neighbouring Pt atoms and the O-O bond aligned along a bridge site on Pd(111), Pt(111), Cu(111), Ag(111) and Au(111). The transition state structure of the dissociation of HOOH atop Co obtained in the present study, has one OH atop a Co atom with the O-O bond aligned over a 3-fold-hollow fcc site as shown in Figure 5.12. For HOOH dissociating from atop a Pt atom, the O-O bond is rotated slightly away from the bridge site towards the h_{Co} site as seen in Figure 5.12.

The direct and overall activation energies for HOOH dissociation atop Co are lower than those calculated for HOOH dissociation atop Pt. The direct activation energy for HOOH dissociation from atop Pt is more than double the direct activation energy for HOOH dissociation from atop Co, this indicates that the transition state for dissociation from atop Co is stabilised more relative to the transition state for dissociation from atop Pt. The stabilisation of the transition state for HOOH dissociation from atop Co is due to the transition state geometry being directly bonded to a surface Co atom, whilst that for HOOH dissociation from atop Pt is not bonded to a surface Co atom.

The dissociation of HOOH is an exothermic reaction with the Pt based pathway being 0.03 eV more exothermic. The slight exothermicity of the Pt based pathway over the Co based pathway is probably due to the orientation of the OH products for both pathways. For the Pt based pathways the product is such that the H of one OH is directed towards the O of the other OH, and this geometry may be slightly more stable than the orientation of the Co based pathway, due to maximization of hydrogen bonding whereas for the Co based pathway the opposite direction of the H atoms of the OH's does not lead to maximization of hydrogen bonding. The Co based pathway product state is 0.04 eV more stable than the product state for the Pt based pathway. The calculated heat of reaction for HOOH dissociation from the lowest energy reaction pathway on Pt(111) in the present study is -1.37 eV.

The reaction pathway for HOOH dissociation was not studied in the study by Madala(2012) hence there is no data to use to calculate the activation energies for HOOH dissociation on Pt(111) using the PW91 functional in the present study.

The overall dissociation activation energy of HOOH from atop Co of 0.13 eV is lower than the activation energy of 0.25 eV calculated on Pt(111) by Ford et al. (2010) (PW91 functional).

5.3 Comparison of the different ORR mechanisms

To compare the different possible ORR mechanisms on the $Pt_3Co(111)$ surface, a potential energy diagram is constructed using the lowest overall activation energy pathways for each elementary step presented in Figure 5.13. For the dissociative, associative 1 and associative 2 ORR mechanisms, the reference state for constructing the potential energy diagram is gas phase O_2 and the stoichiometry is balanced against O_2 and 4 non-interacting hydrogen atoms on the surface. For the O-assisted H_2O ORR mechanism, the reference state for construction of the potential energy diagram was gas phase O_2, 2 gas phase H_2O molecules and 4 hydrogen atoms infinitely apart on the surface (i.e. non-interacting).

Figure **5.13** details the 4 possible proposed ORR mechanisms which may occur during the ORR.

Dissociative Mechanism	**Associative 1 Mechanism**	**Associative 2 Mechanism**
O_2 + * $\rightarrow$ O_2* [1]	O_2 + * $\rightarrow$ O_2* [1]	O_2 + * $\rightarrow$ O_2* [1]
O_2* + * $\rightarrow$ 2O* [2]	O_2* + (H^+ + e^-) $\rightarrow$ OOH* [3]	O_2* + (H^+ + e^-) $\rightarrow$ OOH* [3]
O* + (H^+ + e^-) $\rightarrow$ OH* [5]	OOH* + * $\rightarrow$ O* + OH* [4]	OOH* + (H^+ + e^-) $\rightarrow$ HOOH* [6]
OH* + (H^+ + e^-) $\rightarrow$ H_2O* [9]	O* + (H^+ + e^-) $\rightarrow$ OH* [5]	HOOH* + * $\rightarrow$ 2OH* [7]
	OH* + (H^+ + e^-) $\rightarrow$ H_2O* [9]	OH* + (H^+ + e^-) $\rightarrow$ H_2O* [9]

O-assisted H_2O Dissociation Mechanism
O_2 + * $\rightarrow$ O_2* [1]
O_2* + * $\rightarrow$ 2O* [2]
O* + H_2O* $\rightarrow$ 2OH* [8]
OH* + (H^+ + e^-) $\rightarrow$ H_2O* [9]

Figure 5.13: Four possible ORR mechanisms which may occur during ORR

Table 5.9 is a summary of the data used to construct the potential energy surface. The heat of reaction for the dissociation of O_2 used to construct the potential energy diagrams is different to that reported in Table 5.1 for the lowest energy pathway for O_2 dissociation form the b2_f$_{Pt}$_t$_{Co}$ configuration, because for construction of the potential energy diagram the heat of reaction for O_2 dissociation was calculated with respect to the product state of two non-interacting O's at 0.25 ML adsorbed at the f$_{Pt}$ site. Similarly, the heat of reaction for the dissociation of OOH used to construct the potential energy diagram is with the product state with O and OH occupying the lowest energy sites at 0.25 ML, and the heat of reaction for HOOH dissociation used in the potential energy diagram is calculated with respect to the product state of non-interacting OH's at 0.25 ML adsorbed at the lowest energy site, the t$_{Co}$ site. Furthermore the heat of reaction for reaction [8] used in the potential energy diagram is calculated with respect to the product state of non-interacting OH's at 0.25 ML adsorbed at the lowest energy site, the t$_{Co}$ site.

Table 5.9: Lowest energy activation energies, heats of reaction for the possible ORR elementary reaction steps and the adsorption energies of the most stable ORR species on $Pt_3Co(111)$ used to construct the potential energy diagram.

Reaction step	**E_{act}(eV)**	**$\triangle E_{rxn}$(eV)**	**E_{ads}(eV)**
O_2* + * $\rightarrow$ 2O* [2]	0.08	-2.23	O_2 = -0.97, O = -4.62
O_2* + (H^+ + e^-) $\rightarrow$ OOH* [3]	0.56	0.08	H = -2.68, OOH = -1.37
OOH* + * $\rightarrow$ O* + OH* [4]	0.05	-2.24	OH = -2.58
O* + (H^+ + e^-) $\rightarrow$ OH* [5]	0.86	0.06	
OOH* + (H^+ + e^-) $\rightarrow$ HOOH* [6]	0.71	-0.24	HOOH = -0.52
HOOH* + * $\rightarrow$ 2OH* [7]	0.13	-1.94	
O* + H_2O* $\rightarrow$ 2OH* [8]	0.84	0.41	H_2O = -0.35
OH* + (H^+ + e^-) $\rightarrow$ H_2O* [9]	0.38	-0.35	

Table 5.10: Lowest energy activation energies, heats of reaction for the possible ORR elementary reaction steps and the adsorption energies of the most stable ORR species on Pt(111) used to construct the potential energy diagram.

Reaction step	**E_{act}(eV)**	**$\triangle E_{rxn}$(eV)**	**E_{ads}(eV)**
O_2* + * $\rightarrow$ 2O* [2]	0.59	-1.10	O_2 = -0.63, O = -4.17
O_2* + (H^+ + e^-) $\rightarrow$ OOH* [3]	0.52	-0.17	H = -2.62 , OOH = -1.12
OOH* + * $\rightarrow$ O* + OH* [4]	0.11	-1.56	OH = -2.21
O* + (H^+ + e^-) $\rightarrow$ OH* [5]	0.95	-0.50	
OOH* + (H^+ + e^-) $\rightarrow$ HOOH* [6]	0.37	-0.20	HOOH = -0.29
HOOH* + * $\rightarrow$ 2OH* [7]	0.25	-1.37	
O* + H_2O* $\rightarrow$ 2OH* [8]	0.92	0.59	H_2O = -0.15
OH* + (H^+ + e^-) $\rightarrow$ H_2O* [9]	0.21	-0.61	

For completeness of the Pt(111) potential energy surface, in Table 5.10 the value for the activation energy of OH hydrogenation to H_2O of 0.21 eV was taken from Michaelides and Hu (2001) and the activation energy value of 0.25 eV for HOOH dissociation was taken from Ford et al. (2010). No calculations for these reactions were performed on Pt(111) in the present study and the study by Madala (2012).

From Figure 5.14 it is observed that on $Pt_3Co(111)$ the activation energy for O_2 dissociation is more facile than the hydrogenation of O_2 to form OOH. The activation energy for O_2 dissociation is 0.08 eV whilst the activation energy for O_2 hydrogenation to OOH is 0.56 eV, therefore the dissociation of O_2 is kinetically (excluding the concentration and entropic effects) preferred over the hydrogenation of O_2 to OOH. Thus, on $Pt_3Co(111)$ the preferred ORR mechanism is likely to

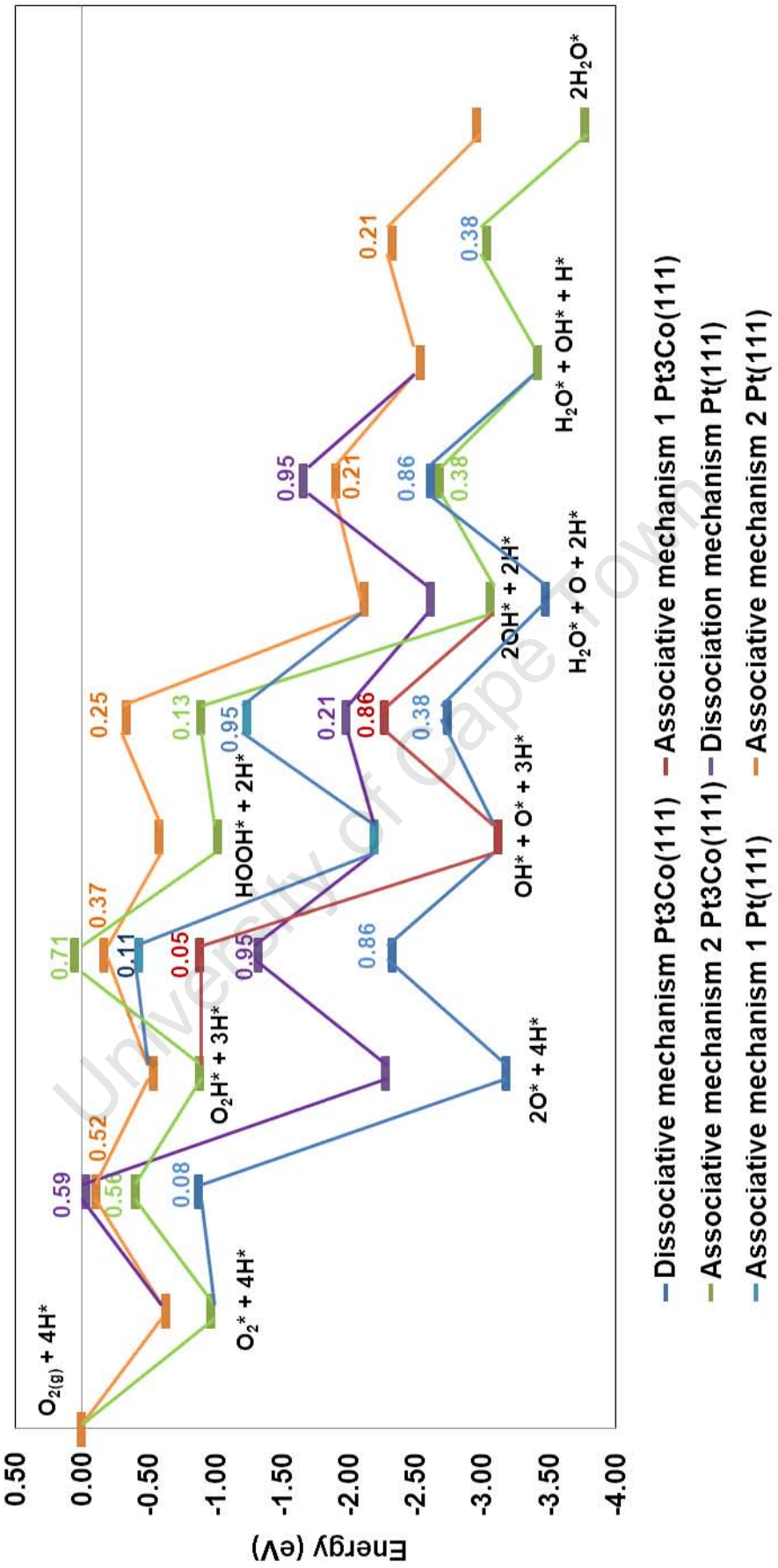

Figure 5.14: Potential energy diagram of the ORR mechanisms (dissociative and associative) on $Pt_3Co(111)$ and Pt(111). The reference state for the potential energy diagram is gas phase O_2 and the stoichiometry is O_2 and 4 non-interacting hydrogen atoms on the surface. All energy value on the potential energy diagram include zero point energy corrections.

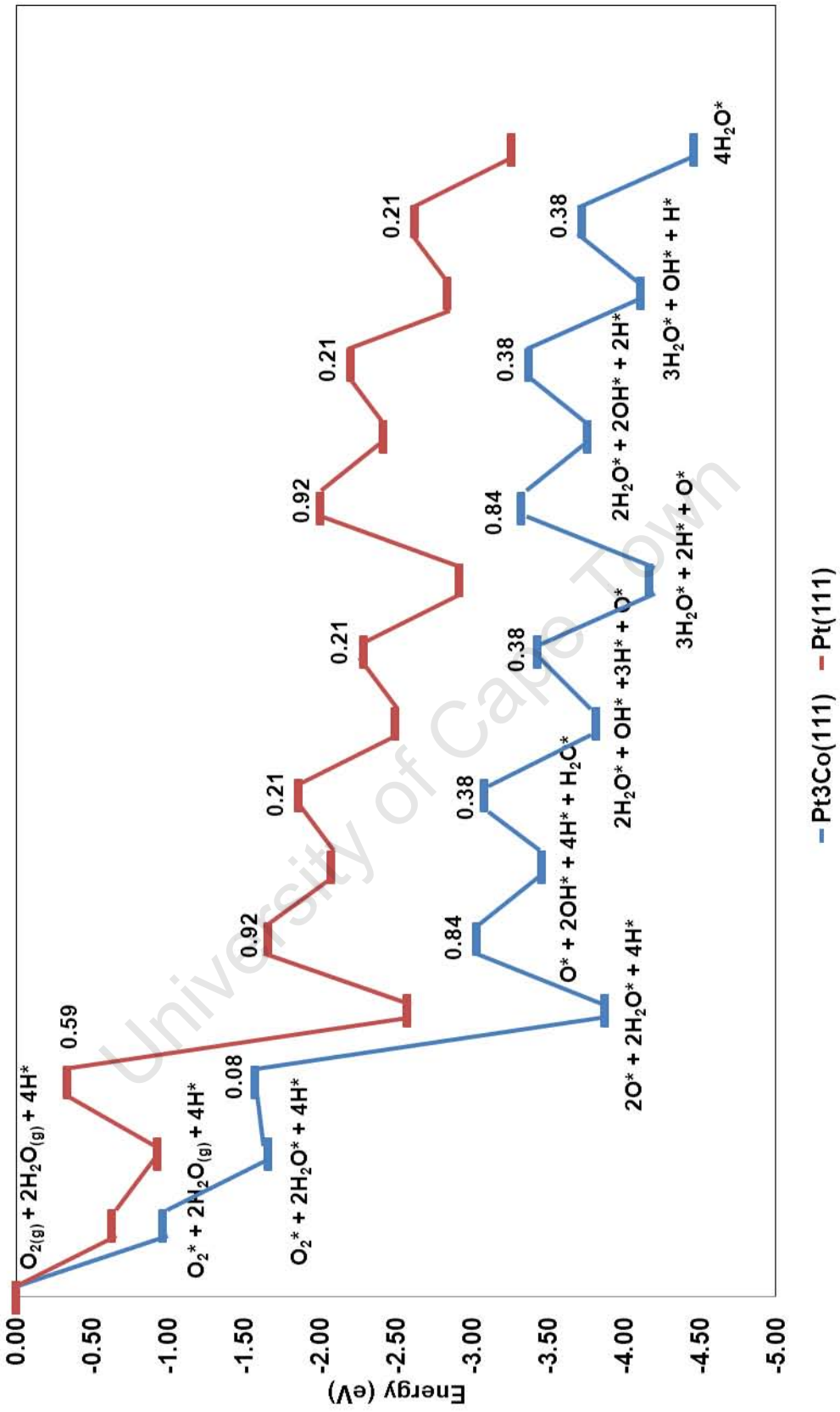

Figure 5.15: Potential energy diagram of the O-assisted H_2O dissociation mechanism on $Pt_3Co(111)$ and Pt(111). The reference state for the potential energy diagram is gas phase O_2, two gas phase H_2O molecules and the stoichiometry is O_2, $2H_2O$ and 4 non-interacting hydrogen atoms adsorbed on the surface. All energies on the potential energy surface include zero point energy corrections.

be the mechanism which proceeds through the O_2 dissociation pathway, and the dominant ORR mechanisms that occur on $Pt_3Co(111)$ are the dissociative and the O-assisted H_2O dissociation mechanisms.

On comparing reactions [2] and [3] on Pt(111) and on $Pt_3Co(111)$, it is observed that on Pt(111) reactions [2] and [3] occur with similar activation energies of 0.59 eV and 0.52 eV, respectively whilst on $Pt_3Co(111)$ the activation energies are different. Therefore, on Pt(111) reaction [2] and [3] would be expected to be in competition and occur simultaneously depending on the availability of H^* due to similar activation energies. Hence, on Pt(111) the dissociative and the associative mechanisms are expected to occur concurrently as proposed by Nørskov et al. (2004). Due to the presence of the surface Co on $Pt_3Co(111)$ the activation energy for O_2 dissociation is reduced to 0.08 eV compared to 0.59 eV on Pt(111) due to O being strongly adsorbed on $Pt_3Co(111)$ than on Pt(111) which results in ease of O_2 dissociation on $Pt_3Co(111)$. The presence of surface Co on $Pt_3Co(111)$ slightly increases the activation energy for O_2 hydrogenation to O_2H by 0.04 eV relative to the activation energy on Pt(111).

The heat of reaction for O_2 dissociation on $Pt_3Co(111)$ is highly exothermic at -2.23 eV, this indicates that the reverse reaction of the combination of two O's to form O_2 is highly activated with an activation energy of 2.31 eV.

For the likely preferred ORR mechanisms on $Pt_3Co(111)$, i.e. the dissociative and the O-assisted H_2O dissociation mechanism, the highest activation energy reaction step for the mechanisms is reaction [5] ($O^* + (H^+ + e^-) \rightarrow OH^*$) and reaction step [8] ($O^* + H_2O^* \rightarrow 2OH^*$), respectively. For the dissociative mechanism the highest activation energy step has an activation energy of 0.86 eV and for the O-assisted H_2O dissociation mechanism the highest activation energy step has an activation energy of 0.84 eV. For both mechanisms the highest activation energy and likely rate-determining reaction steps involve the strongly adsorbed O being used as a reactant.

The dissociative and O-assisted H_2O dissociation ORR mechanisms involve the same elementary reaction steps, except the reaction steps using O as a reactant. Therefore, the dominant mechanism will depend on the concentration of the co-reactants of O, i.e. $(H^+ + e^-)$ for the dissociative mechanism and H_2O^* for the O-assisted H_2O mechanism.

On Pt(111) the highest activation energy reaction step for the dissociative, associative 1 and the O-assisted H_2O dissociation mechanism is also the reaction step which uses O as a reactant. For the dissociative and the associative 1 mechanisms reaction step [5] has the highest activation energy of 0.95 eV, whilst for the O-assisted H_2O dissociation mechanism the highest activation energy reaction step [8] has an activation energy of 0.92 eV on Pt(111). Therefore, on both $Pt_3Co(111)$ and Pt(111) the highest activation energy and likely rate-determining steps are the same and involve the consumption of strongly bound O as a reactant. On $Pt_3Co(111)$ the highest activation energy steps are approximately 0.10 eV lower than the highest activation energy steps on Pt(111). Thus, on $Pt_3Co(111)$ the surface Co allows for the formation of OH through lower activation energy pathways than on Pt(111), and the lower activation energies for OH formation on $Pt_3Co(111)$ maybe responsible for the experimentally observed higher ORR rates on $Pt_3Co(111)$ than on Pt(111) by Stamenković et al. (2002).

The activation energy for OOH dissociation is lower at 0.05 eV than the activation energy for HOOH formation of 0.71 eV on $Pt_3Co(111)$. Therefore, the dissociation of OOH is kinetically (excluding the concentration and entropic effects) favored over the hydrogenation of OOH to HOOH on $Pt_3Co(111)$. Of the four possible ORR mechanisms on $Pt_3Co(111)$, the associative 2 mechanism which proceeds via the formation of HOOH is the least likely ORR pathway on $Pt_3Co(111)$. The dissociation of OOH to O and OH is highly exothermic on $Pt_3Co(111)$ with a heat of reaction of -2.24 eV. This high exothermic heat of reaction indicates that the reverse reaction of the combination of O and OH to form OOH is highly activated with an activation energy of 2.29 eV. Similarly, the heat of reaction for the dissociation of HOOH is exothermic with a heat of reaction of -1.94 eV, this is an indication that the reverse reaction of the combination of two OH's to form HOOH is highly activated with an activation energy of 2.07 eV.

The high activation energy of 0.71 eV at the Pt site for the formation of HOOH on $Pt_3Co(111)$ together with the facile dissociation of HOOH into 2OH's (E_{act} = 0.13eV) may be considered as indication that HOOH will be formed in low concentrations and even if it is formed it could

dissociate readily if the sites are available on the surface. The low concentration of HOOH implies that the detrimental effects of HOOH on the membrane of the PEMFC may be minimised, hence the durability of the membrane might be improved for cathodes utilizing the Pt_3Co alloy as the electrocatalyst. HOOH has been reported by Balbuena et al. (2006) to have detrimental effects on the PEMFC membranes.

Associative 2 mechanism does not include the reaction step involving the consumption of strongly adsorbed O and thus would be an alternative option to mechanisms which include steps consuming O. However, the highest activation energy step (with an energy of 0.71 eV) ocucurs for associative 2 mechanism, this activation energy is lower than the overall activation energy of 0.86 eV and 0.84 eV which are the highest energy steps for the dissociative, associative 1 mechanism and the O-assisted H_2O dissociation mechanism, respectively.

Despite having the highest energy step with a lower overall activation energy than the highest energy steps for the other ORR mechanisms, associative 2 mechanism is not likely to be the preferred ORR mechanism on $Pt_3Co(111)$ since it occurs via the formation of OOH which has a higher overall activation energy of formation than the overall activation energy for O_2 dissociation. Thus ORR mechanisms which occur through O_2 dissociation are kinetically preferred (excluding concentration and entropic effects) over mechanisms occurring through OOH formation, hence associative 2 mechanism is not kinetically preferred (excluding concentration and entropic effects).

On $Pt_3Co(111)$ the activation energy for O_2 dissociation compared to the activation energy for O_2 hydrogenation to OOH is important in determining which ORR mechanism is kinetically (excluding concentration and entropic effects) preferred. The reaction steps in which O is consumed as a reactant are important as they can be used to identify the likely rate-determining steps.

Comparing the activation energies of reaction step [9] on $Pt_3Co(111)$ and Pt(111), it is observed that on $Pt_3Co(111)$ the reaction occurs with a 0.17 eV higher activation energy than the calculated overall activation energy of 0.21 eV by Michaelides and Hu (2001) on Pt(111). Therefore, on $Pt_3Co(111)$ the surface Co atom increases the activation energy for OH hydrogenation to H_2O by 0.17 eV relative to Pt(111). The higher activation energy on $Pt_3Co(111)$ may be due to strongly bound OH on $Pt_3Co(111)$ atop Co compared to OH atop Pt on Pt(111). However, the increase of the activation energy for OH hydrogenation to H_2O on $Pt_3Co(111)$ relative to Pt(111) is not expected to affect the rate of the ORR on $Pt_3Co(111)$ relative to Pt(111), since the activation energy of this reaction step is 0.48 eV and 0.46 eV lower than the highest activation energy steps for the dissociative and the O-assisted H_2O dissociation mechanisms, respectively. Thus, the 0.17 eV higher activation energy for OH hydrogenation to H_2O on $Pt_3Co(111)$ relative to Pt(111) is not the likely rate determining step on $Pt_3Co(111)$.

On Pt(111) the activation energy for OOH dissociation is 0.11 eV whilst on $Pt_3Co(111)$ the activation energy for OOH dissociation is 0.06 eV lower, indicating that the surface Co on $Pt_3Co(111)$ lowers the activation energy for OOH dissociation. On Pt(111) the activation energy for OOH hydrogenation to HOOH is 0.21 eV, this value is 0.50 eV lower than the calculated activation energy on $Pt_3Co(111)$. Therefore on $Pt_3Co(111)$ the presence of the surface Co atom increases the activation energy for the hydrogenation of OOH to HOOH.

5.4 Conclusions

From the results and discussion presented in this chapter the following conclusions are made:

The presence of the surface Co atom on $Pt_3Co(111)$ stabilises the transition state structures for the possible elementary reaction steps, the result of which is the Co based reactions pathways occur with lower direct and overall activation energies than the Pt based reaction pathways on $Pt_3Co(111)$. The only exception is the reaction step of OOH hydrogenation to HOOH, for which the Pt based reaction pathway was calculated to have lower direct and overall activation energies than the Co based reaction pathway on $Pt_3Co(111)$.

For O_2 dissociation the lowest energy pathway identified on $Pt_3Co(111)$ occurs with a low overall activation energy of 0.08 eV compared to the overall activation energy of 0.59 eV calculated for

the lowest energy pathway on Pt(111). Other reaction pathways on $Pt_3Co(111)$ exists which occur with lower overall activation energies than the overall activation energy for the lowest energy pathway for O_2 dissociation on Pt(111). O_2 dissociates with lower direct and overall activation energies on the f_{Pt} site than on the h_{Pt} site on $Pt_3Co(111)$. Subsurface Co on the h_{Co} position leads to a higher overall activation energy for O_2 dissociation on $Pt_3Co(111)$ than the overall activation energy for O_2 on Pt(111). However, the direct activation energy for O_2 dissociation from the h_{Co} site on $Pt_3Co(111)$ of 0.45 eV is lower than the lowest energy reaction pathway for O_2 dissociation on Pt(111) of 0.59 eV.

The Pt based reaction pathways for all investigated possible ORR elementary reaction steps on $Pt_3Co(111)$ have direct and overall activation energies which are higher than the corresponding activation energies for the lowest energy reaction pathways on Pt(111). Therefore, the Co atoms in $Pt_3Co(111)$ serves to modify the properties of the surface Pt atoms within $Pt_3Co(111)$ such that they have different electronic properties to the Pt atoms within Pt(111). The result of the modified electronic properties of the surface Pt atoms within $Pt_3Co(111)$ is that the ability of these surface Pt atoms to catalyse the various possible ORR elementary reactions steps is reduced relative to Pt(111). The consequence is that the calculated direct and overall activation energies for the Pt based reaction pathways are higher on $Pt_3Co(111)$ relative to the calculated activation energies on Pt(111).

The calculated direct and overall activation energies for the lowest energy pathways for the dissociation reaction steps on $Pt_3Co(111)$ are lower than those calculated on Pt(111). The most strongly affected dissociation is the dissociation of O_2, which is lowered from 0.59 eV on Pt(111) to 0.08 eV on $Pt_3Co(111)$. Thus, the surface Co allows O_2 dissociation to become facile on $Pt_3Co(111)$. The overall dissociation activation energy of OOH dissociation is lowered by 0.06 eV and that for HOOH dissociation is lowered by 0.12 eV on $Pt_3Co(111)$ relative to Pt(111).

For hydrogenation reaction steps the different hydrogenation steps are affected to varying extends with some having higher activation energies, others having similar activation energies and other hydrogenation steps have lower activation energies on $Pt_3Co(111)$ than on Pt(111). The direct and overall activation energies for O_2 hydrogenation to OOH on $Pt_3Co(111)$ and on Pt(111) are similar, the direct activation energies are 0.23 eV and 0.22 eV and the overall activation energies are 0.56 eV and 0.52 eV, respectively. Thus the surface Co on $Pt_3Co(111)$ does not significantly change the activation energy for O_2 hydrogenation to OOH relative to the calculated value on Pt(111).

For O hydrogenation to OH the overall activation energy is approximately 0.10 eV lower on $Pt_3Co(111)$ than on Pt(111). The hydrogenation of O to OH is the highest activation energy step on both $Pt_3Co(111)$ and Pt(111) and is therefore the likely rate-determining step. The surface Co on $Pt_3Co(111)$ lowers the activation energy for the likely rate-determining step.

For OH hydrogenation to H_2O the direct activation energy on $Pt_3Co(111)$ of 0.15 eV for the lowest energy pathway is comparable to the direct activation energy of 0.12 eV by Michaelides and Hu (2001) (PW91 functional) and 0.14 eV by Kandoi et al. (2004) (PW91 functional) reported on Pt(111). However, the overall activation energy calculated on $Pt_3Co(111)$ of 0.38 eV for the lowest energy reaction pathway is higher than the reported overall activation energy of 0.21 eV (Michaelides and Hu (2001)) and 0.20 eV (Kandoi et al. (2004)) reported on Pt(111). The reason for the higher overall activation energy on $Pt_3Co(111)$ is due to the strongly adsorbed reactants which result in a higher repulsive lateral interaction energy which needs to be overcome in order to coadsorb OH and H prior to reaction on $Pt_3Co(111)$ relative to the less strongly bound reactants on Pt(111) which leads to low repulsive lateral interactions which need to be overcome.

The direct and overall activation energies for OOH hydrogenation to HOOH on $Pt_3Co(111)$ are 0.08 eV and 0.34 eV, respectively higher than the calculated activation energies calculated on Pt(111). The surface Co atom in $Pt_3Co(111)$ leads to higher activation energies for OOH hydrogenation to HOOH on $Pt_3Co(111)$ relative to Pt(111), making this reaction kinetically unfavorable on $Pt_3Co(111)$.

The low direct and overall activation energies for O_2 dissociation relative to O_2 hydrogenation to OOH on $Pt_3Co(111)$ is likely to dictate which ORR mechanisms are kinetically (excluding concentration and entropic effects) preferred. The kinetically (excluding concentration and entropic

effects) preferred ORR mechanisms on $Pt_3Co(111)$ are the dissociative and the O-assisted H_2O mechanisms. These two mechanisms are expected to occur in parallel with the dominant mechanism depending on the concentration of the co-reactants involved in the likely rate-determining step, i.e. ($H^+ + e^-$) for the dissociative mechanism and H_2O^* for the O-assisted mechanism.

On Pt(111) the dissociative and associative mechanisms are expected to occur in competition as the overall activation energy for O_2 dissociation of 0.59 eV is comparable to the overall activation energy for O_2 hydrogenation to OOH of 0.52 eV.

The reaction steps consuming strongly adsorbed O on the surface occur through the highest activation energy and are likely to be the rate-determining reaction steps based on the high kinetic (excluding concentration and entropic effects) barriers calculated for these reaction steps.

The O-assisted H_2O dissociation reaction step occurs with lower direct and overall activation energies on $Pt_3Co(111)$ than on Pt(111). Thus on $Pt_3Co(111)$ the surface Co atom lowers the direct and overall activation energy for the O-assisted H_2O dissociation. The low activation energy for this step on $Pt_3Co(111)$ provides an alternative route for strongly adsorbed O consumption and for OH formation. The O-assisted H_2O dissociation mechanism acts as an autocalytic ORR mechanism since H_2O is used up as a reactant and regenerated as a product. Two H_2O molecules are used as reactants and four water molecules are produced as products, hence the two H_2O reactant molecules are regenerated at the end.

The presence of Co in $Pt_3Co(111)$ changes the heat of reaction for O_2 hydrogenation to OOH from exothermic on Pt(111) to slightly endothermic on $Pt_3Co(111)$. Therefore, the Co in $Pt_3Co(111)$ changes the energetics of the various possible ORR elementary reaction steps of the ORR mechanisms on $Pt_3Co(111)$ relative to Pt(111). This is a direct consequence of the varying degrees to which the adsorption of the various ORR species are affected on $Pt_3Co(111)$ relative to adsorption on Pt(111).

The O-assisted H_2O dissociation reaction step is the most endothermic reaction step on $Pt_3Co(111)$ with a heat of reaction of 0.41 eV.

There is no apparent linear relation between the activation energy for O_2 dissociation and the dissociative adsorption energy of O_2 for pathways accessing the top-fcc/hcp- bridge transition state structures, therefore more calculations would need to be performed in order to establish whether a linear relation exist or not. Similarly, for OH formation the plot of activation energy as a function of the adsorption energy of OH is inconclusive as to whether there is a linear relation between the two variables. Hence more calculations would need to be performed in order to establish reliably whether a linear relation exist or not between the activation energy of OH formation and the adsorption energy of OH.

5.5 List of references

Balbuena, P.B., Calvo, S.R., Lamas, E.J., Salazar, P.F. and Seminario, J.M. 2006. 'Adsorption and dissociation of H_2O_2 on Pt and Pt-alloy clusters and surfaces.' *Journal of Physical Chemistry B* 110: 17452-17459.

Blöch, P.E. 1994. 'Projector augmented-wave method.' *Physical Review B* 50: 17953-17979.

Czerminski, R. and Elber, R. 1990. 'Reaction path study of conformational transitions in flexible systems: Applications to peptides.' *Journal of Chemical Physics* 92: 5580-5601.

Elber, R. and Karplus, M. 1987. 'A method for determining reaction paths in large molecules: Application to myoglobin.' *Chemical Physics Letters* 139: 375-380.

Eichler, A., Mittendorfer, F. and Hafner, J. 2000. 'Precusor-mediated adsorption of oxygen on the (111) surfaces of platinum-group metals'. *Physical Review B 62*: 4744-4755.

Ford, D.C., Nilekar, A.U., Xu, Y. and Mavrikakis, M. 2010. 'Partial and complete reduction of O_2 by hydrogen on transition metal surfaces.' *Surface Science* 604: 1565-1575.

Gilhan, R.E. and Wilson, K.R. 1992. 'Shadowing, rare events and rubber bands. A variational Verlet algorithm for molecular dynamics.' *Journal of Chemical Physics* 97: 1757-1772.

Henkelman, G. and Jónsson, H. 2000*a*. 'Improved tangent estimate in the nudged elastic band method for finding minimum energy paths and saddle points.' *Journal of Chemical Physics* 113: 9978-9985.

Henkelman, G., Ubernaga, B.S. and Jónsson, H. 2000*b*. 'A climbing image nudged elastic band method for finding saddle points and minimum energy paths.' *Journal of Chemical Physics* 113: 9901-9904.

Henkelman, G. 2001. *Methods for calculating rates of transitions with application to catalysis and crystal growth*. PhD Thesis., University of Washington: Washington.

Kandoi, S., Gokhale, A.A., Grabow, L.C., Dumesic, J.A. and Mavrikakis, M. 2004. 'Why Au and Cu are more selective than Pt for preferential oxidation of CO at low temperature.' *Catalysis Letters* 93: 93-100.

Kresse, G. and Joubert, D. 1999. 'From ultrasoft pseudopotentials to the projector augmented -wave method.' *Physical Review B* 59: 1758-1775.

Kresse, G. and Hafner, J. 1993. '*Ab initio* molecular dynamics for liquid metals.' *Physical Review B* 47: 558-561.

Li, H. and Jensen, J.H. 2002. 'Partial hessian vibrational analysis: the localization of the molecular vibrational energy and entropy.' *Theoretical Chemistry Accounts* 107: 211-219.

Logadottir, A., Rod, T.H., Nørskov, J.K., Hammer, B., Dahl, S. and Jacobsen, C.J.H. 2001. 'The Brønsted-Evans-Polanyi relation and the volcano plot for ammonia synthesis over transition metal catalysts.' *Journal of Catalysis* 197: 229-231.

Madala, T. 2012 (In preparation). *Reaction pathways for the formation of hydrogen peroxides in fuel cells: a DFT study.* MSc. Thesis., University of Cape Town: Cape Town.

Methfessel, M. and Paxton, A.T. 1989. 'High precision sampling for Brillouin-zone integration in metals.' *Physical Review B* 40: 3616-3621.

Michaelides, A. and Hu, P. 2001. 'Catalytic water formation on Platinum: A first principles study.' *Journal of American Chemical Society* 123: 4235-4242.

Michaelides, A., Liu, Z.P., Zhang, C.J., Alvi, A., King, D.A. and Hu, P. 2003. 'Identification of general linear relationships between activation energies and enthalpy changes for dissociation reactions at surfaces.' *Journal of American Chemical Society* 125: 3704-3705.

Mills, G., Jónsson, H. and Scheuter, G.K. 1995. 'Reversible work transition state theory: application to dissociative adsorption of hydrogen.' *Surface Science* 324: 305-337.

Monkhorst, H.J. and Pack, J.D. 1976. 'Special points for Brillouin-zone integrations.' *Physical Review B* 13: 5188-5192.

Neugebauer, J. and Scheffler, M. 1992. 'Adsorbate-substrate and adsorbate-adsorbate interactions of Na and K adlayers on Al(111). *Physical Review B* 46: 16067-16080.

Nørskov, J.K., Rossmeisl, J., Logadottir, A., Lindqvist, L., Kitchin, J.R., Bligaard, T. and Jónsson, H. 2004. 'Origin of the overpotential for oxygen reduction at a fuel cell cathode.' *Journal of Physical Chemistry B* 108: 17886-17892.

Perdew, J.P., Chevary, J.A., Vosko, S.H., Jackson, K.A., Pederson, M.R., Singh, D.J. and Fiolhais, C. 1992. 'Atoms, molecules, solids and surfaces: applications of the genaralized gradient approximation for exchange and correlation.' *Physical Review B* 46: 6671-6687.

Stamenković, V., Schmidt, T.J., Ross, P.N. and Marković, N.M. 2002. 'Surface composition effects in electrocatalysis : kinetics of oxygen reduction on well defined Pt_3Ni and Pt_3Co alloy surfaces.' *Journal of Physical Chemistry B* 106: 11970-11979.

Xu, Y., Ruban, A.V. and Mavrikakis, M. 2004. 'Adsorption and dissociation of O_2 on Pt-Co and Pt-Fe alloys.' *Journal of American Chemical Society* 126: 4717-4725.

Chapter 6

Concluding Remarks

In this chapter the key questions and the hypothesis proposed in chapter 1 are revisited to check whether through the results obtained in this study the key questions are answered and the hypothesis supported.

Key question 1: How do the different ORR species interact with the $Pt_3Co(111)$ surface and what is the strength of the ORR species on the $Pt_3Co(111)$ surface relative to the Pt(111) ?

From the calculations reported in chapter 3 the following answers to this key question are provided:

On $Pt_3Co(111)$ some ORR species adsorb in geometries which are not stable on Pt(111), e.g. for O_2 adsorption the bridge-fcc-bridge adsorption geometry becomes stable on $Pt_3Co(111)$ whilst on Pt(111) it is not.

The lowest adsorption geometries on $Pt_3Co(111)$ are the same type of geometries obtained on Pt(111). The type of adsorption geometries refers to geometries on either the atop, bridge, hcp or fcc positions.

For adsorbates that have an O-O bond, i.e. O_2, OOH and HOOH the O-O bond is activated more on $Pt_3Co(111)$ than on Pt(111). The O-O bond activation manifests itself through the lengthening of the O-O bond length and lowering of the O-O stretching frequency on $Pt_3Co(111)$ relative to Pt(111).

OOH does not adsorb at 3-fold-hollow sites based on Pt, i.e. f_{Pt} and h_{Pt} sites since no stable OOH configuration are obtained at these sites, instead O_2H dissociates to O and OH while adsorbed at these sites. Furthermore no stable OOH adsorption structures were obtained at 3-fold-hollow sites based on Co, i.e. f_{Co} and h_{Co} sites since the OOH structures at these sites optimised to bridge site structures.

No stable O_2 adsorption structures were obtained at the f_{Co} site which has subsurface Co at the fcc position. Thus subsurface Co at the fcc position destabilises O_2 adsorption at this site.

The lowest energy ORR species adsorption geometries on $Pt_3Co(111)$ have stronger adsorption energies than the lowest energy ORR species geometries on Pt(111). In Table 6.1 a summary of the adsorption energies of the lowest energy ORR species on both $Pt_3Co(111)$ and Pt(111) and the difference between the adsorption energies on both surfaces is presented.

Table 6.1: Summary of the calculated adsorption energies at 0.25 ML of the lowest energy ORR species and the difference in adsorption energies between $Pt_3Co(111)$ and Pt(111). The adsorption energies include zero point energy corrections.

ORR	**E_{ads} (eV)**			**Adsorption**	**ν_{O-O} (cm^{-1})**		**d_{O-O} (Å)**	
species	**$Pt_3Co(111)$**	**Pt(111)**	**$\triangle E_{ads}$ (eV)**	**site**	**$Pt_3Co(111)$**	**Pt(111)**	**$Pt_3Co(111)$**	**Pt(111)**
O_2	-0.97	-0.63	0.34	bridge	865	-	1.38	-
	-0.96	-0.59	0.37	top-fcc-bridge	713	818	1.43	1.40
O	-4.62	-4.17	0.45	fcc	-	-		
OH	-2.58	-2.21	0.37	bridge	-	-		
	-2.56	-2.19	0.37	top				
OOH	-1.37	-1.12	0.25	top-bridge	636	766	1.51	1.46
H_2O	-0.35	-0.15	0.20	top	-	-		
HOOH	-0.52	-0.29	0.23	top-bridge	774	852	1.48	1.47

Key question 2: How does the presence of Co on the surface affect the adsorption of the ORR species in comparison to adsorption on the Pt(111) surface?

From the calculations reported in chapter 3 the following answers to this key question are provided:

The surface Co atom stabilises the adsorption of all the ORR species relative to adsorption on Pt(111). The adsorption energies of the ORR species are stabilised to varying extents on $Pt_3Co(111)$ relative to adsorption on Pt(111). All the adsorption energies for the lowest energy adsorption geometries listed in Table 6.1 for adsorption on $Pt_3Co(111)$ are for all the ORR species bonded directly to a surface Co atom. The stabilisation of the ORR species on $Pt_3Co(111)$ relative to the lowest energy structures on Pt(111) are: O_2 = 0.34 eV and 0.37 eV, O = 0.45 eV, OH = 0.37 eV, OOH = 0.25 eV, H_2O = 0.20 eV and HOOH = 0.23 eV.

The surface Co atom modifies the electronic properties of the Pt atoms in $Pt_3Co(111)$ such that the adsorption energy of OH and OOH on $Pt_3Co(111)$ bonded to surface Pt atoms only, have adsorption energies higher than the adsorption strength of the lowest energy structures on Pt(111).

The surface Co atom in $Pt_3Co(111)$ results in more unique stable adsorption structures for the ORR species on $Pt_3Co(111)$ compared to the unique stable structures on Pt(111). Thus there are unique sites on $Pt_3Co(111)$ which are not present on Pt(111).

The presence of the surface Co atom in $Pt_3Co(111)$ stretches the O-O bond and lowers the O-O stretching frequency for adsorbates which have the O-O bond, i.e. O_2, OOH and HOOH relative to adsorption on Pt(111)

The surface Co atom in $Pt_3Co(111)$ does not stretch the O-H bond in ORR species having the O-H bond, i.e. OH, OOH, H_2O and HOOH since the O-H bond length is the same on $Pt_3Co(111)$ and on Pt(111).

The role of the surface Co atom in $Pt_3Co(111)$ in donating charge to the adsorbates varies for the different ORR species. For O_2 adsorption the highest charge transfer from the surface Co atom does not occur for the most strongly adsorbed O_2 configuration. For O, OH, OOH, H_2O and HOOH adsorption the highest charge transfer from the surface Co atom corresponds to the lowest energy adsorption configurations which are directly bonded to a surface Co atom.

Key question 3: What are the activation energies for the different elementary reaction steps on the $Pt_3Co(111)$ surface and how do they compare to those calculated on the Pt(111) surface?

Table 6.2: Calculated overall activation energies for the lowest energy reaction pathways for the possible ORR elementary reaction steps on $Pt_3Co(111)$ and Pt(111). The reported activation energies include zero point energy corrections.

	E_{act} (eV)		
Reaction step	**$Pt_3Co(111)$**	**Pt(111)**	**$\triangle E_{act}$(eV)**
O_2* + * $\rightarrow$ 2O*	0.08	0.59	0.51
2O* $\rightarrow O_2$* + *	2.31	1.69	-0.62
O_2* + ($H^+ + e^-$) $\rightarrow$ OOH*	0.56	0.52	- 0.04
OOH* $\rightarrow O_2$* + ($H^+ + e^-$)	0.48	1.04	0.56
O_2H* + * $\rightarrow$ O* + OH*	0.05	0.11	0.06
O* + OH* $\rightarrow O_2$H* + *	2.29	1.67	-0.62
O* + ($H^+ + e^-$) $\rightarrow$ OH*	0.86	0.95	0.09
OH* $\rightarrow$O* + ($H^+ + e^-$)	0.80	1.45	0.65
OOH* + ($H^+ + e^-$) $\rightarrow$ HOOH*	0.71	0.21	- 0.50
HOOH* $\rightarrow$OOH* + ($H^+ + e^-$)	0.95	0.41	-0.54
HOOH* + * $\rightarrow$ 2OH*	0.13	0.25	0.12
OH* + OH* $\rightarrow$HOOH* + *	2.07	1.62	-0.45
O* + H_2O* $\rightarrow$ 2OH*	0.84	0.92	0.08
OH* + OH* $\rightarrow$O* + H_2O*	0.43	0.33	-0.10
OH* + ($H^+ + e^-$) $\rightarrow$ H_2O*	0.38	0.21	- 0.17
H_2O* $\rightarrow$OH* + ($H^+ + e^-$)	0.73	0.82	0.09

From the calculations reported in chapter 5 the following answers to this key question are provided:

In Table 6.2 the calculated overall activation energies for the lowest energy pathways for the possible elementary ORR reaction steps on $Pt_3Co(111)$ and Pt(111) are shown.

On $Pt_3Co(111)$ O_2 dissociates with an overall activation energy of 0.08 eV which is significantly lower by 0.51 eV than that on Pt(111) of 0.59 eV.

For other dissociation reaction steps OOH on $Pt_3Co(111)$ dissociates with an overall activation energy which is 0.06 eV lower than on Pt(111) and for HOOH dissociation the overall dissociation activation energy is 0.12 eV lower on $Pt_3Co(111)$ than on Pt(111). All 3 dissociation reactions have very low activation energies of only 0.08, 0.05 and 0.13 eV for O_2, OOH and HOOH dissociation respectively.

For O hydrogenation to OH the overall activation energy for the lowest energy pathway on $Pt_3Co(111)$ is 0.09 eV lower than the overall activation energy calculated on Pt(111) for the lowest energy reaction pathway.

For OH hydrogenation to H_2O the overall activation energy on $Pt_3Co(111)$ for the lowest energy reaction pathway is 0.17 eV higher than the calculated overall activation energy for the lowest energy pathway on Pt(111).

For OOH hydrogenation to HOOH the calculated overall activation energy for the lowest energy reaction pathways is 0.50 eV higher than the calculated lowest energy reaction pathway overall activation energy on Pt(111). The big difference in the activation energy for HOOH formation on $Pt_3Co(111)$ compared to Pt(111) indicates that HOOH formation is kinetically (excluding concentration and entropic effects) facile on Pt(111) than on $Pt_3Co(111)$.

For O_2 hydrogenation to OOH the calculated overall activation energy for the lowest energy reaction pathway is 0.04 eV higher than the calculated overall activation energy for the lowest energy reaction pathway on Pt(111).

The calculated overall activation energy for the lowest energy reaction pathway for O-assisted H_2O dissociation reaction, i.e. O* + H_2O* $\rightarrow$ 2OH* on $Pt_3Co(111)$ is 0.08 eV lower than the calculated overall activation energy for the lowest energy reaction pathway on Pt(111).

The lowest energy reaction pathways for all the elementary reaction steps except for the hydrogenation of OOH to HOOH involves the reactants, transition state and the products bonded to a surface Co atom. Therefore, the surface Co atoms increases the overall activation energies for all hydrogenation steps except for O hydrogenation to OH whose overall activation energy is reduced by 0.09 eV on $Pt_3Co(111)$ relative to the activation energy on Pt(111). Furthermore the surface Co atoms lead to lower overall activation energies for the reactions involving the O-O bond scission steps on $Pt_3Co(111)$ compared to the calculated overall activation energies on Pt(111).

The overall activation energies for all the possible investigated elementary reaction steps likely to occur during the ORR which do not involve the reactants, transition state and the products bonded to a surface Co atom but only bonded to Pt atoms (i.e. Pt based reaction pathways) are higher than the calculated overall activation energies on Pt(111). Thus, the surface Co atoms leads to the overall activation energies of the ORR elementary reaction steps being higher for the Pt based reaction pathways on $Pt_3Co(111)$ than the calculated activation energies on Pt(111). The only exception is HOOH formation where the Pt based pathway has a lower overall and direct activation energy than the Co based pathway.

On $Pt_3Co(111)$ all the ORR species are strongly adsorbed relative to adsorption on Pt(111) and the consequence of the strong adsorption as discussed in chapter 4 is that there is a strong endothermic $\triangle E_{mix}$ required to get the species to the coadsorbed state prior to reaction. The endothermic $\triangle E_{mix}$ is linked to strong repulsive lateral interactions which need to be overcome to coadsorb the reactants prior to reaction. The consequence of the highly endothermic $\triangle E_{mix}$ calculated on $Pt_3Co(111)$ is the difference between the calculated direct and overall activation energies on $Pt_3Co(111)$ which range from 0.08 eV to 1.07 eV, with the highest difference of 1.07 eV calculated for OH formation in configuration b3-b and the lowest difference of 0.08 eV calculated for the dissociation of O_2 from configuration b1_f$_{Pt}$_b1.

Key question 4: Which reaction steps are likely rate-determining for the ORR on the $Pt_3Co(111)$ surface?

From the calculations reported in chapter 5 the following answers to this key question are provided:

The calculated highest activation energy reaction step which is likely to be rate-determining on $Pt_3Co(111)$ is the hydrogenation of O to OH, with an overall activation energy of 0.86 eV for the dissociative and associative 1 ORR mechanisms. For the O-assisted H_2O dissociation ORR mechanism the highest activation energy reaction step, likely to be rate-determining is the reaction O* + H_2O* $\rightarrow$ 2OH* with an overall activation energy of 0.84 eV. For the associative 2 ORR mechanism the highest activation energy reaction step, likely to be rate-determining is the hydrogenation of OOH to HOOH with a calculated overall activation energy of 0.71 eV.

In chapter 1 the following hypothesis were postulated:

1. The alloying element Co is expected to lead to ease of O_2 dissociation on the alloy surface with lower activation energies than on Pt(111).

The results presented in chapter 5 for the calculation of the activation energies for O_2 dissociation supports this hypothesis. On $Pt_3Co(111)$ O_2 dissociates with an overall activation energy of 0.08 eV which is 0.51 eV lower than the activation energy for O_2 dissociation from the lowest energy reaction pathway on Pt(111).

2. The alloying element Cobalt is expected to lead to selective stabilisation of O-containing intermediates.

From the adsorption calculations presented in chapter 3 the results support this hypothesis, since the adsorption energy of O_2, O, OH, OOH, H_2O and HOOH is stabilised on $Pt_3Co(111)$

relative to adsorption on Pt(111). The most stabilised adsorption energies on $Pt_3Co(111)$ are for O,OH and O_2 with 0.45 eV, 0.37eV and 0.34 eV extra stabilisation, respectively relative to adsorption on Pt(111).

3. The alloying element Co is expected to selectively lower the activation energies of certain elementary reaction steps and the affected reaction steps are therefore important in determining the rate of the ORR.

The calculated overall activation energies in chapter 5 support this hypothesis. The overall activation energy for O hydrogenation to OH is lowered by 0.09 eV on $Pt_3Co(111)$ relative to the calculated overall activation energy on Pt(111). The activation energy for O hydrogenation to OH is the highest overall activation energy step and is likely to be the rate-determining for the dissociative and associative 1 ORR mechanisms on $Pt_3Co(111)$.

The overall activation energy for the reaction O* + H_2O* $\rightarrow$ 2OH* is also lowered by 0.08 eV on $Pt_3Co(111)$ relative to the calculated overall activation energy on Pt(111). This reaction step is the highest overall activation energy step and likely to be rate-determining for the O-assisted H_2O dissociation mechanism. From the results presented in chapter 5 it can be concluded that the alloying element Co lowers the overall activation energy for the reaction steps using strongly adsorbed O on the surface as a reactant. Moreover, the reaction steps using O as a reactant are the highest overall activation energy steps and likely to be rate-determining steps.

On $Pt_3Co(111)$ the stable adsorption of the ORR species having the O-O bond leads to lower dissociation activation energies of these species on $Pt_3Co(111)$ relative to the activation energies calculated on Pt(111). The dissociation activation energy of O_2 is the most affected and the low activation energy for O_2 dissociation compared to the activation energy for O_2 hydrogenation to O_2H is likely to dictate which ORR mechanism is kinetically (excluding the concentration and entropic effects) preferred on $Pt_3Co(111)$. The ease of O_2 dissociation on $Pt_3Co(111)$ may lead to ORR mechanisms proceeding through adsorbed atomic O from direct O_2 dissociation to be preferred mechanisms, the mechanisms occurring through direct O_2 dissociation are the dissociative and the O-assisted H_2O dissociation ORR mechanisms.

On $Pt_3Co(111)$ the strongest adsorbing ORR species relative to adsorption on Pt(111) is O and the reactions using strongly adsorbed O as a reactant have the highest overall activation energy. The surface Co in $Pt_3Co(111)$ strongly adsorbs O but also makes the hydrogenation of O to OH occur slightly easier on $Pt_3Co(111)$ by approximately 0.10 eV lower overall activation energy than on Pt(111) by providing lower energy reaction pathways.

On the contrary the strong adsorption of OH on $Pt_3Co(111)$ relative to adsorption on Pt(111) results in a higher overall activation energy for OH hydrogenation to H_2O by 0.17 eV relative to the calculated overall activation energy on Pt(111). However, the overall activation energy for OH hydrogenation to H_2O on $Pt_3Co(111)$ of 0.38 eV is 0.48 eV lower than the overall activation energy for the highest overall activation energy step for the dissociative mechanism and 0.46 eV lower than the highest overall activation energy for the highest activation energy step for the O-assisted H_2O dissociation mechanism. Therefore, hydrogenation of OH to H_2O is not expected to be the likely rate-determining step for the two likely to be preferred ORR mechanisms on Pt(111).

Appendix A

Equations of thermodynamic corrections

The Gibbs Free energy for an ideal gas is given by:

$$G = E_{ads} + (H_{vib} + H_{trans} + H_{rot}) - T(S_{vib} + S_{trans} + S_{rot} + kTln\left(\frac{P}{P_0}\right)) \tag{A.1}$$

$$E_{ads} = E_{electronic} \tag{A.2}$$

$$H_{trans} = \frac{3}{2}RT \tag{A.3}$$

$$H_{rot(linear)} = RT \tag{A.4}$$

$$H_{rot(non-linear)} = \frac{3}{2}RT \tag{A.5}$$

Temperature dependent vibrational corrections to the enthalpy are described as:

$$H_{vib} = \frac{R}{k}\sum \frac{h\nu_i exp\left(\frac{-h\nu_i}{kT}\right)}{1 - exp\left(\frac{-h\nu_i}{kT}\right)} \tag{A.6}$$

$$ZPE = \frac{R}{k}\frac{1}{2}\sum h\nu_i \tag{A.7}$$

$$S_{trans} = \frac{5}{2}R + Rln\left[\frac{V}{N_A}\left(\frac{2\pi MkT}{h^2}\right)^{\frac{3}{2}}\right] \tag{A.8}$$

$$S_{rot(linear)} = Rln\left[\frac{8\pi IkT}{\sigma h^2}\right] + R \tag{A.9}$$

$$S_{rot(non-linear)} = \frac{1}{2}R\left[3 + ln\left(\left(\frac{\sqrt{\pi}}{\sigma}\right)\frac{8\pi^2 kT}{h^2}\right)^{\frac{3}{2}}\sqrt{I_1 I_2 I_3}\right] \tag{A.10}$$

Temperature dependent vibrational corrections to the entropy are described as:

$$S_{vib} = R\sum \frac{\left(\frac{h\nu_i}{kT}\right)exp\left(\frac{-h\nu_i}{kT}\right)}{1 - exp\left(\frac{-h\nu_i}{kT}\right)} - R\sum ln\left[1 - exp\left(\frac{h\nu_i}{kT}\right)\right] \tag{A.11}$$

h is the Planck's constant, ν_i is the vibrational frequency, k is Boltzmann costant, T is the temperature in Kelvin, σ is the symmetry number, I is the moment of inertia, M is the mass, N_A is Avogadro's constant and R is the gas constant.

The enthalpy and Gibbs free energy of formation at 298.15K are calculated by adding the rotational, translational and the vibrational corrections at 298.15 K for the enthalpy and the entropy to the electronic energy calculated at 0 K. The temperature corrections at 298.15 K are calculated using the above expressions.

$$\triangle H_f^0 = H_{products}^{298.15K} - H_{reactants}^{298.15K} \tag{A.12}$$

$$\triangle G_f^0 = G_{Products}^{298.15K} - G_{reactants}^{298.15K} \tag{A.13}$$

Bibliography

Steward, J.J.P. MOPAC Manual. http:// openmopac.net/ manual (accessed 31 May 2012).

Appendix B

Frequencies for the adsorption of the ORR intermediates

B.1 O_2 adsorption

O_2 adsorption configuration	ν (cm^{-1})
b1	864.67, 507.70, 399.14, 220.69, 174.73, 110.54
b2_f$_{Pt}$_t$_{Co}$	712.91, 440.49, 357.82, 273.75, 219.86, 143.83
b1_f$_{Pt}$_b1	709.32, 465.86, 343.20, 248.10, 193.08, 115.87
b1_f$_{Pt}$_t$_{Pt}$	772.93, 474.36, 369.22, 266.28, 213.47, 151.67
b1_h$_{Pt}$_t$_{Pt}$	781.90, 467.16, 364.64, 251.09, 187.34, 67.19
b3	904.58, 529.44, 362.26, 226.17, 186.86, 92.22
b3_h$_{Pt}$_t$_{Co}$	776.77, 439.62, 330.99, 226.22, 175.28, 39.67
b2	914.07, 519.82, 333.26, 205.56, 171.50, 81.68
b2_h$_{Co}$_t$_{Pt}$	828.93, 491.27, 353.28, 278.86, 189.65, 102.28
t$_{Co}$	1325.71, 281.42, 113.16, 108.74, 27.87, 7.71

B.2 O adsorption

O adsorption configuration	ν (cm^{-1})
f$_{Pt}$	442.74, 372.69, 363.28
h$_{Pt}$	434.25, 359.80, 310.22
f$_{Co}$	449.60, 355.10, 350.42
h$_{Co}$	458.28, 285.02, 281.94

B.3 OH adsorption

OH adsorption configuration	ν (cm^{-1})
b1	3635.10, 659.40,607.47, 389.86, 199.32, 154.29
t_{Co-a}	3664.75, 700.92, 523.21, 144.04, 92.84, 60.23
t_{Co-b}	3668.51, 694.51, 524.52, 243.87, 94.25, 28.61
f_{Pt}	3718.04, 538.03, 382.41, 356.20, 204.09, 174.94
b2-a	3681.96, 648.58, 642.81, 367.44, 211.83, 97.16
b3-a	3659.01, 690.06, 669.58, 347.40, 160.07, 130.17
b2-b	3638.48, 710.10, 661.11, 373.11, 197.29, 152.00
t_{Pt-b}	3671.95, 881.34, 489.08, 236.76, 113.33, 36.50
t_{Pt-a}	3681.81, 880.73, 496.56, 197.36, 117.56, 52.39
b3-b	3662.42, 710.80, 648.81, 352.07, 150.81, 145.73

B.4 OOH adsorption

OOH adsorption configuration	ν (cm^{-1})
b1	3559.01, 1175.54, 636.34, 541.04, 443.63, 293.54, 176.19, 147.18, 85.94
b2	3563.77, 1215.31, 697.88, 557.87, 454.32, 284.27, 146.27, 134.40, 65.63
b3	3577.54, 1242.00, 757.97, 472.62, 454.95, 269.03, 126.12, 88.21, 72.61

B.5 HOOH adsorption

HOOH adsorption configuration	ν (cm^{-1})
t_{Co-a}	3477.73, 3242.59, 1367.73, 1232.36, 773.88, 557.86, 290.56, 255.75, 171.59, 118.36, 94.72, 31.93
t_{Co-b}	3542.09, 3176.93, 1374.29, 1233.20, 779.39, 529.13, 320.26, 256.97, 172.54, 114.12, 102.50, 41.63
t_{Pt-a}	3599.97, 3170.74, 1388.20, 1282.04, 862.23, 503.27, 352.20, 202.49, 123.47, 114.98, 89.42, 21.62
t_{Pt-b}	3609.61, 3239.48, 1389.22, 1285.03, 868.71, 484.22, 324.17, 189.64, 123.70, 103.39, 79.56, 26.57

B.6 H_2O adsorption

H_2O adsorption configuration	ν (cm^{-1})
t_{Co-a}	3661.68, 3559.33, 1550.92, 542.79, 501.42, 215.01, 138.50, 117.27, 78.93
t_{Co-b}	3669.28, 3563.60, 1551.87, 537.38, 506.77, 213.31, 127.33, 114.54, 71.48
t_{Pt-a}	3746.13, 3614.89, 1566.72, 453.86, 406.63, 133.79, 116.38, 90.07, 60.48
t_{Pt-b}	3752.46, 3591.01, 1568.50, 457.97, 397.58, 120.80, 102.13, 88.92, 84.01

B.7 H adsorption

O adsorption configuration	ν (cm^{-1})
f_{Pt}	1254.74, 886.76, 341.43
h_{Pt}	1216.90, 863.35, 392.30
h_{Co}	1146.01, 597.30, 507.06
f_{Co}	1089.93, 760.38, 744.07
t_{Pt}	2210.97, 380.70, 286.38

Appendix C

Frequencies for the coadsorbed configurations

C.1 Coadsorbed O's

Dissociating O_2 configuration	ν (cm^{-1})
b2_f$_{Pt}$_t$_{Co}$	732.22, 466.90, 313.87, 304.18, 115.71, 100.33
b1_f$_{Pt}$_b1	507.95, 481.98, 456.56, 404.30, 358.61, 336.74
b1_h$_{Pt}$_t$_{Pt}$	669.31, 432.93, 381.04, 351.87, 88.86, 26.78
b3_h$_{Pt}$_t$_{Co}$	715.36, 455.57, 376.48, 373.99, 95.76, 87.75
b2_h$_{Co}$_t$_{Pt}$	519.32, 506.21, 461.15, 440.20, 391.19, 378.41

C.2 Coadsorbed O_2 and H

OOH adsorption configuration	ν **(cm^{-1})**
b1	2227.20, 882.75, 508.37, 450.67, 397.79, 367.96, 225.37, 192.39, 129.15
b2	2236.85, 908.72, 542.73, 529.04, 358.92, 306.46, 235.08, 194.74, 115.60
b3	2216.89, 935.40, 514.46, 498.76, 330.25, 322.96, 203.90, 178.32, 101.79

C.3 Coadsorbed OH and O

OOH adsorption configuration	ν **(cm^{-1})**
b1	3653.47, 720.04, 547.03, 447.63, 301.58, 265.81, 250.46, 130.34, 92.01
b2	3654.13, 920.14, 509.63, 430.47, 366.76, 325.40, 238.41, 124.82, 97.04
b3	3626.46, 982.88, 524.11, 466.46, 380.19, 340.26, 307.81, 152.57, 71.71

C.4 Coadsorbed O and H

OH adsorption configuration	ν (cm^{-1})
b1	2215.89, 470.00, 444.34, 372.51, 370.15, 327.25
t_{Pt-a}	2215.12, 464.21, 444.62, 377.57, 369.19, 341.45
b2	1258.60, 852.14, 507.58, 448.50, 376.51, 358.24
b3-a	2209.69, 451.32, 427.28, 358.17, 352.78, 315.02
b3-b	1455.63, 999.84, 447.75, 343.03, 330.69, 300.66

C.5 Coadsorbed OH+H

H_2 O adsorption configuration	ν (cm^{-1})
t_{Co}	3655.81, 2182.21, 713.06, 523.31, 410.80, 371.66, 285.30, 114.12, 26.79
t_{Pt}	3662.17, 2187.19, 906.38, 510.67, 486.02, 297.26, 216.00 157.12, 36.49

C.6 Coadsorbed H_2O and O

H_2 O adsorption configuration	ν (cm^{-1})
t_{Co}	3708.16, 2120.23, 1498.60, 1064.72, 699.47, 541.99 464.87, 364.20, 319.81, 236.97, 130.88, 127.86
t_{Pt}	3714.70, 3449.00, 1584.67, 716.94, 539.94, 416.52, 334.61, 315.48, 269.64, 164.00, 143.72, 117.38

C.7 Coadsorbed OOH and H

HOOH adsorption configuration	ν (cm^{-1})
t_{Co}	3459.82, 2168.83, 1214.41, 679.64, 586.08, 473.08, 454.61, 397.55, 297.99, 184.10, 158.70, 93.61
t_{Pt}	3558.48, 2202.03, 1206.29, 693.91, 583.08, 533.55, 451.60, 305.91, 289.40, 152.13, 143.74, 53.21

C.8 Coadsorbed OH's

Dissociating HOOH configuration	ν **(cm**$^{-1}$**)**
t_{Co}	3470.14, 3257.45, 1043.51, 952.74, 647.69, 545.14, 495.97, 466.53, 251.54, 136.00, 91.46, 70.50
t_{Pt}	3386.32, 3362.38, 1128.64, 1040.90, 676.14, 521.84, 513.85, 496.74, 281.18, 146.44, 61.81, 36.63

Appendix D

Frequencies for the transition state structures

D.1 Transition state for O_2 dissociation

Dissociating O_2 configuration	ν (cm^{-1})
b2_f$_{Pt}$_t$_{Co}$	610.46, 450.74, 294.17, 245.12, 147.29, 261.21i
b1_f$_{Pt}$_b1	470.22, 466.51, 277.63, 245.01, 229.46, 412.11i
b1_h$_{Pt}$_t$_{Pt}$	611.83, 453.22, 297.59, 243.30, 144.17, 255.05i
b3_h$_{Pt}$_t$_{Co}$	587.37, 436.84, 235.33, 226.39, 147.86, 335.89i
b2_h$_{Co}$_t$_{Pt}$	574.46, 494.19, 297.90, 229.33, 134.14, 418.23i

D.2 Transition state for the formation of OOH

OOH adsorption configuration	ν **(cm^{-1})**
b1	1280.86, 837.36, 752.25, 462.52, 362.44, 280.36, 204.84, 121.47, 825.30i
b2	1364.30, 874.48, 782.42, 503.80, 361.29, 306.90, 193.49, 139.79, 770.95i
b3	1008.75, 887.30, 803.69, 482.13, 325.81, 272.38, 191.79, 140.81, 975.96i

D.3 Transition state for the dissociation of OOH

OOH adsorption configuration	ν **(cm^{-1})**
b1	3581.22, 944.17, 621.83, 499.84, 377.84, 215.21, 159.97, 20.76, 346.18i
b2	3426.44, 1038.39, 640.98, 414.82, 275.76, 204.36, 137.24, 45.74, 399.62i
b3	3635.83, 840.56, 676.28, 543.76, 364.98, 208.40, 147.57, 75.63, 353.93i

D.4 Transition state for OH formation

OH adsorption configuration	ν (cm^{-1})
b1	1173.78, 605.03, 471.68, 299.69, 221.92, 995.82i
t_{Pt-a}	1212.69, 604.13, 473.26, 302.59, 213.74, 981.30i
b2	1804.70, 430.18, 305.90, 269.20, 130.56, 1204.06i
b3-a	1254.05, 587.32, 466.15, 309.73, 195.13, 1006.07i
b3-b	1914.57, 483.77, 269.87, 247.71, 115.85, 1095.02i

D.5 Transition state for H_2O formation

H_2 O adsorption configuration	ν (cm^{-1})
t_{Co}	3670.63, 1660.76, 695.01, 587.99, 477.48, 340.85, 220.23, 93.70, 412.11i
t_{Pt}	3659.94, 1622.06, 818.58, 617.41, 460.62, 395.40, 246.42, 103.22, 352.56i

D.6 Transition state for the reaction: O + $H_2O \rightarrow$ 2OH

H_2 O adsorption configuration	ν (cm^{-1})
t_{Co}	3684.16, 3416.43, 912.85, 745.22, 642.68, 494.17, 414.83, 242.98, 182.08, 132.78, 85.60, 126.27i
t_{Pt}	3698.73, 3658.01, 910.62, 859.78, 504.48, 472.04, 249.93, 198.42, 123.70, 64.15, 45.10, 236.24i

D.7 Transition state for the formation of HOOH

HOOH adsorption configuration	ν (cm^{-1})
t_{Co}	3595.02, 1443.48, 1199.73, 762.70, 497.10, 346.81, 221.50, 159.01, 105.04, 101.68, 100.10, 700.10i
t_{Pt}	3562.64, 1274.44, 1224.09, 820.85, 773.33, 545.63, 360.64, 305.96, 220.04, 152.87, 115.49, 561.00i

D.8 Transition state for the dissociation of HOOH

HOOH adsorption configuration	ν **(cm^{-1})**
t_{Co}	3631.08, 3462.52, 870.65, 801.97, 552.41, 410.47, 321.14, 162.13, 125.38, 110.75, 65.56, 245.53i
t_{Pt}	3627.62, 3462.48, 860.81, 829.71, 591.48, 380.37, 227.69 136.48, 118.01, 87.90, 11.69, 360.57i